The University Of Sheffield.

Instability and mixing of flow of supercritical water between subchannels

Muhsin Mohd Amin

A thesis submitted in partial fulfilment of the requirements for the degree of Doctor of Philosophy

The University of Sheffield
Faculty of Engineering
Department of Mechanical Engineering

April 2018

Acknowledgement

Praise to Allah s.w.t for giving me a chance to experiencing this wonderful PhD journey. In the four years of study, there are too many people come to my life that I should thank for their support and help along my journey. First and foremost, I would like to express my sincere gratitude to my dearest supervisor, Professor Shuisheng He for his guidance and support during my study. His experience and knowledge really have inspired and guided me along the way during my research. I really appreciate his patience while keeping motivating me. Thank you also to Dr Yu Duan who plays an important role in my LES research using *Code_Saturne*. He provides technical knowledge based on his experience on the research topic and I am indebted to his assistance.

Thanks to Dr Juan Uribe and Dr Charles Moulinec who provides technical support on *Code_Saturne*. To each and every one in Heat, Flow and Turbulence Research Group, I greatly appreciate all your help and encouragements. Every person in the group is always helpful, supportive and motivates each other, which have made my PhD experience more meaningful. I am also grateful for the financial support by Majlis Amanah Rakyat (MARA) who sponsored my study at the University of Sheffield.

Last but not least to all my family and friends back home who are always there and cheer for me. It makes me feel accompanied even though we are miles apart. I am grateful to them to understand and encourage me throughout my study.

Abstract

The effects of flow acceleration due to thermal expansion and those due to buoyancy have been investigated to study the flow and heat transfer behaviour in the flow of water at a supercritical pressure in a channel with a tight gap. The objective of these investigations is to develop a better understanding of the turbulent flow behaviour and heat transfer between subchannels specifically relevant to Supercritical Water-cooled Reactor (SCWR). Large eddy simulations with an SGS WALE model are carried out in a trapezoid annulus, which represents a tightly packed rod bundle configuration. The studies considered are (i) forced convection to study the flow acceleration due to thermal expansion and (ii) mixed convection to study the buoyancy influences.

In the case of forced convection, large flow structures have been observed in the narrow gap all heating cases considered, but such flow structures are much weaker in higher heat fluxes. The main reason for the weakening flow structures in the high heating cases is the severe variations of thermal properties. In particular, the streamwise fluctuations are reduced significantly downstream of the heated channel. The spanwise turbulence component reflecting the swinging flow structure is also found to be the highest in the narrow gap across the channel, but reduces as in forced convection swinging flow structure is weakened. The effect of variations of thermal properties has been found to be very similar to that of buoyancy.

In the case of mixed convection, the behaviour of the flow and heat transfer in the low buoyancy influence case is very similar to that of the forced convection. In high buoyancy influence cases, significant heat transfer deterioration has been found to occur. It has been

demonstrated that the swinging flow structures in the narrow gap in high buoyancy case are almost non-existent downstream in the heated channel. A number of potential reasons have been identified that the heat transfer deterioration in high buoyancy influences. They include the significantly reduced streamwise turbulence, disappearing of large flow structures as well as low mixing, and lastly significant variations of thermal properties.

Table of Contents

List of Figures

List of Tables

Nomenclature

A, B, C	Constants
C_s, C_s^d, C_w	Subgrid-scale constants
D	Diameter of the rod
D_h	Hydraulic diameter
$E_{uu}(f)$	Power spectrum density function
f^*	Friction factor
f_p	Frequency for the peak
g	Gap width
h_{ave}	Average heat transfer coefficient
k	Wavenumber, Turbulence kinetic energy
L	Length
LES_IQv	LES quality parameter [25]
ℓ	Lengthscale
p	Pressure
Q^+	Dimensionless heat flux
q	Wall heat flux
R_{ij}	Two-point correlation coefficient
s	LES quality parameter
S	The size of the narrow gap
$\mathbf{S}_{ij}$	Rate of strain tensor
t	Time

T_b	Bulk temperature
T_{pc}	Pseudocritical temperature
T_w	Wall temperature
u', v', w'	Fluctuating velocity component
$ueff$	Effective mixing velocity
U_b	Bulk velocity
U_c	Mean convection velocity of coherent structure
u_τ	Friction velocity
u	Characteristic velocity
u_i	$=(U, V, W)^T$,(i = 1, 2, 3), Velocity components
x_i	$=(x, y, z)^T$, (i = 1, 2, 3), Cartesian coordinates
Y	Mixing coefficient

Greek Symbols

Δ	Difference, filter width or delay
β	Thermal expansion rate
δ_{ij}	Distance between two subchannels
ε	Turbulence Dissipation Rate
η	Kolmogorov lengthscales
Θ	Normalized wall temperature
λ	Wavelength, thermal conductivity
μ	Dynamic viscosity
ν	Kinematic viscosity
ρ	Density

$\boldsymbol{\tau_0}$	Timescale
$\boldsymbol{\phi}$	Random variable
$\boldsymbol{\omega}$	Vorticity
$\boldsymbol{\Omega_{ij}}$	Rotation tensor

Subscripts or Superscripts

$\boldsymbol{ave}$	Average
$\boldsymbol{b}$	Bulk
$\boldsymbol{c}$	Convective, cut-off
$\boldsymbol{eff}$	Effective
$\boldsymbol{h}$	Hydraulic
$\boldsymbol{ij}$	Two adjacent subchannels
$\boldsymbol{max}$	Maximum correlation
$\boldsymbol{p}$	Peak
$\boldsymbol{pc}$	Pseudocritical
$\boldsymbol{sgs}$	Subgrid-scale
$\boldsymbol{T}$	Total
$\boldsymbol{t}$	Heated
$\boldsymbol{w}$	Wall
$\boldsymbol{\eta}$	Kolmogorov scales
$\boldsymbol{\tau}$	Friction value
$\mathbf{0}$	Initial or isothermal, large scale
$\mathbf{1}$	Final or outlet
$*, +$	Normalized

Nondimensional Numbers

$Bo*$	Buoyancy parameter
$Gr*$	Grashof number
Nu	Nusselt number
Pr	Prandtl number
Re	Reynolds number
St	Strouhal number

Other symbols

$\tilde{}$	Favre-averaged fields
$\bar{}$	Filtered fields
$\langle ... \rangle$	Time-averaged
$'$	Fluctuating component
$''$	Favre-averaged fluctuating component

Acronyms or Abbreviations

CFD	Computational Fluid Dynamics
CFL	Courant-Friedrich-Lewy
CS	Coherent structures
DNS	Direct Numerical Simulation
GIF	Generation-IV International Forum
HTC	Heat transfer coefficient
HTD	Heat transfer deterioration

HTE	Heat transfer enhancement
LES	Large eddy simulation
$LMFBR$	Liquid Metal Fast Breeder Reactor
POD	Proper orthogonal decomposition approach
PSD	Power spectrum density
$RANS$	Reynolds-Averaged Navier-Stokes
RSM	Reynold stress model
SCP	Supercritical pressure
$SCWR$	Supercritical Water-cooled Reactor
SEM	Synthetic Eddy Method
SGS	Subgrid-scale
SMR	Small modular reactors
$URANS$	Unsteady Reynolds-Averaged Navier-Stokes
$WALE$	Wall-Adapting Local Eddy-Viscosity

Chapter 1

Introduction

1.1 Background

Supercritical Water-cooled Reactor (SCWR) is one of the six prominent nuclear reactor concepts that have been selected under Generation-IV International Forum (GIF) and is currently under development. SCWR has the advantage of a high thermal efficiency, which is between 45-50%. In comparison, the thermal efficiency of current light water reactors is around 33-35% [1]. The understanding of the flow and heat transfer characteristics of the coolant water of SCWR is essential for both design and operation. This is because even though the water at supercritical pressure does not undergo any boiling process through heating, the thermophysical properties vary dramatically as the temperature goes through the pseudo-critical point. This 'anomaly' behaviour of the thermophysical properties often leads to unusual characteristics with regards to heat transfer. The phenomena of heat transfer deterioration or enhancement have been reported by many researchers. Heat transfer deterioration (HTD) should be avoided to maintain the integrity of the fuel cladding [2]. It is acknowledged that for the supercritical fluid flow, it is hugely important to be able to predict

the detailed flow and temperature distributions for the development of reactor design and safety.

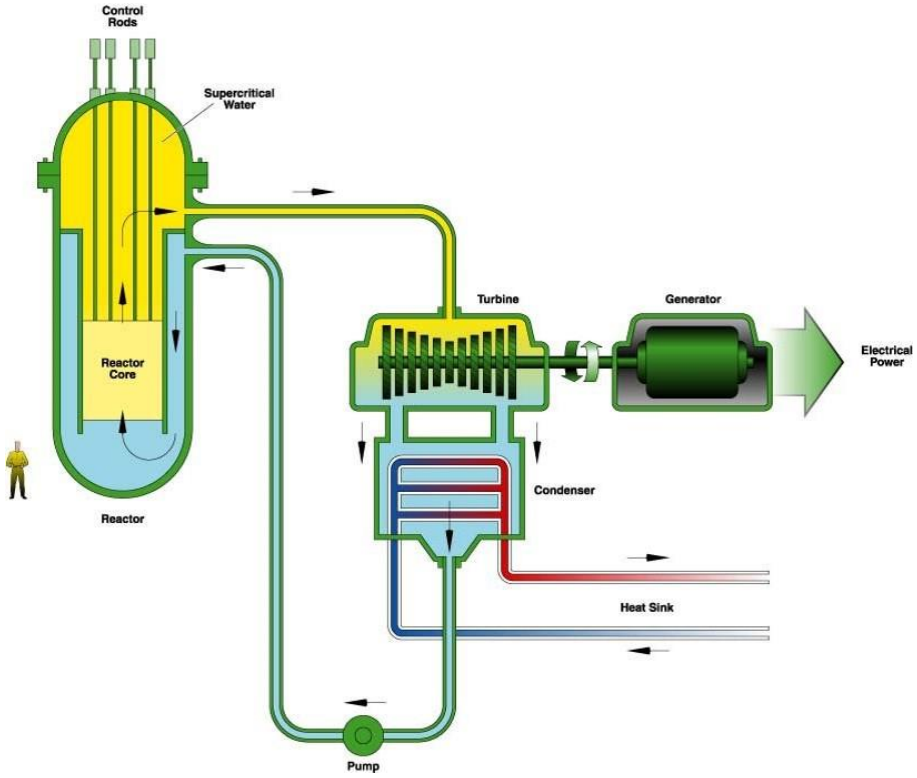

Figure 1.1: Schematic diagram of SCWR pressure-vessel [3]**.**

Recently, small modular reactors (SMR) have become popular. They potentially provide a simpler and much safer design [4–7]. SMR is a fraction of the size of a conventional nuclear power plant. This makes SMR ideal for providing the electricity at a location with small, limited, or distributed electricity grid system. It can also be useful for countries with limited financial resources, as the investment requirements are much less than that of a large nuclear power plant [4]. The supercritical reactor system has also been selected in some of the SMR designs [8–10]. Similar to the conventional of the proposed design of SCWR, supercritical type of SMR has the potential advantage of increasing the efficiency and the simplicity of the design as no phase change occurs at supercritical pressure.

In nuclear reactor designs, the typical configuration of fuel assemblies is usually in the

form of rod bundles and this is also true for the SCWR. The coolant in a rod bundle flows through via subchannels that are formed in the interstices of the fuel rods. Subchannels in the fuel rods array are connected to each other by the gaps that formed between the fuel rods. These gaps are commonly characterised by the pitch-to-diameter ratios. Within these gaps, they may be an occurrence of instability and inter-channel mixing of the flow. Understanding the behaviour of this flow and its influence on the overall flow and heat transfer at supercritical pressure in a rod bundle could be an essential input to the SCWR core design. An International Atomic Energy Agency (IAEA) Coordinated Research Project (CRP) has identified that the study of the flow between subchannels at supercritical pressure to be an area where better knowledge needs to be developed [11]. This information can assist the further development of subchannel codes.

1.2 Aims and Objectives

The goal of the present research is to develop knowledge of the turbulent mixing and instabilities of the flow across the gaps between subchannels in supercritical water flow. The focus of this research is on the effect of large flow structures in the tight gap to the flow and heat transfer at supercritical pressure. The present work is an extension to the recent study of mixed convection on the behaviour of the flow and heat transfer in the trapezoid annulus by Duan & He [12,13]. It was reported that the behaviour of large flow structures in the flow channel plays a dominant role in the complicated buoyancy influence flow, which intertwines with other factors such as the redistribution of the mass flow rate and the variation of buoyancy influence to local turbulence in different regions of the channel.

The present PhD study aims to further investigate the behaviour of the turbulent flow and

heat transfer in the rod-bundle-like configuration specifically relevant to SCWR. Also, the thesis aims to complement the numerical experiment study of the behaviour of the large flow structures in supercritical water by investigating the effect of the thermal expansion due to the thermal property variation in forced and mixed convection.

The specific objectives covered by this thesis are:

1. To develop a Large Eddy Simulation (LES) model within the framework of *Code_Saturne* for the study of flow and heat transfer in supercritical water.
2. To investigate the flow instability and large unsteady flow structures in a rod-bundle-like configuration for supercritical water under the condition of forced convection.
3. To investigate the flow instability and large unsteady flow structures in a rod-bundle like configuration for supercritical water under the influence of buoyancy.
4. To develop mixing parameters between subchannels as an input for use in subchannel codes.

1.3 Thesis Outline

The present thesis consists of six chapters. Chapter 2 presents a summary of literature reviews on relevant subjects on the supercritical fluid flow and the flow in rod bundles. The instability and mixing phenomenon between channels across the narrow gaps are reviewed. Next chapter (Chapter 3) introduces the background of turbulence studies, followed by the statistical description for turbulence characteristics. This chapter also discusses the Large Eddy Simulations (LES) approach with the SGS models and present numerical schemes used in *Code_Saturne* for the present investigations.

The study of forced convection for supercritical water in trapezoid annulus is discussed in Chapter 4, whereas in Chapter 5 the investigations on the buoyancy-aided flow in the trapezoid annulus are presented. Finally, in Chapter 6, conclusions of the present studies and discussion of future work are outlined.

Chapter 2

Literature Review

2.1 Fluid Characteristics at Supercritical Pressure

At supercritical pressure, fluid properties behave differently compared to those at subcritical pressure. As the temperature increases at constant pressure, the fluid does not undergo any boiling process, that is, the phase of the fluid does not change. However, the fluid does change from the liquid-like to gas-like condition with a significant variation of thermal properties around the pseudocritical point. This anomaly could affect the turbulence behaviour in a heated channel and consequently change the heat transfer rate, especially around the pseudocritical point. Fluid in this condition may also be simply referred to as supercritical fluid.

The thermophysical properties of a fluid at supercritical pressure (SCP) vary dramatically and this can cause a decrease in the heat transfer rate. The phenomenon could take place within the near-critical and pseudocritical regions. For water, the critical pressure and temperature are 22.064 MPa and 373.95ºC respectively. The heating process at a constant

supercritical pressure will change the water from a liquid-like phase to a gas-like phase with a dramatic and fast change of thermophysical properties near the pseudocritical temperature, T_{pc}. Some properties decrease drastically across T_{pc}, such as density, thermal conductivity and dynamic viscosity, while the specific heat reaches its peak value at T_{pc}.

The strong variations of thermal properties may have a significant effect on the turbulent flow. Many researchers have worked in this area to determine the general behaviour or characteristics of the turbulence at this condition. The properties variations could largely affect the turbulence production in very complex manner, consequently affecting the effectiveness of the heat transfer. Therefore, the in-depth understanding of the turbulent flow structure at supercritical pressure is very important for the development of SCWRs.

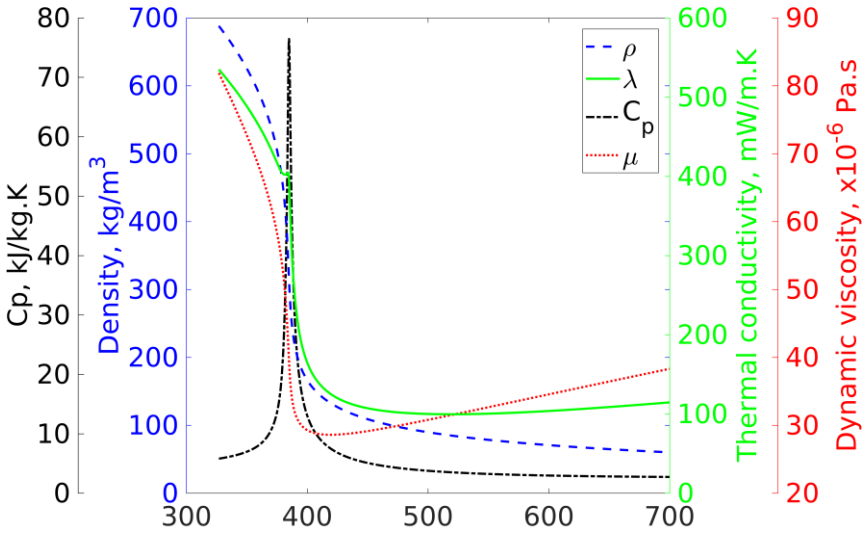

Figure 2.1: Thermal properties of water around pseudocritical temperature at 25MPa. (T_{pc}=385°C)

2.1.2 Supercritical Flow Studies

The heat transfer in supercritical fluids has applications in many industrial applications, including, for example, supercritical steam generators in fossil-fuelled power plants, supercritical hydrogen fuelled chemical nuclear rockets, supercritical fluids for transforming geothermal energy into electricity, air-conditioning and refrigerating systems with supercritical CO_2 refrigerant, and processes such as supercritical chromatography, supercritical fluid extraction and polymer processing in pharmaceutical and chemical industries [14]. The idea to increase the thermal efficiency of fossil-fuelled power plants by using the supercritical water for steam generators was found attractive in the 1950s. With the same technology employed in the modern supercritical fossil-fuelled power units, it is expected that the thermal efficiency of modern nuclear power plants could be increased from 33-35% to 45-50%. The concept of supercritical water reactor (SCWR) has been recommended as one of the next generations of nuclear types in the Generation IV International Forum (GIF) for further development [15]. A better understanding of problems associated with the supercritical fluid flow and heat transfers in the fuel assemblies is much needed in developing SCWR.

Most studies published on the heat transfer to the supercritical flow, usually concerned in a heated circular tube or channel. However, the behaviour of the flow and heat transfer in fuel assemblies in the reactor could be more complicated than the simple geometry of a tube or heated channel. The literature review will cover some conditions related to the supercritical flow. The general behaviour and characteristics of the supercritical flow in heated tubes and channels are discussed here, while the heat transfer in rod bundles or subchannels will be discussed later in §2.2.2, which focuses on this topic specifically.

The general behaviour of heat transfer

The heat transfer of the supercritical flow can be classified into three groups, namely, 'normal,' 'deteriorated' and 'improved' modes [16,17]. The normal heat transfer mode can be described to be similar to the heat transfer that is outside from the pseudocritical range, where a monotonic change of wall temperature is observed in a uniformly heated tube. Heat transfer deterioration is encountered in a test section whenever a sudden increase of wall temperature due to a sudden drop in heat transfer coefficient occurs. In contrast, an increase of heat transfer coefficient suggests an 'improved' heat transfer mode. Heat transfer deterioration (HTD) usually occurs at high heat flux and low mass flux. The effect of flow acceleration or the buoyancy force, are often the causes of HTD, where both effects may lead to a decrease in turbulent kinetic energy by reducing the level of Reynolds stresses near the wall region. Consequently, heat transfer is impeded (refer to [17]). It is also worth noting that a sudden increase in wall temperature may raise a safety concern as it could potentially cause damage to the pipe or cladding of the fuel pin. It has been an interest of many researchers to understand this phenomenon. Some review of the work carried out on this topic can be found in [16–22]. In this section, a summary of the heat transfer at supercritical pressure will discuss briefly.

When strong variations of thermophysical properties occur near T_{pc}, the supercritical water flow behaves in a complicated manner and flow instability may occur along with pressure pulsations and oscillations of T_w, consequently making the system unstable. This has been observed by several researchers [23–27]. The unusual behaviour can be explained by the combination of single-phase and two-phase fluid dynamics theory. The former is based on the unstable characteristics of the thin boundary layer due to excessive changes in the

thermophysical properties, while the latter is based on the unusual phenomena due to the transition from pseudonucleate to pseudofilm boiling process. However, there is no consensus among researchers on the real causes of flow instability and it is still subject to the further investigation [28].

In essence, the peculiarity of heat transfer to supercritical fluids is caused by buoyancy and flow acceleration due to the thermal expansion, as supported by the comparison made experimentally for the upward flows and downwards flows under the same conditions [29–31]. Yamagata *et al.* [32], among others discussed another interesting feature of the heat transfer of supercritical fluids, that is, the peak value of the convective heat transfer coefficient found near the critical or pseudocritical point. This is due to the abrupt change of thermophysical properties of the fluid. This phenomenon was seen to persist in both vertical and horizontal tube flow. The magnitude of the peak of heat transfer coefficient decreased with increasing heat flux and pressure. Similar results were also observed later by Yoshida & Mori [33].

In an upward flow, the buoyancy effect may cause an enhancement or deterioration of the heat transfer, while in a downward flow only an enhancement may occur [34]. Meanwhile, the acceleration effect due to thermal expansion only causes a deterioration in both upward and downward flows. The buoyancy effect and the flow acceleration are respectively a result of the gradient of density in radial and axial direction [28]. A theoretical explanation has been provided by Hall & Jackson [29], where the main factor of the HTD phenomena is due to the modification of the shear-stress distribution across the pipe with consequential changes in turbulence production. A study by Tanaka *et al.* [31] investigated the effects of buoyancy and flow acceleration due to the thermal expansion on turbulent

forced convective heat transfer to supercritical fluids in vertical tubes. The authors found that the effects of the two factors operate similarly with a very rapid decrease of the shear stress near the wall and they proposed a criterion of the reverse transition from turbulent to laminar flow. A general criterion for the onset of the buoyancy effect applicable to both SCP and the subcritical pressure was later provided by Jackson & Hall [35,36]. In addition, HTD is not restricted to the pseudocritical region, but it occurs in all temperature ranges including subcritical pressures [37]. Experimental work on annuli tube has been conducted by Glushchenko *et al.* [38] and Ornatskiy *et al.* [39] and it has found that in the upward flows of water in annuli, the wall temperature variations were similar to that in tubes when both tubes and annuli are long [37].

Numerous engineering correlations proposed were based on experimental data. These correlations will usually relate Nusselt number to the Reynolds number and Prandtl number. The modification of Dittus-Boelter equation is very popular among many proposed correlations in predicting the temperature distribution in a cylindrical tube. To improve the accuracy of heat transfer predictions for supercritical fluids, the effect of property variations such as density and specific heat at constant pressure has also been adopted in many correlations [40–45]. There are a few studies which introduced Grashof number and dimensionless heat flux, q^+ into the correlation to consider the buoyancy and thermal acceleration effect [46,47] but the predictions are still quite poor. It is noted from the report by IAEA [11] that the correlations available are mostly for tubes and at specific conditions. Research has to be extended to several other aspects (e.g., geometries, gap sizes, spacing devices, axial power profile, etc.) before correlations can be implemented for safety analyses and fuel design supports. This also includes the use of correlation in the subchannel

application, where those data are still rather limited

Numerical studies

Following computational advancement, the work on supercritical fluid flow has also been extended numerically since the 1980s to further investigate the physics of turbulent convective heat transfer. Most work has focused on developing a reliable turbulence model that can provide reasonable accuracy in predicting the heat transfer of supercritical fluids flows at different situations. Most of the turbulence models available are able to capture the general behaviour of heat transfer for the forced convection of supercritical fluids in channels [48–50]. That is, in such conditions, the turbulent only influenced by the flow acceleration caused by the property variation of the fluids, while no buoyancy influence is included. It is a challenge for the turbulence modelling in the heat transfer of supercritical fluids flow with the effect of buoyancy. Under such conditions, it must be able to predict reasonably accurate results for heat transfer when a significant laminarisation effect due to the buoyancy force is present. This phenomenon can occur in both vertical and horizontal flows.

An assessment of some low Reynolds number turbulence models for their performance on predicting the heat transfer and flow of supercritical CO_2 in a heated tube has been carried out by He *et al.* [51–53]. All turbulent models assessed were compared with DNS data. The general behaviour of the buoyancy influences on heat transfer was able to be captured by the models tested, but the performance varied from one model to another. The performance of V2F model [54] was the best among all turbulence models assessed. All tested models were preformed varied significantly between one another, but most are able to reproduce turbulent kinetic energy recovery under strongly influenced buoyancy reasonably well. However, they were still unable to reproduce the heat transfer enhancement fully which partly due to their

inability to reproduce the turbulent heat flux using a constant turbulent Prandtl number [55].

On the other hand, SST-k-ω model has also found to be a good turbulence model by some authors asserting that it is as good as the V2F model [54]. Wen & Gu [56,57] found that their numerical simulations with the SST model had good agreement with experimental data that they compared with under both studies at the same flow conditions. Similarly, Jaromin & Anglart [58] found good agreement between the SST model and the experimental data by Shitsman (1963) and Ornatskij *et al.* (1973) where the authors discussed the significant influence of turbulent Prandtl number on predicting the wall temperature and consequently the HTD. Moreover, Liu *et al.* [59,60] found that the SST model performs the best in their mixed convection study of annular and circular tubes of water at supercritical pressure under a specific condition. Comparisons were made with experimental data similar to above of Shitsman (1963) and Ornatskij *et al.* (1973) for the tube [60], while data from Glushchenko & Gandzyuk (1972) was used for the annular channel [59,60].

In addition to the above models, an RNG k-ε, model as well as Reynold stress model (RSM) with an enhanced wall treatment, have been tested by Kao *et al.* [61]. They compared their results with experimental data of Yamagata *et al.* [32]. The predictions from both models showed good agreement with experimental data on predicting the heat transfer enhancement (HTE). The RSM model has also been tested for its capability to simulate HTD. Comparisons were made with the data from Shitsman (1963) and the authors concluded that it was capable of predicting HTD. Similar to other work, the authors also discussed the importance of the treatment of turbulent Prandtl number on predicting the deterioration.

For DNS, Bae *et al.* [33] have documented the supercritical CO_2 upwards and downwards flow in a circular pipe. In order to obtain a fully developed isothermal turbulent inflow flow,

Bae *et al.* implemented a spatially periodic domain at the inlet which is non-heated before the main heating domain. From their results, they observed that the change in the streamwise turbulent heat flux is strongly influenced by the buoyancy condition in an upward flow. When the maximum deterioration of heat transfer occurred at a reduced turbulence region, a positive distribution of the streamwise turbulent heat flux found to be dominant in the cross-section. From their results, they indicated that buoyancy production terms have a direct effect on the Reynolds stresses and turbulent heat flux, where this is true in vertical supercritical flows. An annular supercritical CO2 flow was also studied by Bae *et al.* [37] to investigate the flow behaviour in the near wall region in an upward direction. The authors found that when the wall temperature surpassed the pseudocritical temperature ($T_w > T_{pc} > T_b$), a strong stabilizing effect from the variations of properties and buoyancy occurred that the turbulence cannot be self-sustained. It is also observed that a high radial turbulent heat flux within the cross-section of the channel may co-exist with a nearly flat temperature distribution outside the viscous region due to the increase of energy of the fluid without changing the temperature.

Some studies used large eddy simulations (LES) in their work. Kunik *et al.* [62] study the forced convection in a circular tube for supercritical CO_2 by using LES. They implemented an inflow generator to ensure a fully developed at the inlet of their heated domain. SGS models that were tested in the paper are Smagorinsky, Dynamic kinetic energy and Kinetic energy. It was shown from their results that the best prediction when the mesh was coarse was that of the dynamic kinetic energy SGS model. Meanwhile the LES study by Niceno & Sharabi [63] tested a WALE SGS model with two SGS models as metnioned above (Smagorinsky and Dynamic Smagorinsky SGS model). The advantages and disadvantages of each model were discussed. The WALE model was found to be the best, stable and

performed well in the near wall region. In comparison, even though the Dynamic model is quite good as the SGS viscosity can be damped in the near-wall region, but it is numerically unstable as the produced SGS viscosity can be negative. On the other hand, the WALE model is able to keep the eddy viscosity positive thereby making it more stable. This advantage makes WALE capable of achieving a result similar to DNS simulation if the mesh is fine enough. LES simulation is shown to be performed well to predict the heat transfer deterioration and turbulent kinetic energy. The authors observed that from the total production of turbulence in upward flows, the buoyancy production is significant whereas its contribution was small to the total production in the downward flow.

2.2 Flow Studies in Rod Bundles

2.2.1 Studies for Fluids at Subcritical Pressure

The standard configuration of a nuclear reactor core is normally in the form of rod bundles, where the main heating takes place through these rods (fuel pins). Several types of fuel rod bundle configurations have been considered in previous work. The rod bundle configurations used for research work are either in the form of a whole rod bundle, a section of it or some subchannels. The latter may be categorised into four different types depending on its location in a fuel assembly, namely, ordinary, edge, corner, or guide tube. In a subchannel analysis [64], the degree of subchannel heterogeneity is measured by the ratio of the heated perimeter to the flow area, H/A.

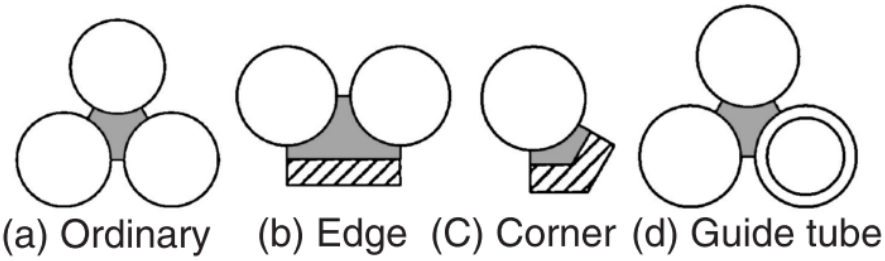

Figure 2.2: Subchannel types [64]**.**

The significant difference of turbulence structures between a subchannel rod bundle and an axisymmetric pipe flow were first discovered by Rowe *et al.* [65]. The flow conditions inside the rod bundles have been revealed to be very different from the typical pipe flow, as the flow in subchannels is bounded by adjacent rods and the containing pressure tube walls. Flow through a subchannel is very complex and may exhibit patterns that are not present in pipe flows [66–68]. The formation of secondary vortices inside these configurations is a result of the near-wall turbulence anisotropy that causes the coolant to spiral through the rod bundles and also between subchannels. Hooper & Rehme [69] were the first to demonstrate the existence of periodic azimuthal variations of the turbulent-velocity component through the gaps of closely spaced rod arrays. The azimuthal turbulent-velocity component is not associated with the secondary-flow velocities driven by the Reynolds-stress gradients.

Even though there are some experimental investigations on flows in rod bundles, work considering mixed convection is still rather limited. As mentioned earlier, in a rod bundle turbulent mixing and crossflow between subchannels occur, which makes the heat transfer in rod bundle more complicated than in simple channels such as circular or annular tubes.

In nuclear rod bundles, spacer grids are used to maintain the position of each fuel rod. They also have the function of safeguarding the structural integrity of the rod bundle as the fuel rod expands at higher temperatures. The presence of spacer grids may hinder the coolant flow and cause an additional pressure drop. However, the heat transfer performance may be

enhanced by spacer grids due to an increase in the local heat transfer coefficient [70–73]. Some correlations for the local Nusselt number downstream of a spacer grid has also developed [74,75].

Some CFD work has been conducted in 5 × 5 rod bundle [76–78] to study the effect of spacer grids and mixing vanes to the flow. A recent experiment study by Liu & Gu [79] has considered a 5 × 5 square arrayed rod bundle. They tested Reynolds numbers ranging from 1×10^{3} to 3×10^{4} with Bo^{*} number from 1×10^{-6} to 5×10^{-2}. In rod bundles, the effect of mixed convection was found to be similar to that in simple channels deterioration of heat transfer followed by the recovery as the buoyancy is increased. They concluded that the effect of buoyancy on the heat transfer should not be neglected especially at low Reynolds number.

CFD simulations tend to be a popular tool used by researchers in the study of the flow behaviours within a rod bundle. Specifically, the RANS/URANS approach is found to be the most popular adopted approach. Its flexibility and relatively cheaper resource requirement make it the best choice for many applications.

With regards to the application of the rod bundle flow, RANS predictions may perform poorly if no any specific adjustments are considered. This has been shown by Lee & Jang [80], where they used a non-linear k–ε model without any adjustments on the closely spaced bare rod arrays. They found that the model strongly underestimated the strong azimuthal turbulence intensity shown by Hooper & Rehme [69]. Meanwhile, Xiong *et al.* [81] tested two types of Reynolds stress models, i.e., the SSG model and the baseline-RSM (BSL-RSM) for an experimental validation study of 3×3 rod bundle. The authors concluded that the failure in calculating the strongly negative $\overline{u'w'}$ in the gap region connecting subchannels caused large discrepancies of axial flow velocity between the numerical and experimental results.

These examples showed that the lateral flow pulsations could not be predicted by a steady RANS calculation and they are also incapable of resolving the flow unsteadiness.

Rod bundles considered in previous work are restricted to the geometries where only elementary sections are simulated using the assumption of symmetry across the boundaries [80–83]. When unsteady structures are concerned, this is not appropriate as it oversimplifies the condition at the symmetry, especially around the gaps. Most numerical studies on subchannels do not capture the complete flow phenomena in the whole bundle, where several types of subchannels may be present. Taking the 37-rod bundle of the CANDU reactor as an example, it consists of different kind of subchannels such as triangular, square and edge subchannels. To capture the possible interactions between different types of subchannels require full bundle simulations. This approach can be computationally expensive, even though it could provide more information and develop a better understanding of the mixing network within the whole bundle. In addition, most studies in rod bundles considered an isothermal flow and only a few studies were concerned with mixed convection at constant properties.

Three different types of subchannels, including an ordinary, edge and corner subchannels have been studied by Gou *et al.* [84,85]. Among all turbulence models chosen, the Speziale quadratic non-linear high Re k-ε model with two layers near-wall treatment has the capability to reproduce the anisotropic turbulence flow in non-circular flow channels. From the chosen model, secondary flows were observed in their studies. The same model has been applied by some other researchers for rod bundle studies in supercritical water and has been shown to perform well [86–88].

Natesan *et al.* [89] investigated the flow in a 19-rod bundle of a liquid metal fast breeder

reactor (LFMBR) with wire wrapped rods using k-ε, k-ω and a Reynolds stress model. From the simulations, it was found that Nusselt number and the heat transfer coefficient are insensitive to the pitch of the rod bundle. In terms of the fuel assembly design, the wire wraps in the rod bundles could enhance mixing in the coolant and hence reduces temperature variations among the sections of the subassembly.

Ninokata *et al.* [90] studied the flow in a tight lattice triangular configuration of rod bundle at low Reynolds number using three different approaches, i.e., Direct Numerical Simulation (DNS), Large Eddy Simulation (LES) and Unsteady Reynolds-Averaged Navier-Stokes (URANS). They developed simple analytical methods to detect and capture coherent structures, the cause of instabilities and the onset conditions of local laminar-turbulent transitions. By comparing the three approaches used, it was concluded that LES is the most promising approach to conduct thermal hydraulics study in fuel subassemblies as it gives sufficient information but is not as expensive as DNS. Another LES study was carried out by Zhang & Yu [91] to investigate the flow excitation in 43-pin CANDU caused by the endplates at the entrance and bundle-to-bundle interface. They found that the major disturbance source to the flow was from the endplates. They also confirmed that bare fuel elements without endplates do not produce significant flow fluctuations and wakes in the entrance region.

Results from LES have been demonstrated to be more superior than those from the RANS/URANS approach even though the implementation of this approach is still quite limited due to the large requirement of computational time and mesh density needed. The predictions of the characteristics of the flow such as the vortex street and flow pulsations in the rod bundles can be investigated further using LES and could provide more information

to the general behaviour of the flow in such configurations.

2.2.2 Flow Studies in Rod Bundles at Supercritical Pressure

There have been only a few experimental studies that have been done for flows at the supercritical condition for configurations other than tubes, e.g., an annulus and especially flow in a rod bundle. One of the early studies at supercritical pressure for rod bundle was done by Dyadyakin & Popov [92] and Silin *et al.* [93]. Dyadyakin & Popov [92] investigated the flow in a tight bundle of seven rods in which all rods had four helical fins on them and pressure oscillations were recorded in their study. A correlation was developed from this study, which has been referenced in several later studies [94–97]. Silin *et al.* [93] reported that the there is no heat transfer deterioration observed in the multi-rod bundles compared to the same test parameter range in tubes where the phenomenon exists.

An experimental study by Richards *et al.* [97] considered supercritical Freon R-12 in a 7-element rod bundle. The data obtained from this study has been compared with several correlations. They found that all correlations predict the HTC poorly with the experimental data. The effect of spacers has also been observed to either deteriorate or enhance heat transfer depending on the parameters tested. Similar effects on heat transfer were noted for wire wrapped pins by Li *et al.* [28].

There are also a few recent studies on a 2×2 rod bundle with rounded corners in supercritical water. Experimental studies from Shanghai Jiao Tong University considered the rod bundle with and without wire wraps [98–100], and several correlations have been compared with their experimental data. From those studies, they concluded that the correlations that produced the best prediction are those of Jackson & Fewster [44], and

Bishop *et al.* [41]. Gu *et al.* [98] also showed that the buoyancy parameter developed by Cheng *et al.* [101] characterises the dependence of heat transfer coefficient quite well. Meanwhile, similar work of 2×2 rod bundle was also investigated by Wang *et al.* [102] and among the eight correlations that were compared with their experimental results, only the correlations by Jackson [45] and Ornatsky [103] predicted the more accurate Nusselt number reasonably well. A new correlation was developed using their new dataset.

In addition to the above experiments, an experiment of a central square subchannel in supercritical water was conducted by Wang et al. [104]. The configuration considered represented a 2×2 rod bundle. The author produced a new correlation based on the expression of Mokry correlation, which satisfied the prediction of the subchannel to further improve the accuracy. However, this experiment did not take into consideration of imbalance of the flow and the transverse mixing in the 2×2 bare rod bundle.

Numerical studies

RANS method may not be capable of accurately predicting flow and heat transfer in supercritical flow fully, but it is a very handy practical engineering tool and in some cases, the only variable method. Many approaches and assessments have been done concerning heat transfer in supercritical water flow within rod bundles. A selection of literature is discussed here.

Research on subchannel configurations of tight square lattice and triangular lattice fuel rod bundles at supercritical pressure was conducted by Yang *et al.* [105], where some turbulence models implemented in Star-CD were used. Experimental data by Yamagata *et al.* [32] were compared with their results. The authors observed that the two-layer model with a near wall function (Hassid & Poreh) performed the best in the prediction of the heat transfer

coefficient. In addition, the authors claimed that the heat transfer deterioration would be likely to occur in the narrow gap region due to the low mass flow rate. Yang *et al.* concluded that without considering the cross flow effects, the large non-uniformity of the flow area causes a strong circumferential temperature gradient at the cladding. The circumferential temperature gradient on the cladding surface was also observed to be high in the bundle with a square arrangement but not in a triangular arrangement of a rod bundle.

Cheng *et al.* [106] simulated flows in a circular tube as well as those in subchannels of square and triangular fuel assembly configurations for supercritical flow. From their assessment, they recommend the use of SSG-RSM model, which was found performed better than other turbulence models (e.g., *k-ε* model and RNG model) that they tested. The authors have established the advantage of the SSG-RSM model in predicting the heat transfer of supercritical fluid flow in rod bundles because the model can capture the anisotropic behaviour of turbulence in such a geometric configuration, including the HTD.

Similarly, Gu *et al.* [107,108] have also used the SSG-RSM model in their study of supercritical water flow which focused on the subchannels of both square and triangular lattice bundles. In these studies, the effect of pitch-to-diameter ratio on the secondary flow and the turbulent mixing between subchannels were discussed. They found that P/D ratio directly influence the turbulence mixing, where this result agrees with to the finding that of Zhang *et al.* [109]. However, the effect of the gap flow instability phenomenon that can occur when P/D is small was not considered in these studies.

Vertical upward and downward flows of a supercritical fluid in three types of fuel assembly arrangements were considered by Shang [110], i.e., a square, a hexagon and a cylindrical geometry. In the study, the author used the Speziale quadratic non-linear high

Reynolds number $k-\varepsilon$ turbulence model with a two-layer near wall treatment (Hassid & Poreh). The hexagon geometry frame was able to attain the lowest wall temperature compared with the other two. It has been reported that heat transfer controlled by the P/D ratio. For example, the heat transfer at the larger P/D ratio can be worse even though at the wall temperature can be obtained quite low with a small difference between its maximum and minimum value. Thus, a suitable P/D ratio should really be considered for both the efficiency and safety. The work on those fuel assemblies has been extended to horizontal flow by Shang & Lo [86,87]. As expected, the temperature profile of the rod was affected by the direction of the flow with higher temperature at the top and the temperature would be even out by the mixing between channels in some locations.

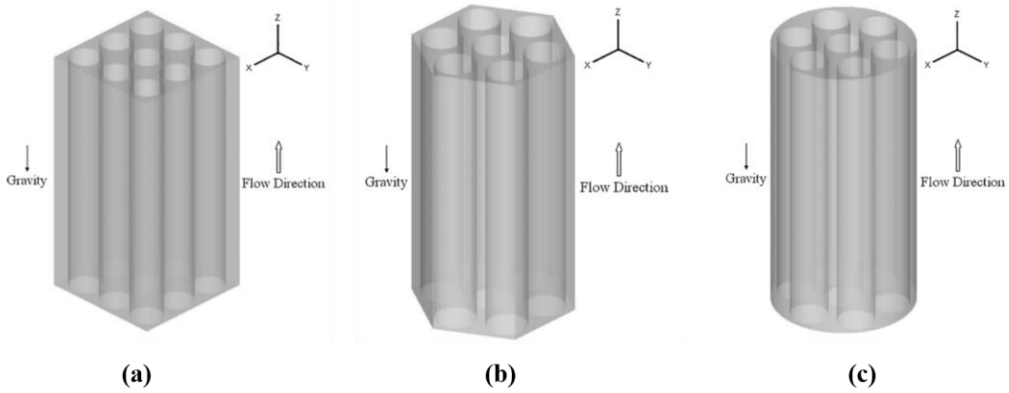

Figure 2.3: Types of geometric frames for the fuel assemblies (credit to Shang [110]**). a) square b) hexagon c) cylinder**

Studies on a section of the whole rod bundle of the Canadian SCWR design were conducted by Podila & Rao [111,112]. Both wire-wrapped and bare fuel bundles were considered in these studies. The presence of wire was found to help the inter-subchannel mixing and decrease the circumferential wall temperature compared with the bare bundles. Moreover, the chosen SST $k-\omega$ model was capable of capturing the HTD phenomenon, but the RSM could not [111].

It can be concluded that some low Reynolds number turbulence models and RSM models are able to predict the heat transfer deterioration caused by the buoyancy at certain conditions. In spite of this, all turbulence models are unable to resolve the supercritical fluid flow under all conditions. To the author's knowledge, DNS and LES have been used by very few researchers to study supercritical fluid flow in rod bundles. Consequently, there is lack of published work for this condition.

2.3 Studies on the Gaps Instability

When rod-to-rod and rod-to-wall gaps regions of a rod bundle are small relative to the dimension of the subchannel, the flow is characterized by strong transverse flow pulsations, which can contribute significantly to the momentum and heat transfer across the gaps. It is widely accepted that these instabilities in the form of flow pulsations are associated with large-scale vortices, which form quasi-periodically in pairs on either side of the gap. Such flow structures are sometimes referred to as coherent structures [113–115]. The background on the study of flow instabilities can be found in the review article by Meyer [116].

The flow instability phenomenon can be considered to originate from an experiment of wall-bounded 4-rod channel conducted by Hooper & Rehme [69]. The authors found strong periodic low-frequency oscillations in the axial and peripheral turbulent velocity components. The experiment was repeated with a symmetrical squared-pitch rod cluster channel and similar structures with smaller amplitudes of velocity components were found. The reason for the smaller amplitude was attributed to the larger pitch-to-diameter ratio in comparison with the former experimental configuration. The conclusions made from the experiments were, for developed single-phase turbulent flow through closely spaced rod

arrays, the mass, momentum and heat transfer processes are characterised by strong quasiperiodic azimuthal turbulent velocity directed through the gap. The azimuthal turbulent velocity has been found to be apparently generated by incompressible-parallel-channel flow instabilities and is not associated with the mean secondary flow velocities driven by Reynolds stress gradients. Furthermore, the length scales of the axial and azimuthal turbulent transport processes have been found to be significantly affected by the gap width, which indicates that the anisotropy of the turbulent transport processes in the rod gap is an essential feature to be reproduced in numerical simulations of rod bundle flows.

Möller [117,118] extended the work of the wall-bounded of the 4-rod channel to further investigate the quasi-periodic behaviour of the fluctuating velocities by varying the gap width and Reynolds number. The author found that the large-scale fluctuations could easily be determined with the identification of peaks in the power spectra of the azimuthal velocity. As the flow velocity increased or the gap width reduced, the frequency is increased. The Strouhal number that is, the frequency non-dimensionalized using the rod diameter and friction velocity is given as follows,

$$St_\tau = \frac{fD}{u_\tau} \tag{2.1}$$

The Strouhal number was found to be independent of Reynolds number and inversely proportional to the gap width. Möller proposed a flow model of a street of vortices in the centre of the gap that rotates alternately in opposite directions (refer to Figure 2.4). They move in the axial direction with their axis perpendicular to the rod surface in the gap. These large-scale vortices were attributed to the velocity gradient, similar to that near a wall. Since there is no wall at the centre of the gap, the motions of eddies were not obstructed, therefore large eddies can be sustained and cross the gap as they are transported by the main flow.

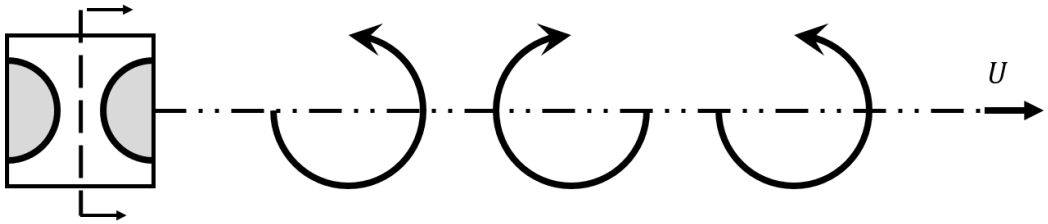

Figure 2.4: Flow model of street vortices in the gap by Möller [117]**.**

Krauss & Meyer conducted investigations in a 37-rod bundle with wall subchannels of W/D=1.06 [119] and a central channel with P/D=1.06 [114]. It was concluded that the vortex trains in a rod bundle are highly synchronized. From the two-point measurements results, they proposed a flow model shown in Figure 2.5, which is quite similar to Möller's. Two vortices are driven by the higher velocity at either side of the gap and rotate in opposite directions. Unlike in Möller's model, axes of the vortices are on either side of the gap instead of at the gap centre, with those vortices are moving axially within the gap by a convection speed (U_c) and are half wavelength ($\lambda/2$) apart.

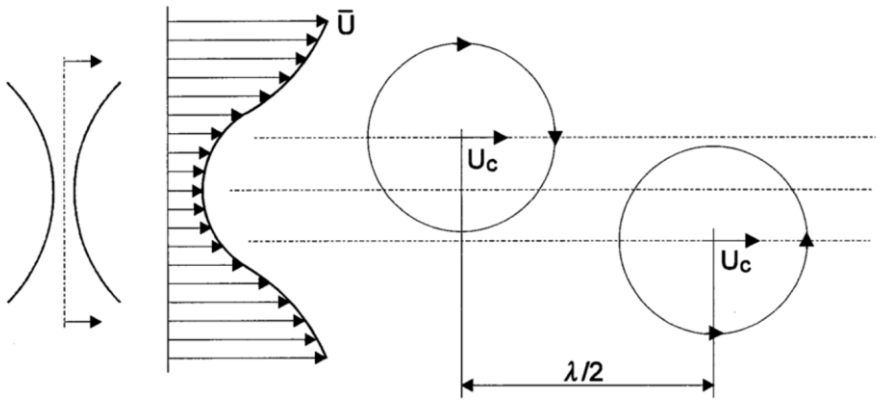

Figure 2.5: Flow model of street vortices in the gap by Krauss & Meyer [114]**.**

The gap instabilities are not only present in rod bundles, but can be observed in other non-uniform geometries. Wu & Trupp [120,121] investigated the flow structures at the gap formed between a trapezoid channel and an enclosed rod (Figure 2.6). They have confirmed the existence of significant turbulence in the rod-to-wall gap region in their studies. On the other hand, Meyer & Rehme [122,123] conducted experiments on square channels connected

by a narrow cross-section to investigate if the instability phenomenon is not restricted to the flow in rod bundles (Figure 2.7). The gap width and gap length connecting the square channels were varied. Similar vortices at the gap were found have diameters roughly equivalent to the gap depth and the centres of vortices were located on both sides of the centreline of the gap similar to the proposed model by Krauss& Meyer.

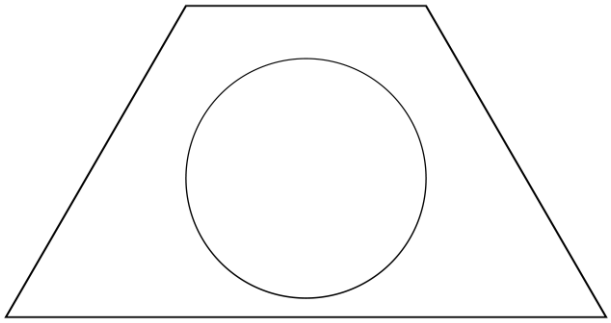

Figure 2.6: Cross-section of trapezoid channel with an enclosed rod by Wu & Trupp [120,121]**.**

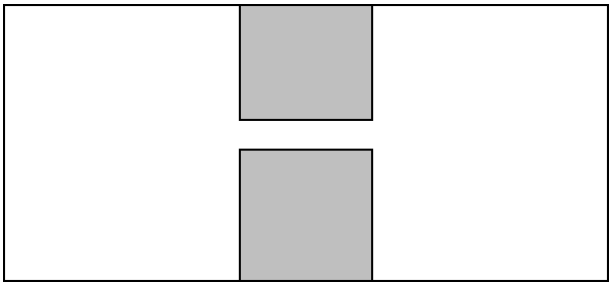

Figure 2.7: Cross-section of connecting rectangular channels by Meyer & Rehme [122,123]**.**

The experimental work to fully characterize the coherent structures has also been conducted at the University of Ottawa by Guellouz & Tavoularis [124]. A rectangular channel containing a cylindrical rod was chosen. Gaps between wall and rod were varied and their results were in agreement with previous work. Guellouz & Tavoularis [125] investigated the onset of the flow instability by considering laminar flow. The pulsating flow was also observed at low Reynolds numbers. There are two types of instabilities, namely symmetric mode and anti-symmetric mode. The former results from the Kelvin–Helmholtz

instability of the wall-normal profile, while the latter results from the wake-like instability of the span-wise profile. Similar instabilities have also been observed by Choueiri & Tavoularis [126,127] in an eccentric channel. The "gap vortex street" was attributed to the instability of two mixing layers on both sides of the gap.

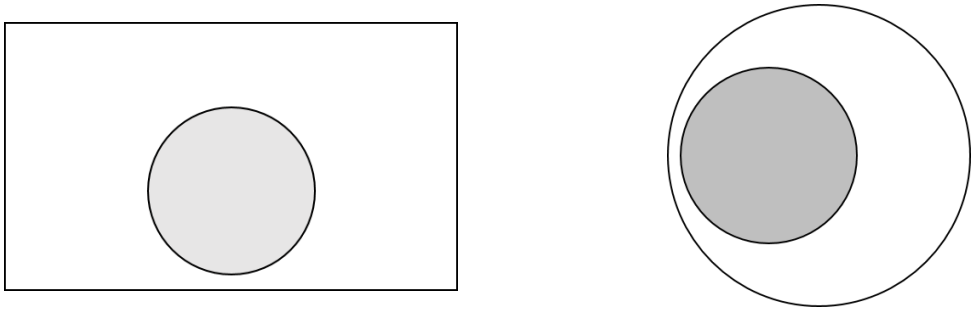

(a) **(b)**

Figure 2.8: Cross-sections of a) rectangular channel with enclosed rod by Guellouz & Tavoularis [124,125] **b) eccentric channel by Choueiri & Tavoularis** [126,127]**.**

From the same configuration of Guellouz & Tavoularis [124,125], additional work by Chang & Tavoularis [128] considered isothermal flow numerically. They used a URANS approach with RSM as turbulence model and produced time-averaged and phase-averaged velocity measurements including turbulence characteristics. Results obtained showed agreement to the experimental data with matched mean velocity and turbulent stresses distribution. The characteristics of coherent structures in the gap region from the experiment were also reproduced numerically. A further study by Chang & Tavoularis [129] considered heating from a rod in a rectangular duct to demonstrate the importance of coherent structures on heat transfer in the gap. In this study, the temperature increase was low where the effect of temperature variation on the velocity and the fluid properties is negligible. The structures in the gap were observed to be capable of transporting fluid across the gap, creating substantial local variations of the instantaneous temperature and heat transfer coefficient. The authors suggested that these fluctuations may need to be taken into consideration in safety analyses.

The experiment conducted by Lee *et al.* [130] used the ratio of the sum of the gap width and the rod diameter to the rod diameter, $\left(\frac{g+D}{D}\right)$ to replace the pitch to diameter ratio to study the mixing between subchannels due to the pulsating flow structure. Furthermore, Jeong *et al.* [131] introduced a new parameter to characterise the "gapping" based on the ratio of the distance between two adjacent subchannel centres (δ_{ij}) to the hydraulic diameter. They found that this geometrical parameter ratio δ_{ij}/D is a dominant factor affecting the turbulent mixing and correlates better with the experimental data than does the gap to diameter parameter.

Ninokata *et al.* [90] simulated strong and large-scale pulsation flow in the narrow gap for a wide range of geometrical and hydraulic parameters. They have considered several approaches including RANS, LES and DNS in their study and preferred LES to study the global flow pulsation phenomena that dominate the mixing between subchannels. Merzari & Ninokata [132] has used LES simulation for a flow in tight-lattice rod bundle. Using proper orthogonal decomposition approach (POD), they suggested POD could provide more complex dynamical behaviour in rod bundles. The interaction of higher modes from POD might explain the presence of "missing period" from the structures observed experimentally.

Yan *et al.* [133–136] conducted numerical studies of the large-scale flow pulsation in the tight lattice and rectangular channels with the URANS approach in conjunction with a Reynolds Stress Model. They concluded from their results that in any channel that they studied, the large-scale periodic vortex structures have developed from the flow disturbance due to the transverse vorticity gradient. The distribution of vorticity corresponds to the vortex structures. When the pitch to diameter ratio, P/D was close to the critical value, coherent structures and the mixing become more apparent. They discovered that the critical P/D of

tight lattice is about 1.03. For this kind of lattice, the local heat transfer, the average heat transfer capability and fluid mixing between subchannels are maximized.

Duan & He [12,13] investigated the effect of buoyancy-aided flow on large flow structures in the trapezoid annulus channel using LES based on the Boussinesq approximation. The chosen configuration was the same used by Wu & Trupp [120,121]. The authors concluded that the buoyancy force has non-negligible effects on the behaviour of the large flow structures. The scales of large flow structures temporally and axially are influenced by buoyancy in a similar as is the turbulence. That is, the scales of large flow structures reduce when the flow is laminarised by the buoyancy and so do the mixing factors between the subchannels. The authors also concluded that several factors make the effect of buoyancy complicated. The factors include different non-uniform buoyancy effects on turbulence in different regions of the domain, the redistribution of the mass flow in the various subchannels as well as large flow structures in the flow channel. The effect of the last factor was found to be most dominant.

Mixing factor

Thanks to the existence of pulsating behaviour in the narrow gap, mixing of the flow between the subchannels is strengthened. Rehme [113] has introduced an equation to evaluate the mixing factor due to the large flow structures which is shown below.

$$Y = \frac{u_{eff}\delta_{ij}}{\bar{\varepsilon}} \tag{2.2}$$

where u_{eff} is the effective mixing velocity and δ_{ij} is the distance between the subchannels, and $\bar{\varepsilon}$ is the reference eddy viscosity. u_{eff} is defined by Wu & Trupp [121] as follows:

$$u_{eff} = \sqrt{\int_{f_p-\frac{f_p}{4}}^{f_p+\frac{f_p}{4}} E_{uu}(f)\, df} \tag{2.3}$$

where f_p is the peak frequency and $E_{uu}(f)$ is the power spectrum density function. The reference eddy viscosity, $\bar{\varepsilon}$ in equation (2.2) is given by Rehme as [113]:

$$\bar{\varepsilon} = \nu \frac{Re}{20} \sqrt{\frac{f^*}{8}} \tag{2.4}$$

where ν is the average kinematic viscosity and the f^* is friction factor. Following Rehme [113], an estimated f^* is obtained from the turbulent isothermal flow in a smooth pipe at similar Reynolds number, which is given by:

$$f^* = 0.18\, Re^{-0.2} \tag{2.5}$$

Rehme [113] also stated that u_{eff} may be calculated away from the centre of the gap. The semi-empirical correlation to estimate u_{eff} at the location away from the centre of the gap is given by Rehme [113] as:

$$u_{eff} = u_{eff,x=0}\, 10^{-0.78\left(\frac{S}{D}\right)^{-0.33}(x/\delta_{ij})} \tag{2.6}$$

2.4 Summary

In the last few decades, the understanding of the heat transfer to supercritical water has been significantly improved. The heat transfer can be enhanced due to the increase of c_p when the buoyancy is weak. When the buoyancy effect is not negligible, the heat transfer is normally enhanced in a downward flow, whereas in an upward flow the behaviour is more complicated. Heat transfer deterioration is likely to happen when the heat flux is high and/or mass flux is low. When the buoyancy is really strong, the heat transfer recovery occurs.

Several correlations have been developed to predict the wall temperature. Most correlations are strictly for tubes and at specific conditions. These correlations are not necessarily reliable for other geometries especially fuel assembly configurations.

Numerous studies have focused on flow in rod bundle, either experimentally or numerically. However, with regards to mixed convection and data of heat transfer in rod bundles, there is still quite limited experimental work that has been done. Specifically, experimental studies for flow and heat transfer in a supercritical fluid are limited. Correlations that have been proposed for circular tubes are found not particularly reliable for the supercritical flow in rod bundles. Correlations by Jackson & Fewster [44], and Bishop *et al.* [41] were found to predict the best in 2×2 rod bundle recent studies. Consequently, more experiments for rod bundles, in general, are needed for more reliable correlations to be proposed for safety analyses and fuel design supports. As for the instability phenomena in the gaps, the general understanding has been developed by many researchers. The phenomenon in the gaps of rod bundles can also be found in other non-uniform configurations. However, there are not many studies on the effect of buoyancy and/or large variation properties on the flow instabilities in the gaps. This is true for both experimental and numerical investigations.

Most numerical studies of flows in fuel bundles used RANS approach. It has been found that low Reynolds number turbulence models and RSM models may able to predict some heat transfer deterioration in buoyancy influence flow at supercritical pressure to a certain degree, but quantitatively none of them is able to predict the phenomena accurately for a range of conditions. The accuracy of the predictions of turbulence models is dependent on the cases studied. The RANS approach also struggles to resolve the supercritical fluid flow

under many conditions and are unable to provide information on the instabilities and cross flow between subchannels. Some authors, however, have built some confidence on the applicability of the URANS approach to simulate the flow in a rod–bundles or rod-bundle-like configurations to study instabilities phenomena, even though the predictions are generally less reliable than DNS and LES especially, for the detailed flow field.

It is the LES and DNS assuredly could provide more detailed flow structures and additional insight into the flow phenomenon. Yet the work with the use of DNS and LES is still limited especially for configurations other than simple circular tubes as the higher computational cost is involved for such flows. DNS/LES can be viewed as an alternative option for experiments to study the effect of supercritical fluid flow and heat transfer as well as the flow instabilities in the gaps. The work using LES and DNS in rod bundles for mixed convection cases, specifically in the supercritical flow is much needed as there is still a lack of published work on these conditions. Some authors suggested LES be the best option as an intermediate approach in providing detailed information on a reasonable cost.

The PhD work presented here is concerned with the supercritical flow in a rod-bundle-like configuration. The work is based on large eddy simulations. Chapters 4 and 5 describe studies of forced convection and mixed convection, respectively.

Chapter 3

Turbulence, Large Eddy Simulation and Numerical Methods in *Code_Saturne*

3.1 Introduction to Turbulence Theory

Turbulent is a distinct physical phenomenon in dynamic fluid flow and has been an interest to many researchers for a very long time. It could go back circa 1500 from the illustration work of Leonardo da Vinci, but the understanding of this phenomenon comes around later in the 19th century. Research in turbulence can be categorised in into three distinct overlapped "movements" as suggested by Chapman & Tobak [137]. The first movement can be called as a statistical movement, which started around late 19th century with the work of Osborne Reynolds and all the way to the present with recent work. This movement considered the nondeterministic approaches such as the use of RANS and LES approaches, where studies are based on the statistical average of the flow. The next movement is the structural movement which according to Chapman & Tobak [137] began with the discovery of Tollmien-Schlichting waves and their measurement by Schubauer &

Skramstad in 1948. This movement basically detects and analyses coherent structures in turbulent flows, which were not be provided by the previous movements. The last movement is the deterministic movement that began with the work of Lorenz in 1963, but can easily include the studies as far back as the work of Poincaré in 1899. The deterministic movement includes the deterministic approaches such as DNS and LES that undoubtedly incorporate some aspects of both the statistical and structural movements. Even though LES might also be seen as a part of the statistical movement due to the use of SGS model, it is however indirectly incorporate aspects of structural and deterministic movements as the large scales are computed directly. This chapter aims to present the fundamental turbulence theory, the characterisation techniques for the turbulence statistics, the description of the Large Eddy Simulation and finally the numerical method in *Code_Saturne* employed throughout this study.

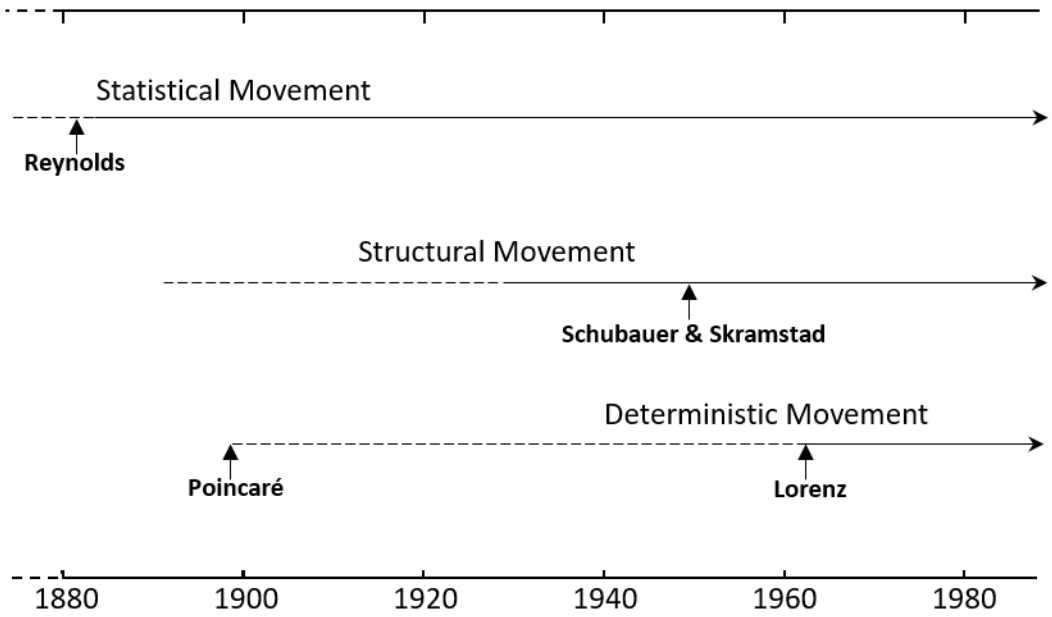

Figure 3.1: Movements in the study of turbulence [137]**.**

3.1.1 The Energy Cascade

The concept of the energy cascade is that turbulence comprises of eddies of different sizes, and it was first coined by Richardson in 1922. The idea is that large eddies are unstable and breakup and transfer energy into smaller eddies. These smaller eddies go through a similar breakup and transfer the energy into even smaller eddies and this process continues until the eddy motion is small enough that is stable, and molecular viscosity is effective in dissipating the kinetic energy. Smaller scales may also be present within the large eddies of the flow. This is succinctly summarised by Richardson in his poem:

"Big whorls have little whorls,
which feed on their velocity;
and little whorls have lesser whorls,
and so on to viscosity
(in the molecular sense)".

Eddies of the largest size range can be characterized to their lengthscale ℓ_0 and characteristic velocity $u_0 \equiv u(\ell_0)$. The lengthscale ℓ_0 is comparable to the flow scale $\mathcal{L}$ and the characteristic velocity u_0 is on order of the root mean square turbulence intensity and $u' \equiv \left(\frac{2}{3}k\right)^{1/2}$ which is comparable to $\mathcal{U}$. The last sequence of the energy cascade process is dissipation. Its rate can be determined by the transfer of energy from the largest eddies. The large scale eddies have an energy of the order of u_0^2 and timescale $\tau_0 = \ell_0/u_0$, which implies that the rate of energy transfer is $u_0^2/\tau_0 = u_0^3/\ell_0$. The rate of dissipation, ε scaled with u_0^3/ℓ_0 at high Reynolds number is independent of ν. The framework of turbulence modelling is generally motivated by this view of energy cascade.

3.1.2 The Kolmogorov Hypotheses

In understanding the concept of the size characteristics of eddies and its energy, Kolmogorov has formed three hypotheses that could assist in this identification process. The hypotheses aim to answer questions on the size of the smallest eddies that are responsible for dissipating energy and the behaviour of both velocity $u(\ell)$ and timescale $\tau(\ell)$ when the lengthscale ℓ decreases. The three hypotheses are as following:

Kolmogorov's hypothesis of local isotropy. The small-scale turbulent motions ($\ell \ll \ell_0$) are statically isotropic at a sufficiently high Reynolds number. Lengthscales can then be separated between the anisotropic of large eddies and the isotropic small eddies. The information brought down from the large scales can be argued lost as the energy is passed down the cascade. This results in the universal form of the statistics of the small-scale motions.

Kolmogorov's first similarity hypothesis. At sufficiently high Reynolds number, the small-scale motions of every turbulent flow have a universal form that is uniquely determined by the mean energy dissipation rate, ε and the kinematic viscosity, ν. Given these two parameters, the unique length, velocity and timescales can be obtained respectively in the form of:

$$\eta \equiv (\nu^3/\varepsilon)^{1/4} \qquad u_\eta \equiv (\varepsilon\nu)^{1/4} \qquad \tau_\eta \equiv (\nu/\varepsilon)^{1/2}$$

Two identities can be obtained from above definitions, indicating that the Kolmogorov scales represent the smallest dissipative eddies. First the Reynolds number based on the Kolmogorov scales is unity ($Re_\eta = \eta u_\eta/\nu = 1$), and the second identity is that the

dissipation rate is given by $\varepsilon = \nu\left(u_\eta/\eta\right)^2 = \nu/\tau_\eta^2$, where, $u_\eta/\eta = 1/\tau_\eta$ can be equivalently obtained. This provides a consistent characterisation of the velocity gradients of the dissipative eddies.

Moreover, from the dissipation rate scaling $\varepsilon = u_0^3/\ell_0$, the ratios of the length scale, velocity scales and timescales of the large and small eddies of the flow are as following:

$$\eta/\ell_0 \sim Re^{-3/4} \quad u_\eta/u_0 \sim Re^{-1/4} \quad \tau_\eta/\tau_0 \sim Re^{-1/2}$$

where $Re = \frac{u_0\ell_0}{\nu}$. It is therefore evident that, at high Reynolds number, the velocity scales and timescales of the smallest eddies (u_η and τ_η) are small compared with those of the largest eddies (u_0 and τ_0).

Kolmogorov's second similarity hypothesis: At sufficiently high Reynolds number, the statistics of the turbulent motions of scale ℓ, which is much smaller than ℓ_0 yet is still larger than η, i.e., $\ell_0 \gg \ell \gg \eta$, have a universal form that can be uniquely determined by ε and is independent of ν. From the second similarity hypothesis, the energy-containing range (large) eddies and the dissipation range (small) eddies can be separated. Motions between this range are called the inertial subrange which is determined by inertial effects, with the viscous effects being negligible. The motions in the dissipation range experience significant viscous effects. The various ranges can be seen in Figure 3.2, where the demarcation lines between inertial subrange and the dissipation range and energy containing range are respectively denoted by ℓ_{DI} and ℓ_{EI}. The characteristic velocity scales and timescales are formed from the dissipation rate, ε and the inertial lengthscale, ℓ as:

$$u(\ell) = (\varepsilon\ell)^{1/3}, \quad \tau(\ell) = (\ell^2/\varepsilon)^{1/3}$$

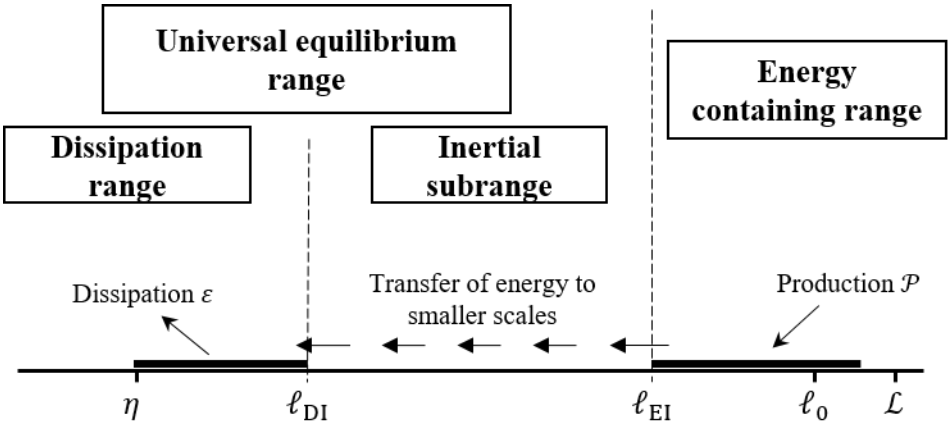

Figure 3.2: Various lengthscales and ranges of eddy sizes ℓ, and the process of energy cascade in turbulent flow [138]**.**

3.1.3 An Introduction to Modelling and CFD Simulations

There are several approaches either experimentally or numerically to study the problem of turbulent flows. In principle, numerical simulations are efficient and relatively cheaper than experimental methods, but it is required for numerical models to be validated with experimental results. The fundamental equations for any flow problems are the Navier-Stokes equations including the conservation of mass, momentum and energy that describe the motion of a fluid. For an incompressible flow, the mass and momentum equations are given as:

Continuity equation:
$$\frac{\partial u_i}{\partial x_i} = 0 \tag{3.1}$$

Momentum equation:
$$\frac{\partial u_i}{\partial t} + \frac{\partial (u_i u_j)}{\partial x_j} = -\frac{1}{\rho}\frac{\partial p}{\partial x_i} + \nu \frac{u_i}{x_i x_j} \tag{3.2}$$

where, u_i and x_i are velocity components and coordinates in the i^{th} direction, t is the time, ρ the density, p the pressure and ν the kinematic viscosity.

Directly solving the NS equations are impractical for most engineering problems. The

most used numerical approach in engineering application for its flexibility and cost efficient is the Reynolds-Averaged Navier-Stokes (RANS) method. RANS solves statistically averaged information that can be used for high Re flows as well as complex geometry problems. In the RANS, the Navier-Stokes equations are time-averaged by using the Reynolds decomposition introduced by Osborne Reynolds, where the flow variables can be decomposed into mean and fluctuating components. Therefore, the instantaneous velocity, u_i and instantaneous pressure, p can be expressed as:

$$u_i = \langle u_i \rangle + u_i' \qquad p = \langle p_i \rangle + p' \tag{3.3}$$

where the angle brackets $\langle ... \rangle$ denotes the time-averaged component and the prime $(')$ denotes the fluctuating component. Consequently, the average of the fluctuating components become zero ($\langle \phi' \rangle = 0$). Using (3.3), equation (3.1) & (3.2) can be rewritten as follows:

Continuity equation:
$$\frac{\partial \langle u_i \rangle}{\partial x_i} = 0 \tag{3.4}$$

Momentum equation:
$$\frac{\partial \langle u_i \rangle}{\partial t} + \langle u_j \rangle \frac{\partial \langle u_i \rangle}{\partial x_j} = -\frac{1}{\rho}\frac{\partial \langle p \rangle}{\partial x_i} + \nu \frac{\partial^2 \langle u_i \rangle}{\partial x_i \partial x_j} - \frac{\partial \langle u_i' u_j' \rangle}{\partial x_j} \tag{3.5}$$

From the transformation, an additional term is added at the right hand side of equation (3.5), which is a nonlinear term of fluctuating velocity components. This additional nonlinear term results in a closure problem of turbulence, where one or more extra equations are needed to solve it.

Without time-averaging, the Navier-Stokes equations can be solved directly and this approach is called Direct Numerical Simulation (DNS). No turbulence modelling assumptions are required as DNS resolves all temporal and spatial scales of motions. However, in order to resolve all scales of motions, the number of the grid points required is

proportional to $Re^{9/4}$, consequently there is a very high computational cost for moderate to high Reynolds number ranges. Consequently, the aforementioned DNS is rarely used in industrial applications but is more commonly used in the fundamental study of physics flow.

There is another approach that resolves more flow physics than RANS does and requires a lower computational cost than DNS does. The approach is called Large Eddy Simulations (LES). The turbulent kinetic energy is mostly stored in the large-scale eddies, in LES method large scales of motions are resolved using filtered Navier-Stokes equations while modelling the smaller turbulent eddies. The influences of the smaller scales on the larger scales momentum flux is represented by the subgrid-scale (SGS) model. Since the computational grids in LES do not resolve the small scales, this approach is cheaper than that of DNS and is convenient for higher Reynolds numbers with reasonably accurate results. In the present study, LES is being used to study the large flow structures and coherent structures. Further details on the LES approach and its SGS models are discussed in §3.3. More details on all mentioned numerical approaches can be found in Pope (2000) [138], Davidson (2004) [139] and Fergizer & Peric [140].

3.2 Statistical Description for Turbulence Characteristics

The complexity of turbulent flows is that solutions of the Navier-Stokes equations are generally random. This is due to turbulent flow sensitivity to the initial and boundary conditions, especially at high Reynolds number. Therefore, to determine the evolution of the flow field, statistical methods are used in the description of turbulence. Averages, correlations and spectral analysis are presented in the following sections.

3.2.1 Averaging

The statistics of turbulence flow can be computed by performing stochastic mean (ensemble, spatial and temporal averaging), which are denoted with $\langle \dots \rangle$. The statistical moment of order n for any random variable, ϕ is defined as the mean of ϕ^n:

$$\langle \phi^n \rangle = \int \phi^n f(x) dx \tag{3.6}$$

where f is the probability density function (PDF) such that:

$$P\{a \leq \phi \leq b\} = \int_a^b f(x) dx \tag{3.7}$$

The mean of a series of discrete points regularly sampled with *N* realizations can be defined as:

$$\langle \phi \rangle = \lim_{N \to \infty} \frac{1}{N} \sum_{i=1}^{N} \phi_i \tag{3.8}$$

where ϕ_i is a finite sample at one realization. It is associated with the turbulent fluctuation ϕ' that can be derived in the mathematical expression of:

$$\phi_i' = \phi_i - \langle \phi \rangle \tag{3.9}$$

By the above construction, $\langle \phi' \rangle$ is a property equivalent to zero. However, the fluctuation moments of second or higher order are not necessarily zero. Thus, variance can be defined to be the mean-square of the fluctuations and expressed as:

$$\begin{aligned} \langle \phi'^2 \rangle &= \lim_{N \to \infty} \frac{1}{N} \sum_{i=1}^{N} [\phi - \langle \phi \rangle]^2 , \\ &= \langle \phi^2 \rangle - \langle \phi \rangle^2 \end{aligned} \tag{3.10}$$

The standard deviation or root mean square of variance (r.m.s) value of the random

variable ϕ by ($\phi'_{rms} = \sqrt{\langle \phi' \rangle^2}$) can be used to measure the strength of the fluctuation or known as turbulence intensity. The second moment or covariance of the fluctuation velocity can be used to calculate Reynolds stresses in form of:

$$\langle u_i' u_j' \rangle = \langle u_i u_j \rangle - \langle u_i \rangle \langle u_j \rangle \tag{3.11}$$

Additional information regarding the statistical structure of turbulence can be inspected using higher-order statistics. The normalised third and fourth order moments are called the skewness, S and flatness, F (or kurtosis) respectively,

$$S\langle \phi \rangle = \frac{\langle \phi'^3 \rangle}{\langle \phi'^2 \rangle^{3/2}} \quad \text{and} \quad F\langle \phi \rangle = \frac{\langle \phi'^4 \rangle}{\langle \phi'^2 \rangle^2}$$

The skewness is to determine the lack of symmetry between the positive and negative fluctuations; whereas the flatness indicates the possibility of extreme amplitudes instances.

3.2.2 Correlations

A correlation of fluctuating motions can be conducted between two points in space or in time, which can quantify the lengthscales and timescales respectively. The two-point spatial correlation between velocity fluctuations at spatial points x and $x + r$ can be defined as:

$$R_{ij}(x, x + r) = \langle u_i'(x) u_j'(x + r) \rangle \tag{3.12}$$

In normalized form, the correlation function can be expression as:

$$R_{ij}(x, x + r) = \frac{\langle u_i'(x) u_j'(x + r) \rangle}{\langle u_i'^2(x) \rangle} \tag{3.13}$$

The terms autocorrelation and cross-correlation are adopted for $i = j$ and $i \neq j$, respectively. The integral lengthscale characteristic can then be measured using the two-point

spatial correlation and it is defined as:

$$L_{ij} = \int_0^\infty R_{ij}(r)dr \tag{3.14}$$

For a statistically stationary process, the temporal correlation can be determined by a similar approach to the spatial correlation by measuring signal in time. For signals measured at a given point with a time delay of τ, the two-time correlation function can be written as:

$$R_{ij}(\tau) = \frac{\langle u_i'(t)u_j'(t+\tau)\rangle}{\langle u_i'^2(t)\,\rangle} \tag{3.15}$$

Hence, the definition of an integral timescale of turbulence can be derived as:

$$\mathrm{T}_{ij} = \int_0^\infty R_{ij}(\tau)d\tau \tag{3.16}$$

which indicates the period which turbulent fluctuations remain correlated.

3.2.3 Spectral Analysis

To analyse the structure of different sizes of turbulence, it is convenient to re-express the turbulent fluctuations in terms of wavenumber spectrum. Transformation from the physical domain to the spectral domain can be obtained by using a Fourier transform. The three dimensional Fourier transform of the spatial correlation for a statistically homogenous turbulence is given as:

$$\Phi_{ij}(\kappa) = \frac{1}{(2\pi)^3}\iiint_{-\infty}^{\infty} R_{ij}(r)e^{-i\kappa\cdot r}dr \tag{3.17}$$

and its inverse transform as:

$$R_{ij}(r) = \iiint_{-\infty}^{\infty} \Phi_{ij}(\kappa)e^{-i\kappa\cdot r}d\kappa \tag{3.18}$$

where i is the imaginary unit, $i^2 = -1$, κ is the wavenumber vector, with a dimension of (Length)$^{-1}$. The lengthscale $\ell = O(\kappa^{-1})$ is qualitatively interpreted as a representation of the wavenumber κ in the spatial scale.

Alternatively, the Fourier transform and its inverse can be used on the time correlation of equation (3.15) to move between time and frequency domains. Therefore, equation (3.17) & (3.18) can be reformulated as a function of frequency, f instead of in a function of wavenumber κ. With the energy calculated as the square of the Fourier coefficients, the energy spectrum function may represent the contribution of the turbulent structures to the turbulent kinetic energy in terms of frequency or wavenumber.

Fourier transform requires sample values of R_{ij} in the numerical computations hence the Discrete Fourier Transform (DFT) is performed. For a number of N samples, the DFT of R_{ij} is computed as:

$$\phi(k) = \frac{1}{N}\sum_{n=1}^{N} R_{ij}(n)\omega_N^{(k-1)(n-1)} \tag{3.19}$$

where $\omega_N = e^{(-2\pi i)/N}$ and k is the non-dimensional wavenumber in the range $1 \leq k \leq N$. In practice, the Fast Fourier Transform (FFT) algorithm manages to reduce the complexity of computing DFT which equivalently reduces the required number of computations from the order of N^2 to $NlogN$.

3.2.4 Turbulence Structures

3.2.4.1 Vortex Identification

The turbulent flow can be studied by analysis of the so-called coherent structures (CS).

There is no consensus on the definition of CS. However, to demonstrate the general concept of the phenomena, some definitions from a few researchers are described here. Hussain [115] defined CS as a large-scale turbulent mass that is connected with a phase-correlated vorticity over its spatial extent. Robinson [141] referred CS as "a three-dimensional region of the flow over which at least one fundamental flow variable (velocity component, density, temperature, etc.) exhibits significant correlation with itself or with another variable over a range of space and/or time that is significantly larger than the smallest local scales of the flow." Meanwhile, Jeong & Hussain [142] described CS as "spatially coherent, temporally evolving vortical structures." Vortices appear to be widely accepted in describing coherent structures in turbulent flows, which, according to Hussain [115], have distinct boundaries and independent territories.

The identification of CS is pretty difficult as it can be easily confused with non-coherent turbulence and mean vorticity. It must be based on an unambiguous quantitative criterion. Some of the early criteria were rather intuitive and identified as iso-vorticity surfaces or circular streamlines. There are two quantitative criteria proposed to identify vortex namely Q-criterion and λ_2-criterion. Both characterisation techniques are briefly introduced below, but a detailed review of the method of vortex identification can be found in Jeong & Hussain [142] and Cucitore *et al.*[143].

Q-criterion

The Q criterion is the second invariant of the gradient tensor, ∇u which gives:

$$Q = -\frac{1}{2}\frac{\partial U_i}{\partial x_j}\frac{\partial U_j}{\partial x_i} = \frac{1}{2}\left(\Omega_{ij}\Omega_{ij} - S_{ij}S_{ij}\right) \tag{3.20}$$

where Ω_{ij} and S_{ij} are an anti-symmetric part (rotation tensor) and a symmetric part (rate of

strain tensor), respectively, and defined as

$$S_{ij} = \frac{1}{2}\left(\frac{\partial U_i}{\partial x_j} + \frac{\partial U_j}{\partial x_i}\right) \qquad \Omega_{ij} = \frac{1}{2}\left(\frac{\partial U_i}{\partial x_j} - \frac{\partial U_j}{\partial x_i}\right) \tag{3.21}$$

This criterion, first proposed by Hunt *et al.* [144], identifies a vortex core as a spatial region. Vorticity overcomes strain at regions of positive Q, hence distinguishing vortical activity from high-strain activity. This method has an improvement in detecting vortical motions in wall-bounded flows over the previous method such as iso-vorticity surfaces.

λ_2-criterion

λ_2-criterion proposed by Jeong & Hussain [142] determines the local pressure minimum to identify vortex. This is a region with two negative eigenvalues of $\boldsymbol{S^2 + \Omega^2}$. By neglecting the unsteady and viscous effects, the symmetric part of the gradient of the incompressible Navier–Stokes equation can be expressed as

$$\boldsymbol{S^2 + \Omega^2} = -\frac{1}{\rho}\nabla(\nabla p) \tag{3.22}$$

where S_{ij} and Ω_{ij} are the symmetric and antisymmetric components of the velocity gradient tensor ∇u (same as defined above) and p is the pressure and equation above is a representation of the pressure Hessian $\left(\left(\nabla(\nabla p)\right)_{ij} = \partial^2 p/\partial x_i \partial x_j \right)$. To identify the region of local pressure minimum, Jeong & Hussain define the vortex core as a connected region with two positive eigenvalues of the pressure Hessian. If the eigenvalues of the symmetric tensor $\boldsymbol{S^2 + \Omega^2}$ are ordered as $\lambda_1 \geq \lambda_2 \geq \lambda_3$, this definition satisfies to the requirement that $\lambda_2 < 0$ at every point inside the vortex core.

3.2.4.2 Proper Orthogonal Decomposition (POD)

The POD is an eduction technique that was introduced by Lumley [145] to the turbulence

community. It is based on the two-point velocity correlation. The POD is also known as the Karhunen–Loève expansion. Lumley used this method to identify the motions with functions of the spatial variable that contain the most energy.

A proper orthogonal decomposition of the velocity field $u(x,t)$ can be written as an expansion of a series of orthogonal spatial basis functions $\varphi^n(x)$ and the basis-function coefficients $a^n(t)$, where n denotes the mode number:

$$u(x,t) = \sum_{n=1}^{\infty} a^n(t)\varphi^n(x) \tag{3.23}$$

Mathematically, the POD projects the random velocity ($u(x,t) = \{u_1, u_2, \dots u_N\}$) into an orthonormal coordinate system $\varphi^n(x)$. It must be noted that the functions $\varphi^n(x)$ do not represent directly the coherent structures, however, as a consequence of Eq. (3.23), the coherent structures can be identified from the instantaneous flow field by the superposition of some of the basis functions. Therefore, POD is a useful method to recognize the most important modes of turbulence, as well as an effective way to analyse the turbulence dynamics.

The direct solution of the problem could be computationally expensive for a three-dimensional turbulence. Taking an example of the POD from DNS with a mesh size of *N*, the eigenvalue problem will have a size equal to $3 \times 3 \times N$. This can be impractical to engineering problems of Reynolds numbers. A simplified approach to solve this problem has been proposed by Sirovich [146], which is referred to as a ***method of snapshots***.

The method is based on collecting an adequate number M snapshots (linearly independent realizations of the flow field $u_m(x) = \{u_1, u_2\}$), to reconstruct the eigenvalue–eigenfunction problem. The energy associated from each mode is given by the eigenvalue λ of the two-

point temporal correlation tensor C_{nm} of independent snapshots [147] and can be written as:

$$C_{nm}\varphi = \lambda^n \varphi \tag{3.24}$$

where C_{nm} reads as,

$$C_{nm} = \frac{1}{M}\langle u_n(x,t) \cdot u_m^*(x,t')\rangle \qquad n,m = 1 \dots M, \tag{3.25}$$

The operator $\langle \dots \rangle$ denotes ensemble average and $*$ corresponds to the complex conjugate. The solutions are ordered according to the size of the eigenvalues as follows,

$$\lambda^1 > \lambda^2 > \cdots > \lambda^n = 0 \tag{3.26}$$

Each eigenfunction $\varphi^n(x)$ can then be computed from the POD modes through the projection on the original fields using the following equation

$$\varphi^n(x) \cong \sum_{m=1}^{M} \varphi_m^n u_m^n(x) \tag{3.27}$$

where φ_m^n is the mth element of the eigenfunction φ corresponding to the nth eigenvalue λ^n.

The random velocity fields, $(u_m(x) = \{u_1, u_2\})$ from the above derivation may also be replaced by scalar functions such as the vorticity component ω_3 or vector-valued functions. More comprehensive description of POD can be found in [145–147].

3.3 Large Eddy Simulation

As discussed earlier, in the LES approach, larger scales are resolved while small-scale eddies which are supposed to be isotropic are modelled. As a simple description, Pope [138] has listed four conceptual steps on the LES method.

1. By applying a filter operation, the velocity is decomposed into a filtered component

(or resolved) and a residual component (or subgrid-scale, SGS). The filtered component that is resolved represents the large eddies and it is three dimensional and time dependent.

2. The governing equations for the filtered velocity field are derived from the Navier-Stokes equations. These equations are of the standard form with an additional term of the residual stress tensor (which arises from residual motions) in the filtered momentum equation.
3. The residual-stress tensor is modelled to achieve closure, most simply by an eddy-viscosity model.
4. The filtered equations are solved numerically for the filtered velocity $\bar{u}$ which approximates the large-scale motions in one realization of the turbulent flow.

3.3.1 Filtering

In LES, the large-scale motions of the flow are solved by removing (filtering) the small-scale structures from the solution to the Navier Stokes equations. This operation is performed by applying scale high-pass filter (i.e., low-pass frequency) filter to the exact solution. Mathematically, the filtered fields denoted with a bar, is represented in physical space as a convolution product as following:

$$\overline{\phi} = \int \phi(x', t) G(x - x') dx' \tag{3.28}$$

where, G is the convolution kernel (the characteristics of the filter used) which is linked to the cut-off scales in space and time, $\overline{\Delta}$ and $\overline{\tau_c}$ respectively. In Fourier space, the spatial cutoff length is associated with k_c, whilst $\overline{\tau_c}$ associated with ω_c.

The residual field or the unresolved part of ϕ, is defined as

$$\phi'(x,t) = \phi(x,t) - \overline{\phi}(x,t) \tag{3.29}$$

which can be applied to the velocity or pressure field, so that the velocity field and pressure field has the decomposition as

$$\begin{aligned} u(x,t) &= \overline{u}(x,t) + u'(x,t) \\ p(x,t) &= \overline{p}(x,t) + p'(x,t) \end{aligned} \tag{3.30}$$

This equation appears to be analogous to the Reynolds decomposition. However, $\bar{u}(x,t)$ and $\bar{p}(x,t)$ are random fields and time dependent, and the filtered residual is not zero

$$\begin{aligned} \overline{u}'(x,t) &\neq 0 \\ \overline{p}'(x,t) &\neq 0 \end{aligned} \tag{3.31}$$

There are three properties that must be satisfied for a filter to be used on the Navier-Stokes equations [148]:

Conservation of constants:

$$\overline{a} = a \Leftrightarrow \int G(x,t)dx = 1 \tag{3.32}$$

Linearity:

$$\overline{\phi + \psi} = \overline{\phi} + \overline{\psi} \tag{3.33}$$

Commutation with derivation:

$$\frac{\overline{\partial \phi}}{\partial s} = \frac{\partial \overline{\phi}}{\partial s}, \qquad s = \mathrm{x}, t \tag{3.34}$$

There are three classical filtering types specified by Sagaut [148] for Large Eddy Simulation. All three classical filter for cut-off length $\overline{\Delta}$ in one-dimensional are as shown in Table 3.1. There are other filters such as Cauchy & Pao filters that are listed by Pope [138] that are not shown in here. Their transfer function and filter functions are similar to the

Gaussian filter. The filter width in LES is usually defined by the size of the control volume, and it is located within the inertial subrange. The inertial subrange is defined by the Kolmogorov's second similarity hypothesis that states that the motions are determined by inertial effects and independent of the viscous effects in a sufficiently high Reynolds number. Thus, the eddy resolution is determined directly by the grid and the cut-off length $\overline{\Delta}$ does not explicitly appear in the equations. From the spatial discretisation, structures that are twice the size of the cells are the resolved scales. In *Code_Saturne*, the value of the filter width implemented for the hexahedral cells is $\overline{\Delta} = 2|\Omega_i|^{\frac{1}{3}}$, where $|\Omega_i|$ is the volume of the cell i.

Table 3.1: Three classical filters for Large Eddy Simulation.

Type of filter	Filter function	Transfer function
Box or top-hat filter	$\boldsymbol{G(x) = \begin{cases} \frac{1}{\overline{\Delta}} & \text{if } \lvert x\rvert \le \frac{\overline{\Delta}}{2} \\ 0 & \text{otherwise} \end{cases}}$	$\boldsymbol{G(x) = \frac{\sin(k\overline{\Delta}/2)}{k\overline{\Delta}/2}}$
Gaussian filter	$\boldsymbol{G(x) = \left(\frac{6}{\pi\overline{\Delta}^2}\right)^{1/2} \exp\left(\frac{-6\lvert x\rvert^2}{\overline{\Delta}^2}/\right)}$	$\boldsymbol{G(x) = \exp\left(\frac{-\overline{\Delta}^2 k^2}{24}\right)}$
Spectral or sharp cutoff filter	$\boldsymbol{G(x) = \frac{\sin(k_c(x))}{k_c(x)}}$ $\boldsymbol{\text{where } k_c = \frac{\pi}{\overline{\Delta}}}$	$\boldsymbol{G(x) = \begin{cases} 1 & \text{if } \lvert k\rvert \le k_c \\ 0 & \text{otherwise} \end{cases}}$

3.3.2 LES Formulation

By applying filter to equations (3.1) & (3.2), the Navier-Stokes equation can be rewritten as

$$\frac{\partial \overline{u}_i}{\partial t} + \frac{\partial (\overline{u_i}\,\overline{u_j})}{\partial x_j} = -\frac{1}{\rho}\frac{\partial \overline{p}}{\partial x_i} + \nu \frac{\partial^2 \overline{u}_i}{\partial x_j \partial x_j} - \frac{\partial \tau_{ij}^R}{\partial x_j} \tag{3.35}$$

$$\frac{\partial \overline{u}_i}{\partial x_i} = 0, \qquad \frac{\partial u_i'}{\partial x_i} = 0 \tag{3.36}$$

where the additional term τ_{ij}^R is the residual stress term, which arises because the filtered product $\overline{u_i u_j}$ is not the same as the product of the filtered single velocities $\overline{u}_i \overline{u}_j$. The term τ_{ij}^R is the large-scale momentum flux caused by the action of the small scales or the so-called subgrid-scales and it can be expressed as:

$$\tau_{ij}^R = \overline{u_i u_j} - \overline{u}_i \overline{u}_j \tag{3.37}$$

This can be further decomposed into isotropic and anisotropic parts. The anisotropic residual stress can be formed as:

$$\tau_{ij}^r = \tau_{ij}^R - \frac{1}{3}\tau_{kk}^R \delta_{ij} \tag{3.38}$$

then the modified filtered pressure with the isotropic residual stress is expressed as:

$$\overline{P} = \overline{p} - \frac{1}{3}\rho \tau_{kk}^R \tag{3.39}$$

The momentum equation (3.35) can then be reformulated as:

$$\frac{\partial \overline{u}_i}{\partial t} + \frac{\partial (\overline{u_i}\,\overline{u_j})}{\partial x_j} = -\frac{1}{\rho}\frac{\partial \bar{P}}{\partial x_i} + \nu \frac{\partial^2 \overline{u}_i}{\partial x_j \partial x_j} - \frac{\partial \tau_{ij}^r}{\partial x_j} \tag{3.40}$$

The filtered governing equations of (3.40) or (3.36) are not closed and to close the equations, the SGS stress tensor τ_{ij}^r needs to be modelled.

3.3.3 Subgrid-Scale (SGS) Modelling

As mentioned above, the subgrid-scale model is used to close the equations for the filtered variables and remove the energy from the resolved scales. There are three models discussed here, namely Smagorinsky model, Dynamic model and Wall-Adapting Local Eddy viscosity model.

3.3.3.1 The Smagorinsky Model

The first model was developed by Smagorinsky in 1963 and named after him before it was explored further by Deardoff in 1970 [148]. This model is quite simple yet has been proven to perform well. It has formed the basis for more advanced models. This model can be viewed as consists of two steps: first, the linear eddy-viscosity model to relate the residual stress to the filtered strain-rate tensor $\overline{S}_{ij} = \left(\partial\overline{u}_i/\partial x_j + \partial\overline{u}_j/\partial x_i\right)/2$ and by an analogy to the mixing-length hypothesis, the second part is the modelling for the eddy viscosity of residual motions, ν_r. These two steps are represented as following equations.

$$\tau_{ij}^r = -2\nu_r\overline{S}_{ij} \tag{3.41}$$

$$\nu_r = \ell_s^2\overline{S} = (C_s\Delta)^2\overline{S} \tag{3.42}$$

where $\overline{S}$ is the characteristic filtered rate of strain and can be defined in terms of strain-rate tensor $(2\overline{S}_{ij}\overline{S}_{ij})^{1/2}$. ℓ_s is the Smagorinsky lengthscale which is proportional to the filter width, Δ through the Smagorinsky coefficient, C_s. However, there is a weakness of using Smagorinsky model, where the ideal value of the coefficient C_s could be different in different flow regimes.

3.3.3.2 Germano-Lilly Dynamic Model

To resolve the limitation of the Smagorinsky model, C_s can be made to be a variable that responds to the flow. This modification strategy was first proposed by Germano *et al.* in 1991 [149] with further extensions of the model provided by Lilly [150] and Meneveau *et al.* [151], and is called as the Germano-Lilly model. By adapting the Smagorinsky model, the dynamic model provides a methodology for determining a suitable local value of the Smagorinsky coefficient, C_s by introducing a second filter, 'test filter' $\left(\widetilde{\overline{\Delta}}\right)$ that is generally larger than the grid filter.

The dynamic procedure is based on the resolved turbulent stress tensor also called Germano identity that reads as

$$\mathcal{L}_{ij} = T_{ij} - \widetilde{\tau_{ij}^R} = \widetilde{\overline{u}_i \overline{u}_j} - \widetilde{\overline{u}}_i \widetilde{\overline{u}}_j \tag{3.43}$$

where $T_{ij} = \widetilde{\overline{u_i u_j}} - \widetilde{\overline{u}}_i \widetilde{\overline{u}}_j$ is the residual stress tensor corresponding to the test filter operation and τ_{ij}^R is the residual stress tensor for the grid filter that is defined using equation (3.37). The dynamic model finds the coefficient that best complies with the assumption that the two subgrid tensors, τ_{ij}^R and T_{ij}, can be modelled by the same constant C_S^d for both filtering levels. This is achieved by application of the decomposition introduced in equation (3.37). Therefore, the Smagorinsky model for their deviatoric parts can be rewritten as:

$$\tau_{ij}^d = \tau_{ij}^R - \frac{1}{3}\tau_{kk}^R \delta_{\mathrm{ij}} = -2C_S^d \overline{\Delta}^2 \left|\overline{S}\right| \overline{S}_{ij} \tag{3.44}$$

$$T_{ij}^d = T_{ij} - \frac{1}{3}T_{kk}\delta_{ij} = -2C_S^d \widetilde{\overline{\Delta}}^2 \left|\widetilde{\overline{S}}\right| \widetilde{\overline{S}}_{ij} \tag{3.45}$$

By applying the above formulae to the equation (3.43), the deviatoric part of the resolved stress, $\mathcal{L}_{ij}$ can be obtained and defined as:

$$\mathcal{L}_{ij}^{d} = \mathcal{L}_{ij} - \frac{1}{3}\mathcal{L}_{kk}\delta_{ij} = C_S^d \alpha_{ij} - \widetilde{C_S^d \beta_{ij}} \tag{3.46}$$

where $\alpha_{ij} = -2\widetilde{\overline{\Delta}}^2 \left|\widetilde{\overline{S}}\right| \widetilde{\overline{S}}_{ij}$ and $\beta_{ij} = -2\overline{\Delta}^2 |\overline{S}| \overline{S}_{ij}$.

Assuming that the constant, C_S^d, is uniform over the test filter width, it can be taken out of the explicit filtering operator. This leads to the definition of the Smagorinsky model of deviatoric part of the resolved stress, $\mathcal{L}_{ij}$, as:

$$\mathcal{L}_{ij}^{S} = T_{ij}^{d} - \widetilde{\tau_{ij}^{d}} = C_S^d \left(\alpha_{ij} - \tilde{\beta}_{ij}\right) \tag{3.47}$$

In order to determine a single value of the constant C_S^d, Lilly (1992) suggests that the mean-square error minimized by the specification of:

$$C_S^d = \frac{\mathcal{M}_{ij}\mathcal{L}_{ij}^{d}}{\mathcal{M}_{kl}\mathcal{M}_{kl}} = \frac{\mathcal{M}_{ij}\mathcal{L}_{ij}}{\mathcal{M}_{kl}\mathcal{M}_{kl}} \tag{3.48}$$

where $\mathcal{M}_{ij} = \alpha_{ij} - \tilde{\beta}_{ij}$ and $\mathcal{M}_{ij}\mathcal{L}_{ij} = \mathcal{M}_{ij}\mathcal{L}_{ij}^{d}$, since $\mathcal{M}_{ij}$ is deviatoric.

Therefore the value of constant C_S^d can be computed dynamically. This constant parameter can assume negative values. This characteristic can be interpreted as a backward energy cascade mechanism. The constant parameter is not bounded, since the denominator can cancel out. Consequently, these characteristics may lead to an instability in the LES calculation. To avoid this problem it is a good practice to average the numerator and the denominator in equation (3.48) either temporally or spatially to obtain a reasonable value for the constant parameter [149,150].

3.3.3.3 Wall-Adapting Local Eddy-Viscosity (WALE) model

Both models discussed above (Smagorinsky and Dynamic Smagorinsky model) are based on the local strain rate, where the velocity scale is determined arbitrarily at cut-off. Nicoud

& Ducros [152] These models relate the subgrid dissipation to the strain rate of the smallest resolved motion. Nicoud & Ducros [152] argue that this formulation does not account for the contribution of the energy in regions of high vorticity which dominate irrotational strain.

To rectify this, Nicoud & Ducros [152] proposed a subgrid viscosity model called Wall Adapting Local Eddy-viscosity (WALE) model that takes into account both the strain and rotational rates:

$$\nu_{sgs} = L_w^2 \frac{\left(S_{ij}^d S_{ij}^d\right)^{3/2}}{\left(\overline{S_{ij}}\,\overline{S_{ij}}\right)^{5/2} + \left(S_{ij}^d S_{ij}^d\right)^{5/4}} \tag{3.49}$$

where L_w and S_{ij}^d are defined as:

$$L_w = min(\kappa d, C_w \Delta) \tag{3.50}$$

$$S_{ij}^d = \frac{1}{2}\left(\overline{g_{ij}}^2 + \overline{g_{ji}}^2\right) - \frac{1}{3}\delta_{ij}\overline{g_{ij}}^2 \tag{3.51}$$

where $\overline{g_{ij}} = \partial\overline{u_i}/\partial x_j$ is the resolved velocity gradient tensor, and C_w is a model constant.

The proposed model is said to be able to detect all turbulent structures that are relevant for the kinetic energy dissipation. The eddy-viscosity also goes naturally to zero near the wall as a consequence and no damping function is required. Nicoud & Ducros [152] demonstrated that the WALE model produces zero ν_{sgs} in a pure shear flow, hence, can potentially reproduce transitional flows. WALE model is numerically more stable than the Dynamic model, where the SGS viscosity in the former model always positive, whereas a negative value can be generated in the latter. In *Code_Saturne*, C_w in the WALE model is set to 0.25.

3.3.4 Model Performance Parameter

The accuracy of LES is dependent on the numerical methods and the SGS model. The

former is influenced by the grid resolution while the model accuracy depends on the performance of the SGS model in comparison to DNS. The performance of LES could be tested using either a priori or posteriori test. In the former, results from LES are compared with the corresponding quantities filtered from DNS results while the latter compares actual LES results with experimental or those from DNS. A good LES should resolve at least 80% of the turbulent energy [138]. Therefore, independent assessment parameters are developed by some researchers in order to evaluate the quality of LES.

A parameter to quantify LES results with respect to DNS results has been introduced by Geurts & Fröhlich [153], in the form of a subgrid activity parameter,

$$s = \frac{\langle \varepsilon_{sgs} \rangle}{\langle \varepsilon_{sgs} \rangle + \langle \varepsilon_{\mu} \rangle} \tag{3.52}$$

where $\langle \varepsilon_{sgs} \rangle$ and $\langle \varepsilon_{\mu} \rangle$ are the average subgrid-scale dissipation and the average molecular dissipation. This parameter may vary in the range of $0 \leq s \leq 1$, with $s = 0$ corresponding to DNS results and $s = 1$ corresponding LES at infinite Reynolds number.

Celik *et al.* [154] stated that the *s* parameter in the above equation is not sensitive to the resolution of the grid as the numerical dissipation is not taken into account. Thus, an alternative version of subgrid parameter suggested as:

$$s^* = \frac{\langle \mu_{sgs} \rangle + \langle \mu_{num} \rangle}{\langle \mu_{sgs} \rangle + \langle \mu_{num} \rangle + \langle \mu \rangle} \tag{3.53}$$

where $\langle \mu_{num} \rangle$ is the average numerical viscosity and it is not known.

Celik *et al.* [154] demonstrated that in high-velocity gradient flows, the criterion *s* is not sensitive to the resolution of the grid. They proposed another parameter to measure the quality of large eddy simulation to consider the grid resolution and the Kolmogorov

lengthscale:

$$LES\_IQ_v = \frac{1}{1 + \alpha_v \left(\frac{s^*}{1 - s^*}\right)^n}$$

where $\alpha_v \approx 0.05$ and $n \approx 0.53$. LES is considered to be good, when LES_IQ_v is larger than 0.8, where the simulation can be considered to be 80% or above equivalent to DNS. To evaluate the unknown value of numerical viscosity, Celik *et al.* [155] have suggested that it may be approximated by using the following empirical equation:

$$\mu_{num} = \sqrt{C_n} \left(\frac{h}{\Delta}\right)^2 \mu_{sgs} \tag{3.54}$$

where $h = (\Delta x \Delta y \Delta z)^{1/3}$, is the grid size, Δ is the width of filter, and $C_n \approx 1$ for $h = \Delta$. Consequently, it can be concluded as, $\mu_{num} \approx \mu_{sgs}$. The parameter s^*, has been recommended in [155] to be ~0.2, signifying 80% contribution of molecular viscosity towards the dissipation.

3.4 Numerical Methods in *Code_Saturne*

Every solver in CFD is structured with several numerical solution techniques, including the discretisation of the mathematical equations. There are a few common types of discretisation techniques used, including, finite difference, finite element method and spectral method. Finite difference is the oldest method for numerical solution, and the method describes the unknowns ϕ of the flow by means of point samples of a grid co-ordinate lines. The second method, finite element uses simple piecewise functions (e.g., linear or quadratic), valid on elements to describe the local variations of the unknown ϕ. Lastly, the spectral

method approximates unknowns by means of the truncated Fourier series or Chebyshev polynomials. Unlike finite difference and finite element methods, the approximation by the spectral method is not local but valid throughout the entire computational domain.

Apart from the aforementioned methods, there is another method which is widely used in general purpose CFD codes, that is the finite volume method. This method was originally developed as a special finite difference formulation, and it can accommodate any type of grid, hence is suitable for complex geometries. The numerical algorithm for the finite volume method consists of the following steps:

- Formal integration of the governing equations of the fluid flow over all finite control volumes of the solution domain.
- The discretisation involves the substitution of finite-difference approximations for the terms in the integrated equation representing flow process. This converts the integral equations into a system of algebraic equations.
- Solution of algebraic equations is achieved by an iterative method.

More comprehensive discussion of the method used can be viewed in [156,157].

For this PhD study, an open-source solver *Code_Saturne* is utilized. *Code_Saturne* is a general-purpose computational fluid dynamics software that has been developed by Électricité de France (EDF) since 1997. *Code_Saturne* uses a co-located Finite Volume approach that can accept either hybrid, structured or unstructured meshes. *Code_Saturne* is capable of handling incompressible or expandable flows, with or without heat transfer and turbulence. Turbulence models offered in the code range from Reynolds-averaged models (e.g., mixing length model, v2f, Reynolds stress models) and those for

Large Eddy Simulation (LES). A number of dedicated modules for specific physical models are made available in the code (e.g., radiative heat transfer, combustion, magneto-hydro dynamics, compressible flows and two-phase flows). For more flexibility, additional subroutines can be added to the main solver by the user. The numerical approach used in *Code_Saturne* will be discussed briefly herein.

3.4.1 Discretisation in *Code_Saturne*

As a starting point in the computational procedures of the finite volume method, the general equation of the conversation law of the transport in an unsteady flow is given as

$$\frac{\partial(\rho\phi)}{\partial t} + \frac{\partial(\rho\phi u_i)}{\partial x_i} = \frac{\partial}{\partial x_i}(\Gamma \frac{\partial \phi}{\partial x_i}) + q_\phi \qquad (3.55)$$

where Γ is the diffusion coefficient and q_ϕ is the source term. The variable ϕ can be set equal to $1, u_i$ and any scalar variable. Equation (3.55) is integrated over a volume, then the Gauss' divergence theorem is applied to the convection and diffusion terms yielding,

$$\underbrace{\frac{\partial}{\partial t}\int_\Omega \rho\phi \, d\Omega}_{\text{Temporal term}} + \underbrace{\int_S \rho\phi u_i n_i \, dS}_{\text{Convection term}} = \underbrace{\int_S \Gamma \frac{\partial \phi}{\partial x_i} n_i dS}_{\text{Diffusion term}} + \underbrace{\int_\Omega q_\phi \, d\Omega}_{\text{Source term}} \qquad (3.56)$$

where Ω represents volume and S is the bounding surface and n_i is the component of the normal vector to the surface element dS. The temporal term can be explained as the rate of change of the fluid property ϕ in the control volume. The convection and diffusion terms both respectively signify the net rate of decrease of ϕ by convection and rate of increase of ϕ by the diffusion across the control volume surfaces. While the source term is the net rate of increase of property ϕ due to sources inside the control volume. The temporal term and the source term are integrated over the cell volume, while the convection and diffusion term

are integrated over the surface boundaries of the cell, which is simply represented as the sum over all faces.

In the following subsections, further discussion on the discretisation of every term in equation (3.56) will be presented, followed by a description of the cell gradient computation and of the treatment of boundary conditions. A more comprehensive discussion on the approaches applied in *Code_Saturne* may be found in Archambeau *et al.* [157] and the *Code_Saturne* theory guide. The configuration of the internal face between two adjacent cell elements Ω_I and Ω_J is shown in Figure 3.3. The point O in Figure 3.3 is the intersection point between IJ at the corresponding face S_{ij}, while F is the point located at the face centre between two adjacent cells. I' and J' are the points of the projection of I and J orthogonally on the line normal to the face and crossing F.

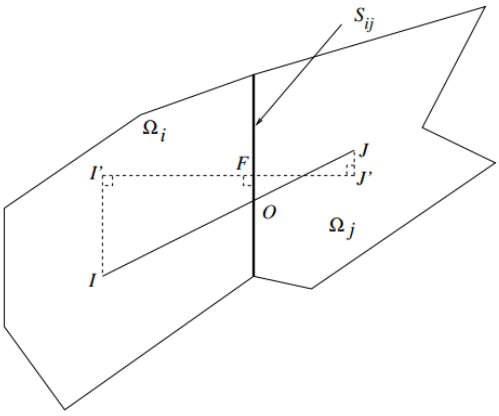

Figure 3.3: Sketch of internal face geometry [158]**.**

3.4.1.1 Temporal and Source Terms

The approximation of the value at point I (ϕ_I)in the control volume Ω_I can be obtained through,

$$\int_{\Omega_I} \phi \, d\Omega = (\phi_I \Omega_I) \tag{3.57}$$

Using the above definition, the temporal term in equation (3.56) can be expressed as,

$$\frac{\partial}{\partial t}\int_{\Omega_I} \rho\phi \, d\Omega \approx \frac{\partial}{\partial t}(\rho\phi_I\Omega_I) \tag{3.58}$$

Similarly, the source term S_ϕ in equation (3.56) which may represent heat generation in the fluid or a pressure gradient when periodic boundary conditions are applied can be computed as

$$\int_{\Omega_I} q_\phi \, d\Omega = q_{\phi I}\Omega_I \tag{3.59}$$

3.4.1.2 Convection Schemes

The convection term in equation (3.56) is discretised as

$$\int_S \rho\phi(u\cdot n)\, dS \approx \sum_{\Omega_I \in \mathcal{F}(\Omega_I)} (\rho\phi_{IJ}(u_{IJ}\cdot n_{IJ})S_{IJ}) = \sum_{\Omega_I \in \mathcal{F}(\Omega_I)} \phi_{IJ}m_{IJ} \tag{3.60}$$

where $\mathcal{F}(\Omega_I)$ represents the faces to the neighbour cells of the volume Ω_I , ϕ_{IJ} is the value of ϕ at the internal face centre, F, between the cells Ω_I and Ω_J , n_{IJ} is the vector normal to the face pointing into Ω_J from Ω_I, and m_{IJ} is the mass flux between these two adjacent cells.

An interpolation needs to be introduced in order to evaluate the unknown value of ϕ_{IJ} at the face centres as the values of ϕ are only calculated at the cell centres. In *Code_Saturne* there are several convection schemes available for such an approximation namely, upwind differencing scheme (UDS), second-order linear upwind (SOLU), and second-order central differencing scheme (CDS) approximation.

Upwind Differencing Scheme

For the 1st-order upwind difference scheme, the value ϕ_{IJ} at the face centres is equivalent to the value of ϕ at cell centre of the nearest upstream cell,

$$\phi_{IJ}^{UDS} = \begin{cases} \phi_I \; if \; m_{IJ} \geq 0 \\ \phi_J \; if \; m_{IJ} < 0 \end{cases} \tag{3.61}$$

UDS is numerically diffusive and it is the only approximation that satisfies the boundedness criteria unconditionally as it will never yield oscillatory solutions.

Second Order Linear Upwind Scheme

The SOLU scheme approximates the value of ϕ_{IJ} at the face using the value of the upwind cell centre. It makes use of the cell centre gradient between neighbouring cells to reach a higher order in space. In contrast, the 1st-order scheme assumes the equality between the value of the cell centre and the face centre.

$$\phi_{IJ}^{SOLU} = \begin{cases} \phi_I + IF \cdot (\nabla\phi)_I \; if \; m_{IJ} \geq 0 \\ \phi_J + JF \cdot (\nabla\phi)_J \; if \; m_{IJ} < 0 \end{cases} \tag{3.62}$$

where *IF* and *JF* are distances between cell centres I and J to the face centre respectively.

Central Differencing Scheme

The CDS is a linear interpolation between the two nearest nodes and can be represented as follows.

$$\phi_{IJ}^{CDS} = \alpha_{IJ}\phi_I + \left(1 - \alpha_{IJ}\right)\phi_J + \frac{1}{2}\left[(\nabla\phi)_I + (\nabla\phi)_J\right] \cdot OF \tag{3.63}$$

where the linear interpolation factor is defined as $\alpha_{IJ} = \frac{FJ'}{I'J'}$ and the value of 0.5 is used for numerical stability reasons. If the mesh grid is orthogonal to each other, equation (3.63) can be simplified by cancelling the final term in the right hand side as it is equal to zero. This scheme is second order accurate. By default, the LES approach in *Code_Saturne* employs the central differencing scheme.

3.4.1.3 The Diffusion Operator

The diffusion term in equation (3.56) is discretised in *Code_Saturne* as follows:

$$\int_S \Gamma \frac{\partial \phi}{\partial x_i} n_i \, dS \approx \sum_{\Omega_I \in \mathcal{F}(\Omega_I)} \Gamma_{IJ} (\nabla \phi)_{IJ} \cdot n_{IJ} S_{IJ} \tag{3.64}$$

$$\approx \sum_{\Omega_I \in \mathcal{F}(\Omega_I)} \Gamma_{IJ} \frac{\phi_{J'} - \phi_{I'}}{I'J'} S_{IJ} \tag{3.65}$$

where $(\nabla \phi)_{IJ} \cdot n_{IJ}$ is the normal gradient computed at F. The values of $\phi_{J'}$ and $\phi_{I'}$ can be computed by using the gradient at the cell centre, $\phi_{I'} = \phi_I + II' \cdot (\nabla \phi)_I$. Therefore, the diffusion term, with the correction terms for non-orthogonal faces included is computed as:

$$\int_S \Gamma \frac{\partial \phi}{\partial x_i} n_i \, dS = \sum_{\Omega_I \in \mathcal{F}(\Omega_I)} \Gamma_{IJ} \left[\frac{\phi_J - \phi_I}{I'J'} + (\nabla \phi)_{IJ} \cdot \left(\frac{J'J}{I'J'} - \frac{I'I}{I'J'} \right) \right] S_{IJ} \tag{3.66}$$

with $(\nabla \phi)_{IJ} = \frac{1}{2} \left((\nabla \phi)_I + (\nabla \phi)_J \right)$

3.4.2 Cell Gradient Computation

For an unstructured finite volume solver, it is a fundamental requirement to compute the cell-centre gradient. Considering non-orthogonal meshes, options available in *Code_Saturne*, are based on two approaches:

1. The ***iterative reconstruction technique*** only uses immediate neighbouring cells that share a common face to a cell I.

2. In addition to the immediate neighbours, the second approach of ***least squares method*** may also use the extended neighbours that share a common vertex with the cell I. This approach is generally faster since it does not involve the solution of an

implicit set of equations.

Due to the diffusive effects of the least squares method, the present LES simulations are conducted using the iterative reconstruction method. More detail on the latter approach is described below. Further information on the implementation for both methods in *Code_Saturne* may be found in Archambeau *et al.* [157].

Using the Gauss theorem, the cell-centre gradient is evaluated using the cell-face values and approximated by applying the mid-point rule of integration, such that:

$$(\nabla\phi)_I = \frac{1}{\Omega_I}\int_{\Omega_I} \nabla\phi \, d\Omega = \frac{1}{\Omega_I}\int_S \phi \underline{n} \, dS \tag{3.67}$$

$$\approx \sum_{\Omega_J \in \mathcal{F}(\Omega_I)} \phi_{IJ} \underline{n}_{IJ} \, S_{IJ} \tag{3.68}$$

The volume integral can be approximated accordingly as:

$$\int_{\Omega_I} \nabla\phi \, d\Omega \approx \Omega_I (\nabla\phi)_I \tag{3.69}$$

and the value of ϕ_{IJ}, which requires the gradient of ϕ_I and its approximation from Taylor series reads:

$$\begin{aligned} \phi_{IJ} &= \phi_O + (\nabla\phi)_O \cdot \underline{FO} \\ &= \alpha_{IJ}\phi_I + (1-\alpha_{IJ})\phi_J + \frac{1}{2}\left[(\nabla\phi)_I + (\nabla\phi)_J\right] \cdot \underline{FO} \end{aligned} \tag{3.70}$$

while ϕ_O is linear interpolated, the gradient at point O (see Figure 4.2) is evaluated using a mere average of $\frac{1}{2}\left[(\nabla\phi)_I + (\nabla\phi)_J\right]$, which has been proven to be sufficient and more robust than linear interpolation. Therefore, the right hand side of equation (3.69) can be formulated as:

$$\Omega_I(\nabla\phi)_I = \sum_{\Omega_J \in \mathcal{F}(\Omega_I)} \left[\alpha_{IJ}\phi_{IJ} + (1-\alpha_{IJ})\phi_J + \frac{1}{2}\left[(\nabla\phi)_I + (\nabla\phi)_J\right] \cdot \underline{FO}\right] \underline{n}_{IJ} S_{IJ} \tag{3.71}$$

To solve the system, the iterative process of cell gradients computation for equation (3.71) can be read as:

$$\Omega_I(\nabla\phi)_I^{k+1} - \sum_{\Omega_J \in \mathcal{F}(\Omega_I)} \frac{1}{2}\left[(\nabla\phi)_I^{k+1} \cdot \underline{FO}\right] \cdot \underline{n}_{IJ} S_{IJ} = \sum_{\Omega_J \in \mathcal{F}(\Omega_I)} \left[\alpha_{IJ}\phi_{IJ} + (1-\alpha_{IJ})\phi_J + \frac{1}{2}\left[(\nabla\phi)_J^k\right] \cdot \underline{FO}\right] \cdot \underline{n}_{IJ} S_{IJ} \tag{3.72}$$

where k denotes the iterations. For the initial guess, the calculation is performed without the gradient reconstruction terms:

$$\Omega_I(\nabla\phi)_I^0 = \sum_{\Omega_J \in \mathcal{F}(\Omega_I)} \left[\alpha_{IJ}\phi_{IJ} + (1-\alpha_{IJ})\phi_J\right] \underline{n}_{IJ} S_{IJ} \tag{3.73}$$

3.4.3 Time-Advanced schemes

Since turbulence varies with space and time, time advancing schemes are implemented to solve the time-dependent problems either implicitly or explicitly. Consequently, the variable ϕ over time $\Delta t = t_{n+1} - t_n$ can be read as:

$$\phi^{n+1} = \phi^n + f\Delta t \tag{3.74}$$

where f is an unknown that may be estimated using several procedures, such as first-order Euler schemes or the second-order Crank-Nicolson methods. The approximation method said to be explicit if f evaluated at times for which the solution is known, whereas if the value at

the new time level is required, the approximation is called an implicit method.

In *Code_Saturne*, the LES formulation is coded with a combination of the explicit Adams-Bashforth and the implicit Crank-Nicolson schemes [159], leading to a second-order scheme in time. The only constant time step is considered in the present work, as it is well suited to LES and the time averaging approach that is needed for the statistics. The application of the relevant time scheme for each of the terms in the transport equation following their discretisation in space is discussed in the following subsections. All terms are centred in time and are therefore expressed at time $n+\frac{1}{2}$.

3.4.3.1 Temporal Term

The temporal term in equation (3.58) is calculated using a fully implicit Euler scheme as:

$$\frac{\partial}{\partial t}(\rho\phi_I\Omega_I) = \rho\Omega_I\frac{\phi_I^{n+1}-\phi_I^n}{\Delta t} \tag{3.75}$$

This formulation becomes second order when the right hand side of equation is expressed at $n+\frac{1}{2}$.

3.4.3.2 Convection Term

For convection term in equation (3.60), mass flux, m_{IJ} is treated explicitly and is evaluated at the time step $n+\frac{1}{2}$ using an Adams-Bashforth scheme:

$$m_{IJ}^{n+\frac{1}{2}} = \frac{3}{2}m_{IJ}^n - \frac{1}{2}m_{IJ}^{n-1} \tag{3.76}$$

Meanwhile the variable ϕ_{IJ} at the face centre is evaluated using a Crank-Nicolson scheme and expressed similarly at time $n+\frac{1}{2}$:

$$\phi_{IJ}^{n+\frac{1}{2}} = \frac{1}{2}\left(\phi_{IJ}^{n+1} + \phi_{IJ}^{n}\right) \tag{3.77}$$

The convection term can, therefore, be rewritten as:

$$\int_S \rho\phi(u \cdot n)\, dS = \sum_{\Omega_I \in \mathcal{F}(\Omega_I)} \frac{1}{2}\rho(\phi_{IJ}^{n+1} + \phi_{IJ}^{n})\left(\frac{3}{2}m_{IJ}^{n} - \frac{1}{2}m_{IJ}^{n-1}\right) \tag{3.78}$$

3.4.3.3 Diffusion Term

The implicit Crank-Nicolson scheme is applied only to the variable ϕ_{IJ}. The diffusivity however is evaluated explicitly to avoid a likely unstable solution arising from negative values. Equation (3.64) then can be expressed as

$$\int_S \Gamma \frac{\partial \phi}{\partial x_i} n_i\, dS = \sum_{\Omega_I \in \mathcal{F}(\Omega_I)} \frac{1}{2}\Gamma_{IJ}^{n}\left[(\nabla\phi)_{IJ}^{n+1} + (\nabla\phi)_{IJ}^{n}\right] \cdot n_{IJ} S_{IJ} \tag{3.79}$$

3.4.3.4 Source Term

The source terms in equation (3.59) are evaluated with the explicit Adams-Bashforth scheme:

$$q_{\phi_I}\Omega_I = \Omega_I\left(\frac{3}{2}q_{\phi_I}^{n} - \frac{1}{2}q_{\phi_I}^{n-1}\right) \tag{3.80}$$

3.4.4 Pressure-Velocity Coupling

Previous sections have discussed the space and time discretisation techniques employed in *Code_Saturne* for a generic conservation equation. However, the discretisation for full Navier-Stokes equations may present some special features.

From the general transport equation (3.55), the momentum conservation equations can be derived by replacing the variable ϕ by u, v and w respectively. Further filter operations to the system of equations are given as:

$$\frac{\partial(\rho\overline{u}_i)}{\partial t}+\frac{\partial\left(\rho\overline{u_i u_j}\right)}{\partial x_j}=\frac{\partial\overline{p}}{\partial x_i}+\frac{\partial}{\partial x_j}\left[(\mu+\mu_t)\left(\frac{\partial\overline{u}_i}{\partial x_j}+\frac{\partial\overline{u}_j}{\partial x_i}\right)\right] \quad (3.81)$$

$$\frac{\partial(\rho\overline{u}_i)}{\partial x_i}=0 \quad (3.82)$$

The equation set above provides two set of problems. First, the convective terms of the momentum equation contain the nonlinear quantities. Second, the set of equations are coupled because every velocity component appears in each momentum and continuity equation. The most complex issue in resolving the Navier-Stokes equations is the role of pressure whose gradient appears in the momentum equations, but it lacks its own independent equation.

Both problems are linked to nonlinearity and pressure-velocity coupling can be resolved by adopting an iterative solution strategy. In *Code_Saturne*, a fractional step scheme based on the SIMPLEC (Semi-Implicit Method for Pressure-Linked Equations - Consistent) algorithm of Van Doormaal & Raithby [160] is used, which consists of a prediction-correction method. The solution procedure is described briefly below. More detail on the approach can be found in Archambeau *et al.* [157].

In the fractional step method, there are two sub-steps performed. The first constitutes velocity prediction and the second is the pressure correction or the velocity projection step, which resolves the mass equation.

Velocity prediction step: The momentum equation is solved with the pressure gradient treated explicitly. The predicted velocities are obtained in this step.

Pressure correction step: The pressure is calculated by solving the Poisson equation, then a divergence free corrected velocity field can be obtained. The pressure is updated by adding

the pressure increment (δP), which is equal to the pressure difference between the time n+1 and n. Pressure increment is obtained at the end of this step. Rhie & Chow [161] interpolation is used. After the velocity has been updated, the scalars are updated according to their time scheme. This step avoids the oscillatory solutions due to the decoupling of the odd nodal values from even nodal values.

3.4.4.1 Convergence and Stability Analysis

Iteration-Convergence

To ensure the convergence of the calculated solution, the system of equations is inspected by means of a Euclidean norm. The convergence error is to determine the iterative procedure to be restarted if it tested positive, and this is repeated until the criteria is achieved. This process helps to ensure the solution obtained to converge with minimal error. In the present study, the convergence criterion is set to a residual value of 10^{-5} and converged solutions are monitored by monitoring several points in different locations.

Numerical Stability Analysis

Discretization errors may arise from the spatial and temporal discretization during the unsteady calculation. Therefore the stability analysis for the explicit treatment for both the convection terms and the diffusion terms, have to satisfy the stability condition known as Courant-Friedriech-Lewy criterion [162], which as follows:

$$CFL = \frac{u_{max}\Delta t}{\Delta x_{min}} \tag{3.83}$$

where $\Delta x_{min}$is the minimum grid width and u_{max}. Generally the CFL criteria is suggested that below unity. In the present study, the CFL was ensured to below than ~0.6.

3.4.5 Boundary Conditions

In general, convective fluxes are prescribed at the inflow boundary, while zero at impermeable walls and symmetry planes. Moreover, a convective flux is usually assumed to be independent of the coordinate normal to an outflow boundary, for which an upwind approximation can be used. Diffusive fluxes are sometimes specified at a wall e.g., specified heat flux (including the special case of an adiabatic surface with zero heat flux) or boundary values of variables are prescribed.

There are two types of boundary conditions, namely Dirichlet and Neumann. Dirichlet boundary condition defines the value of the variable at the centre of the boundary face, whilst the Neumann boundary condition is based on assigning the normal gradient of the variable at the face.

The value of ϕ at the boundary face centre (see Figure 3.4) is defined by means of two coefficients A_ϕ and B_ϕ as:

$$\phi_F = A_\phi + B_\phi \phi_{I'} \tag{3.84}$$

For a Dirichlet boundary condition, the value of A_ϕ is prescribed and B_ϕ = 0, therefore $\phi_F = \phi^{dir}$. For a Neumann boundary condition, the coefficient $B_\phi = 1$ and the value of the variable ϕ at the boundary is given by:

$$\phi_F = (\nabla\phi)^{neu} \cdot I'F + \phi_{I'} \tag{3.85}$$

where $(\nabla\phi)^{neu} = (\nabla\phi)_F \cdot n_F$.

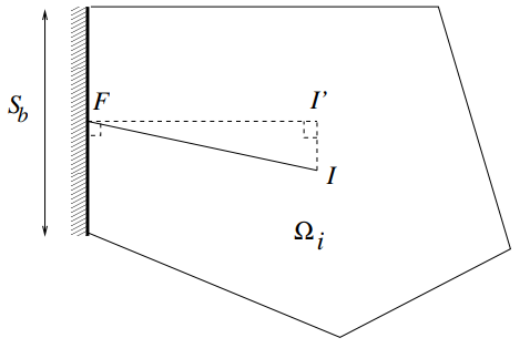

Figure 3.4: Sketch of boundary face geometry [158]**.**

3.4.5.1 Inlet

The Dirichlet boundary condition is prescribed at the beginning of time step n for all transport variables $\phi_{inlet}^{(n+1)}$, such as velocity and scalars, and a homogeneous Neumann condition ($(\nabla p)_F \cdot n_F = 0$) is imposed on the pressure.

3.4.5.2 Outlet

For outlet, a homogeneous Neumann boundary condition is specified for the velocity and scalars, whilst a Dirichlet condition is employed for the pressure.

The application of the homogeneous Neumann boundary condition for ϕ leads to the calculation of the convection term as:

$$\left[\left((\rho u)^{(n)} \cdot n\right)\phi^*\right]_{outlet} = \left((\rho u)^{(n)} \cdot n\right)_{outlet}\phi_{I'}^* \qquad (3.86)$$

where the mass flux $\left((\rho u)^{(n)} \cdot n\right)_{outlet}$ is the previous value obtained from the pressure correction step.

The boundary values for the diffusion terms are set to zero and a first-order approximation in space of the homogeneous Neumann condition is used to set $\phi = \phi_{I'}$ for the source terms (see equation (3.85)).

3.4.5.3 Walls and Symmetries

At walls and symmetry faces, a zero mass flux normal to the boundary is defined and scalars may be prescribed with either Dirichlet or Neumann conditions. The tangential velocity is treated with a homogeneous Dirichlet boundary condition at walls and a homogeneous Neumann condition at symmetry planes. A homogeneous Neumann condition is imposed for the pressure.

The boundary value of the mass flux is set to zero for the convection term. For the diffusion term, the value prescribed for the variable ϕ can be used directly if a Neumann boundary condition is specified. For the source terms, the prescribed value is used as the boundary value if a Dirichlet condition applies to ϕ. For the velocity component normal to the boundary, the boundary value is set to zero to ensure zero mass flux.

Chapter 4

Forced Convection Study on Heat Transfer to Water at Supercritical Pressure in a Trapezoid Annulus

SCWR is one of the six gen-IV reactor that is under development. The key aspects of the reactor design are the safety, simplicity of the plant systems as well as its high thermal efficiency. In the SCWR reactor, the thermophysical properties of the coolant water vary dramatically during heating, especially in the vicinity of pseudocritical temperature. This behaviour could lead to heat transfer deterioration or enhancement in the flow. It is a challenge to predict the detailed flow and temperature distributions for the design development.

Similar to many other nuclear reactor designs, the coolant in the fuel assemblies in the SCWR flows through the rod bundles, which can be divided into subchannels. As discussed in §2, instabilities exist in the rod bundles due to the presence of narrow gaps in between the fuel pins that connect the subchannels. The study of these instabilities is an important input to the design of the SCWR. Previous studies of flow through the narrow gaps were

predominantly done in isothermal conditions and only a few studies focused on the forced or mixed convection study, particularly in the supercritical condition. The knowledge on the effect of the variable properties would be a useful contribution to the knowledge of the flow and heat transfer at supercritical pressure in a rod bundle, especially for the SCWR core design.

The effect of the forced convection on the flow behaviour and heat transfer has been investigated using the CFD method, which is reported in this chapter. The large eddy simulation (LES) with WALE Subgrid-Scale (SGS) model is used herein for an accurate result. Simulations were carried out using *Code_Saturne*, an open-source CFD solver. The obtained results are presented and discussed in this chapter.

4.1 Case Description

The geometry is a trapezoid annulus where the flow passage is similar to the study by Wu & Trupp [120] and Duan & He [12,13]. This configuration can be considered similar to a simplified rod bundle consisting of triangular arrays. An enclosed rod is located in the middle of the trapezoid channel, forming a narrow gap and a wide gap with the outer wall. As can be seen in Figure 4.1, these gaps namely, wide gap (BG) and narrow gap (NG) are located at the top and bottom wall respectively. The main channels of the trapezoid annulus are located at either side of the inner rod and connected by the top and bottom gaps. The diameter of the inner rod is 0.0508 m and the ratio of the narrow gap to the inner rod diameter is 0.079. The height of the trapezoid channel is 0.066 m, and the widths of the top and bottom wall are 0.0508 m and 0.127 m respectively.

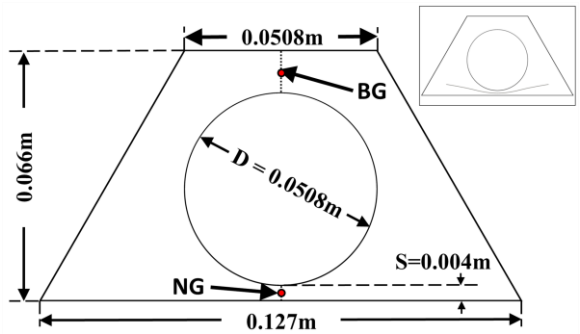

Figure 4.1: A cross-section of the channel. (Inset) An equidistant plane between the bottom wall and the rod wall at the narrow gap.

The hydraulic diameter,D_h of the channel, is 0.0314 m. The total length of the domain is $z = 40D_h$. The schematic diagram of the whole domain is illustrated in Figure 4.2. It is divided into two parts, namely the inflow generator and the test section. An internal mapping method is used to ensure a fully developed incoming flow to the test section. The flow field was first initialised using Synthetic Eddy Method (SEM) [163] at the targeted bulk velocity, and then the internal circulation in the inflow generator section was turned on after several time steps. The velocity field at $z = 5D_h$ in the inflow generator is copied at every time step and fed back to the inlet as a new boundary condition for the next time step. A typical fully developed flow is achieved in the simulation after sufficient time steps, in which considered to be at 3 through time of the length for the inflow generator. The inflow generator is an isothermal domain with a total length of $z = 10D_h$. In the test section, a constant heat flux is applied on the inner rod wall with a length of $z = 30D_h$, and this gives a total domain length of $z = 40D_h$.

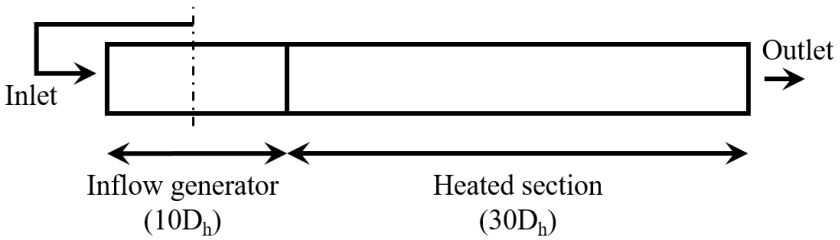

Figure 4.2: The length domain for LES.

To study the effects of the variations of thermal properties on the behaviour of the large flow structures, the heat flux was varied and three different heating cases were considered. The heat fluxes considered are 10kW/m^2, 50kW/m^2 and 75kW/m^2. In the present study, a constant heat flux is imposed on the rod wall in the heated section. The inlet bulk velocity for all cases is 0.0388 m/s. The inlet mass flow rate and Reynolds number are 0.088 kg/s and 10540 respectively. This Reynolds number is double that of Duan & He [12,13], and one-fifth of that of Wu & Trupp [120]. An inlet temperature of 360°C which is below the pseudocritical temperature at the specified pressure of 25 MPa is chosen. The thermal properties were obtained from NIST database.

An overview of the mesh at the cross-section is illustrated in Figure 4.3. A fully structured non-uniform mesh containing 33 million elements was adopted. The generated mesh used comprises of fine and coarser grids respectively near the wall and in the centre of the main channel. The mesh nodes adjacent to the wall are in the range of $5 \leq \Delta x^+ \leq 17$, $0.13 \leq y^+ \leq 0.2$ and $\Delta z^+ \approx 23$ for spanwise, wall normal and streamwise respectively. At wall location of $y^+ \leq 20$, there are about 13 cells with ~9 cells are located in $y^+ \leq 10$. These values were evaluated from the isothermal sub-domain. Based on the above information, the LES carried out can be viewed as well-resolved simulations [164]. The simulation was solved by using WALE subgrid-scale model embedded in *Code_Saturne*. The velocity and pressure coupling is obtained using SIMPLEC algorithm. A second order central difference scheme in space and second-order in time is adopted.

For all three cases, the time step specified was 0.001s where its dimensionless value is $t^* = \Delta t U_b / D_h \approx 0.0012$. The overall maximum Courant-Friedrich-Lewy (CFL) number is able to keep below 0.7 for the stability in each case. The residuals are maintained below than

10^{-5} for Navier Stokes equations for around 3 through-time of the whole domain before the start statistics calculation. The convergence for the statistics is monitored and calculation of the averages are taken at about 4 through-time of the whole domain.

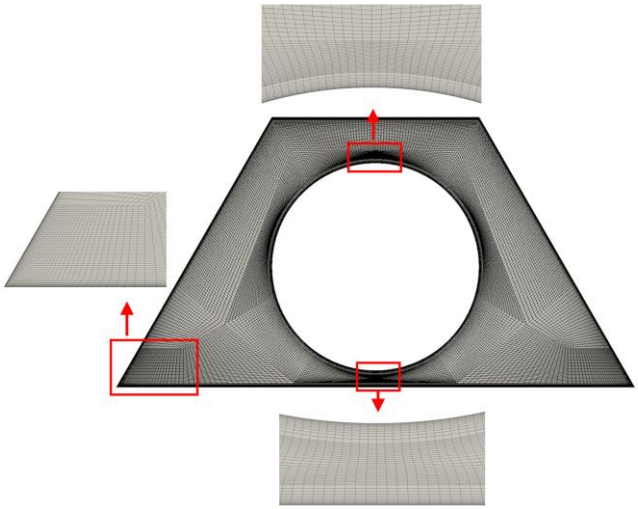

Figure 4.3: Mesh at the channel cross-section.

4.1.1 Predefined Locations for the Results Discussion

In Figure 4.1, the two points NG and BG are located at the midpoint in between the outer wall with the narrow gap and wide gap at the vertical symmetric line of the channel respectively. The histories of instantaneous velocities were recorded for several axial locations at the aforementioned points (NG & BG). Values obtained were used for spectral and correlation analyses. An equidistant plane (inset of Figure 4.1), which is located between the rod wall and the bottom wall is used to present the instantaneous flow and temperature field at the narrow gap across the domain. Some profiles across the channel are plotted at several locations shown in Figure 4.4. The line profiles are named respectively as NL, BL, ML, and MC for the profiles in the narrow gap, wide gap, towards the main channel and across the narrow gap to the main channel. Results from these lines are used to discuss the turbulence statistics.

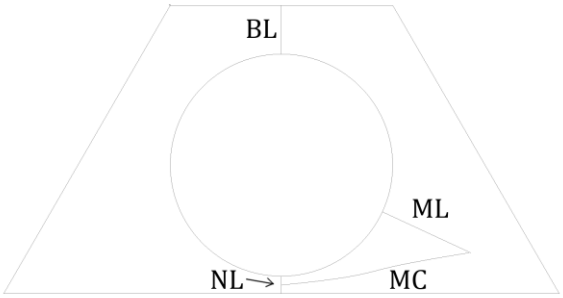

Figure 4.4: Pre-defined lines at the channel cross-section.

4.1.2 The Quality of the Simulations

It is important to evaluate the quality of the results obtained in the present study. To the author's knowledge, there is no experimental data or Direct Numerical Simulation (DNS) data, which can be used to directly validate the current LES study. Therefore, the quality of the mesh used in the LES of the current study is evaluated using the parameter s and LES_IQ_v that have been suggested by Geurts and Fröhlich [153] and Celik *et al.* [154] respectively. Definitions for both parameters can be found in §3. The highest heat flux case of 75kW/m^2 is chosen to discuss the quality of the results obtained. Thanks to the symmetrical channel configuration, only half cross-sections of the full trapezoid annulus channel are presented here. These results are presented at four distances down the channel as illustrated in Figure 4.5 and Figure 4.6.

The value of s can be seen as an estimation of the fraction of the turbulent kinetic energy modelled by LES and hence, the smaller the better. Pope [138] states that to obtain a good LES simulation, the turbulence kinetic energy has to be resolved over 80% i.e., $s < 0.2$. For the current simulations, the values of s are reasonably small in all wall regions. They are only

rather high in some central regions. As shown in Figure 4.5, the overall values of s increases slightly down the channel. The values of s are very low in the near wall regions, being around ~0.15. The region where s >0.45 spreads throughout the cross-section down the channel, especially at the main channel area. However, in the region near the heated rod, the values of s can be seen to decrease down the channel, which can be clearly seen across the top half of the rod pin.

Contrary to the s parameter behaviour, values of LES_IQ_v increase as the mesh is refined, hence the smaller the better. Overall LES_IQ_v parameter in the whole channel is maintained at a range of 0.97-0.98. According to Celik *et al.* [154], LES is considered to be good when LES_IQ_v>0.8. The quality of the results in this study as discussed earlier, the value of LES_IQ_v are found to be around 1 near the wall and >0.97 across the channel. This shows the results obtained are generally in good quality.

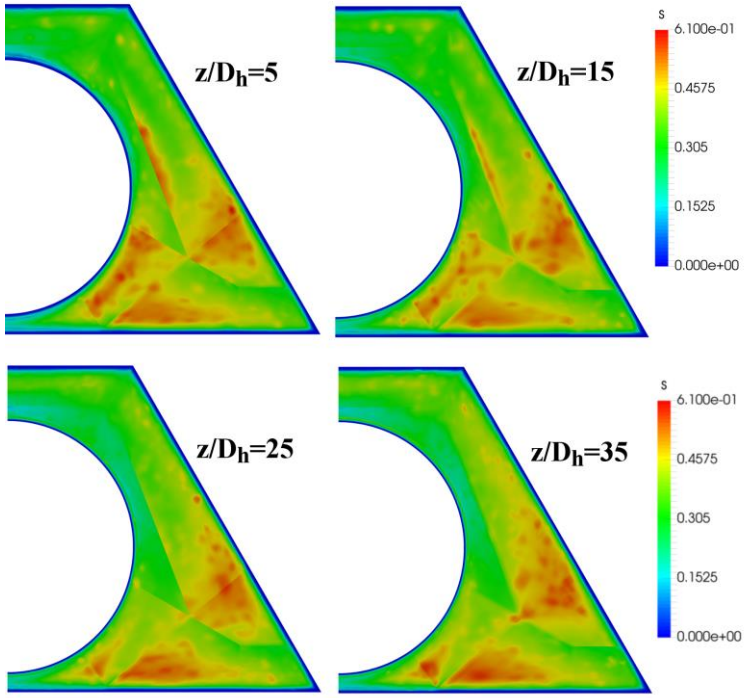

Figure 4.5: LES quality *s*.

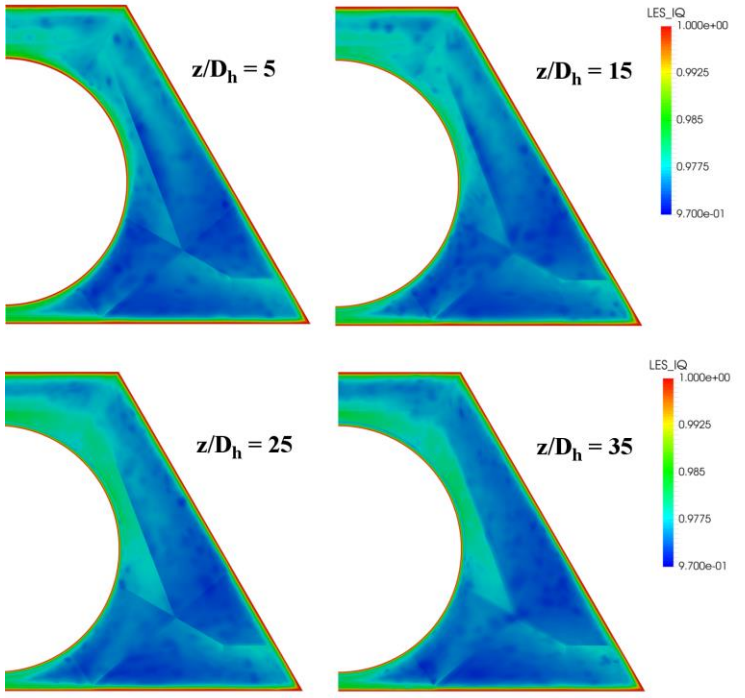

Figure 4.6: LES quality *LES_IQv*.

4.2 Results and Discussion

4.2.1 The Cross-Sectional Mean Velocity and Temperature

It is useful to first investigate the cross-sectional mean results of the flow and temperature for the general behaviour of the flow, before focusing on the flow instability at the gaps due to thermal expansion. This information could provide an insight into better understanding the performance of the large flow structures later on. As the density of the water in the supercritical pressure condition varies greatly around T_{pc}, the mean results are Favre-averaged.

Figure 4.7 shows the flow bulk temperature (T_b), wall temperature (T_w), streamwise bulk velocity (U_b) and heat transfer coefficient (HTC) down the channel. T_b is defined as,

$$T_b = \frac{\int \rho w T \, dA}{\int \rho w \, dA} \tag{4.1}$$

and HTC is calculated based on the cross-sectional averaged wall temperature and bulk temperature as follows:

$$HTC = \frac{q}{T_w - T_b} \tag{4.2}$$

where q is the heat flux applied.

As expected, the bulk fluid temperature and wall temperature increases monotonically down the channel in all cases. The temperature increases more rapidly in the case with a higher heat flux. From these results, it can be noted that for the first heating case of 10kW/m^2, the condition of the average wall temperature and the bulk temperature of the flow are in the $T_b < T_w < T_{pc}$ manner. A gentle change of properties can be expected from this condition.

Meanwhile, for the other two higher heating cases, the average wall temperature exceeds the pseudocritical temperature so that the condition of $T_b < T_{pc} < T_w$ achieved. Hence, in these cases the fluid temperature goes higher than the T_{pc} at some locations, which results in a rapid decrease in density and strong variations in other thermal properties.

Since the density is negatively correlated to the fluids temperature, the bulk velocity is also expected to accelerate down the channel, which is clearly shown in Figure 4.7 (c). It also shows that the acceleration rate is positively related to the heat flux, where there is a steeper increase in velocity down the channel in higher heating cases. In comparison, the acceleration is relatively linear in the case of 10kW/m^2, especially in the initial region of the heated section. This is due to the slower density variation. The averaged Heat Transfer Coefficients (HTC) however shows an opposite trend, that is, it decreases in value with the increase of heat flux. A steep drop can be observed in Figure 4.7 (d) at the beginning of the heated section in the case of heat flux 10kW/m^2. Down the heating channel, the value of HTC starts to decrease gently and this can be observed for the heat flux cases of 50kW/m^2 and 75kW/m^2 too but right from the beginning of heating. The higher the heat flux, has a more rapid decrease in HTC at the beginning of the heated channel, and having a lower overall HTC downstream of the channel.

To assist the discussion in this chapter, the case with a heat flux 10kW/m^2 is referred to as the ‘low heating case’ and the cases of 50kW/m^2 and 75kW/m^2 are referred to as the ‘high heating cases’ from hereafter.

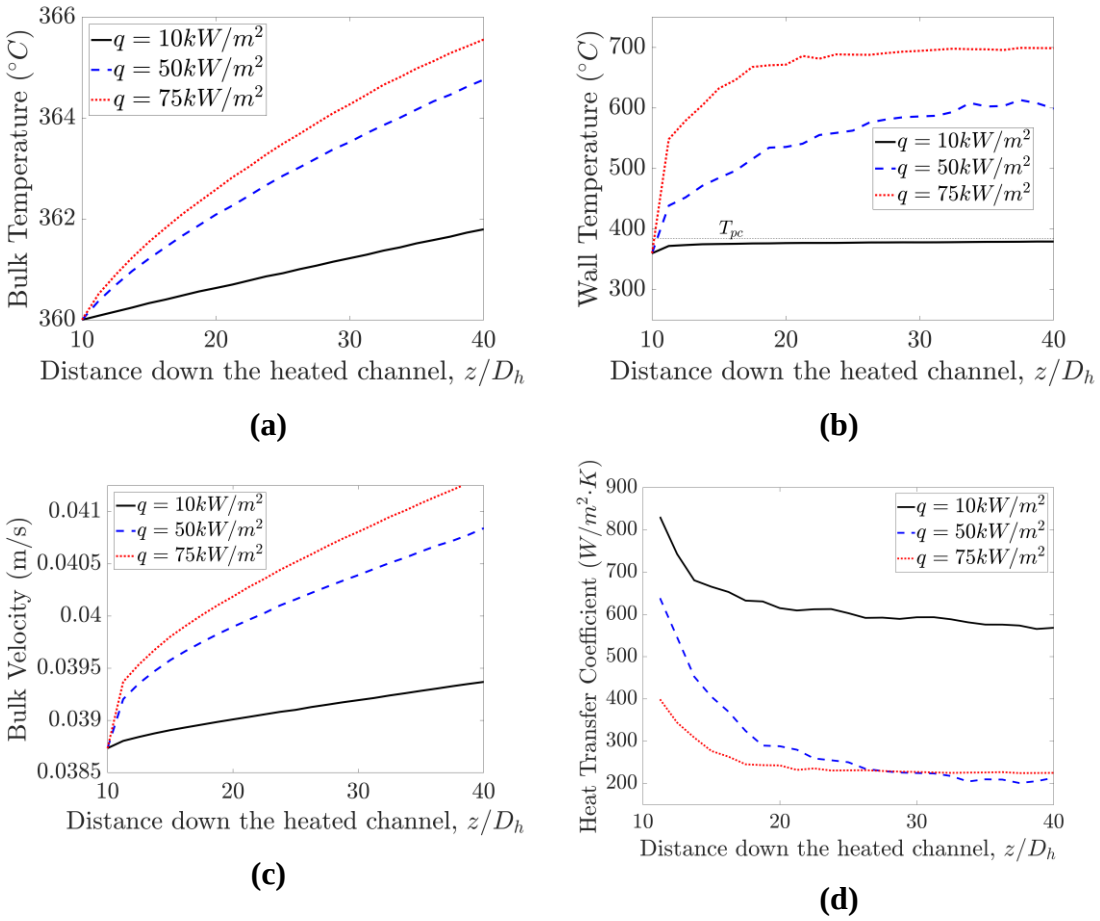

Figure 4.7: The mean quantities of the flow down the heated channel. a) bulk temperature b) rod wall temperature c) bulk velocity d) heat transfer coefficient

4.2.3 Instantaneous Flow Field

4.2.3.1 Equidistant Plane in the Narrow Gap

Figure 4.8 shows the contours of the instantaneous velocity and temperature fields at the equidistant plane between the rod wall and the bottom wall of the trapezoid channel (see inset of Figure 4.1). The general structures of the swinging flow are similar for all heating cases. The streamwise velocity at the centre of the narrow gap increases with the increase of heat flux, which agrees with the results of the bulk velocity shown earlier. Similarly, the temperature reaches its highest value at the centre of the narrow gap in all cases as illustrated in Figure 4.9. The value of the temperature at the gap is also increased down the channel at higher heat flux. The large flow structures, bringing the high-temperature fluid in and out of the narrow gap region, are expected to increase the mixing and help the heat transfer.

4.2.3.2 Rod Wall

It is interesting to study the behaviour of the instantaneous temperature on the rod wall facing the gap regions. To demonstrate this, Figure 4.10 shows the instantaneous temperature on the rod surface facing the narrow gap and the wide gap. A clear difference can be seen in the distribution of the temperature on the rod wall facing these two gaps. Evidently, in the narrow gap region, the swinging flow structures cause an oscillation in the temperature distribution on the rod surface. Flow structures are good for heat transfer thereby reducing the mean temperature in the small gap region; however, such oscillations of the rod temperature may increase the chance of thermal fatigue, a risk that needs to be considered in the design. Meanwhile, there are no obvious temperature oscillations observed on the rod wall facing at the wide gap.

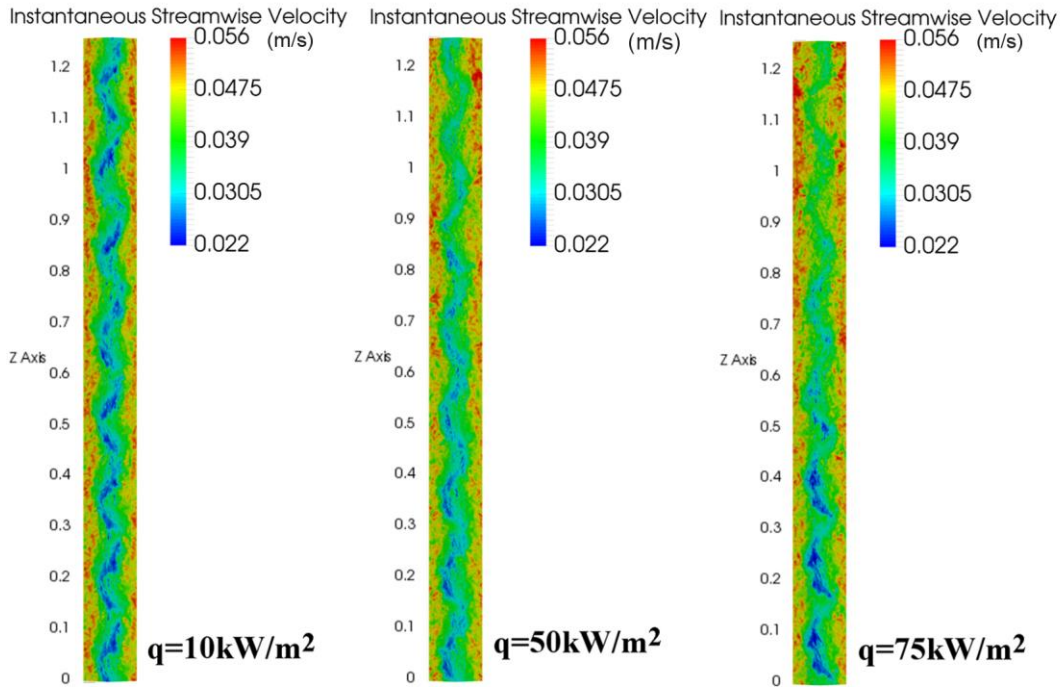

Figure 4.8: Instantaneous streamwise velocity at equidistant plane (see inset of Figure 4.1).

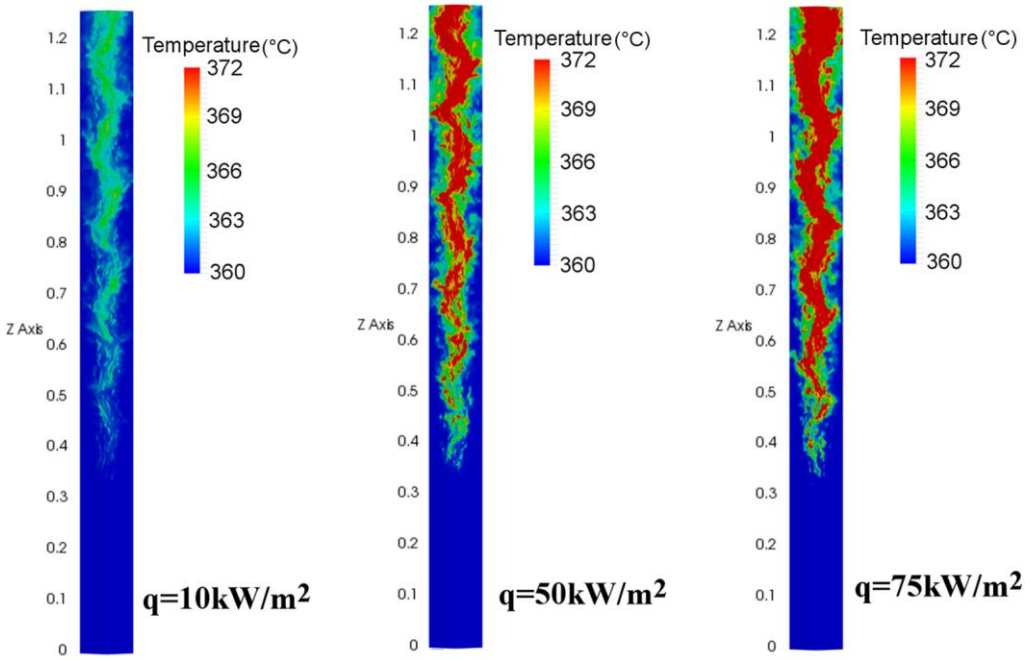

Figure 4.9: Instantaneous temperature at equidistant plane (see inset of Figure 4.1).

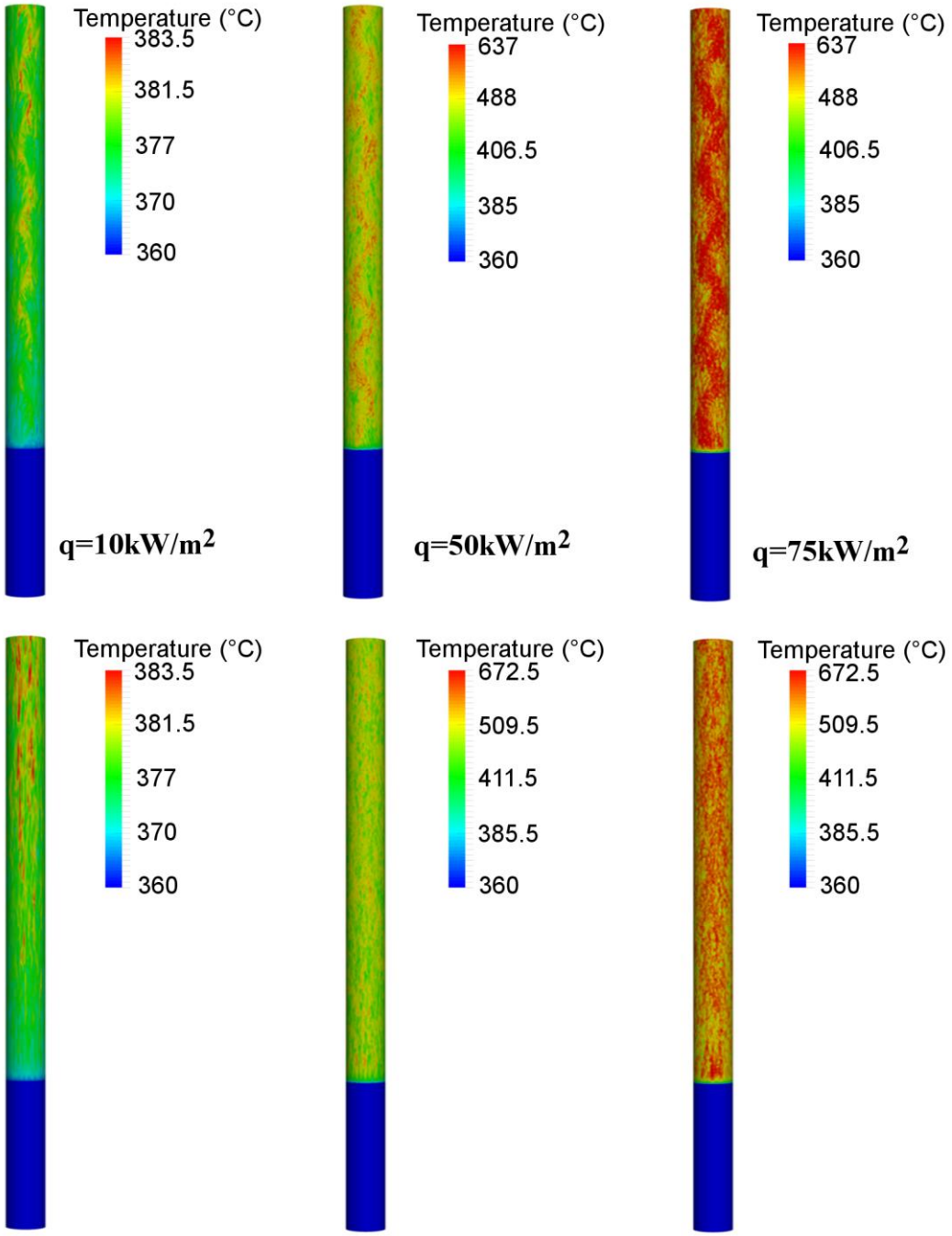

Figure 4.10: Instantaneous pin wall temperature. (Top) pin wall facing narrow gap (Bottom) pin wall facing wide gap.

4.2.3.4 Instantaneous Streamwise Vorticity

Figure 4.11 shows the results of the iso-surfaces for the instantaneous streamwise vorticity for all three heating cases. Results presented are the view of the narrow gap region at the $20D_h$ domain length to the outlet face for each case. The iso-surfaces for the instantaneous streamwise vorticity is generated at the value of ±10, i.e. where the positive value of the vorticity is coloured in red while the negative value is coloured in blue.

From the figure shown, it can be observed that the intensity for the instantaneous streamwise vorticity occurring in each heating case is different between them. In the lowest heating cases, it can be seen that pairs of opposite values for the instantaneous streamwise vorticity are apparently seen occurring throughout the narrow gap continuously. This behaviour could be contributing to the swinging flow structure that dominates the narrow gap. The same vorticity of the same magnitude, however, has reduced its intensity for the $q=50kW/m^2$ case. The vorticities in this case also are separated and more scattered than in the lowest heating case which is in a clustered form. Meanwhile, in the highest heating case, a more significant change can be seen where the intensity of the instantaneous streamwise vorticity is reduced even more dramatically in the narrow gap. The similar alternating of opposite values streamwise vorticities in previous lower heating cases cannot be observed at the narrow gap. A disappearance of the vorticity structures from the middle of the narrow gap can be observed which especially true towards the near the outlet. These phenomena have shown that the contribution of the behaviour of the vorticity structures occurring at the gap to the swinging flow structure can be seen in earlier results.

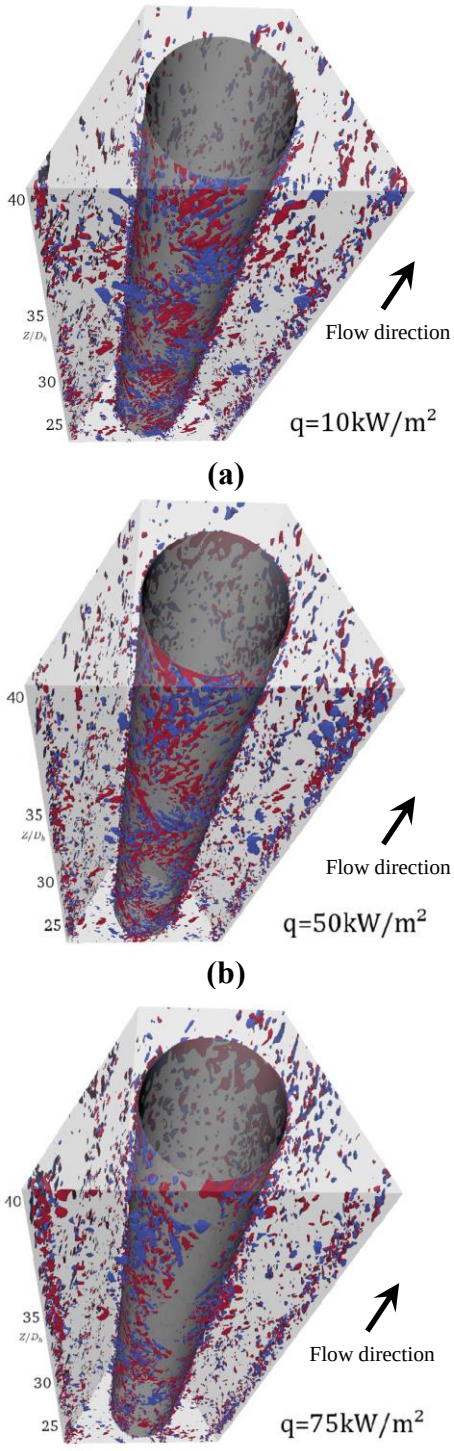

Figure 4.11: Iso-surfaces of instantaneous streamwise vorticity, Ω_z (red= +10 blue= –10) of instantaneous flow at $20D_h$ to the outlet. a) 10kW/m² b) 50kW/m² c) 75kW/m²

4.2.4 Instantaneous Velocity Fluctuation and Power Spectral Density

As mention earlier, several points at varying axial positions, located in the narrow gap (NG) and the wide gap (BG) of the channel are used to monitor the time history of the spanwise velocity. These results provide the instantaneous characteristics of the flow structure at the respective location in more detail.

4.2.4.1 Narrow Gap

The time histories of normalised fluctuating spanwise velocity at NG at several axial locations down the heated channel are shown in Figure 4.12 for each of the heating cases. Similar to the information in contour results earlier, strong quasi-periodic oscillations of the spanwise flow at the narrow gap can be seen in all cases. The trends of the oscillations and the dominant periods seem similar down the heated channel and maintain at around ~5s. In higher heating cases, some noises are observed in the signals recorded. This is probably due to the severe property changes at the location, as a result of the increase in the local flow temperature that could exceed T_{pc} in the narrow gap.

The spanwise velocity at NG *u'* can be evaluated by quantifying the dominant frequency of the quasi-periodic flow structures using the power spectrum density (PSD). PSD for all cases and several distances down the heated channel can be seen as in Figure 4.13. PSD values for the 50kW/m^2 and 75kW/m^2 are multiplied by a factor 10^2 and 10^4 respectively to assist in the presentation of data. In the distribution of the PSD of *u'* at the narrow gap, there are visible peaks for each of the heating cases at each location. The frequencies of these peaks can be identified as the dominant frequencies of the structures and can be referred to as the peak frequencies (f_p). For every case, f_p remains the same throughout the channel with a

value of ~0.21Hz. The dimensionless frequency Strouhal number can be calculated (this parameter is calculated using the bulk velocity, U_b at the unheated section) and the values are obtained to be around $St^{-1} \cong 5.62$ for all three cases. This value is close to the value obtained by Wu & Trupp [120] and Duan & He [12] of $St^{-1} \cong 5.57$, although the current Reynolds number is only 20% that of the former and doubled that in the latter study. Note that flow conditions in the present study are different from there of the previous studies. The current study was conducted at severe variations of properties, while the previous studies were performed at isothermal flow and constant property. This result shows that the Strouhal number is only dependent on the geometric configuration when the buoyancy force is not considered and the effect of the thermal expansion is rather limited.

Stronger dissipations of energy can be seen at the frequencies above 4Hz for all cases. Moreover, the noise level (i.e., the oscillations) at the high-frequency end of the spectra also varies significantly from case to case. For example, the oscillations of PSD at a higher frequency above 10Hz is reduced for the case of 50kW/m^2 (seeing at z/D_h =25 & 35), and significantly lower than in other cases. The differences in noise levels are due to the samples used where some samples seem to bear more noises than the others. Different noises between samples might be linked to the history of the fluid path between each sample. This problem can be avoided by smoothing out the noise/oscillations with ensemble averaging by increasing the number of samples. However, in the present work, only three samples are used for each spectrum average, and each such spectrum requires a time history of 20 seconds. This is already quite resources demanding let alone having more samples.

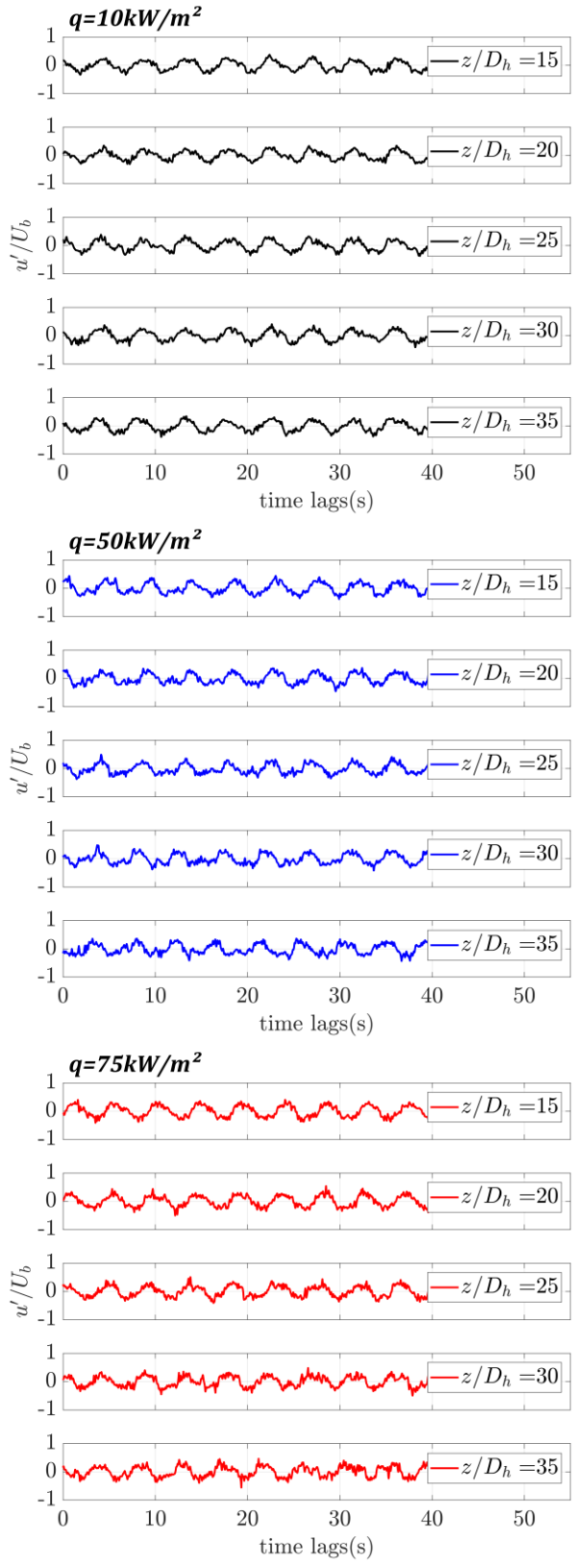

Figure 4.12: Instantaneous spanwise velocity at NG down the heated channel.

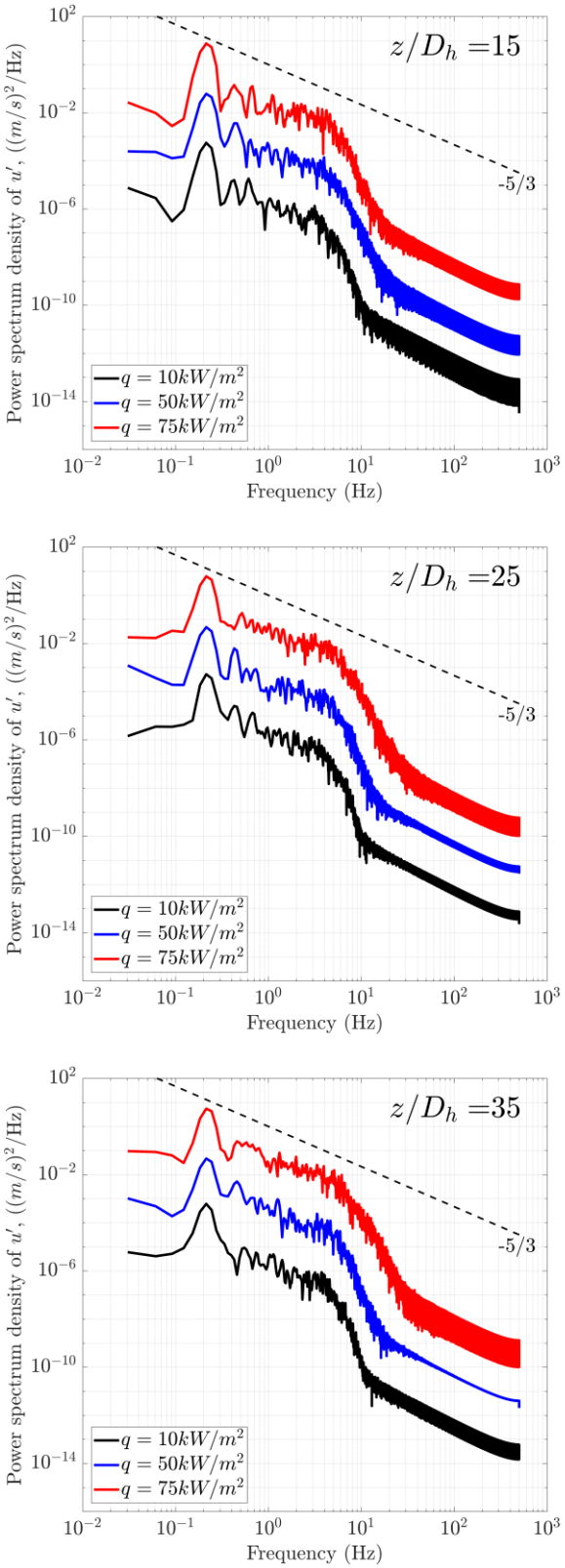

Figure 4.13: Power spectrum density of *u'* at NG at different locations down the heated channel.

4.2.4.2 Wide Gap

Wu & Trupp [120,121] and Duan & He [12] have observed the existence of the large flow structures in the wide gap as well as in the narrow gap, therefore it is useful to inspect the flow structures at this location. The representation of the time history of the normalised fluctuating spanwise velocity down the heated channel for each case can be seen in Figure 4.14. The signals for all heating cases show strong turbulent fluctuations with no obvious regular oscillation. It is probable that the swinging flow structures are weak and the turbulent noises overwhelm their existence in the time wave form. The PSDs of the u' at BG are also evaluated in a similar as those at the narrow gap, where several locations being monitored for each heating case. Some dominant peaks can be seen in the PSD at some axial locations for each heating case as shown in Figure 4.15. The dominant peaks are clearly seen at the length of z/D_h =15, and are reduced down the channel and can hardly be to identified at z/D_h =35. There are two sets of peaks at the beginning of the heating section of z/D_h =15. The first is in the range of 0.2 Hz to 0.25 Hz, and the second set is at around 0.5 Hz. Note that the first set of peaks is very similar to f_p of the flow structures in the narrow gap, but the magnitude of the peaks is lower than those in NG. These results show the existence of large flow structures in the wide gap similar to those in the narrow gap, but weaker in intensity. As these flow structures in both gaps are at the same frequency, they are potentially linked to one another.

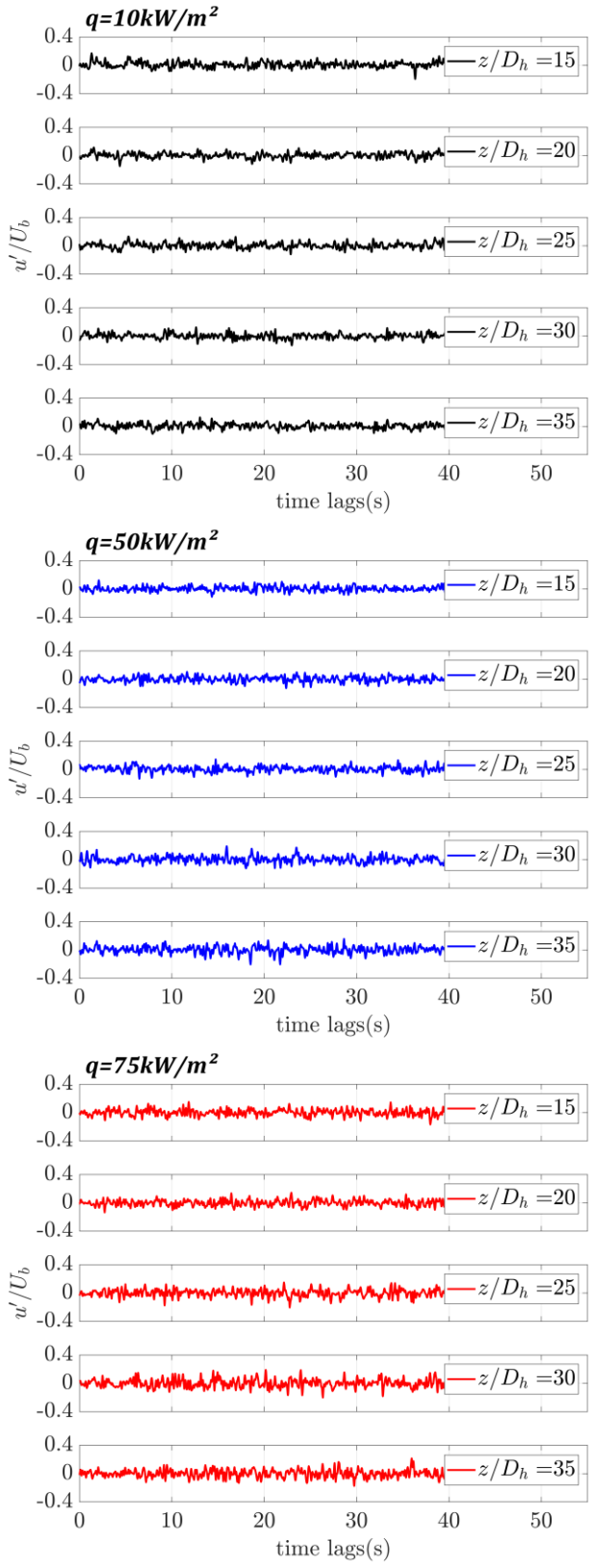

Figure 4.14: Instantaneous spanwise velocity at BG down the heated channel.

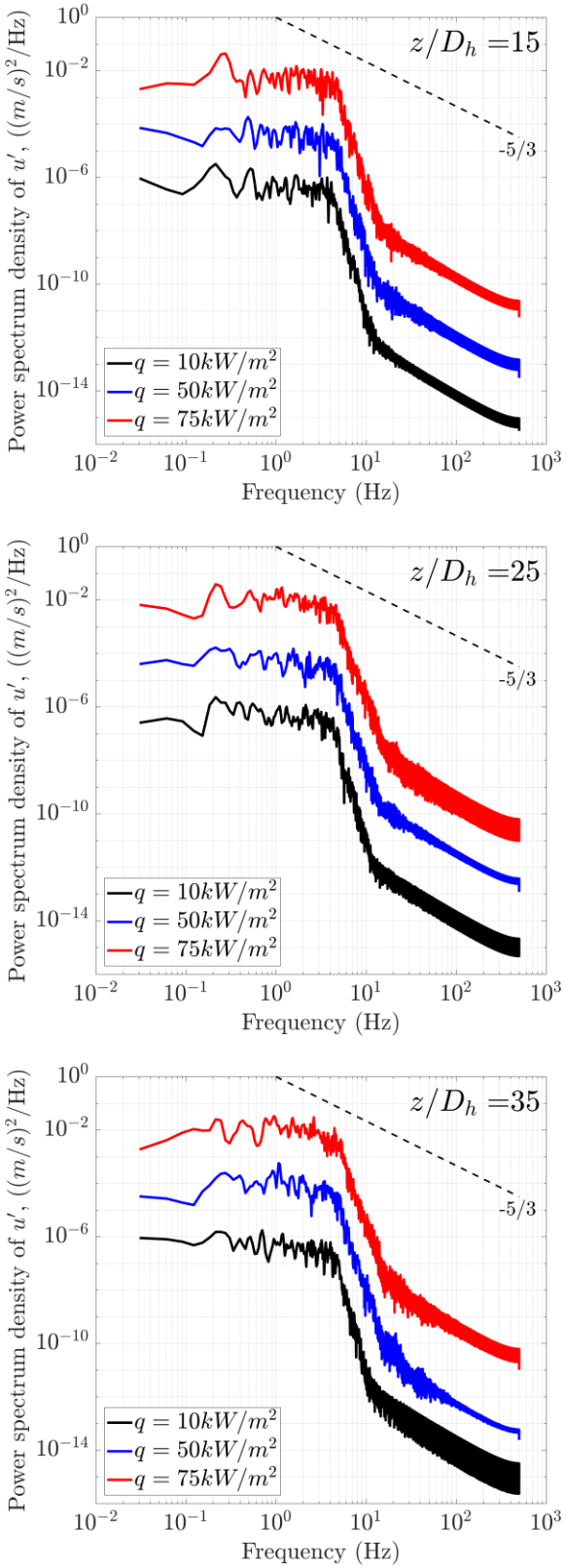

Figure 4.15: Power spectrum density of *u'* at BG at different locations down the heated channel.

4.2.4.3 Relationship between the Flow Structures at Different Locations

To study the relationship between the flow structures passing the narrow and wide gaps, the cross-correlation functions of *u'* between flows at NG and BG can be established. The equation used is as below,

$$R_{uu}(z, \mathrm{z} + \Delta \mathrm{z}) = \langle u'(z) u'(z + \Delta z) \rangle \qquad (4.1)$$

The correlations in Figure 4.16 show that the flows at these two gaps are inversely correlated at 0s lag for all heating cases. For the low heating case, the correlation is very strong upstream but reduces down the heated channel. Meanwhile, for the higher heating cases, the flow structures between the gaps are not as strongly correlated near the heating inlet; then the negative correlation increases before somewhat reducing again. This may be due to the changes in local temperature in the gaps where strong changes of properties occur, consequently leading to changes in the flow structures in these gaps.

It is possible to deduce that a statistically opposite direction of flows passing NG and BG in the spanwise direction. In other words, whenever the flow passing NG to the right in spanwise direction, the flow passing BG will move to the left. These inverse correlations of the flow structures at 0s lag between the gaps are similar to the forced convection case in the study of Duan & He [12]. It is interesting to mention that the study carried out by Duan & He [12] was based on constant properties. However, at high heat fluxes where the wall temperature could exceed the pseudocritical temperature, the correlation of the flow structure between the gaps appears to be reduced. Concurrent with the behaviour of the PSD of u' at BG, it can be said that there are similar structures existed in the wide gap. The flow structures are correlated with those in the narrow gap but are not as strong.

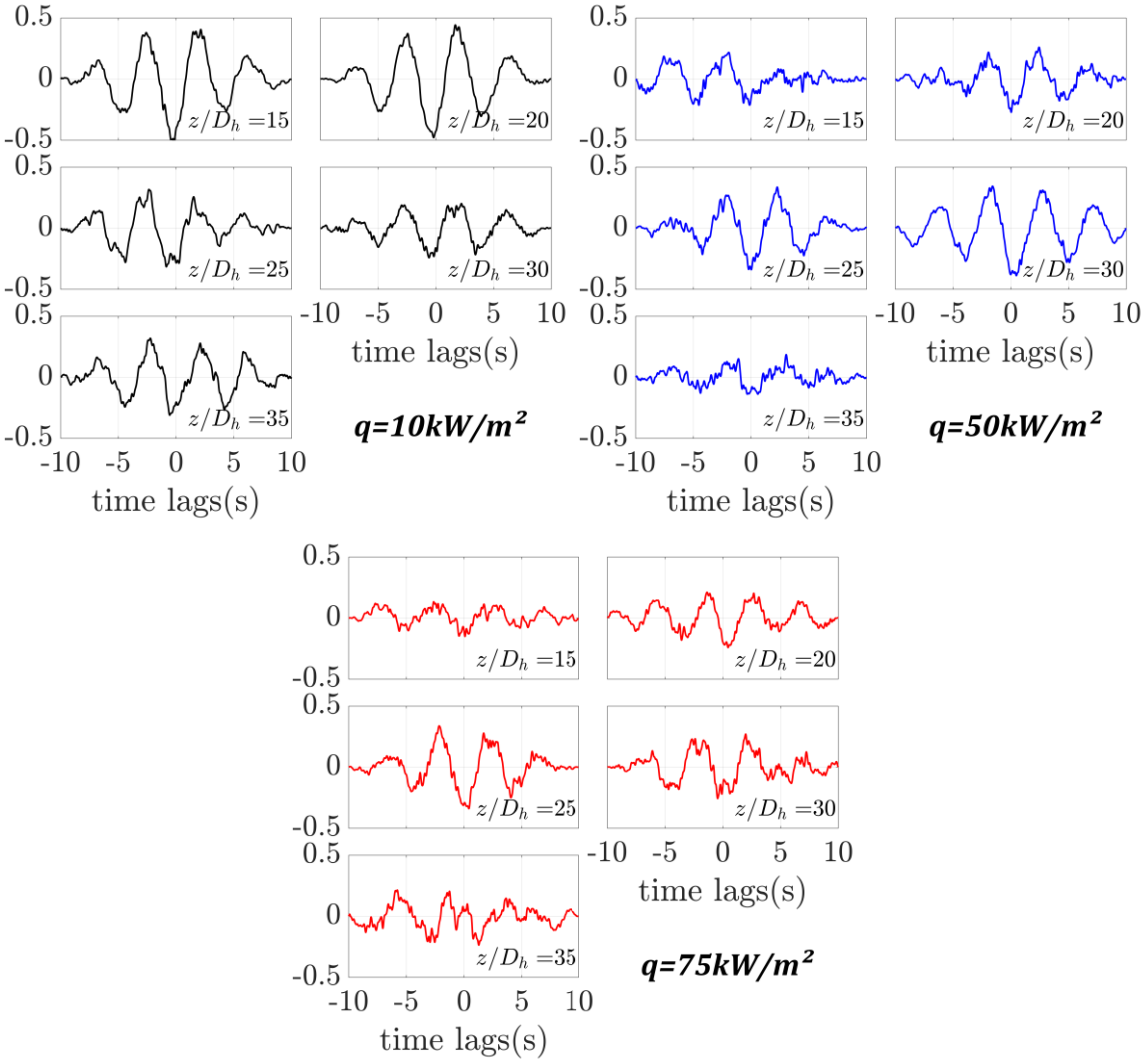

Figure 4.16: The cross correlation function of u' between NG and BG at different locations down the heated channel.

4.2.5 Local Heat Transfer

To observe closer on the behaviour of the heat transfer result by the local structure, the local wall temperature and local Nusselt number are investigated. The local Nusselt number (Nu_{loc}) is calculated as:

$$Nu_{loc} = \frac{h_{loc} D_h}{\lambda} \tag{4.3}$$

where h_{loc} is the average heat transfer coefficient which is determined from:

$$h_{loc} = \frac{q}{T_{w,loc} - T_b} \tag{4.4}$$

where q is the heat flux applied and $T_{w,loc}$ is the local wall temperature.

To see the effect of the flow structure to the heat transfer, the local wall temperature and the local Nusselt number are observed at three axial locations (z/D_h = 15, 25 & 35) as presented in Figure 4.17. From the figure, irregular results may be seen especially for certain cases and at a certain location, this is largely due to the insufficient data for averaged value at each location where longer data are needed for more smooth results.

It can be seen that at a cross-section, the local wall temperature around the rod is quite regular circumferentially for all cases. An overall increase in wall temperature can also be observed for high heating cases down the channel. Meanwhile, the behaviour of the local Nusselt number shows a rather significant change in all heating cases. The Nusselt number can be seen at its highest near the heating inlet which is at z/D_h =15 as in the Figure 4.17 (a), before it reduces down the channel. This is true for all heating cases. The Nusselt number is also observed to be large locally at the region near the main channel and away from the gaps ($60<\theta<120$), but this is not quite significant for the highest heating case of q=75kW/m^2. It

also should be noted that the Nusselt number is higher at the narrow gap than in the wide gap for all heating cases. This may be explained by the existence of the swinging flow structure at the narrow gap region has improved the heat transfer at this location.

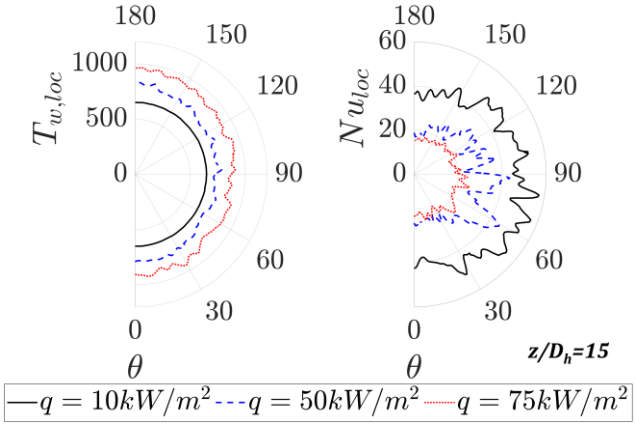

(a)

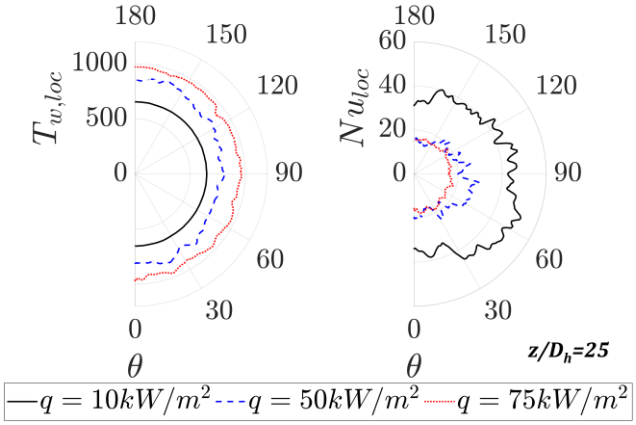

(b)

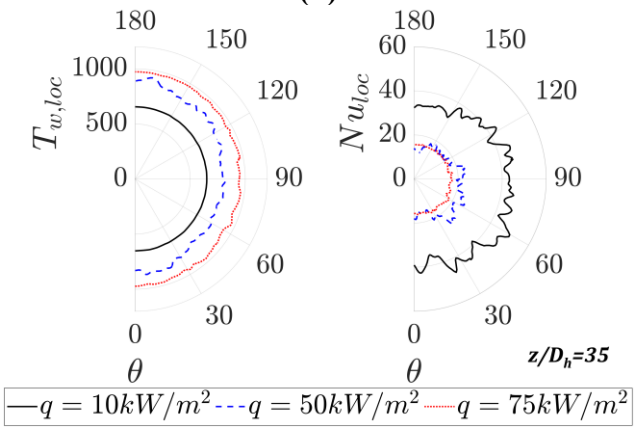

(c)

Figure 4.17: Local temperature and Nusselt number at several axial locations a) z/D_h=15 b) z/D_h=25 c) z/D_h=35.

4.2.6 The Size of Coherent Structures

4.2.6.1 Two-Point Correlations

As shown earlier, the fluctuating velocity *u'* is a convenient parameter in describing the behaviour of the large flow structures. Even though the dominant frequencies of the flow structures at the gap as discussed above are the same in all cases, with the effect of thermal expansion (i.e., due to the property variation of the supercritical water), it is observed that the flow is accelerated in all cases. Therefore, the wavelength of the flow structures must be increased in this case. To investigate this behaviour, the flow structures can be statistically quantified using two-point correlations [138]. The streamwise scale of the large flow structures is analysed using cross-correlation between u' at the point near the entrance of the heating section (z/D_h =11.25) and several positions down the heated channel in the narrow gap and the wide gap. As shown in Figure 4.18 (a), in all cases, the large flow structures passing through the narrow gap are somewhat similar to each other. In higher heating cases, some elongation of the structure is seen where the size starts to increase at z>0.6 m. The relationship between the heat flux and the wavelength is demonstrated to be positive. Hence, accelerated flow in that region is likely to be a result of thermal expansion

Unlike the behaviour of flow structures in the narrow gap, the regular waves of the flow structures in the wide gap as in Figure 4.18 (b) are hardly be seen in most cases. Nevertheless, a pseudo-oscillation behaviour of the peaks could be seen at ($z/D_h < 25$) for the low heating case before it gets elongated further down the channel. The peaks are weak in the high heating cases, but there are some additional peaks around $z/D_h = 14$ and 19. These additional peaks are in between the main peaks, which are similar to the peaks of the narrow gap. These two sets of peaks may be related to the two sets of peaks exhibited in the PSD in Figure 4.15.

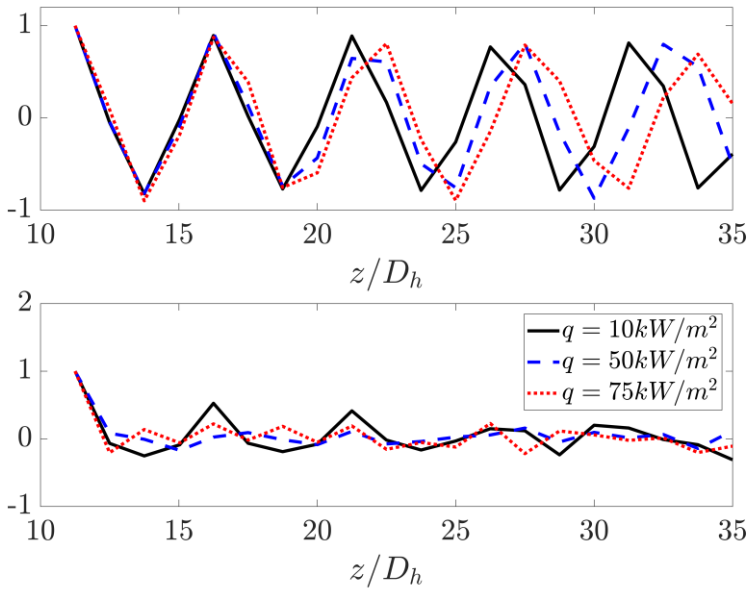

Figure 4.18: The cross correlation of u' at different locations down the channel in a) NG and b) BG.

4.2.6.2 Convection Speed of the Coherent Structure

Figure 4.19 and Figure 4.20 present correlation coefficients of Ruu as suggested by Guellouz & Tavoularis [124], between two points at several axial locations for NG and BG in the test section. To perform the calculation of the correlation coefficient of the flow in gaps, instantaneous velocities are recorded at a point downstream from the heated inlet (z =25Dh) as well as additional points further downstream ($\Delta z/D_h$ =0.2, 0.4, 0.6). Guellouz & Tavoularis [124] estimated the average convection speed, U_c of the structures using these space-time correlations. The convection speed, U_c is the ratio of the streamwise probe separation Δz over the time delay for maximum correlation Δt_{max}. Table 4.1 shows the calculated convection speed for each case in both gaps. The convection speed changes as the heat flux is varied. At the narrow gap, the convection speed is inversely proportional to the increase of the heat flux, while the opposite is true at the wide gap. At the wide gap, the convection speed increases gently as the heat flux is increased.

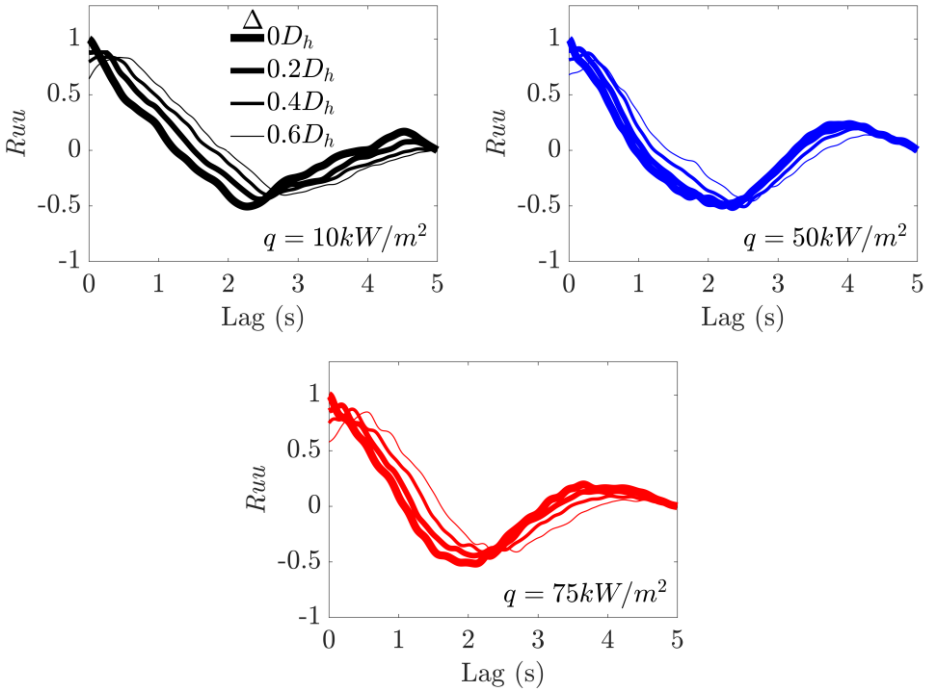

Figure 4.19: The correlation coefficient of *u'* between a point at z=25D_h and several points away down the channel at NG.

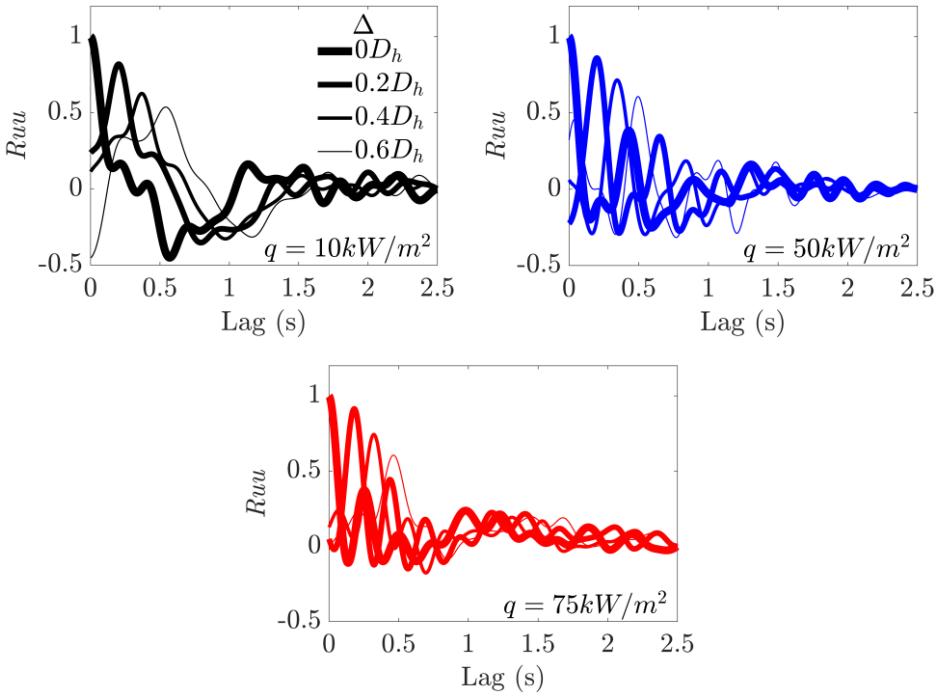

Figure 4.20: The correlation coefficient of *u'* between a point at z=25D_h and several points away down the channel at BG.

Table 4.1: Convection speed for each heating case for both at NG and BG.

Heat flux, q (kW/m^2)	Convection Speed, U_c (m/s)	
	NG	BG
10	0.0561	0.0333
50	0.0486	0.0353
75	0.0360	0.0382

4.2.7 Mixing Factor

The existence of large flow structures in the narrow gap enhances the turbulence mixing between the main channels (in a rod bundle case the mixing at the gaps between subchannels). As discussed in the earlier chapter, Rehme [113] and Wu & Trupp [121] noted that the turbulence parameter can be evaluated using the mixing factor, Y and effective velocity, u_{eff}. More details on these parameters can be seen in §2. Rehme [113] used the following equation to evaluate the mixing factor due to the large flow structures.

The friction factor, f^* to determine the eddy viscosity, $\overline{\varepsilon}$ of Y function is estimated from the turbulent isothermal flow in a smooth pipe at similar Reynolds number, which is given by

$$f^* = 0.18\, Re^{-0.2} \tag{4.2}$$

The results for u_{eff} down the heated channel are normalised with local U_b and presented for both the narrow gap and wide gap in Figure 4.21. At both gaps, the trends of u_{eff}/U_b are clearly different for each case. For the low heating case of 10 kW/m^2, the u_{eff}/U_b is largely unchanged along the heated domain while it reduces for the higher heating cases, u_{eff}/U_b reduces along the heated channel. Hence, the mixing between the subchannels when the

temperature follows $T_b < T_{pc} < T_w$ condition reduces with distance from the start of heating.

In most cases, it is also observed that the variations of u_{eff}/U_b are not monotonic and there is a minimum point (drop in value) before the end of the inspected length. The location of the minimum point moves downstream with the increase of heat flux. These turning points of the trend are at z/D_h =20, 25 & 30 for heat flux 10kW/m^2, 50kW/m^2 and75 kW/m^2 respectively. This can be explained as that a longer distance is needed for the development of mixing in high heating cases. Therefore, it is probably good practice to consider a longer domain to further investigate this phenomenon, especially at higher heating.

An opposite behaviour can be seen in the wide gap. For the higher heating cases, u_{eff}/U_b increases down the heated channel, whilst u_{eff}/U_b gently decreases in the low heat flux case. Generally, the value of u_{eff}/U_b is much lower compared to that in the narrow gap. This is due to the weaker unsteady flow structures at the wide gap as observed earlier. The value of u_{eff}/U_b obtained here can be compared with that of Duan & He [12], which is 0.135 and the value is quite close to the one obtained at z/D_h =35.

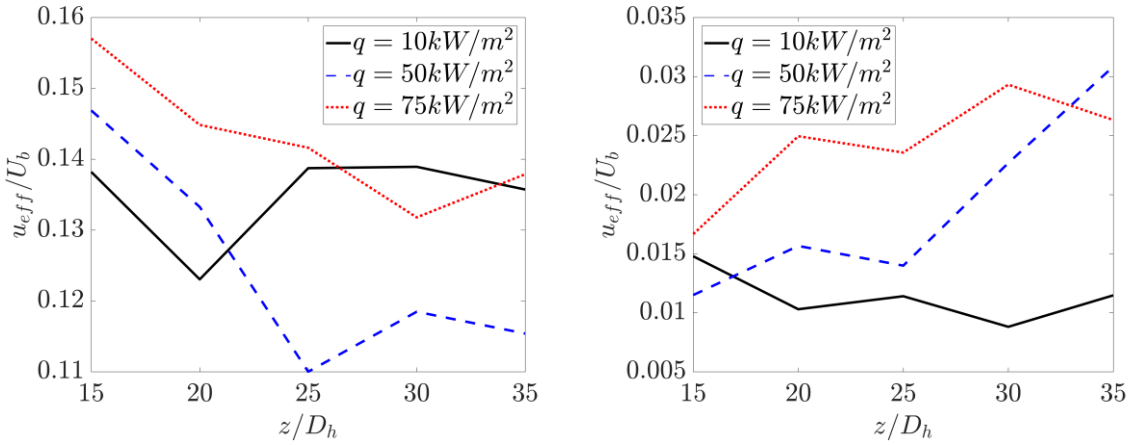

(a) **(b)**

Figure 4.21: u_{eff}/U_b down the heated channel at a) NG and b) BG.

In the study by Rehme [113], u_{eff} also calculated away from the centre of the gap, in this case NG. The semi-empirical correlation to estimate u_{eff} at the location away from the centre of the gap, Equation (2.6) of [113] is used to compare the one obtained by LES. Results can be seen as in Table 4.2 for u_{eff} at x/δ_{ij}=0.18 at the narrow gap. The u_{eff} from the correlation by Rehme does not correlate well with the u_{eff} obtained using LES. The ratio between the results of the correlation and those of LES is around 0.46, which is far lower than the results obtained in Duan & He [12]. This suggests that the effect of the variable properties considered in the present study have a strong influence on the mixing velocity and it is impractical to measure mixing by using Rehme's correlation.

Table 4.2: u_{eff} comparison with Rehme correlation.

Heat flux, q (kW/m^2)	u_{eff} *at* x/δ_{ij}*=0.18*	
	LES	Eq. (2.6)
10	0.00531	0.00245
50	0.00473	0.00218
75	0.00516	0.00238

Figure 4.22 shows the mixing coefficients, *Y*, calculated at NG. The trend of the results obtained for Y is similar to the trend of u_{eff} down the heated channel. Again, results obtained here can be compared with the result of forced convection case in Duan & He [12]. For the heat fluxes 10kW/m^2 and 75kW/m^2, values obtained at z/D_h =35 are around 15 to 20% higher compared to the value of 113.50 in Duan & He [12], while the value obtained for the heat flux of 50kW/m^2 is almost the same with that of Duan & He [12]. Moreover, the differences between the two high heating cases, 50kW/m^2 and 75kW/m^2 for both u_{eff}/U_b and Y and that of Duan & He [12] could be due to the differences in the local temperature at the

gap region. The temperature in this region is exceeding the pseudocritical temperature for some distances in the heated domain. However, as mentioned earlier, it is difficult to determine the trend of the mixing after the recovery due to the limited heated domain length in this present study especially for the 75 kW/m^2. This mixing has shown a complex behaviour in the high heating cases where the temperature is following $T_b < T_{pc} < T_w$ order.

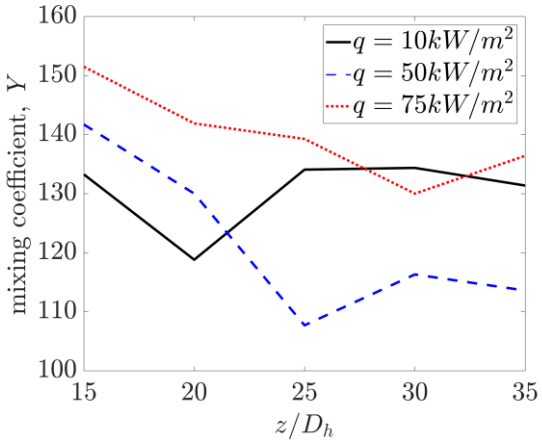

Figure 4.22: Mixing coefficient, *Y* down the heated channel at NG.

4.2.8 Turbulent Quantities

In this section, the statistics of the flow field at several channel locations, for each case will be discussed. The effect of the thermal expansion to the flow distribution in the trapezoid annulus channel is demonstrated herein. Only half of the channel is shown due to the symmetric nature of the channel configuration. The statistics presented here are Favre-averaged due to the severe property variation at supercritical in this study. All Favre-averaged variables is denoted as $\tilde{\phi}$ and they are calculated as follows:

$$\tilde{\phi} = \frac{\langle \rho \phi \rangle}{\langle \rho \rangle} \tag{4. 5}$$

the fluctuations component can be calculated as

$$\phi'' = \phi - \tilde{\phi} \tag{4. 6}$$

4.2.8.1 Statistics Flow Field

Figure 4.23 shows the general mean velocity distribution for all cases. In the lowest heating case, the redistribution of the velocity down the channel is very little, whereas in cases with higher heating, the redistribution of the velocity field is apparent. High-velocity patches can be observed distributed down the heated channel in the wide gap area as well as near to the heating rod seeing Figure 4.23 (b) & (c) at z/D_h =25&35. The differences between the high heating cases and lowest heating case are because in the high heating cases the condition of $T_b < T_{pc} < T_w$ is maintained hence the density changes rapidly downstream. The changes in the properties in the low heating case are much smaller. The velocity is also particularly high in the narrow gap for both high heating cases (50kW/m^2 & 75kW/m^2), especially at z/D_h =25 and z/D_h =35 locations.

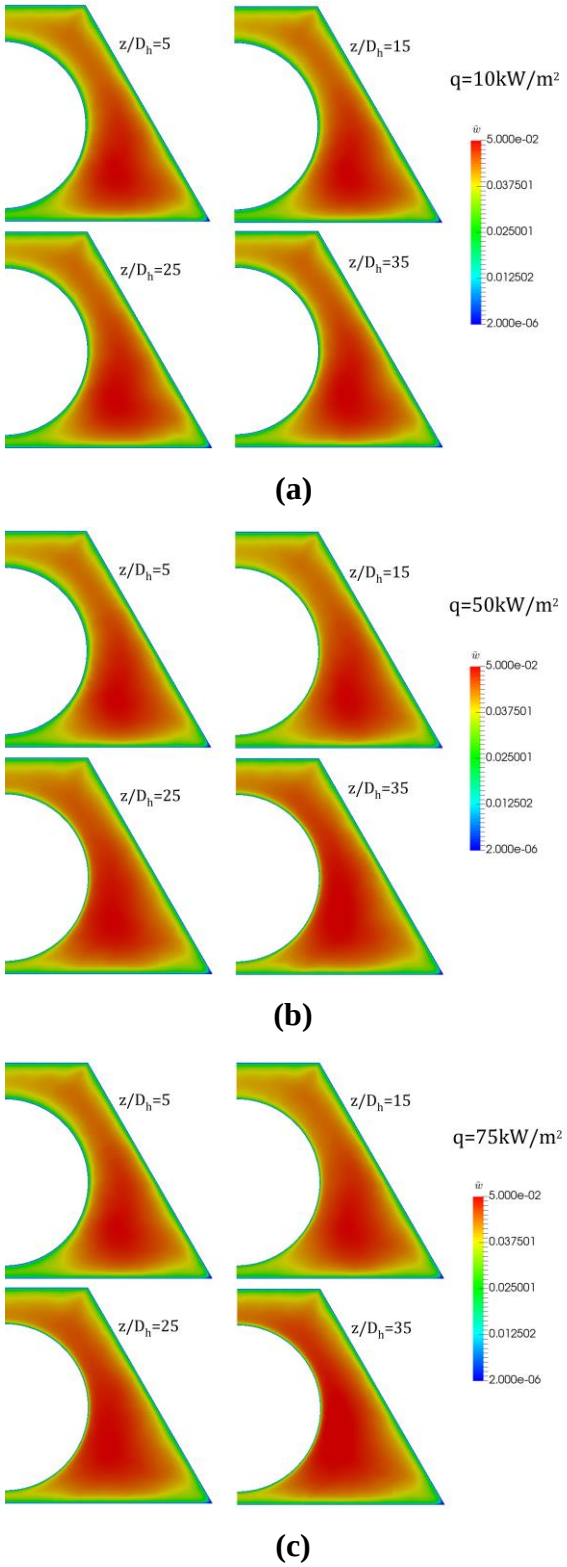

Figure 4.23: Favre-averaged streamwise velocities, $\tilde{W}$ at several locations down the channel. a) q=10kW/m^2 b) q=50kW/m^2 c) q=75kW/m^2

To observe the mean velocity distributions more closely at some regions of the channel, profiles are shown in Figure 4.24. As introduced in §4.2.1, mean velocity profiles are taken at the narrow gap ('NL'), the wide gap ('BL'), at the main channel ('ML') and along the equidistant line across the narrow gap to main channel ('MC'). In each aforementioned region, results are presented at four different axial locations. The velocity in the narrow gap in the low heating case (q=10kW/m^2) can be seen to be similar to a laminar flow profile and this is true for every location. This parabolic profile at the narrow gap is similar to the one obtained by Duan & He [13] The higher heating cases show a significant increase in velocity with an increase in the distance down the flow passage. The peaks of the profiles for both high heating cases are shown to be shifted toward the heating rod down the channel.

In the wide gap, the profiles as illustrated in Figure 4.24 (b) are representative of a typical turbulent profile. In the low heating case, the profile does not change much down the heated channel compared to the high heating cases. In the high heating cases, similar to the one in the narrow gap, velocity increases and peaking near the heating rod. The higher heat flux, the higher the value of the peak profile is noted. This can be seen in both high heating cases at the location (z/Dh =25 & 35). The increase in profile peaks can be attributed to the effect of the thermal expansion. Hence large flow acceleration caused by heating observed in the larger gap in this case.

Similar to the one in the wide gap, a typical turbulent profile is observed at ML in the Figure 4.24 (c). Again, a higher velocity is detected near the heating rod for high heating cases, while the velocity profile in the low heating case is maintained down the flow passage. Meanwhile, for both high heating cases, the velocities are slightly lower than the low heating case. This shows that the flow acceleration happens mainly near the heating wall. Both results

in BL and ML are also similar to that obtained in constant temperature study by Duan & He [13].

Figure 4.24 (d) shows the distribution of the velocity at an equidistant line ('MC') between the bottom wall of the channel and the heating wall. This profile can be used to examine the flow behaviour across the gap (i.e., from the centre of the narrow gap to the main channel). Corresponding to the peak velocity along NL down the heated channel (z/D_h =15, 25&35), the flow at the narrow gap is increased as the heat flux is increased. While similar to the earlier results at ML, in the main channel the velocity is slightly decreased as the heat flux increases. This shows that the difference between the velocities narrow gap and the main channel reduced at higher heat flux. In the lowest heating case, where the temperature difference is small and the variations of the properties are rather mild, the trend is somewhat close to that of Duan & He [13]. In the strong heating cases, the velocity difference across the channel reduces.

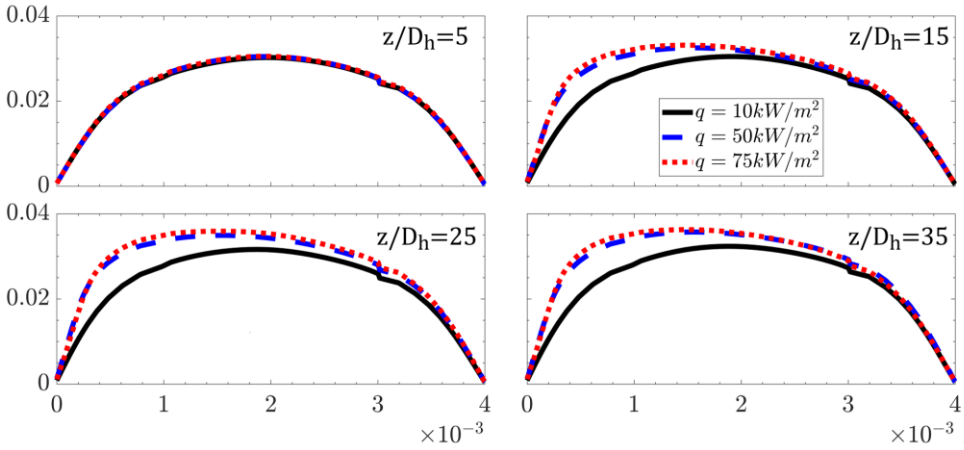

(a)

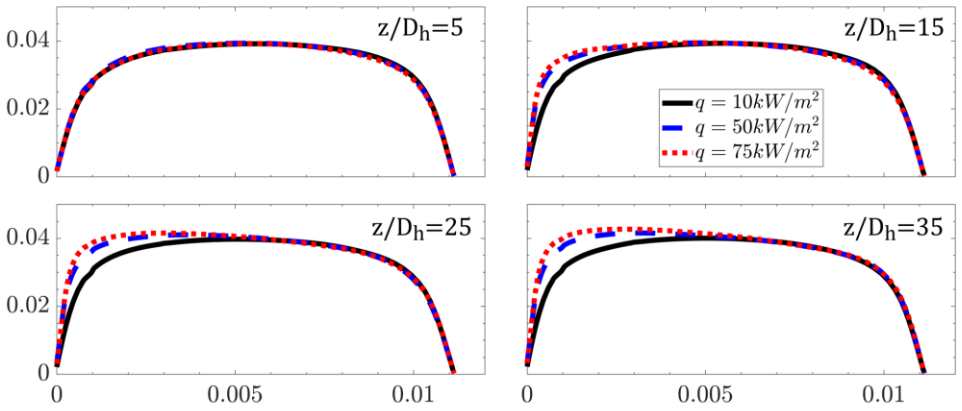

(b)

Figure 4.24: Favre-averaged streamwise velocities, $\tilde{W}$ profiles at several locations down the channel. a) NL b) BL c) ML d) MC

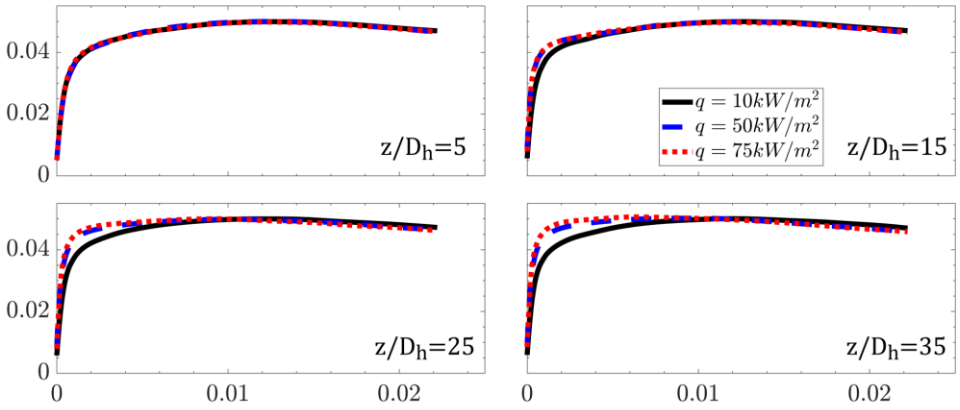
0.04
0.02
0
z/Dh=5
z/Dh=15
$q = 10kW/m^2$
$q = 50kW/m^2$
$q = 75kW/m^2$
z/Dh=25
z/Dh=35
0
0.01
0.02

(c)

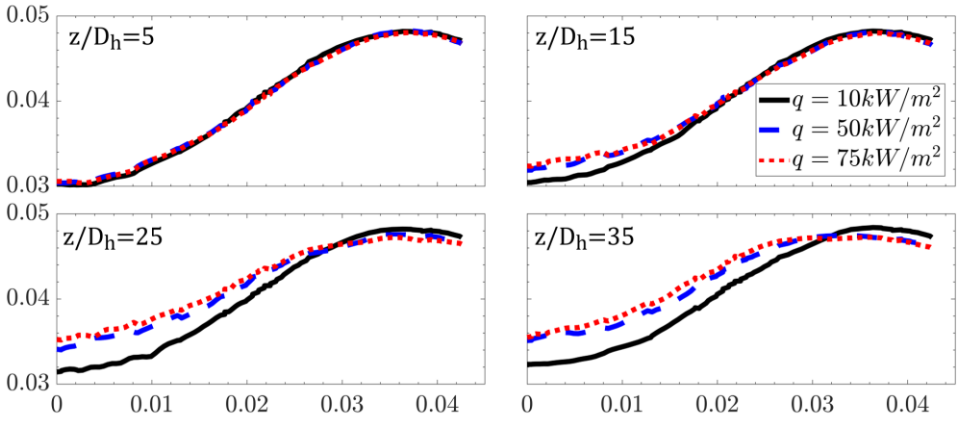
0.05
0.04
0.03
z/Dh=5
z/Dh=15
$q = 10kW/m^2$
$q = 50kW/m^2$
$q = 75kW/m^2$
z/Dh=25
z/Dh=35
0
0.01
0.02
0.03
0.04

(d)

4.2.8.3 General Distributions of Turbulent Parameters

Figure 4.25 shows the general distribution of the turbulent kinetic energy $0.5 * \langle \rho u_i^{"} u_i^{"} \rangle$, $i = 1,2,3$ in the cross sections at several locations of the flow passage. Note that $u_1^{"}$ here stands for $u^{"}$, $u_2^{"}$ for $v^{"}$, and $u_3^{"}$ for $w^{"}$. Due to the existence of the swinging flow structure in the narrow gap, a high value of $0.5 * \langle \rho u_i^{"} u_i^{"} \rangle$ can be seen for all cases. The difference between the low heating case and the higher heating cases can be seen by studying the high intensity of patches down the channel in the narrow gap. In the low heating case the value of $0.5 * \langle \rho u_i^{"} u_i^{"} \rangle$ does not change much down the channel, while in the high heating cases, the turbulence decreases down the heating channel. The higher the heat fluxes, the faster the turbulence quantity reduces, as can be observed in Figure 4.25 (b) & (c). Looking at the region near the heating rod, the value $0.5 * \langle \rho u_i^{"} u_i^{"} \rangle$ reduces at higher heat flux. The decrease of intensity of the flow swinging structure could be the reason for the low $0.5 * \langle \rho u_i^{"} u_i^{"} \rangle$.

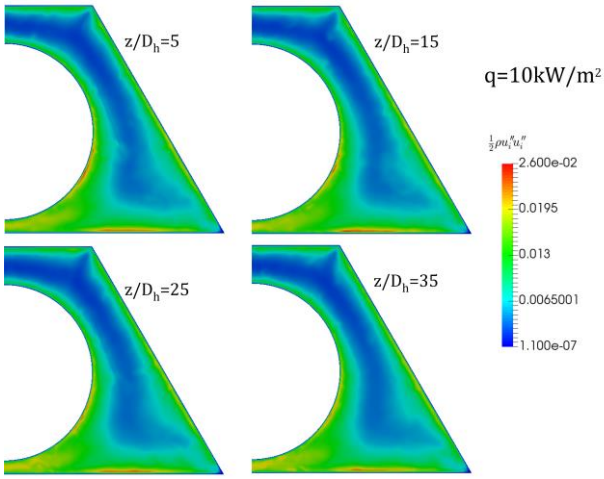

(a)

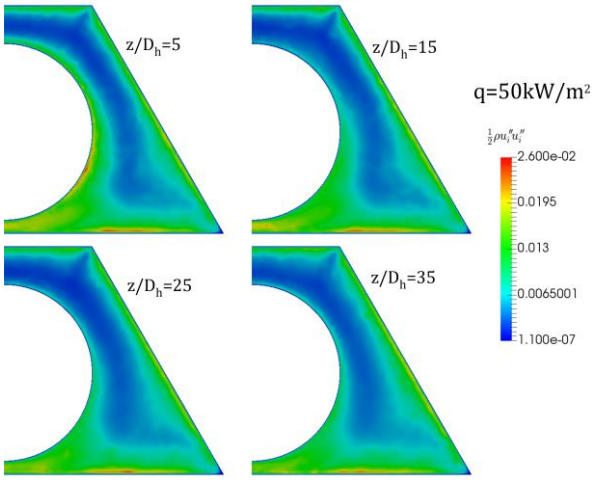

(b)

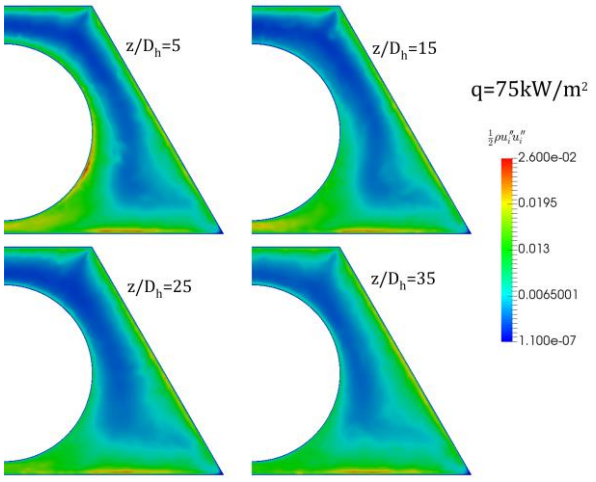

(c)

Figure 4.25: $0.5\langle\rho u_i'' u_i''\rangle$ at several locations down the channel. a) q=10kW/m² b) q=50kW/m² c) q=75kW/m²

The distribution of the streamwise component $\langle \rho w^{"} w^{"} \rangle$ in the cross-section at several locations down the channel is illustrated in Figure 4.26. In isothermal region (z/D_h =5), all three cases show similarities in the distribution of $\langle \rho w^{"} w^{"} \rangle$. For the low heating case, $\langle \rho w^{"} w^{"} \rangle$ is maintained down the heating channel and no significant changes are observed. As the heat flux increases, the low patch in the narrow gap becomes more apparent down the heated channel and transverses closer to the heated wall. This can be seen in Figure 4.26 (b) & (c). This behaviour in the narrow gap in high heating cases is similar to the distributions of the $0.5 * \langle \rho u_i^{"} u_i^{"} \rangle$. Furthermore, the intensities of $\langle \rho w^{"} w^{"} \rangle$ in the vicinity of the heated wall are also reduced down the heated channel. As mentioned earlier, this is largely true for the high heating cases while not much change is observed in the low heating case. A possible cause of this behaviour is the high flow temperature near the heated wall caused a reduction on shear stress at this region. Near the adiabatic wall $\langle \rho w^{"} w^{"} \rangle$ is maintained down the channel for all three cases.

Figure 4.27 shows the distributions of the $\langle \rho u^{"} u^{"} \rangle$ component in the trapezoid annulus. High value patches can be seen in the narrow gap in every location for all heating cases. Similar to the trend of turbulent kinetic energy shown earlier, $\langle \rho u^{"} u^{"} \rangle$ maintains down the heated channel in low heating case when the condition $T_b < T_w < T_{pc}$ is maintained. While in the high heating cases, where the $T_b < T_{pc} < T_w$ is maintained, the intensity in the gap reduces down the heated channel. The reduction of the flow structures down the heated channel is probably the main reason for this behaviour.

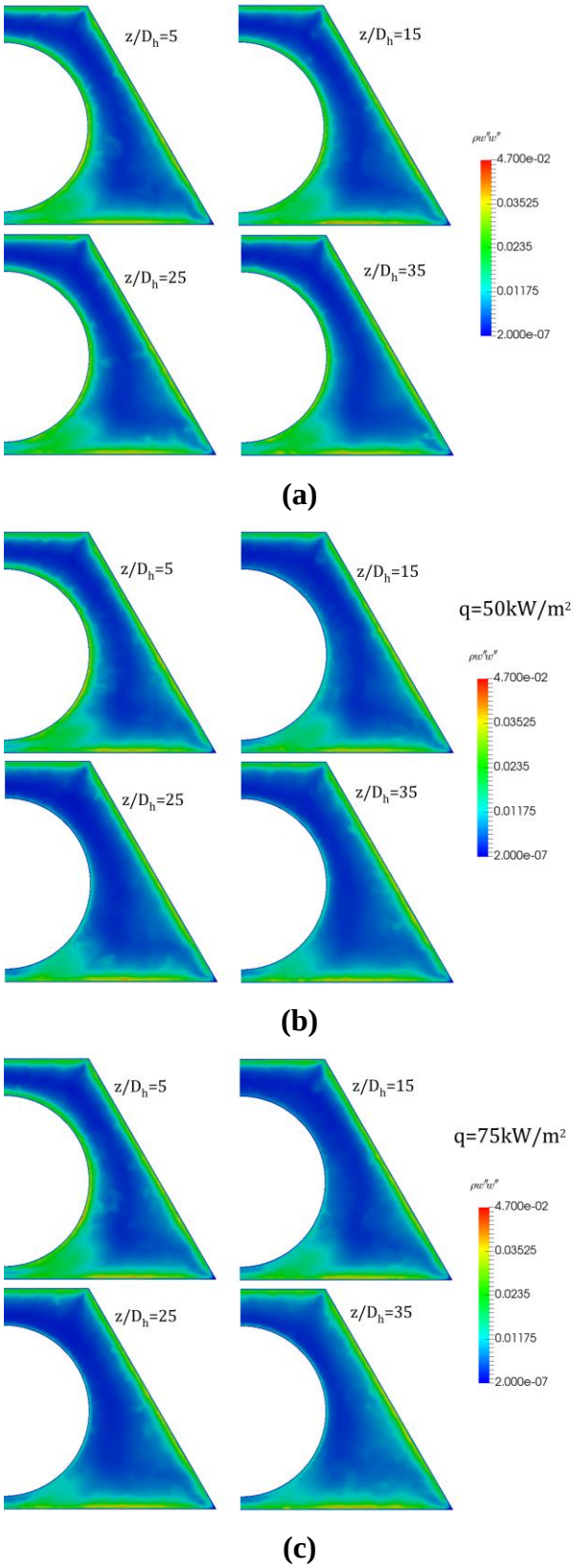

Figure 4.26: $\langle \rho w'' w'' \rangle$ at several locations down the channel. a) q=10kW/m^2 b) q=50kW/m^2 c) q=75kW/m^2

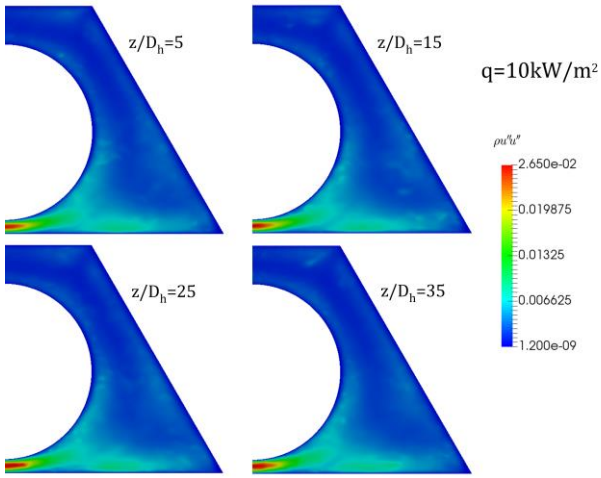

(a)

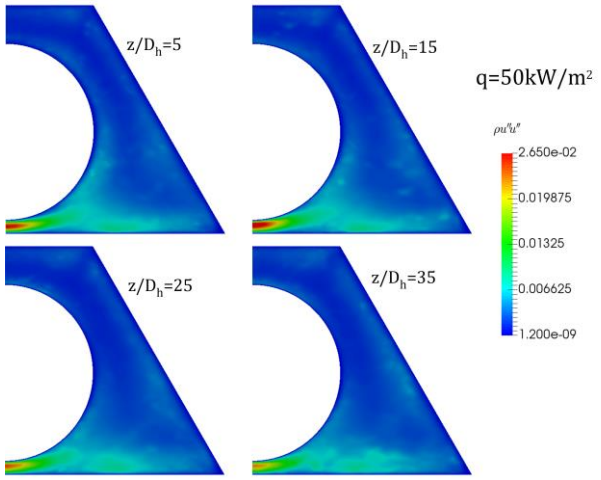

(b)

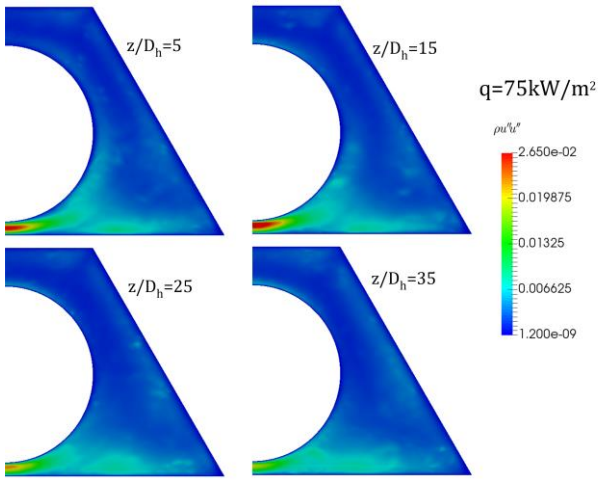

(c)

Figure 4.27: $\langle \rho u'' u'' \rangle$ at several locations down the channel. a) q=10kW/m² b) q=50kW/m² c) q=75kW/m²

Results comparison with Duan & He [13]

Some similarities in the distribution of turbulent quantities can be observed in the present study when it is compared to the study of Duan & He [13]. The lowest heating case, in particular, shows a lot of similarities on the distributions with those observed in the forced convection case from the previous study. High turbulence kinetic energy region is located in the vicinity of the narrow gap in previous study, which is similar as in $0.5 * \langle \rho u_i^{"} u_i^{"} \rangle$ in q=10kW/m^2 case. The axial component of the turbulent intensity is high in value near the wall and in the region close to the narrow gap, but a low value was found in the narrow gap. This agrees with the result of $\langle \rho w^{"} w^{"} \rangle$ in the present study. Even though no heating is applied on the outer wall, similar high value can be seen in the present study and the previous study. This due to the shear stress in this region may not be affected by the existence of the large flow structure. Meanwhile the spanwise component of the turbulent intensity is high in the narrow gap and this again agrees with the result of $\langle \rho u^{"} u^{"} \rangle$. These results show that the low heating case behaves in a way similar to that of the forced convection of previous study [13]. That is, the variation of the temperature, and consequently the variations in thermal properties are small and have little influence on the flow behaviours.

4.2.8.4 The Turbulent Quantities Profiles along 'NL', 'BL', 'ML' and 'MC'

Profiles for the turbulent quantities of $0.5 * \langle \rho u_i^{"} u_i^{"} \rangle$, $\langle \rho w^{"} w^{"} \rangle$ and $\langle \rho u^{"} u^{"} \rangle$ along the NL, BL, ML and MC lines are shown in Figure 4.28 - Figure 4.31. Along NL (narrow gap), the value of $0.5 * \langle \rho u_i^{"} u_i^{"} \rangle$ in Figure 4.28 is high even though the velocity profile at this location implies a laminar-like flow. This is seen as an evidence of the swinging flow structure contributing to the total turbulent kinetic energy. More specifically, the peaks of the $\langle \rho w^{"} w^{"} \rangle$

component are located near the walls, resembles a distribution profile of a typical wall shear flow, even though the profile is distorted by heating in the downstream stations. In contrast, the profile of $\langle \rho u^{"} u^{"} \rangle$ peaks in the centre of the gap and could be to swinging flow structure in this region.

The difference between the low heating case and the high heating cases can be seen clearly. In the low heating case of q=10kW/m^2, the shape does not change much down the channel and maintains similar to its isothermal part. In the high heating cases of heat flux 50kW/m^2 and 75kW/m^2, values of $0.5 * \langle \rho u_i^{"} u_i^{"} \rangle$ and $\langle \rho u^{"} u^{"} \rangle$ increase slightly at the beginning of heating ($z/D_h = 15$) before starting to decrease at higher axial level of $z/D_h =$ 25 & 35. The values of $0.5 * \langle \rho u_i^{"} u_i^{"} \rangle$ and $\langle \rho u^{"} u^{"} \rangle$ decrease as the heat flux increases with the peak of the $\langle \rho u^{"} u^{"} \rangle$ being closer to the heating wall. These changes indicate that the swinging flow structure is weakened, which is consistent with the results presented earlier. On the other hand, the value of $\langle \rho w^{"} w^{"} \rangle$ behaves slightly different for the high heating cases with the peaks near the heating wall decreasing much earlier as can be seen at $z/D_h = 15$. However, the peaks near the adiabatic outer wall increase slightly at $z/D_h = 15$ & 25, before decreasing at $z/D_h = 35$. This is again consistent with the observations presented earlier where turbulence reduces in the narrow gap.

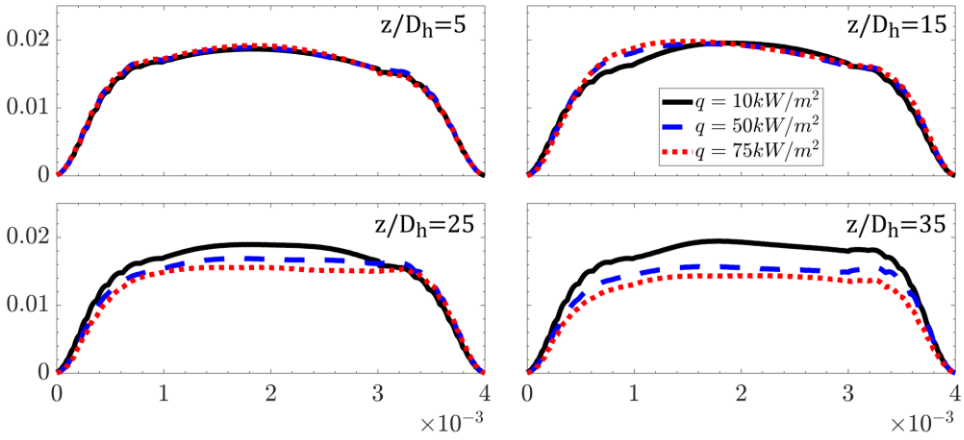

(a)

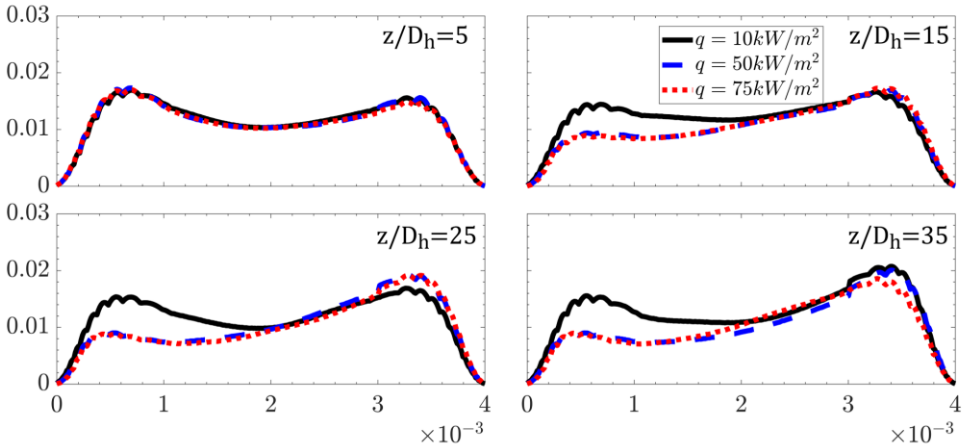

(b)

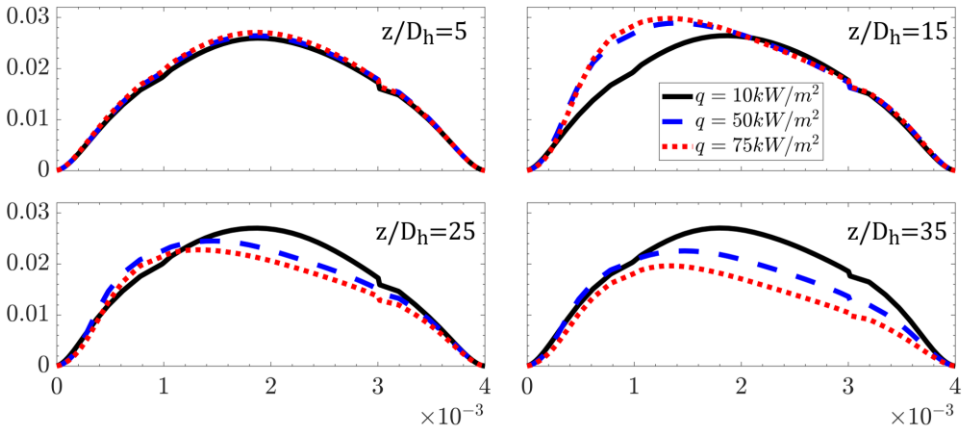

(c)

Figure 4.28: Profiles along NL at several locations down the channel. a) $0.5\langle\rho u_i'' u_i''\rangle$ b) $\langle\rho w'' w''\rangle$ c) $\langle\rho u'' u''\rangle$

In the wide gap BL (Figure 4.29) trends for all turbulent quantities ($0.5 * \langle \rho u_i^{"} u_i^{"} \rangle$, $\langle \rho w^{"} w^{"} \rangle$ & $\langle \rho u^{"} u^{"} \rangle$) are very much the same with the peaks being near the wall. For the low heating case, the distributions of all turbulent quantities ($0.5 * \langle \rho u_i^{"} u_i^{"} \rangle$, $\langle \rho w^{"} w^{"} \rangle$ & $\langle \rho u^{"} u^{"} \rangle$) do not change significantly down the heated channel. The trends for profiles of $0.5 * \langle \rho u_i^{"} u_i^{"} \rangle$ and $\langle \rho w^{"} w^{"} \rangle$ in the wide gap for the high heating cases are somewhat similar to the trend profile of $\langle \rho w^{"} w^{"} \rangle$ in the narrow gap, where peaks decrease near the heating wall and increase near the adiabatic outer wall. It is worth noting that the peaks between the heat flux cases of 50kW/m^2 and 75kW/m^2 are somewhat similar with the latter having a slightly higher peak than the other case. This suggests that the flow is undergoing a laminarisation process when the heat flux is sufficient high. Moreover, across the heating channel, the increase in value $0.5 * \langle \rho u_i^{"} u_i^{"} \rangle$ and $\langle \rho w^{"} w^{"} \rangle$ exceeds the low heating case from the middle of the gap to the adiabatic outer wall.

In contrast, $\langle \rho u^{"} u^{"} \rangle$ increases strongly near the heating wall with higher peak for the higher heat flux case. The increase starts from the beginning of heating (at $z/D_h = 15$). This suggests that there is a strong cross-flow structure generated across the wider gap, which results in a wall shear layer on the walls. Nevertheless, the strength is still rather weak than that in the narrow gap by an order 5.

It can be seen from Figure 4.30 that in the main channel (ML), the distribution of all turbulence quantities largely shows the typical characteristics of a wall shear flow. The effects of the heating on turbulence tend to be similar to that in the wide gap for all cases except that of the $\langle \rho u^{"} u^{"} \rangle$ component. All turbulent quantities down the heating channel show a decrease in the peaks as the heat flux increases. Figure 4.30 (b) & (c) show that the value of ($0.5 * \langle \rho u_i^{"} u_i^{"} \rangle$) is dominantly affected by the $\langle \rho w^{"} w^{"} \rangle$ component.

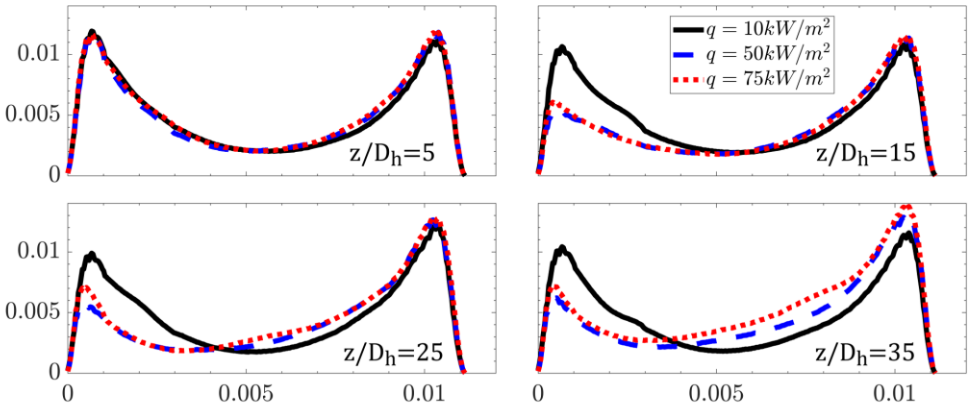

(a)

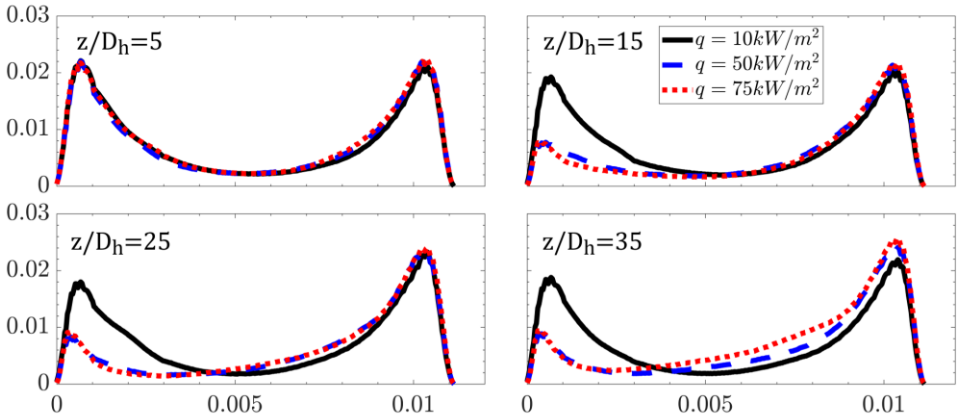

(b)

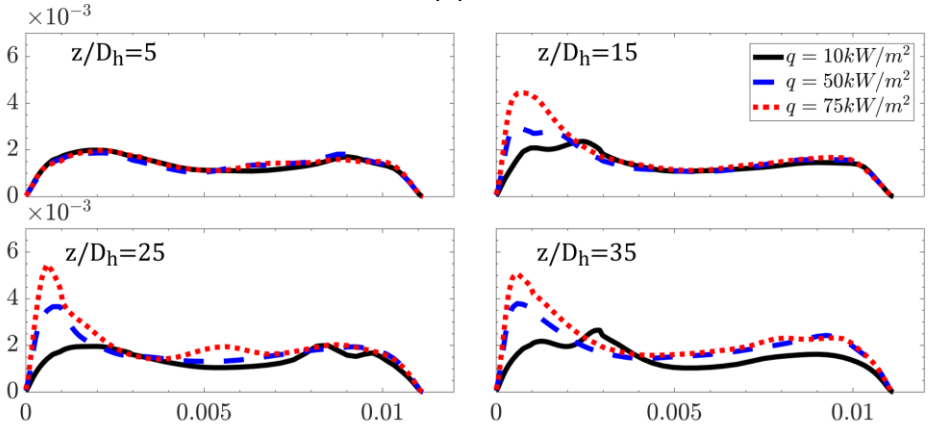

(c)

Figure 4.29: Profiles along BL at several locations down the channel. a) $0.5\langle\rho u_i'' u_i''\rangle$ b) $\langle\rho w'' w''\rangle$ c) $\langle\rho u'' u''\rangle$

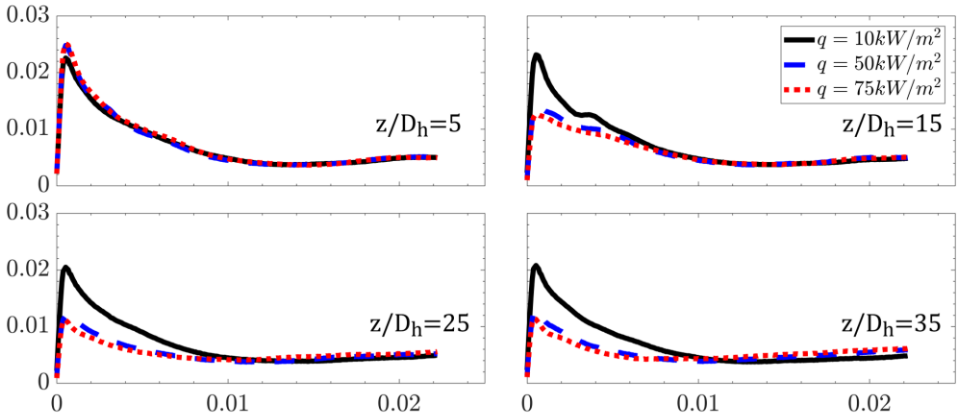

(a)

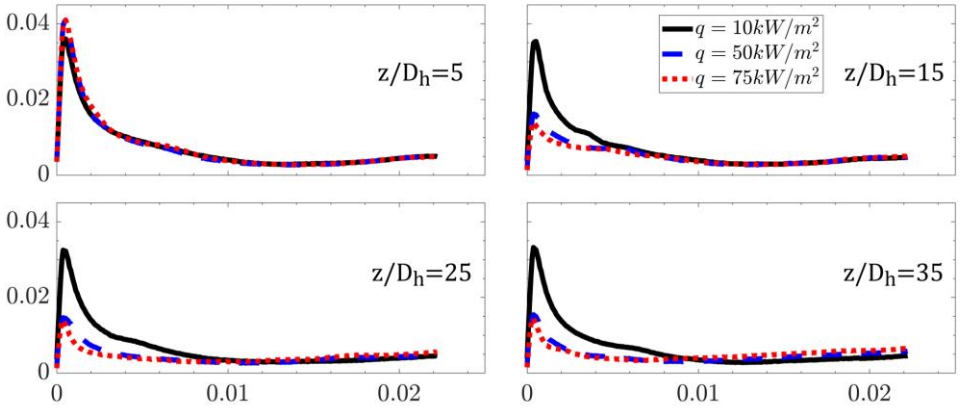

(b)

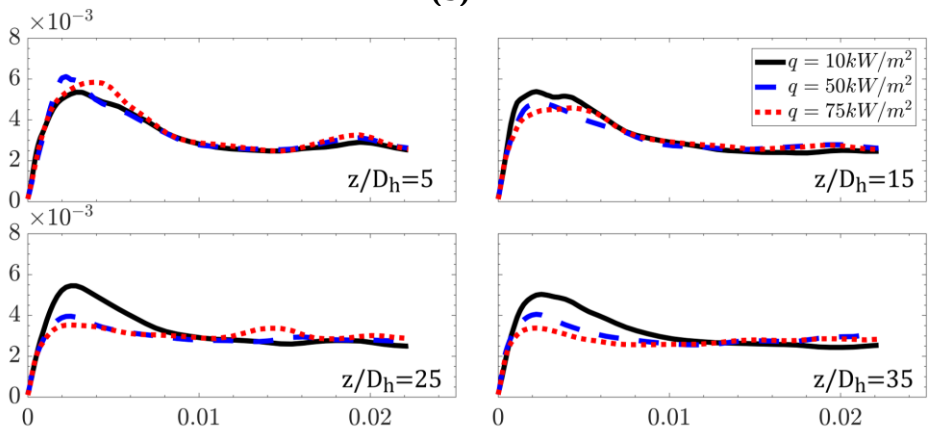

(c)

Figure 4.30: Profiles along ML at several locations down the channel. a) $0.5\langle \rho u_i'' u_i'' \rangle$ b) $\langle \rho w'' w'' \rangle$ c) $\langle \rho u'' u'' \rangle$

Figure 4.31 shows the distribution of turbulent quantities along 'MC'. The value of $0.5 * \langle \rho u_i^{"} u_i^{"} \rangle$ gently decreases across the narrow gap to the main channel. The value becomes lower in high heat flux case. The reduction becomes stronger as the flow moves downstream. This agrees with the results observed earlier along NL. Conversely, the value increases slightly in the main channel at z/D_h =25 & 35. A similar trend can be observed for $\langle \rho u^{"} u^{"} \rangle$, with larger difference in the magnitude at the gap between cases. Meanwhile, the trend for $\langle \rho w^{"} w^{"} \rangle$ is somewhat different. The value increases away from the centre of the narrow gap before decreasing towards the main channel. For all cases the value at the gap is about the same. As the heat flux increases, the magnitude of the $\langle \rho w^{"} w^{"} \rangle$ peak reduces down the heated channel, while a slight increase in value in the main channel is seen, which is similar to the behaviour of $0.5 * \langle \rho u_i^{"} u_i^{"} \rangle$ and $\langle \rho u^{"} u^{"} \rangle$.

Results comparison with Duan & He [13]

Similar to the results for the mean velocities discussed above, the turbulent quantities are also qualitatively compared well with the mixed convection study case of Duan & He [13]. A qualitative comparison of the present study is discussed below with the results by Duan & He [13] as presented in Figure 4.32.

In the narrow gap, the trend for the $0.5\langle \rho u_i^{"} u_i^{"} \rangle$ are not as parabolic as k/U_b^2 used in the previous study. The turbulence kinetic energy is well distributed across the gap. In the wide gap, the profile trends for $0.5\langle \rho u_i^{"} u_i^{"} \rangle$ is quite similar to the trend of turbulent kinetic energy by Duan & He [13]. This trend agrees for all cases with peaks reduce near the heating wall for $0.5\langle \rho u_i^{"} u_i^{"} \rangle$ at higher heat flux, while the peaks near the wall is also reduced from case 2 to case 3 in see Figure 4.32(b). Meanwhile along the line ML towards the main channel, the

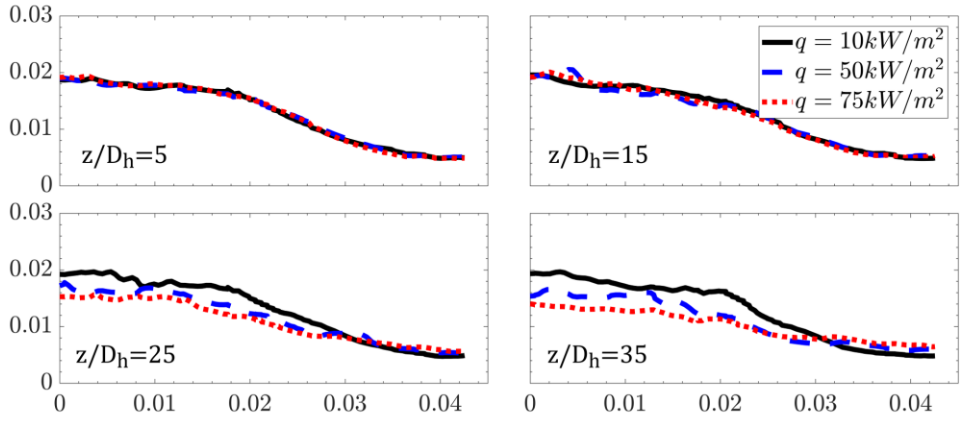

(a)

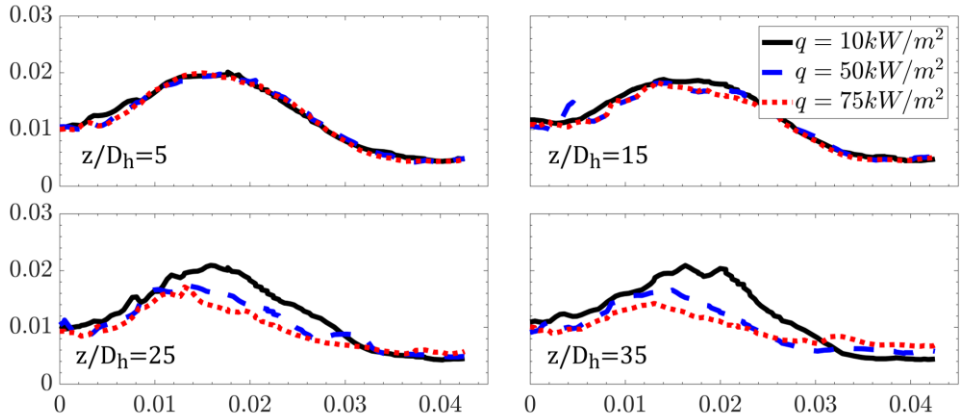

(b)

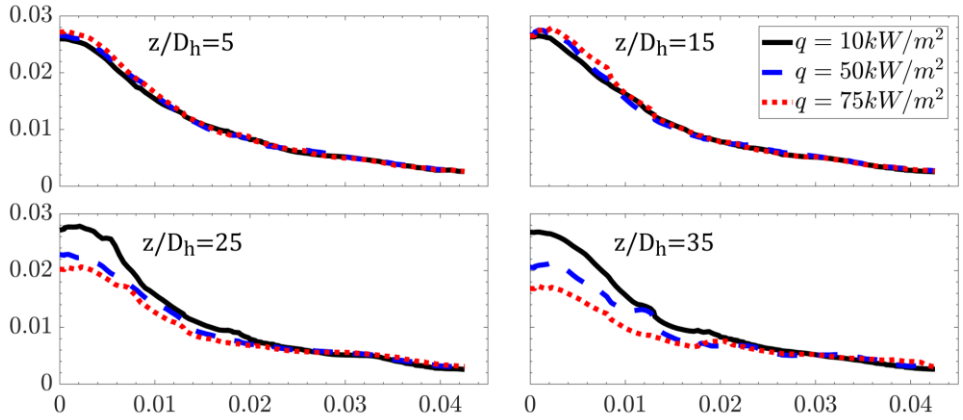

(c)

Figure 4.31: Profiles along MC at several locations down the channel. a) $0.5\langle\rho u_i'' u_i''\rangle$ b) $\langle\rho w'' w''\rangle$ c) $\langle\rho u'' u''\rangle$

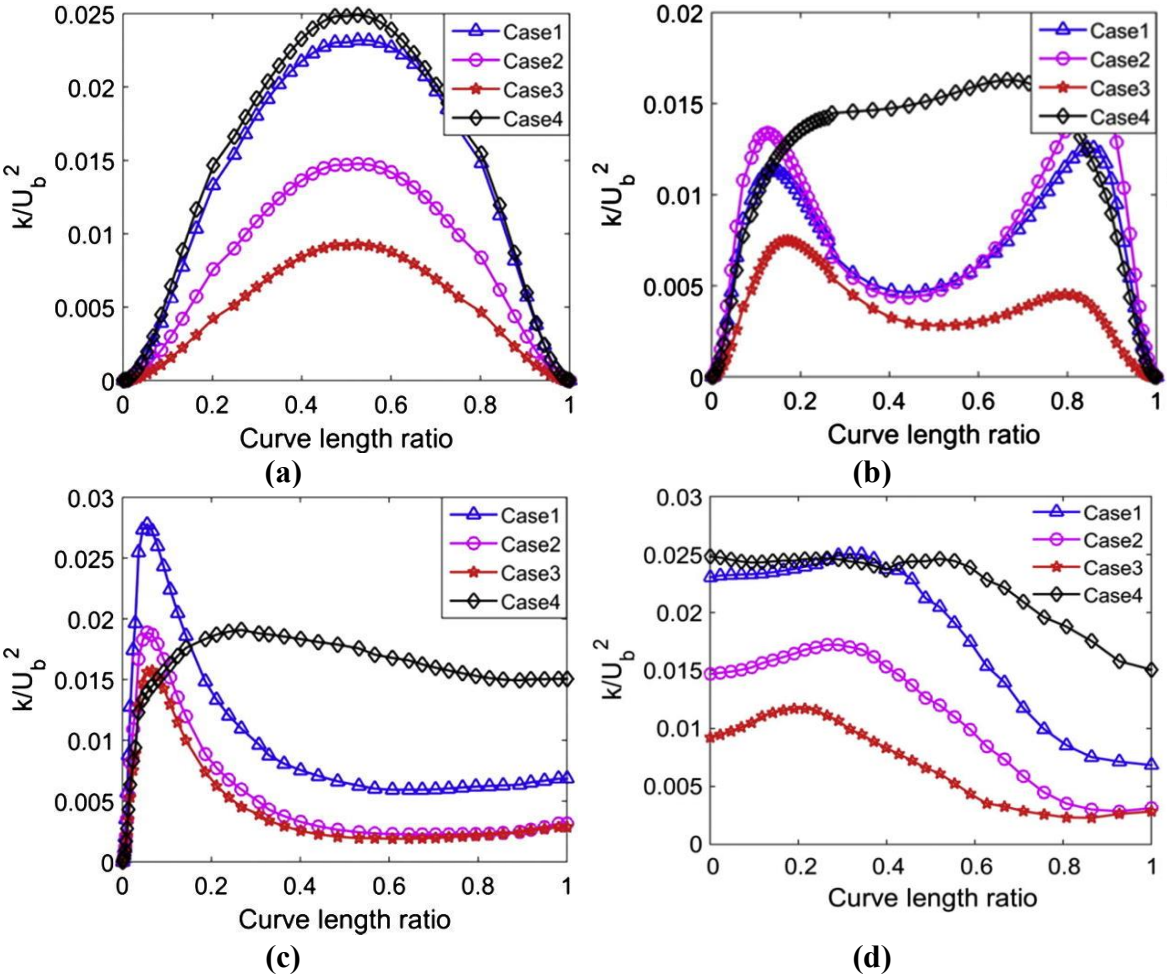

Figure 4.32: The distribution of turbulent kinetic energy at the same lines by Duan & He [13]**. a) NL b) BL c) ML d) MC**

profile trends for $0.5\langle\rho u_i^{"} u_i^{"}\rangle$ in the present study are also similar such in Figure 4.32(c). This trend agrees for every case where peaks are shown reduced near the heating wall for all quantities. It is worth to mention that the behaviour of reduction in peaks near the heating wall at higher heat flux in the present study is comparable to the peaks of buoyancy cases (Case 2 & Case 3) in the previous study. This is interesting as the effect of the thermal expansion to the turbulence is closely similar to the buoyancy effect in constant density. Again similar profile trends as in the main channel can be seen across the narrow gap along the line MC. As $0.5\langle\rho u_i^{"} u_i^{"}\rangle$ reduces at the narrow gap where it also true for the buoyancy cases (Case 2 & Case 3) of Duan & He [13]. This shows the similar effect of the thermal

expansion and buoyancy effect in constant density to the turbulence intensity at this region where similar to the finding of Tanaka *et al.* [31].

4.2.9 Proper Orthogonal Decomposition

To further analyse the coherent structures in the narrow gap, a method suggested by Lumley called proper orthogonal decomposition (POD) was used [145]. The POD can be viewed as a method to identify the most important modes of turbulence structures by decomposing the transient data into a set of orthogonal functions. This method is widely used as an option to study turbulence dynamics. Detail description of POD can be seen in §3.2. In the present study, 100 samples of snapshots were used to examine the energy distribution of the POD modes at the equidistant plane in the narrow gap. To study the effect of the thermal expansion in the narrow gap between cases, the first three energetic modes are presented here in this section.

Figure 4.33 - Figure 4.35 show the first 3 energetic modes of all cases alongside their instantaneous streamwise velocity. It can be seen that the first two modes show two alternating/symmetric structures with Mode 1 having a higher intensity for q=10kW/m^2 (Figure 4.33). The alternating patterns in Mode 1 and Mode 2 work as a pair resultant from the swinging flow structures. The energy contained in these structures is around 28% and 24% respectively. This shows that this structure pair makes up more than half of the total energy content of the flow structures. Meanwhile, the third energetic mode represents smaller structures and makes a contribution of 3.5% to the overall energy of the flow structures.

In the case of q=50kW/m^2, similar alternating patterns of the velocity fluctuations form the first 2 energetic modes which can be seen in Figure 4.34. This again suggests that this

pair contribute strongly to the general swinging flow structure. It can be seen that the contributing energy from Mode 1 and Mode 2 in q=50kW/m^2 is close to each other with 23.5% and 21.4% respectively of the total energy. The third energetic mode shows a structure of reducing fluctuations downstream. The contribution energy from all the first three modes makes up barely half of the total energy content of the flow structure. The third mode explains the weakening of the structures down the channel.

The POD results for the highest heating case of q=75kW/m^2 can be seen in Figure 4.35. A pair of the alternating/symmetric patterns similar to that seen in the earlier two cases can also be found in the highest heating cases. However, the pair is not the first two energetic modes in this case anymore; they become the second and third energetic modes of the swinging flow structures. The contributing energy from the pair is 16.5% and 15%, making up only 31.5% of the total energy of the flow structure. On the other hand, the first energetic mode in this case, contributing 29% to the total, is one with reducing fluctuations pattern downstream. This is similar to the structure found in the case of q=50kW/m^2 as the third most energetic mode. This explains the observation of the weakening flow structure downstream in the highest heating case. This result is in line with the turbulent quantities discussed earlier as well as the behaviour of the instantaneous streamwise vorticity as seen in Figure 4.11. Similar behaviour of vortex reduction also can be seen in high heating cases in Appendix A represented by Q criterion iso-surfaces.

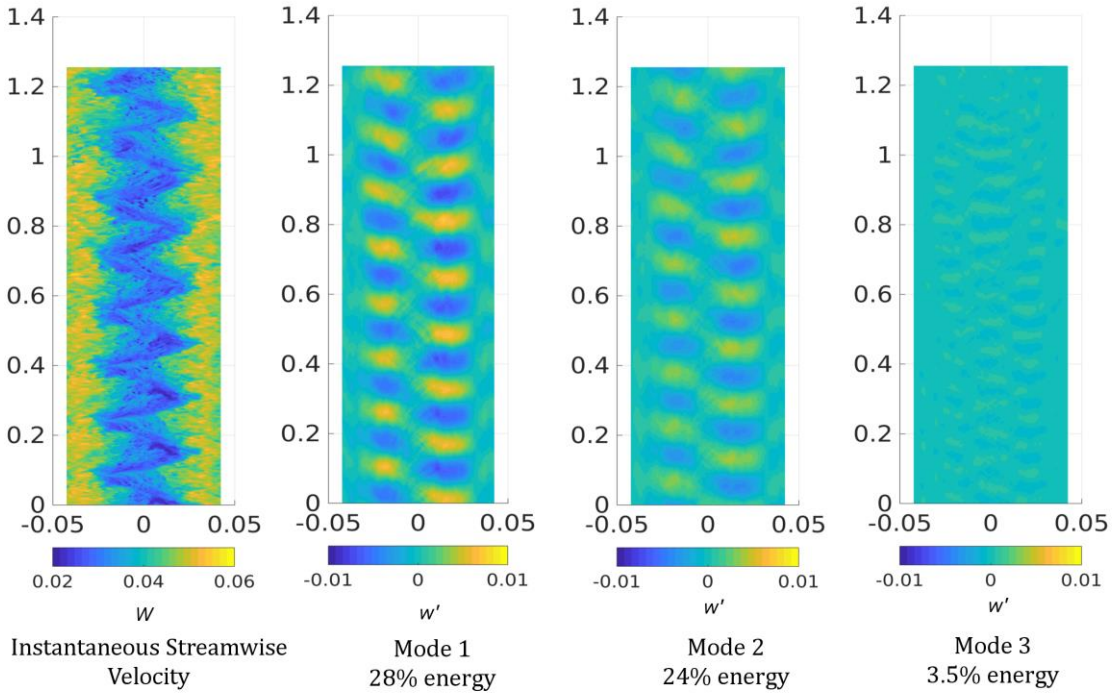

Figure 4.33: The instantaneous streamwise velocity and first 3 energetic modes at the narrow gap in q=10kW/m^2.

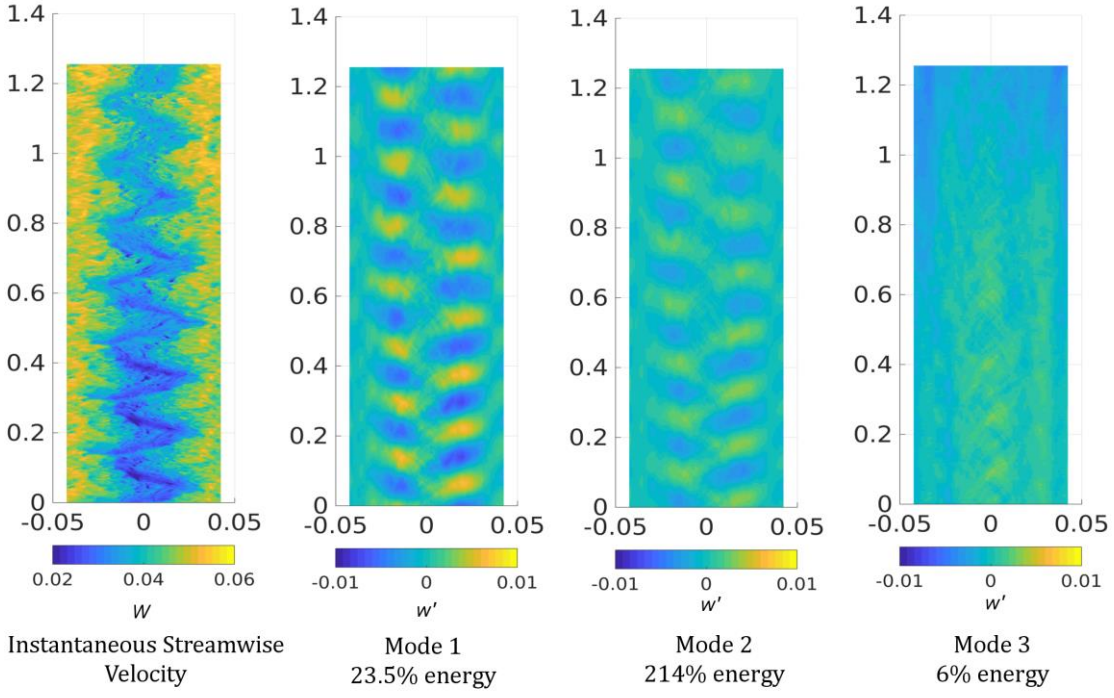

Figure 4.34: The instantaneous streamwise velocity and first 3 energetic modes at the narrow gap in q=50kW/m^2.

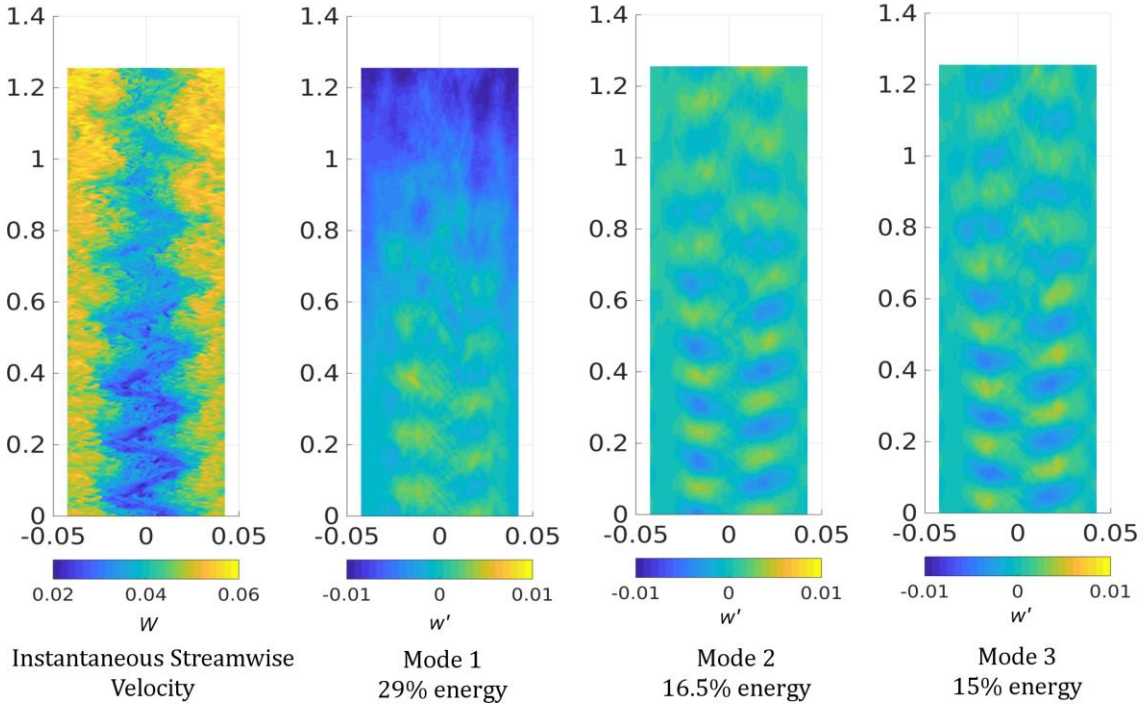

Figure 4.35: The instantaneous streamwise velocity and first 3 energetic modes at the narrow gap in q=75kW/m^2.

4.3 Summary

Large eddy simulations of turbulent forced convection of water at a supercritical pressure in a trapezoid annulus have been performed using *Code_Saturne*. The effects of the thermal expansion and the variation of other properties on the large flow structures in the channel have been discussed. The results obtained clearly demonstrate the existence of the large flow structures in the narrow gap and the wide gap. This agrees with the finding by Wu & Trupp [120] and Duan & He [12]. There are some differences in the behaviours of the large flow structures between the higher heating cases and the low heating case. The swinging flow pulsation observed in the narrow gap led to the temperature variations on the rod wall. This may increase the thermal fatigue of the rod, especially on the side of the narrow gap. The

flow structures in the wide gap are inversely linked to those in the narrow gap, but they are much weaker. The St^{-1} of the channel is found to be similar to that of Duan & He [12] and close to Wu & Trupp [120]. The convection speed in the narrow gap reduces with the increase of heat flux, but the trend is reversed in the wide gap.

The effective mixing velocity, u_{eff} is also investigated at the gaps and a point away from the gap. u_{eff} obtained using LES away from the gap is compared with the Rehme correlation [113]. The Rehme correlation is unable to predict the correct u_{eff} of the results obtained using LES, which implies that the effect of variable property is strong. Indeed, the effect of the variation of the properties on the behaviour of large flow structure in the gaps has been observed as discussed above. The mixing factor, Y and u_{eff}/U_b are also compared with the forced convection result of Duan & He [12]. The significant difference between the present results and that of Duan & He [12], which can be attributed to the effect of the variation of the properties due to heating.

The turbulent statistics at several locations down the channel for each heating case are discussed. The general mean velocity distributions are not strongly influenced by the heating in all the cases though there are detailed differences. For example, a clear distinction can be seen in the distribution of the mean velocity in the wide gap between the low heating case. In the cases of higher heating, the velocity is significantly increased near the heated rod in the wide gap. It has been found that heating causes a reduction in all turbulence quantities, especially near the heating wall. The opposite is seen to be true near the adiabatic wall in the wide gap and main channel, where the turbulent quantities increase with the increase of the heat flux. The magnitude of $\langle \rho u'' u'' \rangle$ in the narrow gap is observed to be largest compared to other regions in the channel cross-section, showing that the spanwise component which

contributed by the flow structures dominate the trend of the total turbulent kinetic energy in this region. Furthermore, results from the present study have been compared with those of the Duan & He [13]. The general trend of results of the high heating cases of the present study in the main channel and across the gap, are similar to those of the buoyancy cases of the Duan & He [13]. From this result it shows that the effect of thermal expansion and that of the buoyancy effect of constant properties flow (based on Boussinesq approximation) appear to be similar which agrees with the finding by Tanaka *et al.* [31].

A POD analysis has also been done for all heating cases using 100 snapshots. The contributions of the dominated modes to the complete general flow structure are discussed. It is found that the swinging flow structures in all heating cases are a pair of alternating/symmetric modes. In high heating cases, an additional mode with a reduced pattern is apparent, which becomes the dominant mode in the case of the strongest heating ($q=75kW/m^2$).

Chapter 5

Buoyancy-Aided Flow of Supercritical Water in a Trapezoidal Annulus Channel

In Chapter 4, the effect of the thermal expansion due to the variation of properties on the behaviour of flow structures in the narrow gap has been demonstrated. When the heat flux is sufficiently high in which the wall temperature exceeds the pseudocritical temperature, the flow structures are weakened and the fluid mixing between subchannels is reduced. In that forced convection study, the buoyancy force was omitted.

However, in real heating applications, the buoyancy cannot be avoided. This chapter will consider the buoyancy-aided flows of supercritical water. The effect of buoyancy on the flow structures will be the focus of this chapter. The combined effects of buoyancy and thermal at supercritical water is investigated herein. The geometric configuration of the flow channel considered is the same as that in Chapter 4, but an additional case of smaller dimension. This trapezoid annulus channel was also studied can be viewed to represent the triangular fuel assembly. The numerical study is again carried out using large eddy simulation with a

WALE SGS model embedded in *Code_Saturne*. A brief introduction to *Code_Saturne* can be found in the Chapter 3.

5.1 Case Description

The same trapezoidal annulus as in the study of forced convection described in Chapter 4 is used to study the effect of buoyancy force here. Again, the total domain is divided into two parts, namely the inflow generator and the heated test section (Figure 5.1). A typical fully developed flow is achieved in the inflow generator section after sufficient time steps. The inflow generator is an upstream isothermal domain with a total length of $L = 10D_h$. The velocity field at $L = 5D_h$ in the inflow generator is copied at every time step and fed back to the inlet as a new inlet boundary condition for the next time step. The length of the heated test section is extended from $30D_h$ in the previous forced convection study to a length of $L_t = 50D_h$ used here. A constant heat flux is applied on the inner rod wall in the heated test section. Therefore, the total domain length is $L_T = 60D_h$.

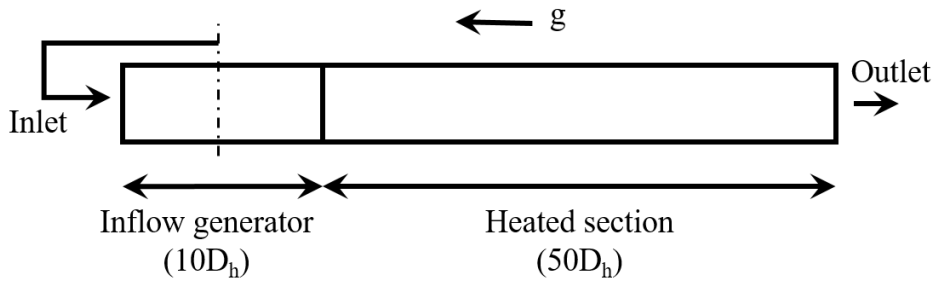

Figure 5.1: The length domain for LES.

Two sizes of the cross-sectional channel were used in the mixed convection simulations reported in this chapter. i) MC_L3 uses the same size as that in Chapter 4 (see Figure 4.1) which has a hydraulic diameter of 0.0314m and ii) MC_S2 and MC_S3 have a dimension of

1/10 of that of MC_L3, and hence having a hydraulic diameter of 0.00314m. It will be shown later, for the same level of buoyancy effect, a channel of a larger size needs a relatively small change in temperature than that in a smaller channel. As a result, MC_L3 represents a case of a strong buoyancy influence but with little changes in fluid properties; hence this is a case where the Boussinesq approximation applies. By contrast, MC_S2 and MC_S3 represent cases where the variation of the temperature in the fluid is strong for the buoyancy-influenced cases, and hence effects of the variations of other thermal properties may also play an important role.

The nondimensional heat fluxes cases MC_L3, MC_S2 and MC_S3 are of $Q^+ = 0.013, 1.73$ & 6.9 respectively. Consequently, the buoyancy parameter for the three cases are given as $Bo^* = 2 \times 10^{-5}, 2.5 \times 10^{-6}$ & 1×10^{-5}. Here Q^+ and Bo^* are given by

$$Q^+ = \frac{qD_h}{\lambda T}$$
$$Bo^* = \frac{Gr^*}{Re^{3.425} Pr^{0.8}} \tag{5.7}$$

where *Re* is the Reynolds number, *Pr* is the Prandtl number and Gr^* is the Grashof number which is based on the wall heat flux.

$$Gr^* = \frac{q\beta D_h^4 q}{\lambda \nu^2} \tag{5.8}$$

The details of the parameters of the test cases are shown in Table 5.1. Also shown are two forced convection cases already discussed in Chapter 4 for comparison. The inlet bulk velocity for D_h=0.0314m is 0.0388 m/s and for D_h=0.00314m is 0.0388 m/s. In both dimensions, the inlet bulk velocity is for a targeted Reynolds number of 10540. In the present study, a constant heat flux is again imposed only on the rod wall in the heated test section. An inlet temperature of below the pseudocritical temperature is chosen at 360°C. The chosen

operating pressure is 25 MPa. The thermal properties were obtained from the NIST database. For some comparison together with the current test cases, two forced convection cases from the previous study were chosen and presented in this study. The lowest and highest heat fluxes cases were considered, namely FC_L1 and FC_L3. The discussion will mainly focus on the current test cases, while further discussion on the forced convection cases can be found in Chapter 4. The summary of all presented cases herein can be seen in Table 5.1.

Table 5.1: Summary of flow and heating conditions at Re=10540, T_0=633K (FC=Forced Convection; MC=Mixed Convection).

Case	Type	Q^+	q (kW/m^2)	D_h (mm)	U_b (m/s)	L_t/D_h	$Bo*$
FC_L1	FC	1.07	10	31.4	0.0388	30	-
FC_L3	FC	8.01	75	31.4	0.0388	30	-
MC_L3	MC	0.01	0.13	31.4	0.0388	50	2×10^{-5}
MC_S2	MC	1.73	161.5	3.14	0.388	50	2.5×10^{-6}
MC_S3	MC	6.90	646	3.14	0.388	50	1×10^{-5}

The same mesh used in the previous study is adopted in this study. The mesh is fully structured, containing 49 million elements. The mesh nodes adjacent to the wall are in the range of $5 \leq \Delta x^+ \leq 17$, $0.13 \leq y^+ \leq 0.2$ and $\Delta z^+ \approx 23$ for spanwise, wall normal and streamwise respectively. For locations of $y^+ \leq 20$, there are about 13 cells with ~9 cells located in $y^+ \leq 10$. These values were evaluated from the isothermal sub-domain. The present LES simulation was again solved using WALE subgrid-scale model in *Code_Saturne*. The velocity and pressure coupling is obtained using SIMPLEC algorithm. A second order central difference scheme in space and second-order of mix Crank-Nicolson and Adams-Bashforth in time is adopted.

For the numerical stability and accuracy, the overall maximum CFL number was restricted to be below 0.6. To achieve this the time step specified at 0.001s for MC_L3 and 10^{-5}s for MC_S2 and MC_S3, where the nondimensional time for each case was $t^* \approx 0.0012$

($t^* = \frac{\Delta t U_b}{D_h}$). For the convergence of the simulations, overall residuals are kept at 10^{-5} for all buoyancy cases, where they are maintained for around 3 through-time of the whole domain before the statistics starts calculated. To achieve the converged results of the statistics, averages are taken at about 4 through-time of the whole domain.

5.1.1 Predefined Locations for the Results Discussion

To ease the discussion later in this chapter predefined locations are shown in Figure 5.2. The two points, NG and BG, are located at the midpoint of the vertical symmetric lines of the channel in the narrow gap and wide gap respectively. The histories of instantaneous velocities were recorded for several axial locations at these points (NG & BG). Values obtained were used for spectral and correlation analyses. Some profiles across the channel are plotted at several locations shown in Figure 5.2. The line profiles are named respectively as NL, BL, ML, and MC for the profiles in the narrow gap, wide gap, towards the main channel and across the narrow gap to the main channel. The line MC is an equidistant plane, located between the rod wall and the bottom wall is used to present the instantaneous flow and temperature field at the narrow gap across the domain. Results from these lines are used to discuss the turbulence statistics.

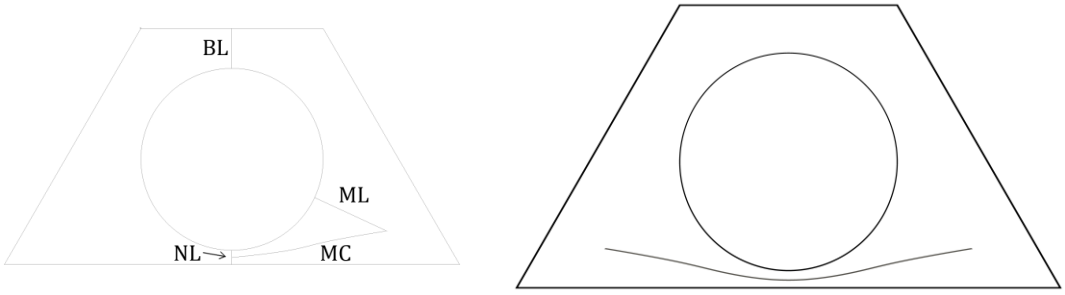

Figure 5.2: Predefined lines and locations.

5.1.2 The Quality of the Simulations

The quality of the simulations with the mesh used in the present study is first evaluated. This is an important step to evaluate the quality of the results obtained as there is no experimental study that can be compared directly to validate the present study. Similar as in Chapter 4, two parameters are used to evaluate the quality of the simulations, namely the parameter s and LES_IQ_v. These parameters have been suggested by Geurts and Fröhlich [153] and Celik *et al.* [154] and their definitions can be found in §3. The quality of the simulation for the highest heat flux case, MC_S3 is presented herein. Figure 5.3 and Figure 5.4 show the contours of parameter s and LES_IQ_v respectively at four locations. Taking the advantage of the symmetrical configuration of the trapezoidal annulus channel, only half of the cross-sections are presented here.

As illustrated in Figure 5.3, the overall values of s increases down the channel. The value of s in the main channel area is around 0.35 and through the cross-section down the heated channel, the value of s increases to around ≈ 0.7. Meanwhile, near all wall regions, the value of s is maintained low, being at $s < 0.17$. The value of s is close to DNS simulations when it is close 0. To obtain a good LES simulation, the turbulence kinetic energy has to be resolved over 80% i.e., $s < 0.2$ [138]. Even though the value of s in the main channel is quite high, the quality of the current LES simulation can still be considered good as the values of s are reasonably small in all wall regions.

The parameter by Celik *et al.* [154], LES_IQ_v, is shown in Figure 5.4. Down the heated channel, LES_IQ_v is overall maintained in a range of 0.97-0.98 in the main channel. The values of LES_IQ_v near the wall are observed to be around 1. According to Celik *et al.* [154],

LES_IQ_v is considered good when it close to 1 (i.e., LES_IQ_v>0.8). These results show that the current simulations are generally of good quality and can be referred to as numerical experiment.

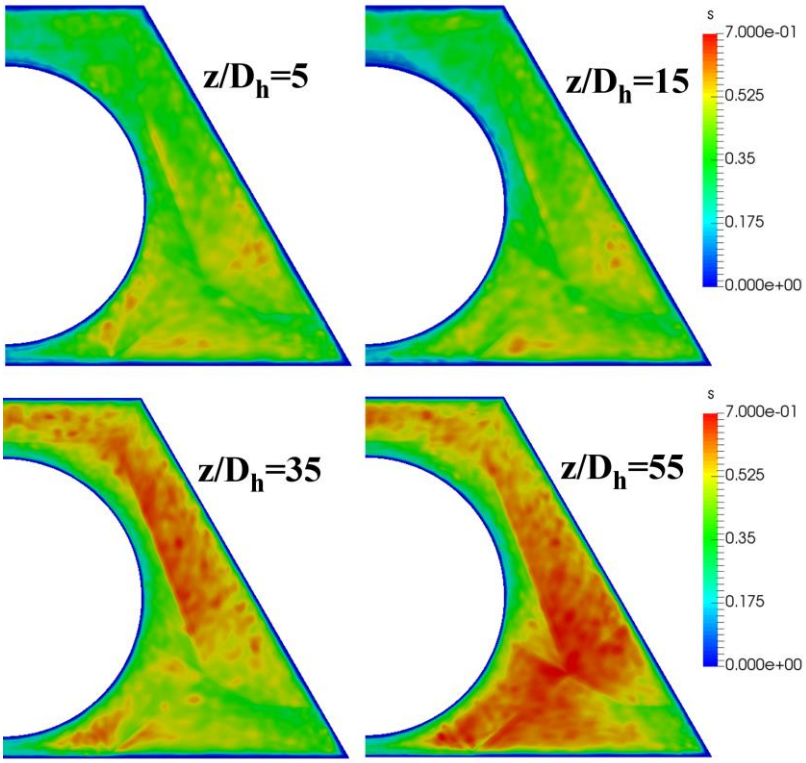

Figure 5.3: LES quality *s* in case MC_S3.

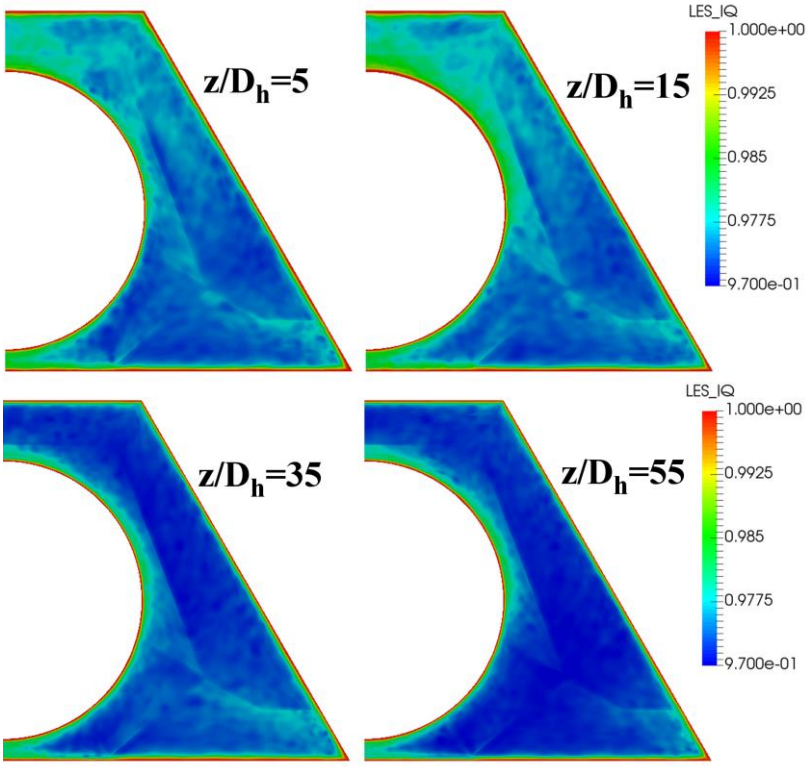

Figure 5.4: LES quality *LES_IQ*$_v$ in case MC_S3.

5.2 Results and Discussion

5.2.1 Variation of Properties

The variations of the properties of the water are investigated for all cases. The values of the properties are obtained from the calculated bulk temperature, which defined as

$$T_b = \frac{\int \rho w T \, dA}{\int \rho w \, dA} \tag{5.9}$$

Figure 5.5 shows the bulk temperature down the heated channel for all cases. As can be seen in the figure, all cases show an increase of the bulk temperature except for the mixed convection case MC_L3. In MC_L3 the temperature is almost unchanged (in this figure) due to a small heat flux applied. The case with the highest temperature increased is MC_S3, where it has the highest value of Q^+ followed by FC_L3. Meanwhile the temperature

increases for MC_S2 and FC_L1 are quite close to each other. None of the cases tested has a bulk temperature higher than the pseudocritical temperature of ~385℃.

Figure 5.6 shows the variations of a few fluid properties down the heated channel, including density, dynamic viscosity, thermal conductivity and Prandtl number. Along the heated channel the density, molecular viscosity and thermal conductivity decrease monotonically for all cases except for MC_L3 in which the remain largely unchanged. Meanwhile, the Prandtl number increases for all cases along with the increase of the bulk temperature. The change in properties is the highest in MC_S3. The property change for case MC_S2 is intermediate, in between the two forced convection cases of FC_L1 and FC_L3.

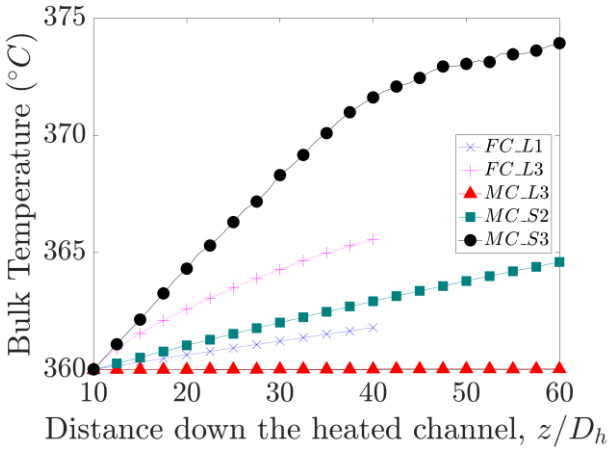

Figure 5.5 Bulk temperature measured down the heated channel.

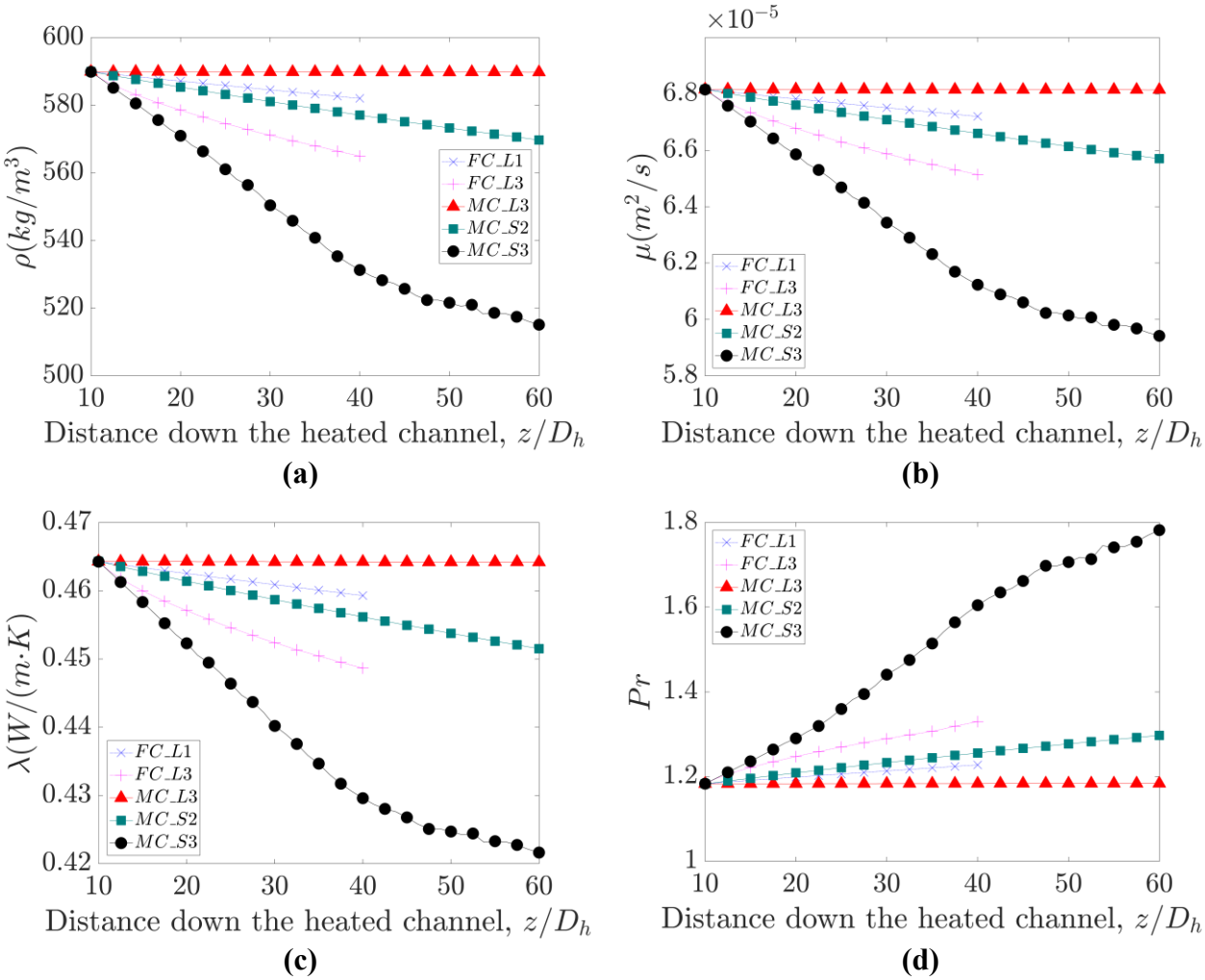

Figure 5.6: Variations of bulk thermal properties down heated channel. a) density b) dynamic viscosity c) thermal conductivity d) Prandtl number

The trends of the temperature and thermal properties across the channel are also investigated at some locations. The variation of the temperature and the properties in the narrow gap and wide gap regions are shown. Only the density and Prandtl number are discussed below. The variation of other properties can be seen in Appendix B.

Figure 5.7 shows the temperature variations along the narrow gap (NL) and wide gap (BL). It can be seen that the temperature is the highest near the heated wall ($y/_{ymax} = 0$) in all cases. MC_S3 has the highest temperature at the heating wall among all cases. Meanwhile, for MC_L3 the temperature is almost unchanged in comparison to other cases.

Both cases of MC_S3 and FC_L3 have a rapid increase in the fluid temperature near the heating wall. In both cases, the fluid temperature can be higher than the T_{pc} down the heated channel. This is also true for MC_S2. In the latter case, the fluid temperature exceeding T_{pc} occurred much closer to the heating wall both in the narrow gap and the wide gap. In the narrow gap, the region where the temperature is higher than the T_{pc} in MC_S3 spreads further towards to the centre to the gap. In this case, the variations of properties at these locations are expected to be high.

Figure 5.8 shows the variation of the density along NL and BL. The density can be seen at the lowest near the heated wall while higher towards the adiabatic wall. This can be clearly seen from all heating cases except for MC_L3 case. Similar to the temperature variations shown earlier, the density varies much rapidly down the heated channel for both MC_S3 and FC_L3. This is due to the fact that the temperature exceeds the T_{pc} away from the heating wall.

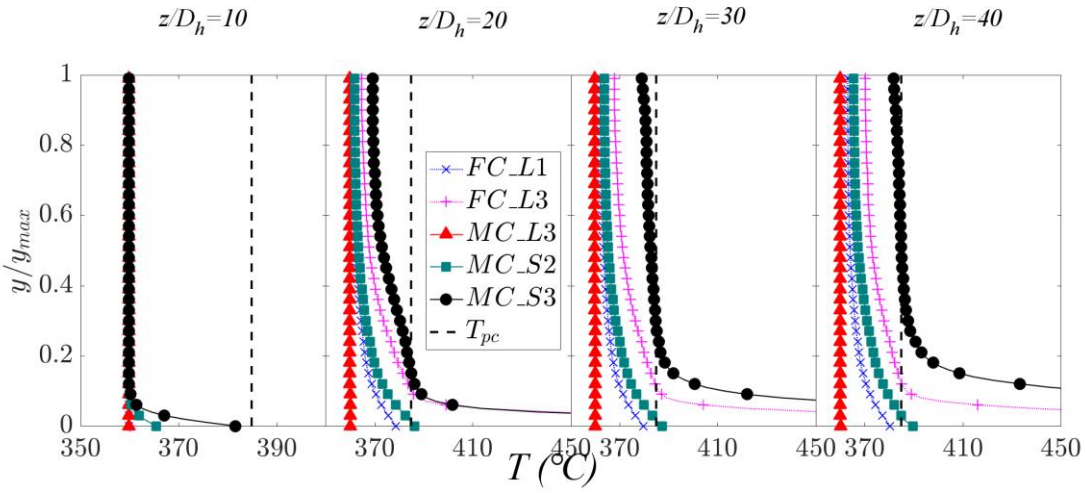

(a)

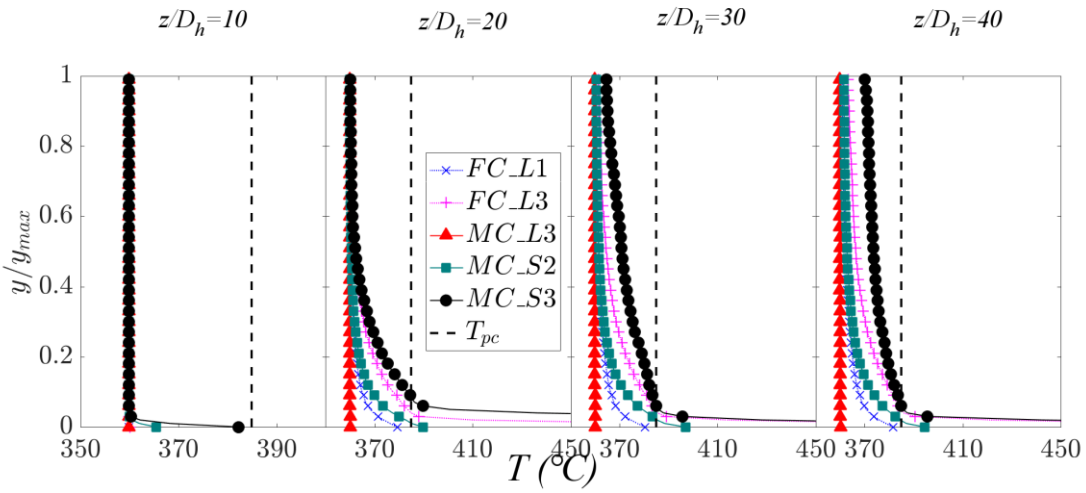

(b)

Figure 5.7: Variation of temperature at several locations along a) NL b) BL.

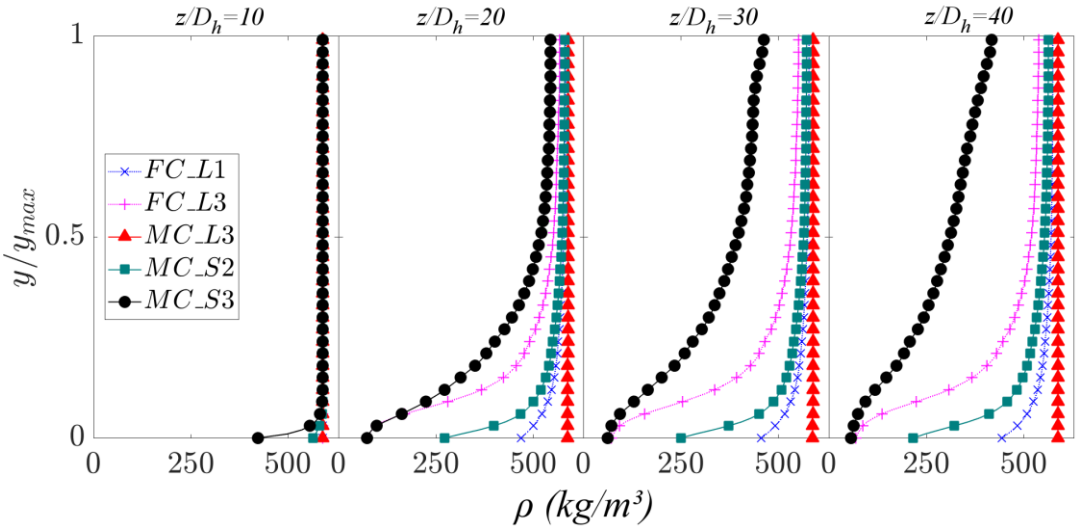

(a)

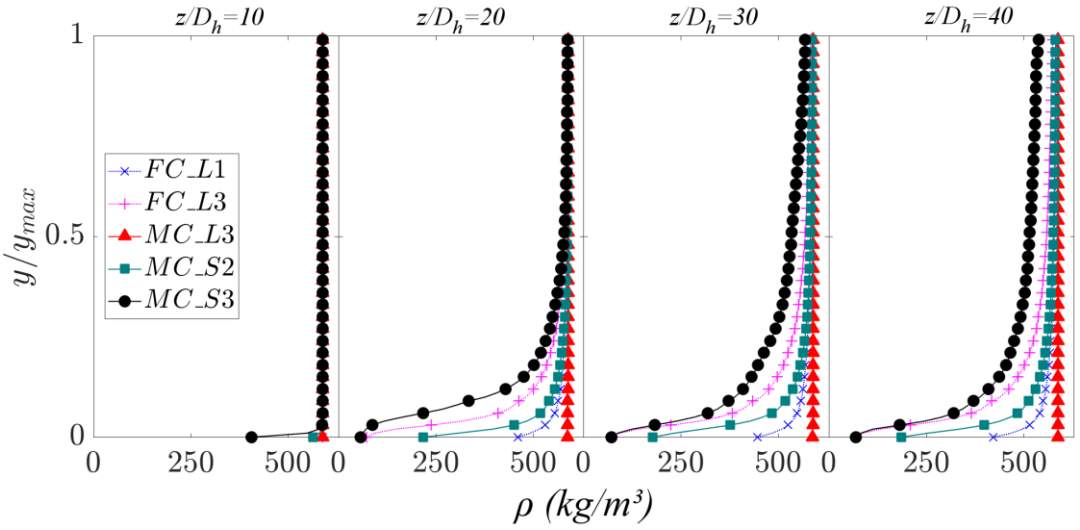

(b)

Figure 5.8: Variation of density at several locations along a) NL b) BL.

The variations of the Prandtl number along NL and BL are illustrated in Figure 5.9. From the figure, it can be seen that a peak appears in the location away from the wall in FC_L3, MC_S2 and MC_S3 cases. The peaks occur when the fluid temperature in the region crosses T_{pc}. The location of the peaks coincides that where $T=T_{pc}$. It can be seen that the Prandtl number for MC_S3 becomes the lowest at the heating wall compared to the other cases.

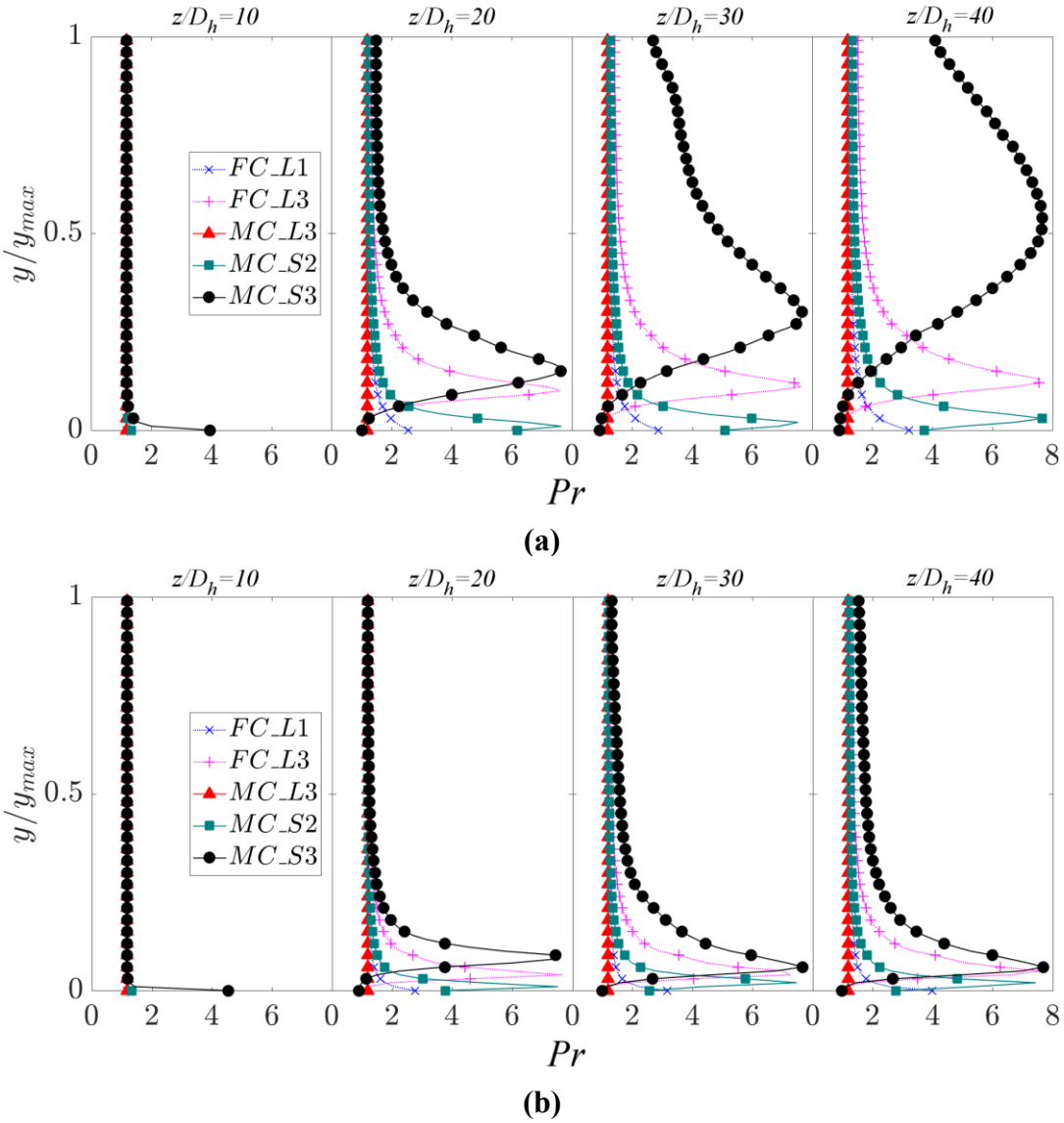

Figure 5.9: Variation of Prandtl number at several locations along a) NL b) BL.

Overall, the variations of the temperature and the fluid properties in all cases show some differences between the cases, but they can be grouped according to their general trends in the variation of the properties. Two cases with most severe changes in properties are FC_L3 and MC_S3. The former case is a forced convection case while the latter is a mixed convection in which the buoyancy influence is non-negligible. Cases FC_L1 and MC_S2 have a mild variation of properties in the cross-sections and the last case, MC_L3 has very small variations of properties, which can be ignored. This implies that this case satisfied the Boussinesq approximation condition.

5.2.2 Bulk Parameters

To study the general trend of the tested cases, the bulk Reynolds number (Re_b) and bulk Nusselt number (Nu_b) are presented in Figure 5.10. The bulk Nusselt number is calculated as:

$$Nu_b = \frac{h_{ave} D_h}{\lambda} \tag{5.10}$$

where h_{ave} is the average heat transfer coefficient which is determined from:

$$h_{ave} = \frac{q}{T_{w,ave} - T_b} \tag{5.11}$$

where q is the heat flux applied and $T_{w,ave}$ is the average wall temperature.

It can be seen from Figure 5.10 (a) that the bulk Reynolds number increases monotonically down the heated channel for all cases. The case with the highest change of Reynolds number is MC_S3, followed by FC_L3, MC_S2 and FC_L1. Meanwhile, the Reynolds number of MC_L3 does not change much in this scale.

The bulk Nusselt number is shown in Figure 5.10 (b). In all the cases, the Nu_b is the

higher at the start of the heated section as expected, but it decreases rapidly downstream. This is where the thermal boundary layer is developing. In FC_L1, FC_L3 and MC_S2, Nu_b gradually decreases and become constant value some distances downstream after the thermal boundary layer achieved its thickness. Meanwhile, for the highest Bo^* of MC_L3, Nu_b rapidly decreases upstream before it increases slightly after z/D_h=30 and reaches a stable value at around 35. A similar trend can be seen for MC_S3 though its Bo^* is half that of MC_L3. The Nu_b in MCS3 decreases downstream initially before increasing slightly around $20<z/D_h<30$. This slight increase of Nu_b in the high heating cases (MC_L3 and MC_S3) is due to the influence buoyancy as will be discussed later.

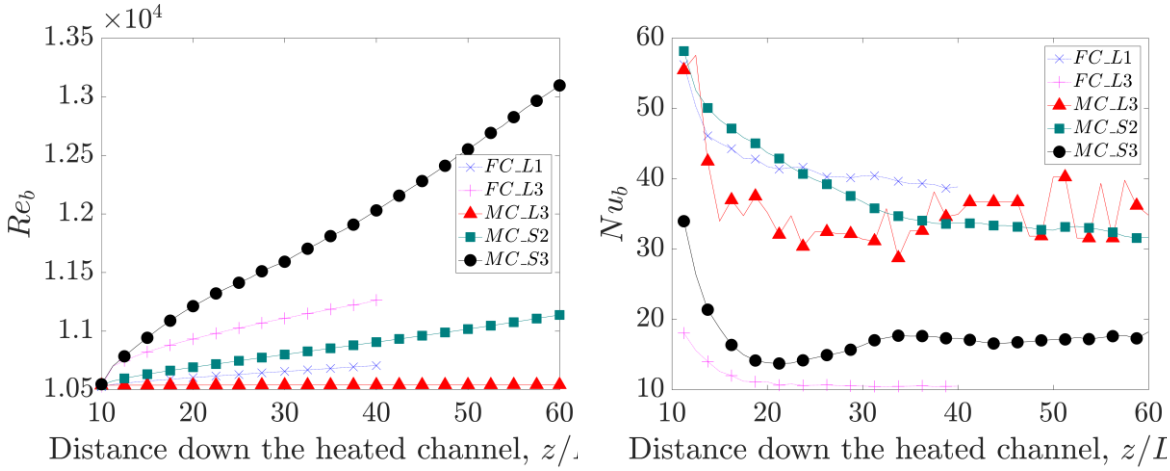

(a) **(b)**

Figure 5.10: Bulk results along the heated test section. a) bulk Reynolds number b) bulk Nusselt number

The normalized wall temperature is presented in Figure 5.11, where it is calculated as:

$$\Theta = \frac{T_{w,ave} - T_{b,0}}{T_{b,1} - T_{b,0}} \tag{5.12}$$

where, $T_{b,0}$ and $T_{b,1}$ are the bulk temperature at the inlet and the outlet for each case respectively. Note that Θ for MC_L3 is multiplied by 10 due to its very small variation of wall temperature. It can be clearly seen that the increase of the normalized wall temperature

for all cases at the beginning of the heating (z/D_h<20). The average wall temperature in MC_S3, increases first reaching a peak at z/D_h≈20 before reducing around 20<z/D_h<30, then becomes more stable. A little bump in temperature is also observed around z/D_h=45. This is expected to be a delayed local heat transfer deterioration. For FC_L3, a rapid increase of the average wall temperature occurs in z/D_h<20, after which it remain more or less unchanged. A gradual increase of temperature in both FC_L1 and MC_S2. Meanwhile, despite its very small changes in the average wall temperature for MC_L3, a rapid increase in average wall temperature can be seen at z/D_h<20 before its roughly stabilized downstream.

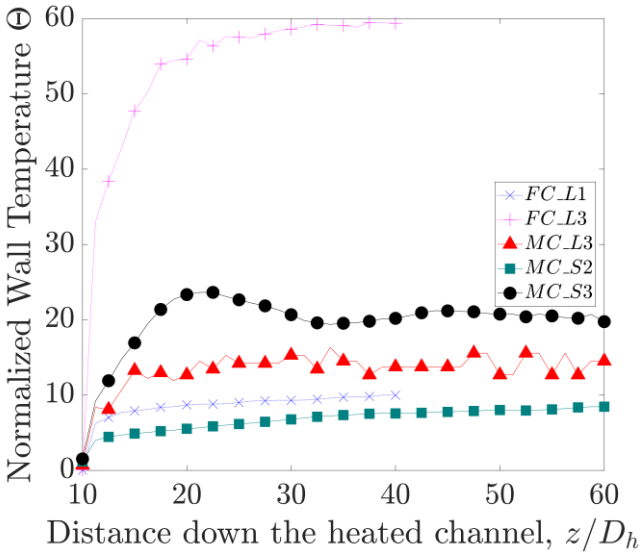

Figure 5.11: Normalized wall temperature, where Θ for MC_L3 is multiplied by 10.

5.2.3 Instantaneous Flow and Thermal Fields

5.2.3.1 Equidistant Plane in the Narrow Gap

The effect of the thermal expansion to the large flow structures in the narrow gap has been studied in Chapter 4. To study the effect of mixed convection on the large flow structures in supercritical water, the streamwise flow in the equidistant plane in the narrow gap is visualized using contours of the instantaneous streamwise velocity in Figure 5.12. it

can be seen that the swinging flow structures are consistent before heating in the isothermal region (z/D_h<10). The low-buoyancy case, MC_S1 shows a steady swinging flow structures along the heated test section but with a weakened intensity. While high-buoyancy cases (MC_L3 and MC_S3) show a disappearance of the swinging flow structures at z/D_h=20. This is the location where the heat transfer deterioration occurrs. In contrast to the low-buoyancy case and forced convection cases, the velocity starts to accelerate in the middle of the narrow gap in these high-buoyancy cases. However, subtle structures start to appear downstream. These structures seem to be in the form of a higher than the local mean velocities whereas the structures in the upstream region were dominated by the lower mean velocities.

In Figure 5.13 contours of the temperature are illustrated. Similar structures in the streamwise velocity contours can also be observed here with the temperature reaching its highest values at the centre of the narrow gap for all cases. In MC_L3 a weak swinging flow structure can be seen in the downstream section of the channel. This suggests that the structures are still present with an accelerated velocity in the middle that converts the structures downstream. This result shows that in the high-buoyancy cases, the flow structures are associated with a reversed velocity gradient in the narrow gap. It is interesting to note that these large flow structures are expected to assist in bringing the high-temperature fluid in and out across the narrow gap region. This behaviour is expected to help the mixing and the heat transfer.

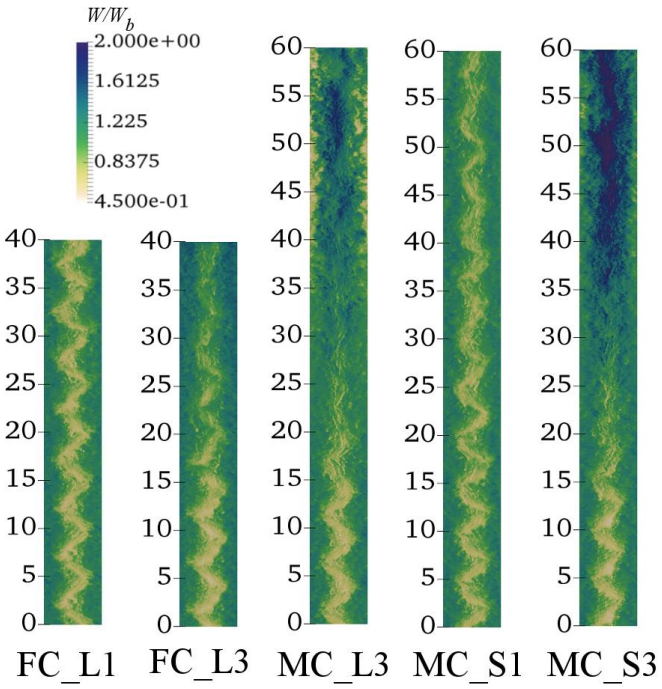

Figure 5.12: Instantaneous streamwise velocity at equidistant planes in the narrow gap.

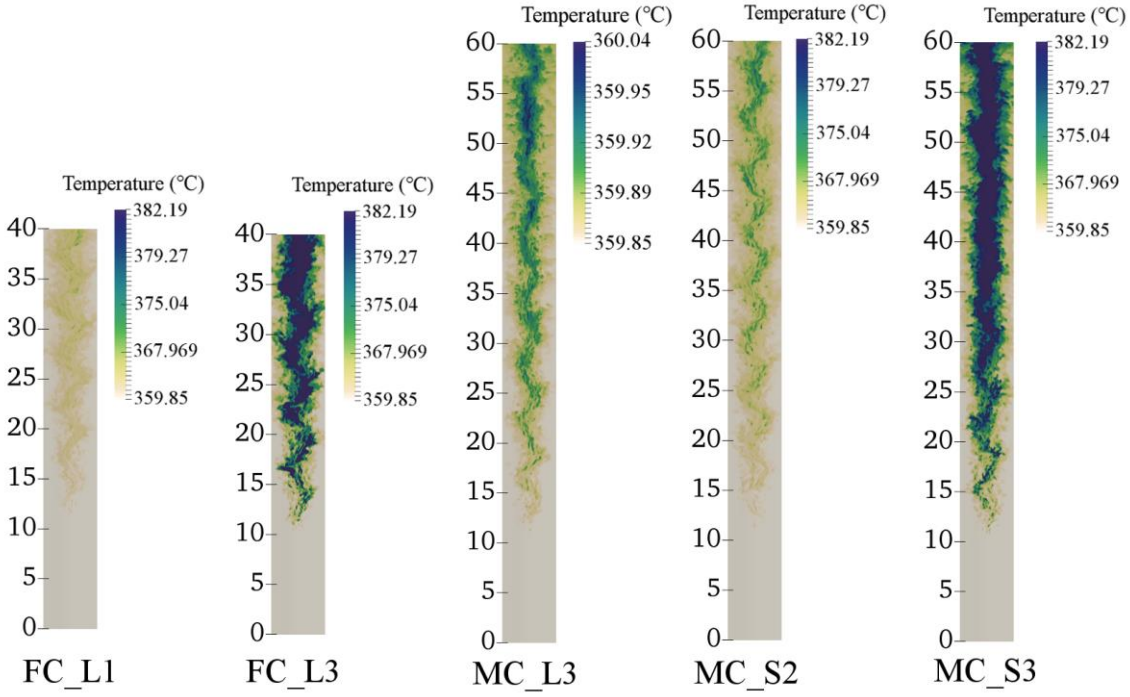

Figure 5.13: Instantaneous temperature at equidistant planes in the narrow gap.

5.2.3.2 Rod Wall

The swinging flow structures cause swinging temperature fluctuations in the flow. It is interesting to see the behaviour of the instantaneous temperature on the heating rod wall. Figure 5.14 and Figure 5.15 show the instantaneous rod wall temperature facing the narrow gap and the wide gap respectively. It can be seen that similar swinging temperature fluctuations occur on the rod-wall facing the narrow gap in all the mixed convection cases. In MC_S2 the swinging temperature on the rod wall is maintained across the entire heating channel. By contrast, the swinging temperature on the rod wall is more irregular and changed downstream in MC_L3 and MC_S3. These structures clearly observed on the rod-wall for high-buoyancy cases confirm that the structures do exist along the entire channel even though some modifications are caused by the effect of buoyancy.

By contrast, no swinging temperature can be seen on the rod wall that faces the wide gap as shown in Figure 5.15. In MC_S2, the temperature is increased and maintained down the heated channel. On the other hand, in the high-buoyancy cases, some high-temperature patches can be seen on the rod wall. They are located in the range of $15<z/D_h<30$ for MC_L3 and $15<z/D_h<25$ for MC_S3. This location coincides with the location where Nu_b is found to be lowest. This result suggests that the heat transfer deterioration only occurs locally near the wide gap, whereas no high-temperature patches can be seen in the narrow gap.

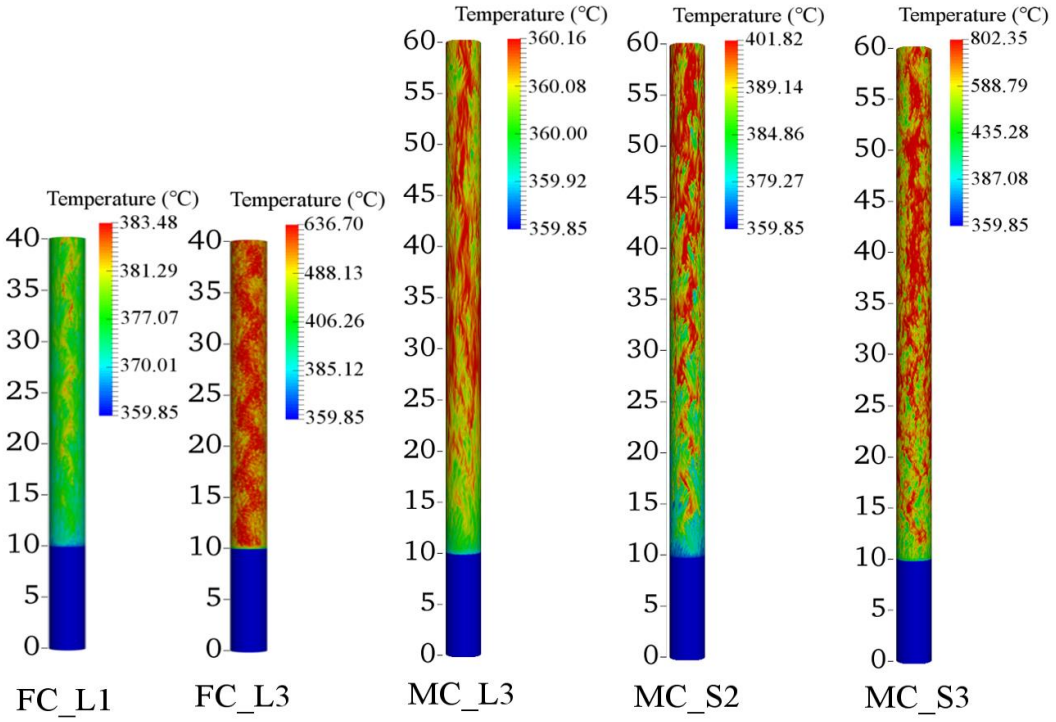

Figure 5.14: Instantaneous rod wall temperature facing the narrow gap.

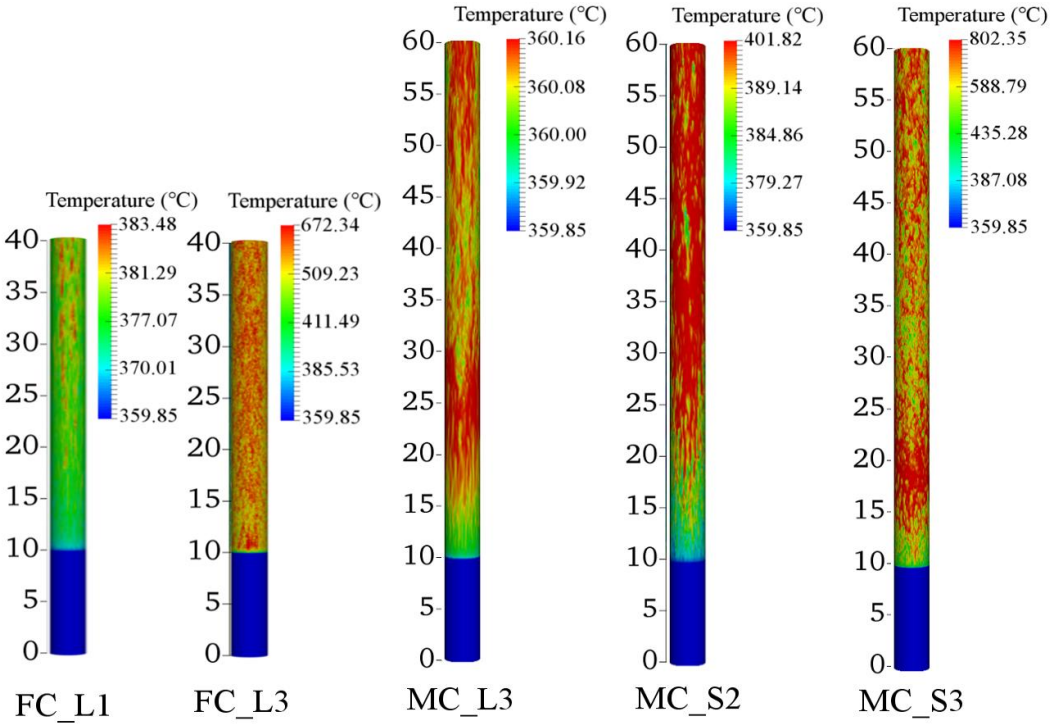

Figure 5.15: Instantaneous rod wall temperature facing the wide gap.

5.2.3.3 Instantaneous Streamwise vorticity

Results of the iso-surfaces for the instantaneous streamwise vorticity are also presented for all three heating cases as presented in Figure 5.16. The view of the domain at $20D_h$ towards the outlet, with a view facing to the narrow gap region. Due two different dimensions are used in this study, the streamwise vorticity Ω_z that presented here are kept at ±10 and ±1000 for large dimension (MC_L3) and small dimension (MC_S2 and MC_S3) respectively, i.e. where in the figure, $+\Omega_z$ is coloured in red while $-\Omega_z$ is coloured in blue.

In Figure 5.16, the different buoyancy cases can be observed has a different level of intensity for the streamwise vorticity in the narrow gap. In MC_L3, it can be seen a sporadic streamwise vorticity distributed within the narrow gap. Note that the magnitude of the streamwise vorticity shown here is at the same magnitude to the forced convection results shown in Chapter 4. However, due to the high buoyancy case (with very low heating), the regular alternating vorticity is hardly be seen nor it is reduced at the narrow gap. Meanwhile, in the lowest buoyancy case, MC_S2, the behaviour of streamwise vorticity occurred along the narrow gap is similar to the result of weak heating of forced convection in Figure 4.11. Vorticities contributes to the swinging flow structures as observed in Figure 5.12. Lastly, the highest buoyancy case MC_S3 shows the streamwise vorticity dominantly distributed throughout the narrow gap with an irregular pattern. This behaviour is similar to the MC_L3. A subtle alternate pattern may be seen in the narrow gap that may suggests a different structure produced to the end of the channel, however, this structure is clearly observed not as similar as the regular alternating vorticity from either side of channel that can be found in such cases with obvious swinging flow structure like MC_S2 or some forced convection cases. This shows a more complicated structure can be found in the case with high buoyancy.

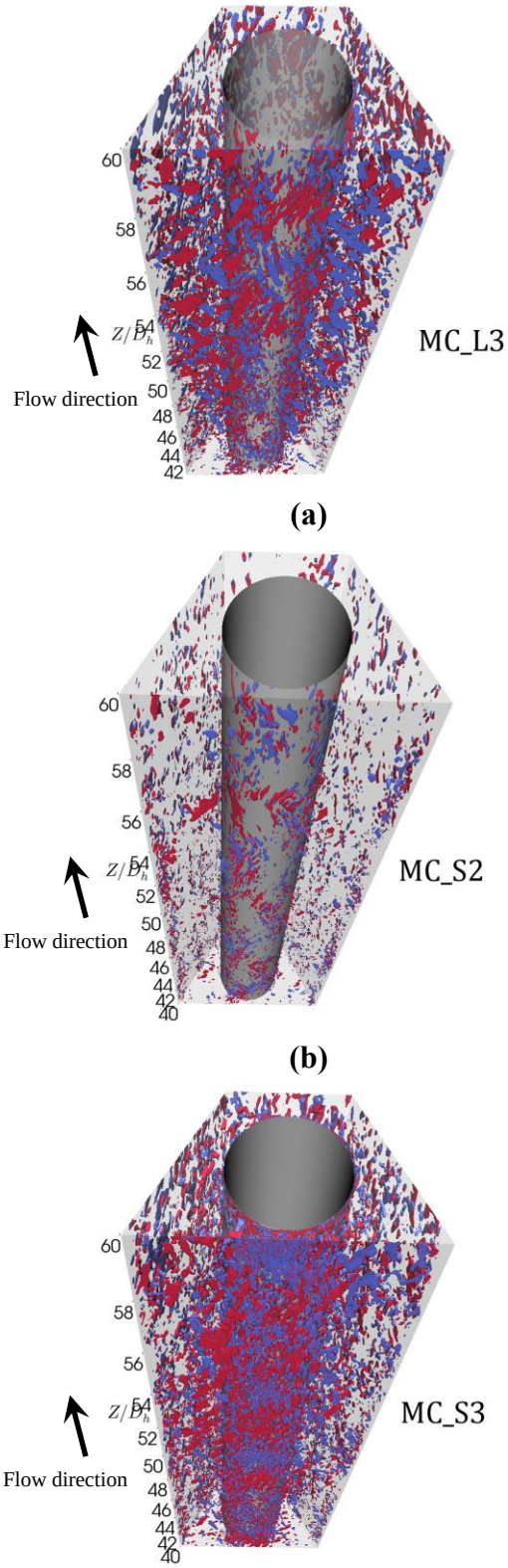

Figure 5.16: The iso-surfaces of streamwise vorticity, Ωz of instantaneous flow at 20Dh to the outlet. a) MC_L3 Ωz=±10 b) MC_S2 Ωz=±1000 c) MC_S3 Ωz=±1000

5.2.4 Instantaneous Velocity Fluctuation and Power Spectral Density

5.2.4.1 Narrow Gap

To investigate further the oscillations of the swinging flow structures, the time histories of the spanwise velocity fluctuations are processed at several locations. Figure 5.17 shows the time histories of the spanwise velocity fluctuations for the mixed convection cases. It can be seen that the spanwise velocity fluctuations in the upstream section (z/D_h=15&25) of the heating section is regular in all cases. These fluctuations persist downstream in case MC_S2 but with weaker strength downstream (z/D_h>35). This is similar to the behaviour of the velocity fluctuations in forced cases. Meanwhile, the fluctuations reduce rather significantly for MC_L3 (z/D_h>35). Here the fluctuations have become more irregular with additional noises at z/D_h>25. This trend can be seen to be even stronger and happen much earlier in MC_S3 (z/D_h=25). However, later downstream some subtle structures can be seen to appear in MC_S3, but with higher frequency. This shows that as buoyancy influences increase, the velocity fluctuations reduce in the narrow gap and some non-monotonic behaviour may occur. Unfortunately, more data of time histories is needed in the recovery region to quantify the behaviour of fluctuations within this region at high-buoyancy.

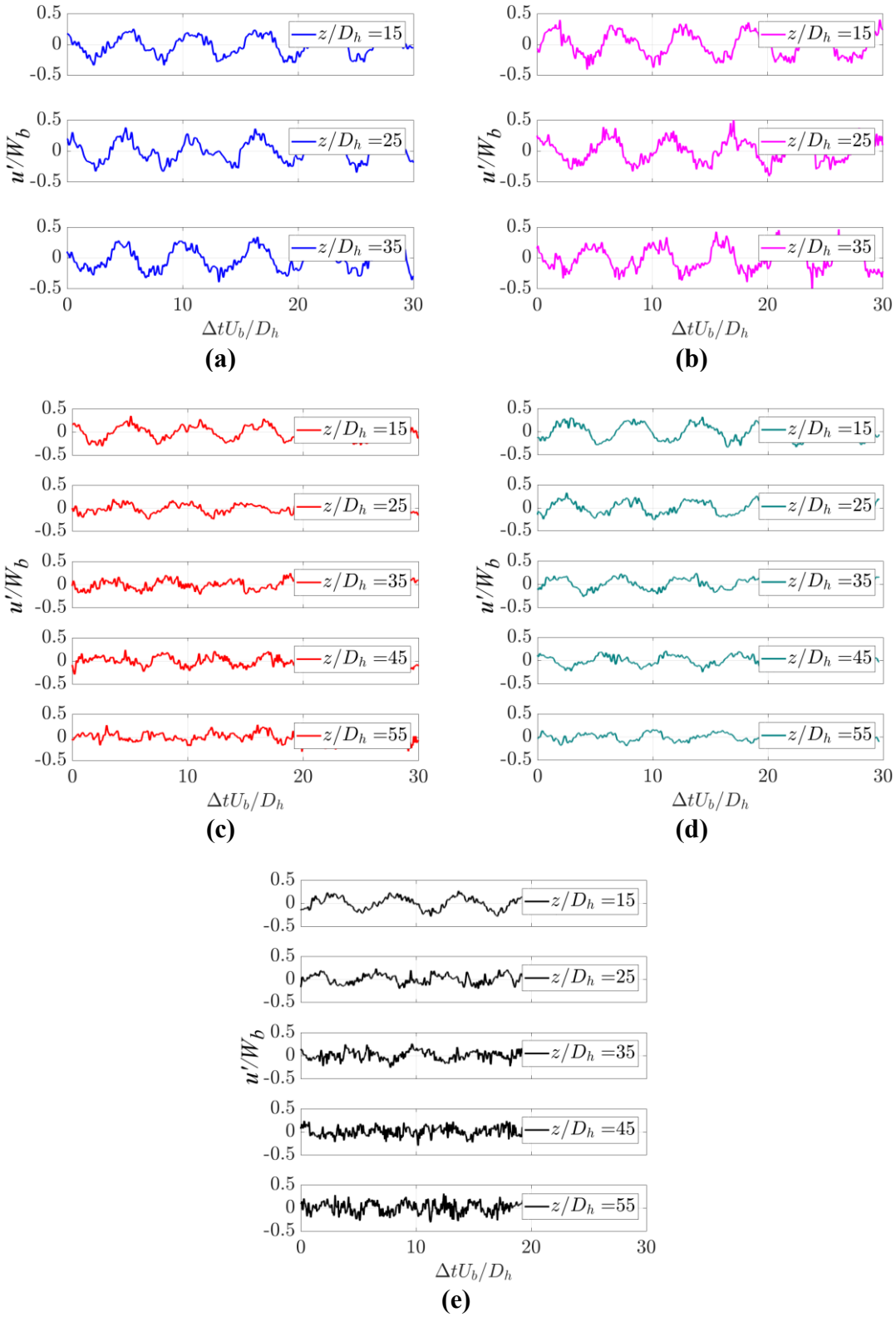

Figure 5.17: Time history for the spanwise velocity at NG down the heated channel. a) FC_L1 b) FC_L3 c) MC_L3 d) MC_S2 e) MC_S3

The spanwise velocity fluctuations at NG can be further evaluated using power spectrum density (PSD) to quantify the dominant frequency of the pseudo-oscillations of the flow structures. The PSD for the larger dimension and the smaller dimension channels are presented separately in Figure 5.18and Figure 5.19 respectively. This is to show the differences in the frequency ranges between these geometry sizes. The PSD is evaluated at the locations used for the time histories of the velocity fluctuations in Figure 5.17.

To assist the presentation of PSD data, results from FC_L3 and MC_L3 are multiplied by 10^2 and 10^4 respectively in Figure 5.18, and MC_S3 is multiplied by 10^2 in Figure 5.19. It can be observed that PSD results for MC_L3 have the same peak as the result from the forced convection cases. This peak maintains at the same frequency (f_p) down the heated channel with a value of ~0.21Hz. However, the peak in MC_L3 has largely reduced in amplitude in comparison to the two forced convection cases. There is also a small secondary peak appearing at z/D_h=35 in MC_L3. The same trend can be seen in the smaller dimension cases. There are peaks visible in both cases MC_S2 and MC_S3 at the same frequency. f_p of these peaks are maintained throughout the channel at around 21Hz. The behaviour of the peak in MC_S3 is also observed to be similar to that of MC_L3 where the peak reduces down the channel. However, at z/D_h=55 a new peak is observed, which is at a frequency that is two times the original peak (~42Hz). This peak may explain the new structures that have been observed earlier in Figure 5.17 (d). The structure is suspected first to be weaken due to the higher buoyancy, but with severe property variation, a new structure may be observed later at the recovery region. The dimensionless Strouhal number for all mixed convection cases in both dimensions that can be evaluated using the peak frequencies obtained at the upstream. The Strouhal number (St^{-1}) obtained for all cases are about ~5.61, which is similar to those

of the forced convection cases in Chapter 4. This again suggests that the Strouhal number for a particular geometric configuration remains more or less the same for different flow condition. This value is not affected by the buoyancy.

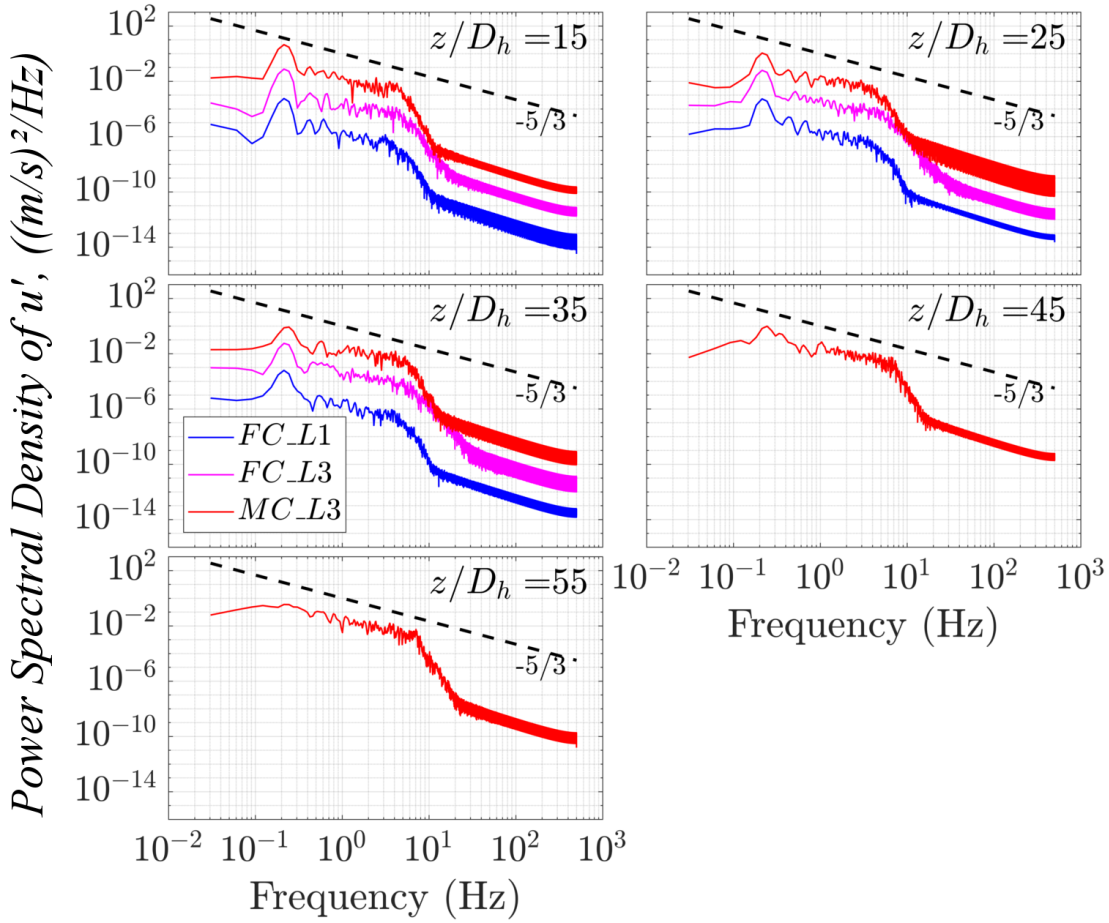

Figure 5.18: Power spectral density at NG in several locations for the large dimension cases.

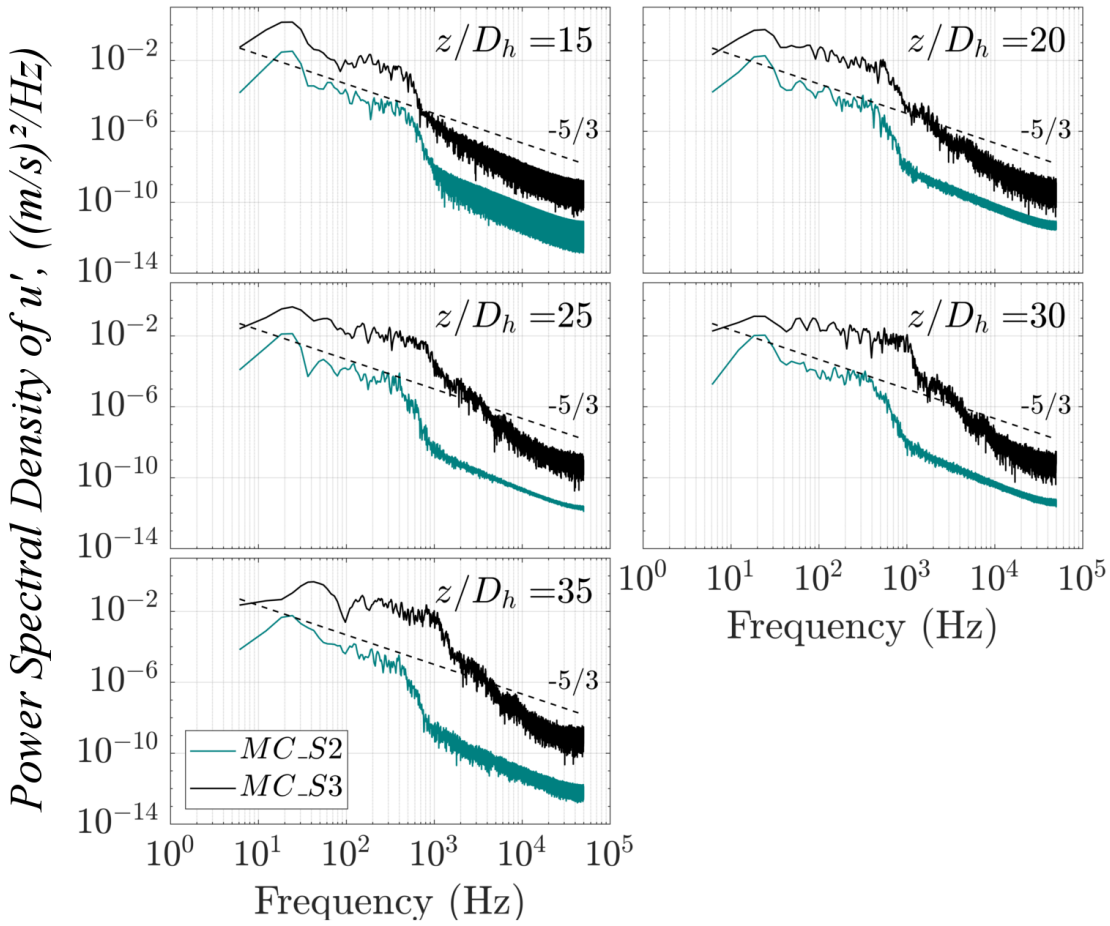

Figure 5.19: Power spectral density at NG in several locations for the small dimension cases.

5.2.4.3 Wide Gap

In Chapter 4, the existence of large flow structures in the wide gap was discussed. Such flow structures in the wide gap had also been found and investigated in previous studies [12,13,120,121]. The fluctuating spanwise velocity at BG is inspected at several locations in the heated section of the trapezoid annulus channel. The signals of the fluctuating spanwise velocity for all cases can be seen in Figure 5.20. No regular oscillations such as the one in the NG can be seen in all cases. Every case shows strong turbulent fluctuations. It also can be seen that as in the high-buoyancy cases of MC_L3 and MC_S3 has much higher noises. These results show that any flow structures that may be present in this region are relatively weak with turbulent noises dominated their existence in the time waveform. This is even worse in high-buoyancy cases.

To further identify the existence of the flow structures in the wide gap, the PSD of the u' at several locations monitored at the locations as aforementioned time histories of the fluctuating spanwise velocity are quantified. The PSD for cases with the larger dimension and the smaller dimension is again separated into two different figures (Figure 5.21 & Figure 5.22). In MC_L3, a small peak is identified early upstream before a reduction downstream (z/D_h>35). Meanwhile, in the smaller dimension, the production of regular dominant peaks is hardly visible, especially in MC_S3. While in MC_S2, some peaks are visible at z/D_h=15, 25&45. No significant peak can be observed in MC_S3. From the PSD results obtained, it is concluded that hardly any coherent structures are distinguished in the wide gap in all buoyancy cases.

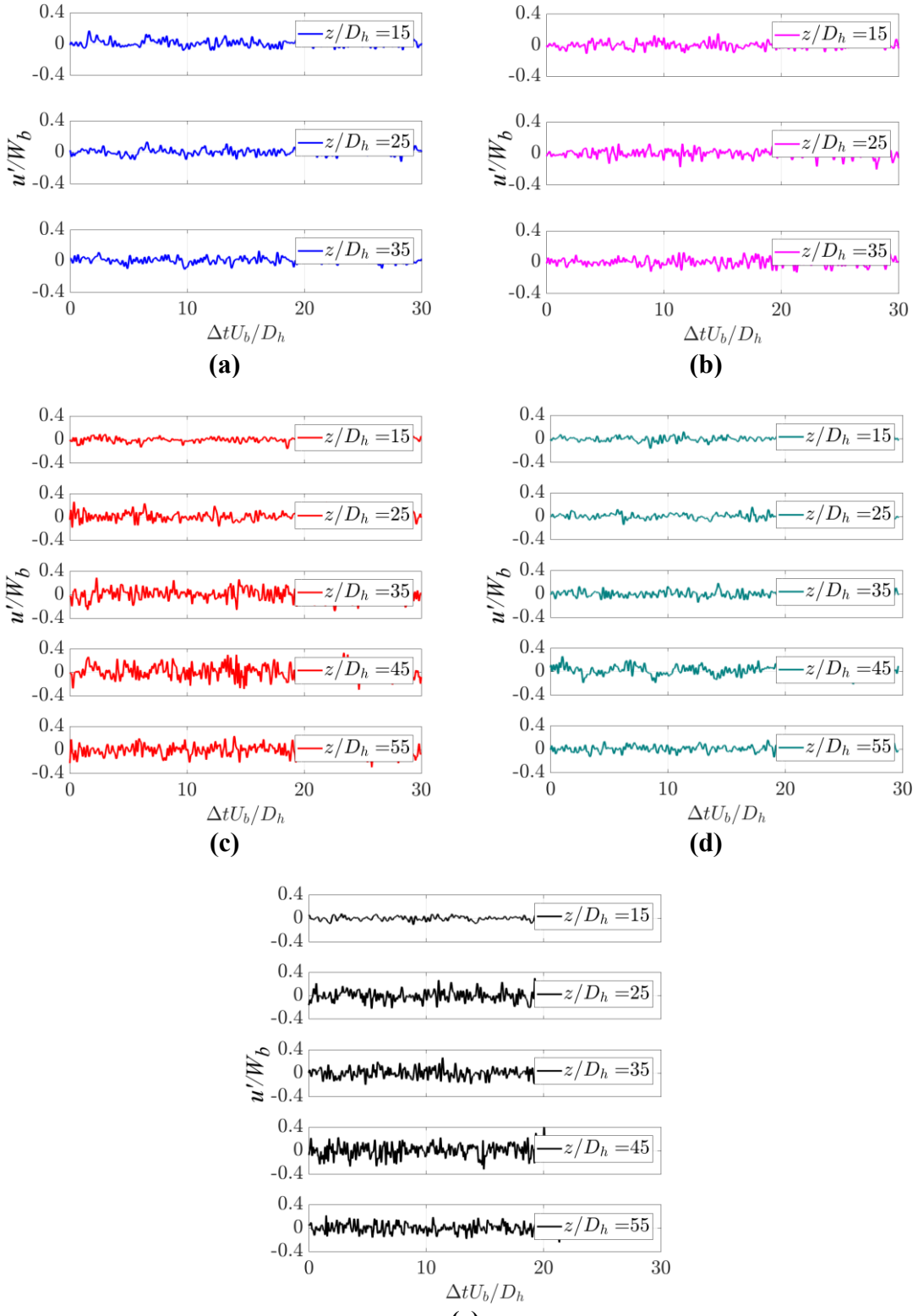

Figure 5.20: Time history for the spanwise velocity at BG down the heated channel. a) FC_L1 b) FC_L3 c) MC_L3 d) MC_S2 e) MC_S3

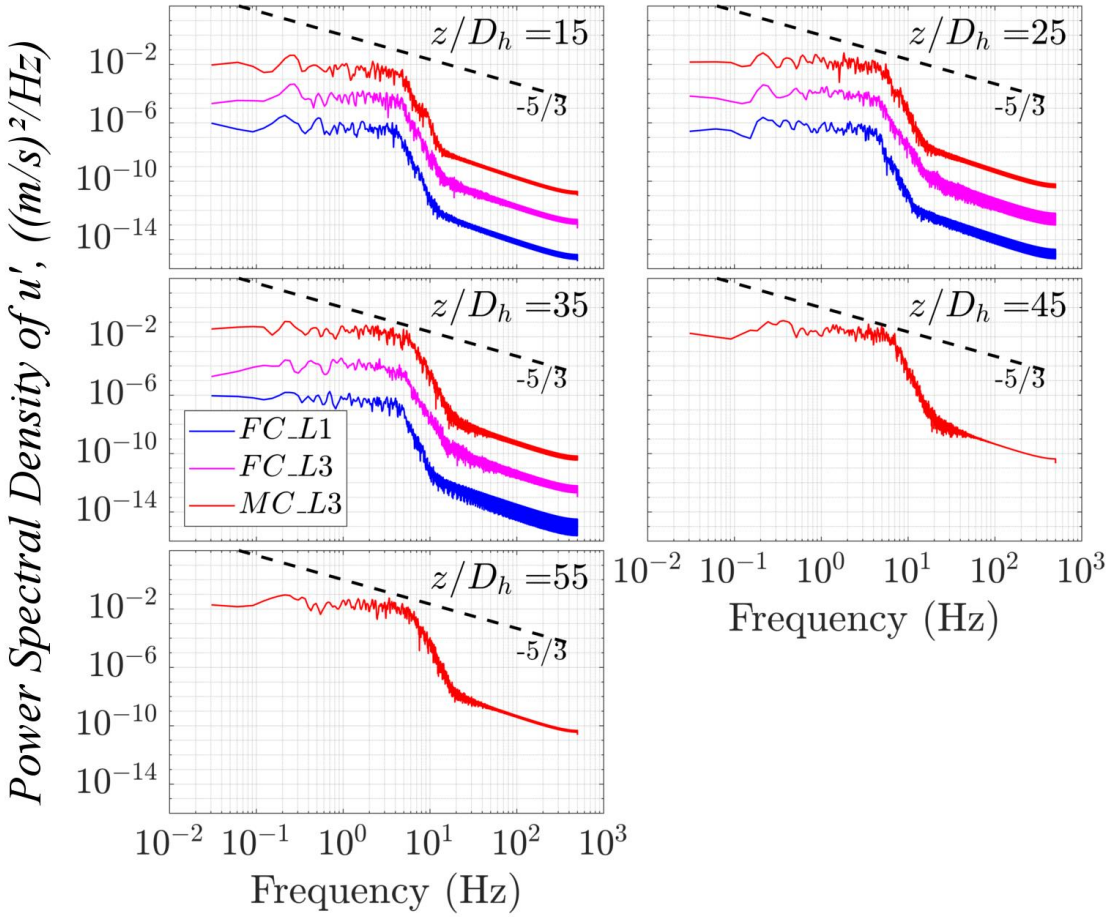

Figure 5.21: Power spectral density in the wide gap for the large dimension case.

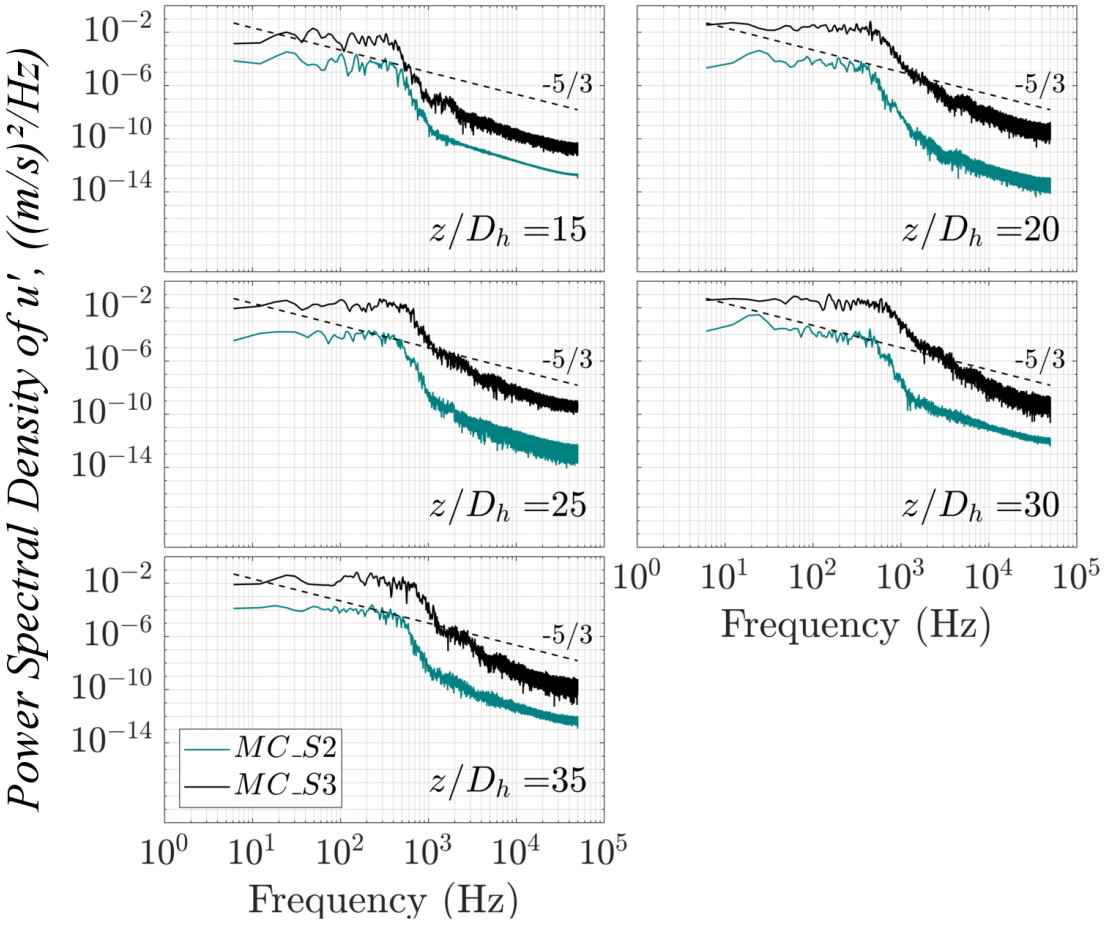

Figure 5.22: Power spectral density in the wide gap for the small dimension case.

5.2.4.4 Relationship between the Flow Structures at Different Locations

The relationship between the flow structures in the narrow gap and the wide gap is investigated by using the cross correlation function of the spanwise velocity at NG and BG. The correlations of the flows at these two gaps are presented in Figure 5.23. At the upstream locations of heating (z/D_h=15~25), the flow at NG case is correlated with BG inversely with 0s lags for every mixed convection. This suggests that at this location the flows in the two gaps are moving at the opposite direction suggesting a large flow structure is rotating around the central rod. This is true for MC_S2 along the entire heated length. For higher buoyancy cases MC_L3 and MC_S3, however, the correlations are shifted positively downstream with a larger shift in MC_L3, but the correlation is much weaker at z/D_h=45&55 in MC_S3. The above change in correlation may be due to the transition of the flow structures in high-buoyancy cases in the narrow gap. This can be explained by referring to the contour results in Figure 5.12 of the streamwise velocity where the velocity patches at the centre of the gap are shifted from the lowest across the plane to the highest at the centre of the narrow gap. A similar behaviour has been found by Duan & He [12] in their highest buoyancy case.

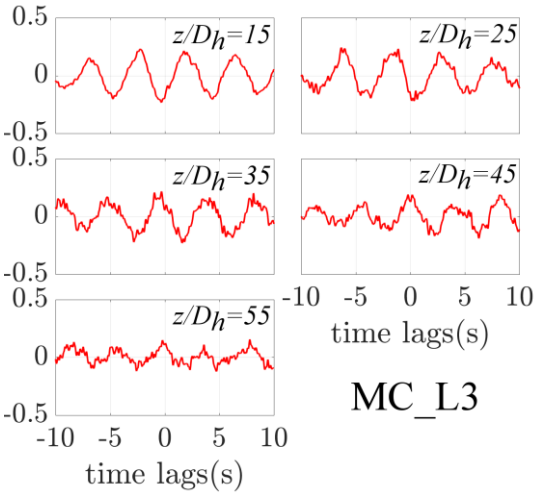

(a)

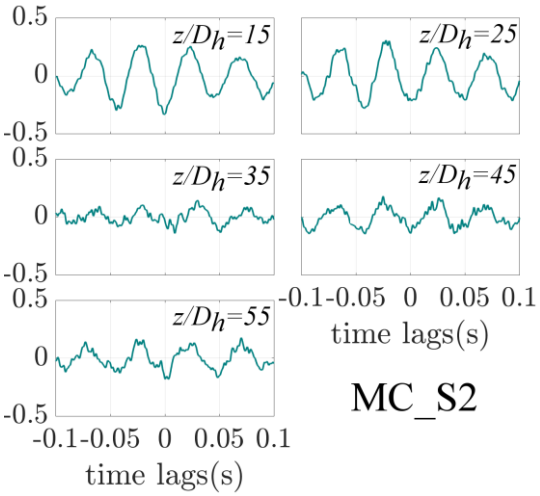

(b)

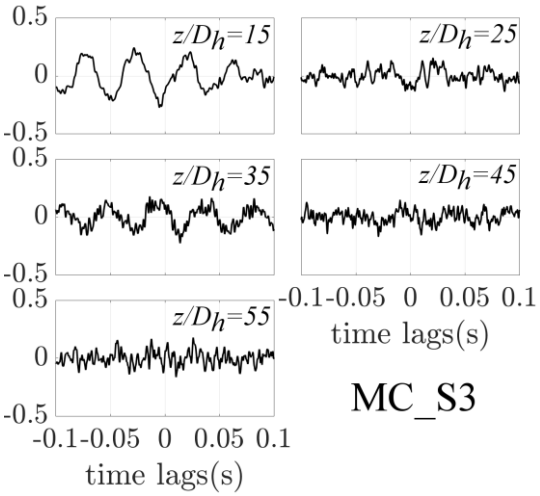

(c)

Figure 5.23: The cross correlation function of u' between NG and BG at different locations down the heated channel. a) MC_L3 b) MC_S2 c) MC_S3

5.2.4.6 Two-Point Correlations

The spanwise fluctuating velocity is a useful quantity in characterising the behaviour of the large flow structure. The scale of the flow structures can be determined by using the two-point correlations [138]:

$$R_{uu}(z, \mathrm{z} + \Delta \mathrm{z}) = \langle u'(z) u'(z + \Delta z) \rangle \qquad (5.13)$$

The axial scale of the flow structures is determined by the approximation of the cross-correlation of *u'* at several distances down the heated channel with a point near the heating inlet (z/D_h =12.5). The correlations for both gaps can be seen in Figure 5.24. It can be seen that the large flow structures in all mixed convection cases of the present study in the narrow gap are behaving similarly at the beginning of the heating channel. The wavelength of the flow structures is elongated further down the heated channel z/D_h>20. This is true for all cases, including the low-buoyancy case MC_S2 which is also elongated in comparison to the FC_L1. Meanwhile, in the wide gap, the peak of the correlation is dampened rapidly, especially for high-buoyancy cases. The pseudo-oscillations can only be visibly seen at the beginning of the heating. However, the disappearance of the peak in MC_S2 is found to be slower than in other cases.

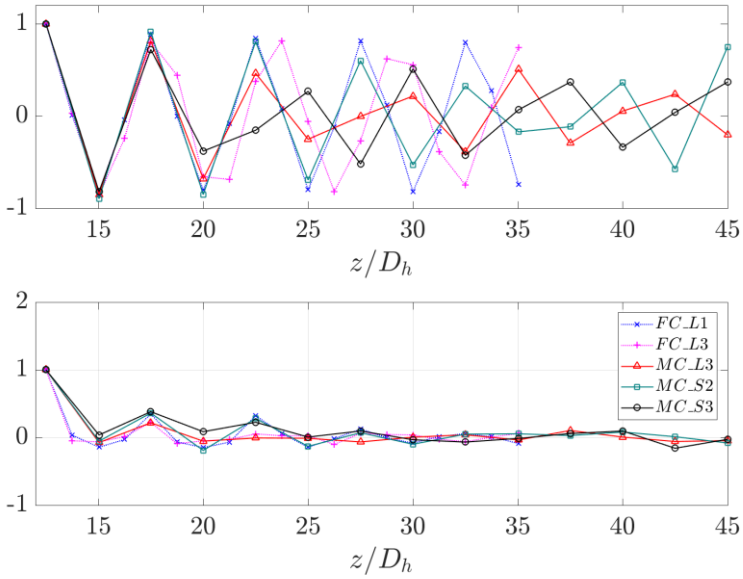

Figure 5.24: The cross correlation of u' at different locations down the channel in (Top) NG and (Bottom) BG.

5.2.5 Local Heat Transfer

To observe closer to the effect of the of the local flow structure to the behaviour of the heat transfer, the local wall temperature and local Nusselt number are investigated. The local Nusselt number (Nu_{loc}) is calculated as:

$$Nu_{loc} = \frac{h_{loc} D_h}{\lambda} \tag{5.14}$$

where h_{loc} is the average heat transfer coefficient which is determined from:

$$h_{loc} = \frac{q}{T_{w,loc} - T_b} \tag{5.15}$$

where q is the heat flux applied and $T_{w,loc}$ is the average wall temperature.

Figure 5.25 shows the local wall temperature and local Nusselt number of half of the

circumferential rod at several axial locations for all buoyancy cases. The axial locations presented here are at z/D_h =15,25,35,45&55. For the local wall temperature, the changes can be really seen much for the MC_L3 due to its very low heating. However, its Nusselt number changes a rather significant with a huge reduction at z/D_h =25, before it recovers down the channel with somewhat regular value across the circumferential location. While for the MC_S2, an overall increase of circumferential temperature can be seen lightly from z/D_h =15 to z/D_h =35 before it regulates down the channel. It is noted that the increase of temperature at the top half of the rod is a little higher at z/D_h =35. This results can be translated by its behaviour of Nusselt number change locally, where the Nusselt number is reduced from z/D_h =15 and reduced largely significant at z/D_h =35, especially at the top half of the channel. This suggests that the inexistent of the swinging flow structure may contribute to the heat deterioration largely locally in the channel.

For the buoyancy case, MC_S3, a similar trend as in MC_S2 can be seen in this case but with the high increase of temperature occurred earlier in the channel at z/D_h =25. The temperature increase at this location can be observed higher near the main channel and away from the gap region ($60<\theta<120$). This again can also be translated with a huge reduction of the Nusselt number at those areas which implies a large deterioration to the overall heat transfer at this axial location as observed in Figure 5.10 (b). The Nusselt number then can be seen to recover down the channel. It also noted that after the recovery, the Nusselt number in the wide gap is somewhat larger than that of in the narrow gap, which is opposite to the behaviour in the upstream part where the Nusselt number is higher in the narrow gap predominantly due to the swinging flow structure before it disappeared later downstream.

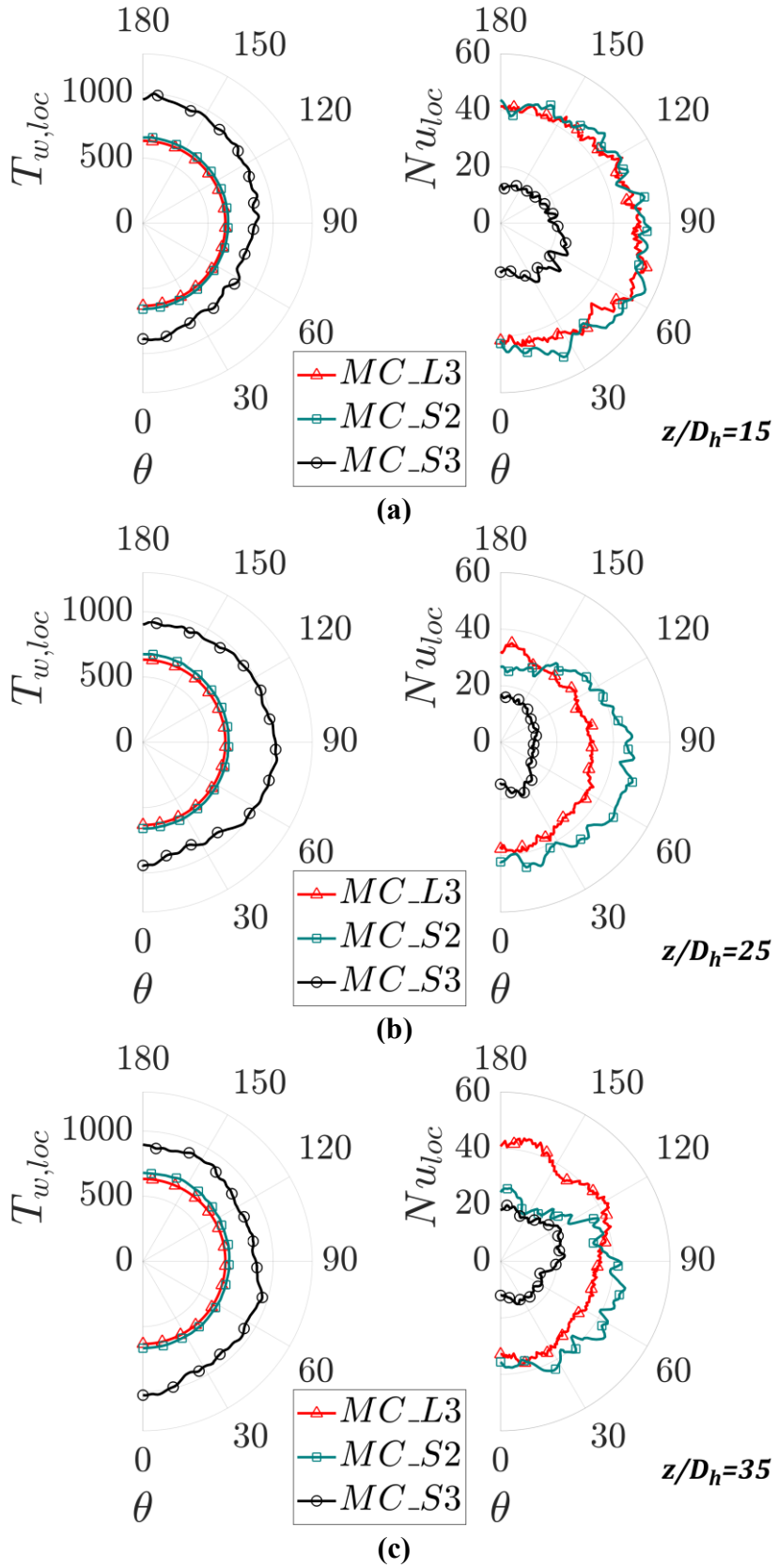

Figure 5.25: Local temperature and Nusselt number at several axial locations a) *z/D*$_h$ *=15* b) *z/D*$_h$*=25* c) *z/D*$_h$ *=35* d) *z/D*$_h$ *=45* e) *z/D*$_h$ *=55.*

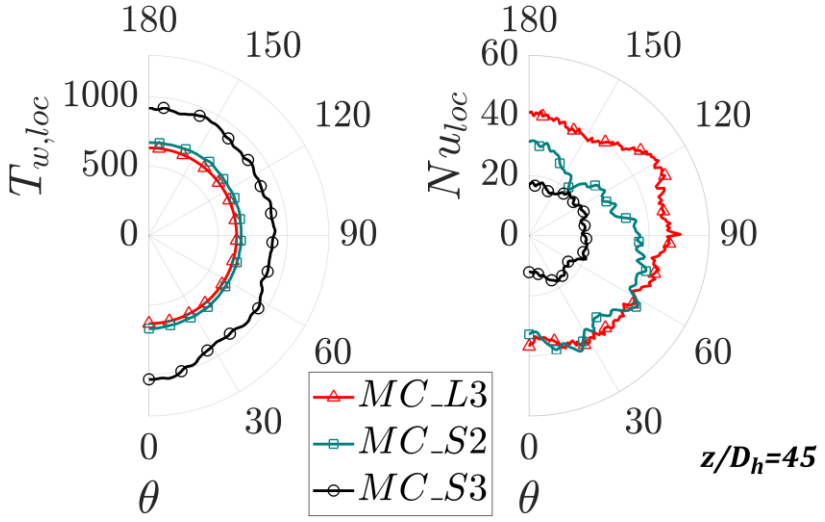
180
150
120
90
60
30
0
1000
500
0
$T_{w,loc}$
θ
60
40
20
0
Nu_{loc}
MC_L3
MC_S2
MC_S3
z/D_h=45

(d)

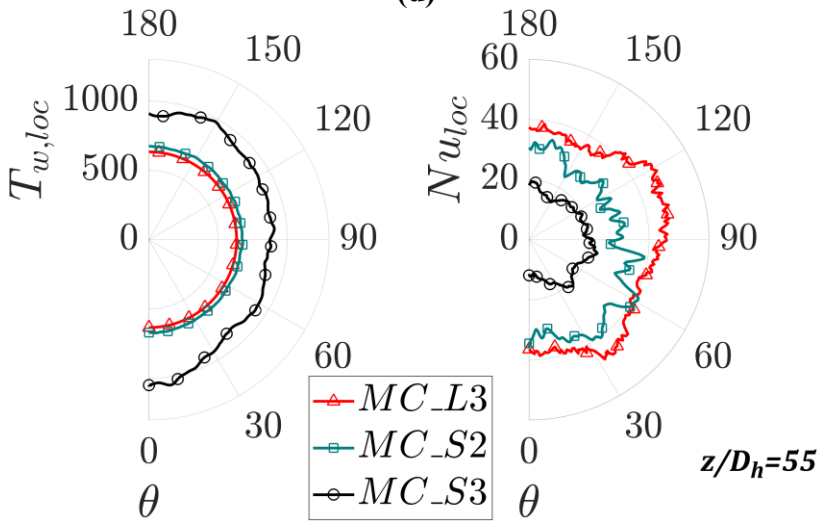
180
150
120
90
60
30
0
1000
500
0
$T_{w,loc}$
θ
60
40
20
0
Nu_{loc}
MC_L3
MC_S2
MC_S3
z/D_h=55

(e)

5.2.6 Mixing Factor

With the presence of swinging large flow structures in the narrow gap, the turbulence mixing between channels at either side of the gap can be significantly enhanced. Similar to the Chapter 4, both the mixing factor and the effective velocity are calculated to see their behaviour in the present cases. Details on how to calculate the parameters can be seen in §2.

The results of u_{eff} down the heated channel are presented in Figure 5.26 for both the narrow gap and wide gap. u_{eff} is normalized with the bulk streamwise velocity. Overall, u_{eff} decreases in the narrow gap down the heated channel for all cases. A monotonic decrease in u_{eff} in MC_S2 suggests a decrease in mixing down the heated channel. Meanwhile, the trend of u_{eff} for the high-buoyancy cases is rather complicated. It is noted that for MC_L3 and MC_S3, the rate of decrease for u_{eff} is about the same up to z/D_h=25. u_{eff} in MC_L3 then increases to about $10D_h$ before linearly decreases downstream. Meanwhile, MC_S3 shows a monotonic decrease of u_{eff} up to z/D_h=40 before a sudden jump in values downstream. Meanwhile, in the wide gap, the trend is irregular for u_{eff} in all cases. Only a significant increase may be observed for MC_L3 but with a sudden drop at z/D_h=50. A similar trend may also be seen for MC_S2 but with a lower magnitude. Meanwhile, u_{eff} in MC_S3 is largely irregular with a fluctuation of the magnitude throughout the heating channel.

The mixing coefficient, Y can be also calculated in the narrow gap and the result is presented in Figure 5.27. The trend of mixing coefficient down the heated channel is typically the same with u_{eff} as Y is a function of u_{eff}. It can be observed that the value of Y for MC_S2 dropped from 163 to 68, and for MC_L3 the value ranges down from 139 to 56. Meanwhile, MC_S3 has the lowest value of Y at 25 in the middle of the heated channel. These reduced values at the downstream section in the present study are much lower than the value of forced

convection cases presented in Chapter 4. The current values of Y are about half those of the forced convection cases. This is consistent with the observations in the study of Duan & He [12]. In their highest buoyancy case, the value of Y is also about half of that of their forced convection case.

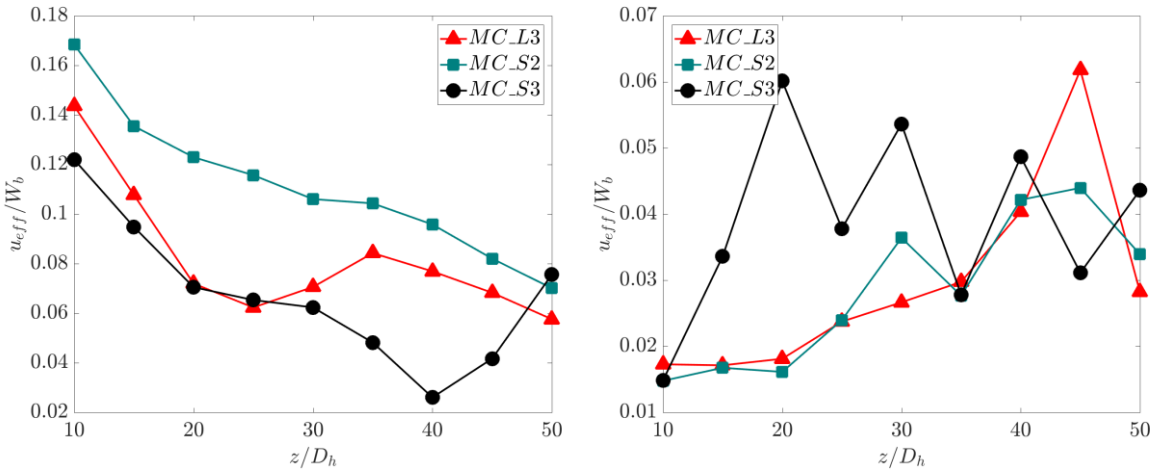

(a) **(b)**

Figure 5.26: u_{eff}/U_b down the heated channel at a) NG and b) BG.

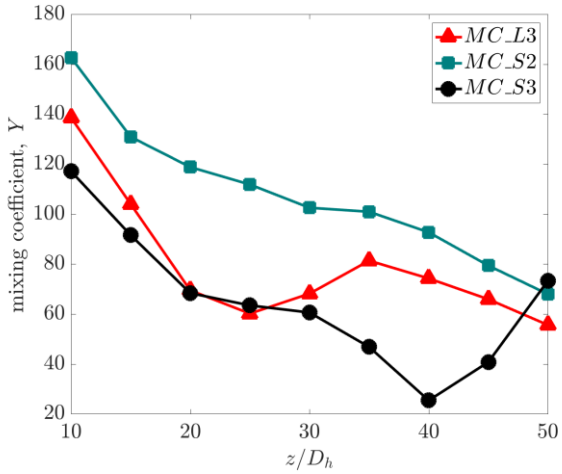

Figure 5.27: Mixing coefficient, Y down the heated channel at NG.

5.2.7 Turbulent Quantities

The effects of the buoyancy of the supercritical water on the flow and turbulent statistics of the flow field are further investigated. In this section, the statistics of flow field and turbulent quantities at several channel locations will be discussed for each case. Note that only half of the channel is shown for the distribution of the results in the cross-section due to the symmetrical configuration of the present trapezoid annulus.

Due to the strong density variations that are involved in the heating of the supercritical water, a Favre-averaging is used. The Favre-average is also referred to as the density-weighted average. The Favre-averaged variable is denoted as $\tilde{\phi}$ and is calculated as follows:

$$\tilde{\phi} = \frac{\langle \rho \phi \rangle}{\langle \rho \rangle} \tag{5.16}$$

where its fluctuation can be calculated as

$$\phi'' = \phi - \tilde{\phi} \tag{5.17}$$

5.2.7.1 Mean Flow Field

Figure 5.28 shows the general distribution of the normalized Favre-averaged streamwise velocity for all mixed convection cases. It can be seen that there is a clear difference between the low-buoyancy case and the higher buoyancy cases. The velocity in MC_S2 shows very little redistribution across the channel down the heating channel. By contrast, in MC_L3 and MC_S3, the high-velocity patches are distributed closer to the heating rod wall as downstream of the heated section. In addition, it can also be seen that the flow is also redistributed to both gaps especially to the narrow gap in both of the high heating cases (z/D_h=40&55). By contrast, the velocity in the narrow gap of MC_S2 is maintained low. This agrees with the results that have been observed earlier in Figure 5.12.

Some velocity profiles are plotted across the channel at several locations down the heated channel to observe the mean streamwise velocity distributions more closely. Velocity profiles are plotted along four lines at the channel cross-section, namely NL, BL, ML and MC, which respectively are located along the narrow gap region, the wide gap region, normal to the rod wall towards the main channel and across the narrow gap (as in Figure 5.2(a)). Note that $y/y_{max} = 0$ is at the heating rod wall for NL, BL and ML, while for MC it is at the centre of the narrow gap. $y/y_{max} = 1$ is at the outer adiabatic wall for NL and BL, while it is at the centre of the channel for ML and MC.

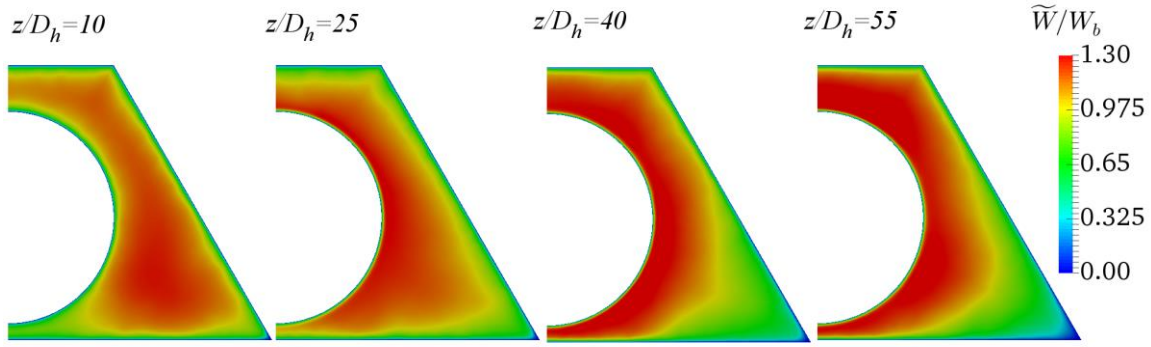

(a)

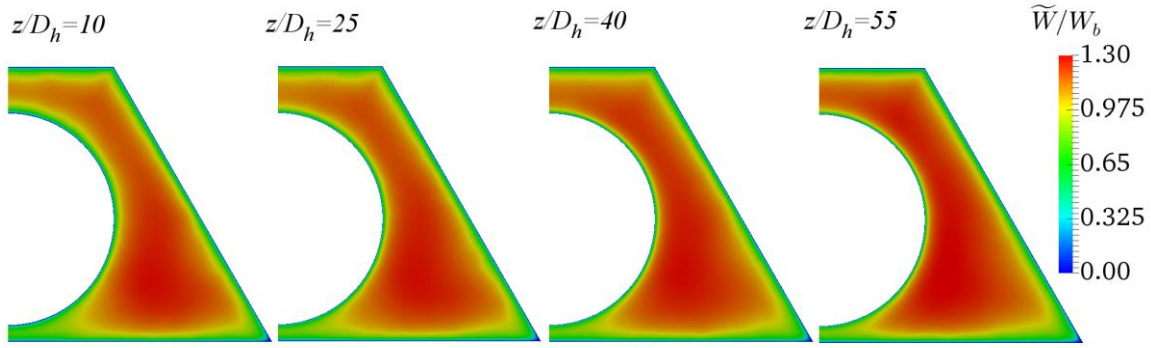

(b)

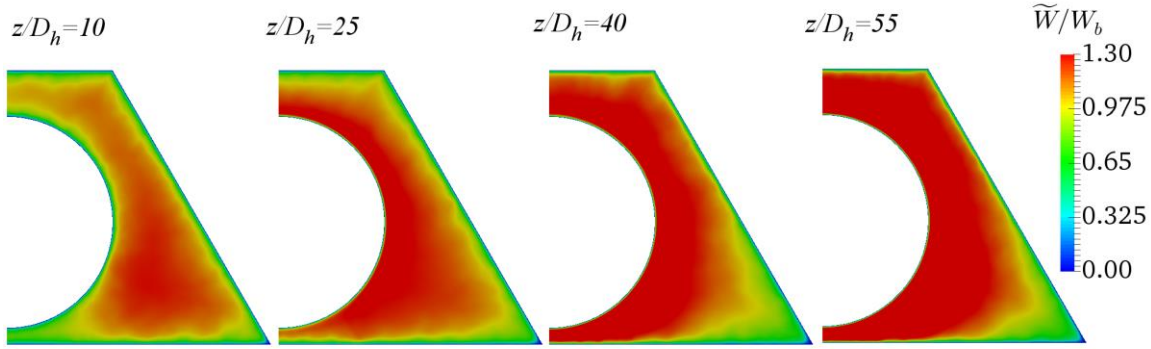

(c)

Figure 5.28: The distributions of the normalized Favre-averaged streamwise velocity $\tilde{W}/W_b$ in the cross-section of the channel. a) MC_L3 b) MC_S2 c)MC_S3

The velocity profiles at several axial locations can be seen in Figure 5.29. Along NL it can be seen that the velocity profiles are parabolic in the forced convection and MC_S2. The velocity is increased significantly down the heated channel in MC_S3 and MC_L3 (stronger in former). In these two cases, the velocity profiles can be seen to accelerate at z/D_h>20. The velocity increases more strongly near the heated rod wall, hence, the profiles are skewed towards the bottom in these two cases. Such velocity profile transformation is stronger in MC_S3 than in MC_L3.

In the wide gap, the velocity profiles for all cases as illustrated in Figure 5.29(b) show a typical turbulent profile. In all the mixed convection cases, the velocity increases near the heated wall due to the thermal expansion and/or buoyancy effect. The overall velocity profiles of MC_L3 and MC_S3 accelerate the strongest. They show a half-M-shaped velocity profile as in a buoyancy aided pipe flow. Meanwhile, the velocity profile in MC_S2 does not change as much downstream. The same trend can be seen in Figure 5.29(c) for the profiles along ML. The typical turbulent profiles are shown in all cases with that MC_L3 and MC_S3 producing a half M-shape profile further downstream.

Considering the velocity distribution across the narrow gap along MC, the profiles for all cases can be seen in Figure 5.29(d). At the start of the heating inlet, the velocity distributed high in the main channel ($y/y_{max} = 1$) and low in the narrow gap ($y/y_{max} = 0$). Moving down the heated channel, the profiles are maintained in MC_S2 while changes occur in both of high-buoyancy cases. At z/D_h=20, both MC_L3 and MC_S3 have almost zero velocity gradient along MC. This occurs as the flow in the narrow gap accelerates and the velocity in the main channel reduces in relative term. The velocity in the narrow gap is further accelerated downstream in both cases.

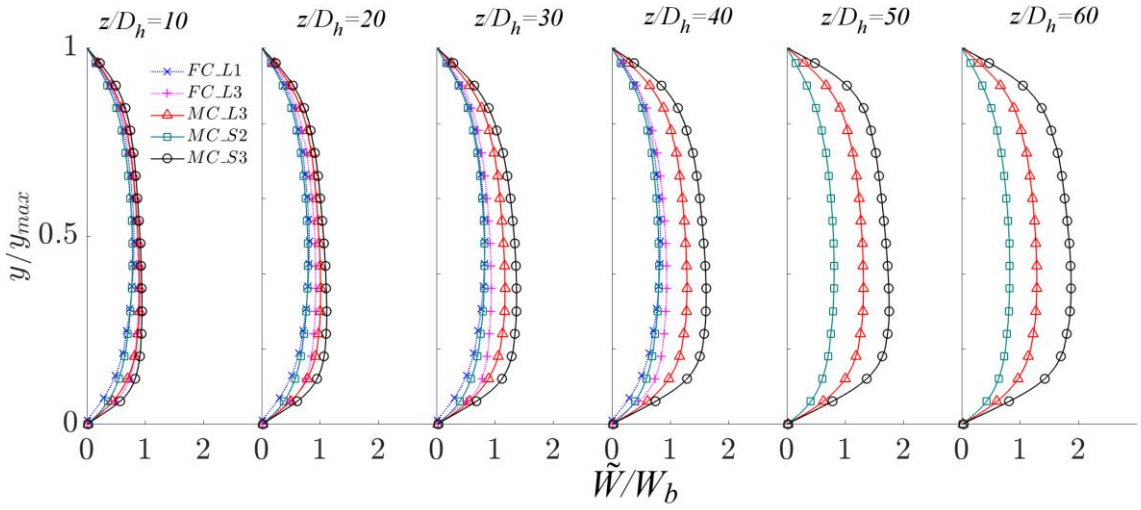

(a)

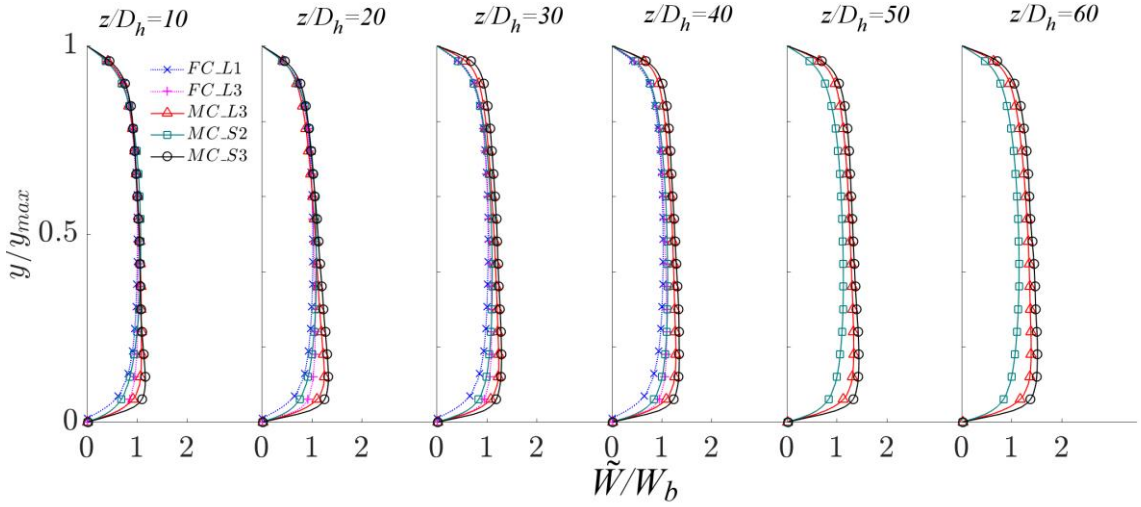

(b)

Figure 5.29: Profiles of normalized Favre-averaged streamwise velocity, $\tilde{W}/W_b$ along a) NL b) BL c) ML d) MC.

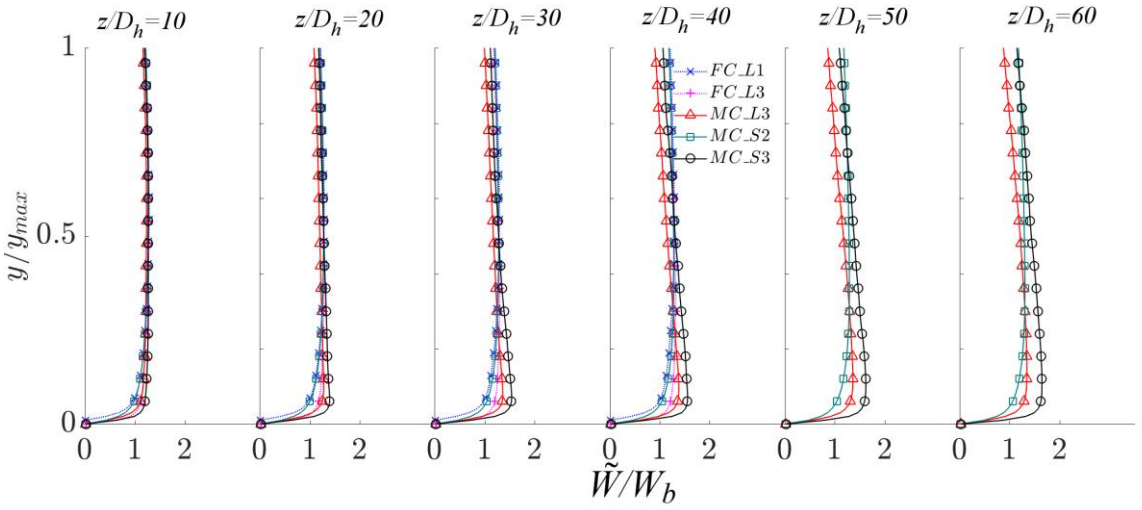
z/D_h=10
z/D_h=20
z/D_h=30
z/D_h=40
z/D_h=50
z/D_h=60
FC_L1
FC_L3
MC_L3
MC_S2
MC_S3
y/y_max
W̃/W_b

(c)

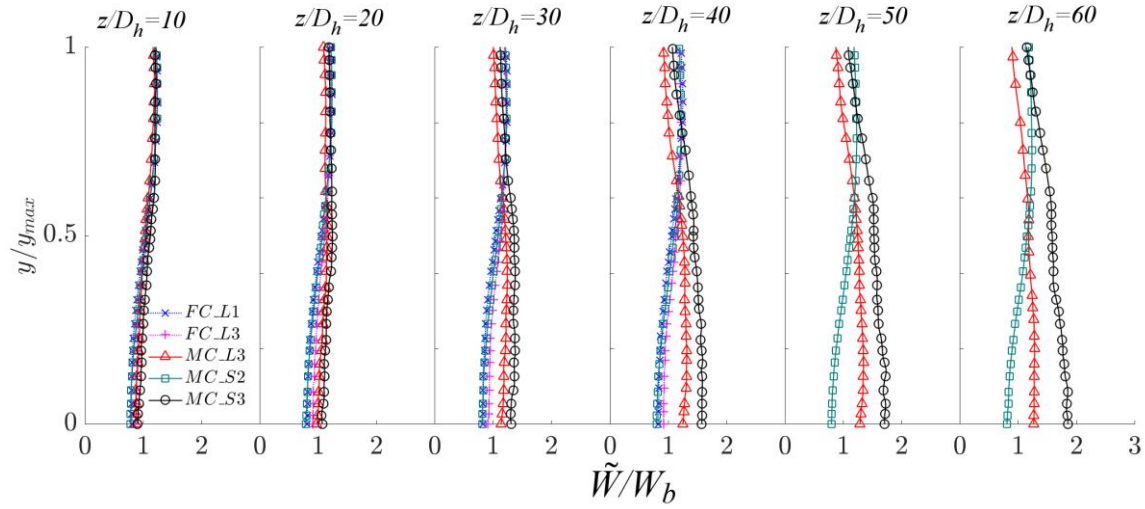
z/D_h=10
z/D_h=20
z/D_h=30
z/D_h=40
z/D_h=50
z/D_h=60
FC_L1
FC_L3
MC_L3
MC_S2
MC_S3
y/y_max
W̃/W_b

(d)

5.2.7.3 General Distributions of Turbulent Quantities

The streamwise and spanwise components of the turbulent intensity and the total turbulent kinetic energy will be studied in this section. The distributions along several locations of the channel cross-sections are presented. The contributions of each element to the general flow will be discussed below.

The distributions of the turbulent intensity of the streamwise component of all cases are presented in Figure 5.30. It is noted that the general trends in the low buoyancy and higher buoyancy cases are significantly different. In MC_S2, the streamwise turbulent intensity shows an increase down the heated channel throughout the cross-sections. In particular, high-value patches can be seen to be located near walls as well as in the narrow gap (z/D_h=55). By contrast, in for MC_L3 and MC_S3, the streamwise turbulence intensity is reduced first in the main channel at some distances in upstream section (z/D_h=25). The streamwise intensity is then increased further down the heated channel, especially high at the location near the wall. A higher value patch can also be seen appearing at the top corner of the trapezoid channel in MC_L3. The reduction in turbulence intensity in the upstream section of the heated rod is the cause of the heat transfer deterioration occurring in this location. Heat transfer recovers further downstream which coincides with the increase of turbulence there.

In Figure 5.31, the distributions of the spanwise turbulent intensity down the heated channel in the channel cross-sections are presented for all cases. Overall, an increase in the intensity across the channel can be identified in the high-buoyancy cases down the heated channel, whereas not much changes are seen in MC_S2. In the latter, the distribution of the spanwise turbulence intensity does not change, except for a little increase in the values near the outer adiabatic walls. It can be noted that there is a high-value patch at the start of heating

(z/D_h=10) in the narrow gap for all mixed convection cases. This high-value patch is disappearing rapidly in MC_L3 and MC_S3 downstream, whereas only a little delay occurs in MC_S2. It should also be noted that a new high-value patch re-occurs in the narrow gap later down the channel (z/D_h=55). This is probably related to the transformation of the swinging flow structure in the narrow gap after the heat transfer deterioration in this high-buoyancy case.

The normalized total turbulent kinetic energy, $\tilde{k}/W_b^2$ is presented in Figure 5.32 at several distances down the heated channel for the mixed convection cases. Note that $\tilde{k}$ is calculated as $\tilde{k} = \frac{1}{2}\langle u_i'' u_i'' \rangle$, where u_i $(i = 1,2,3)$ are the velocity components in spanwise, wall-normal and streamwise directions respectively.

The distributions of the total turbulent kinetic energy also show a clear difference in the low-buoyancy case and the high-buoyancy cases. In the low-buoyancy case (MC_S2), the turbulent kinetic energy does not change much down the channel. However, the kinetic energy is increased near the heating rod wall and in the narrow gap. The development of the turbulent kinetic energy in the narrow gap downstream is largely due to the increase of the streamwise turbulence intensity in this region as observed earlier in Figure 5.30 (b). This behaviour is also true for the high-buoyancy cases, where the total turbulent kinetic energy in the narrow gap is largely dominated by the streamwise turbulence intensity. From this result, it shows that the swinging flow structures that are present in the narrow gap do not contribute much to the total kinetic energy in this region in the buoyancy-aided flow, even though the contribution of such structure to the can be demonstrated from the spanwise turbulence.

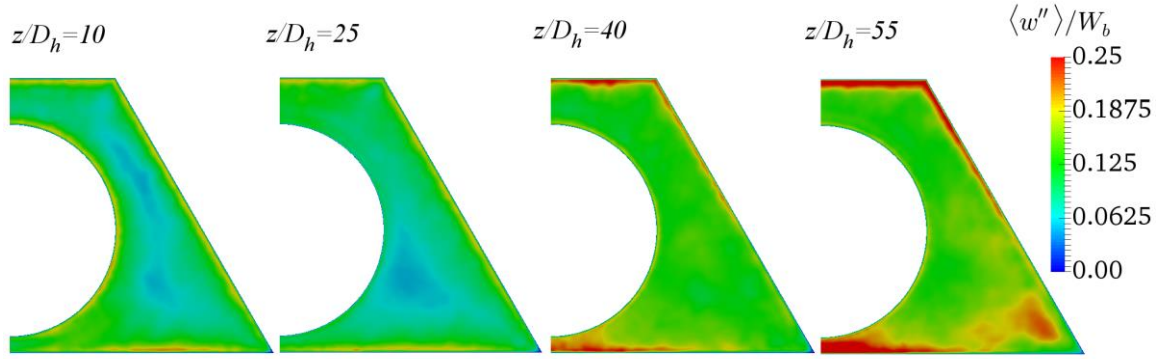

(a)

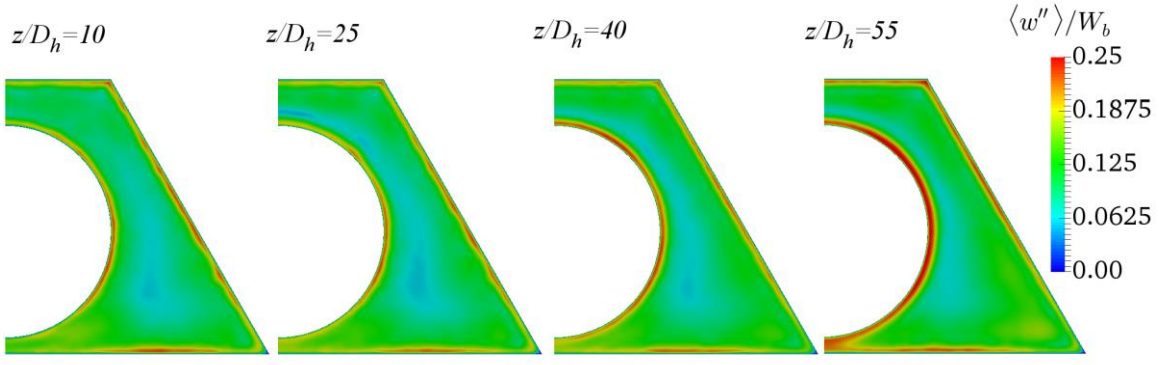

(b)

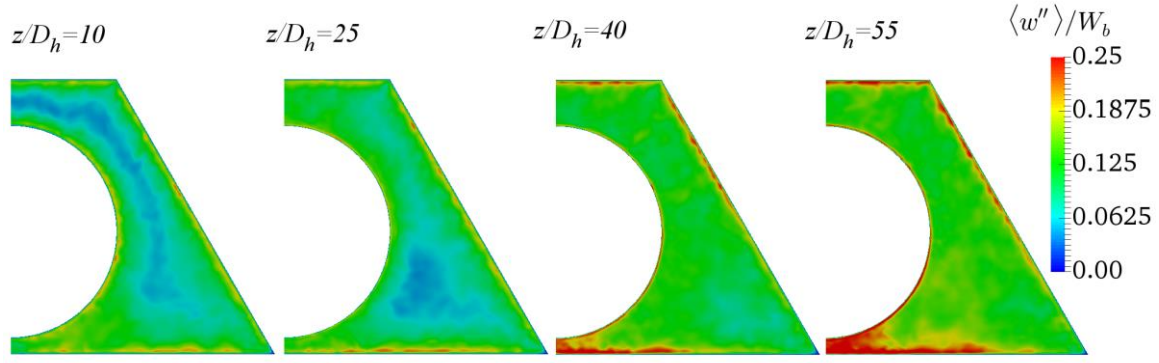

(c)

Figure 5.30: The distributions of the normalized streamwise turbulent intensity $\langle w'' \rangle / W_b$. a) MC_L3 b) MC_S2 c)MC_S3

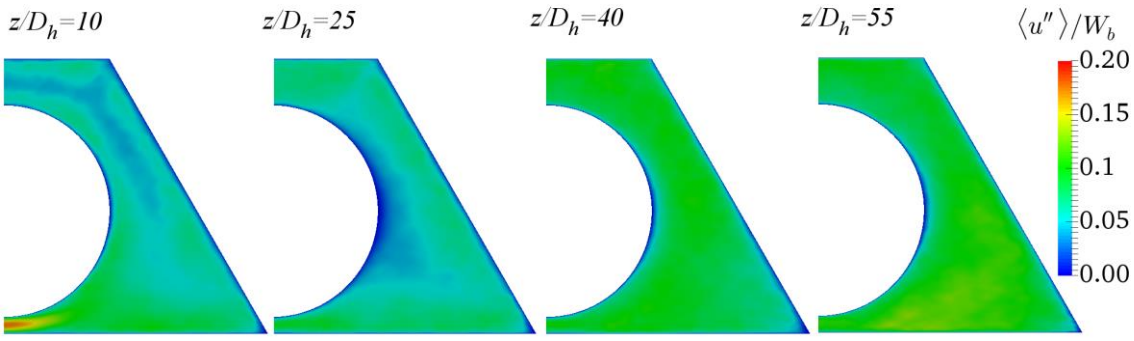

(a)

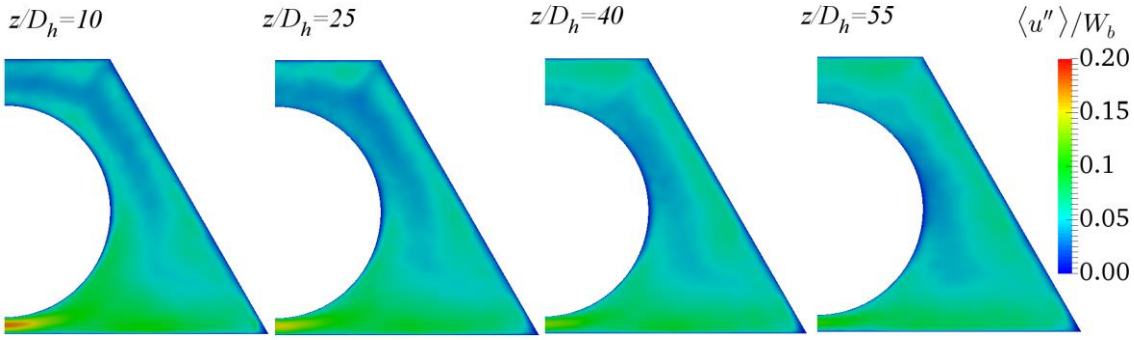

(b)

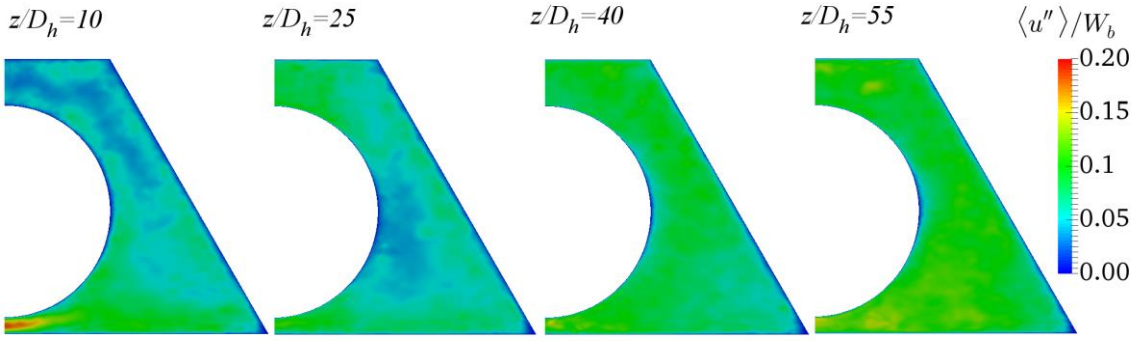

(c)

Figure 5.31: The distributions of the normalized spanwise turbulent intensity $\langle u'' \rangle / W_b$. a) MC_L3 b) MC_S2 c)MC_S3

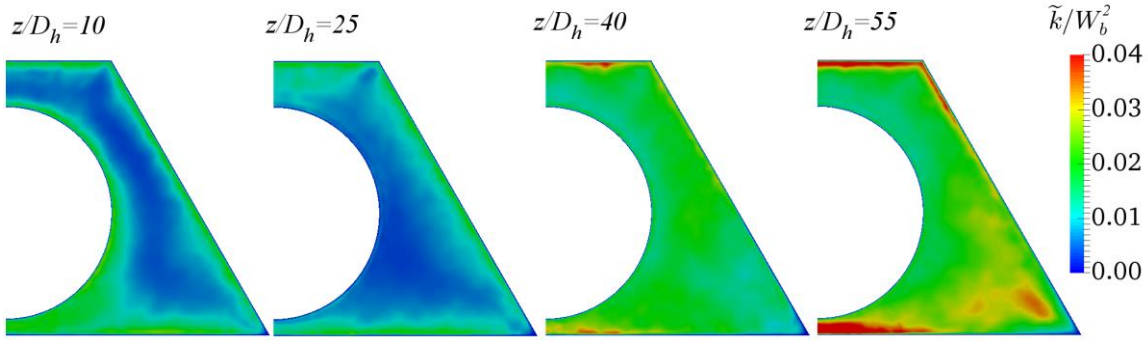

(a)

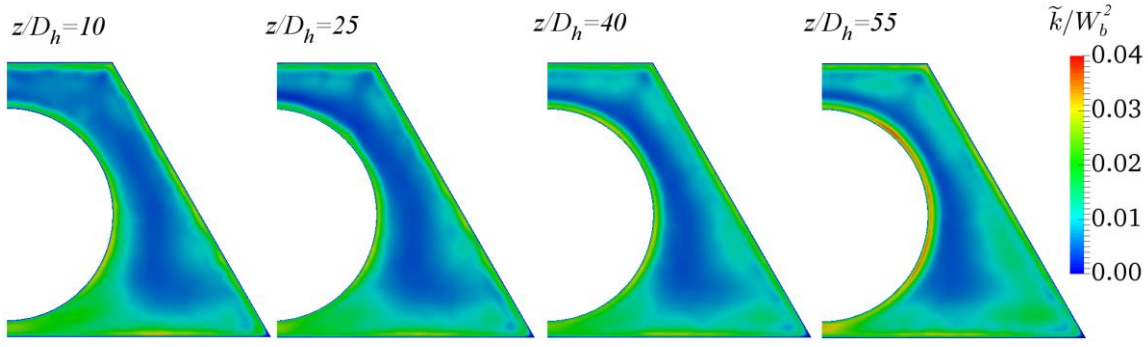

(b)

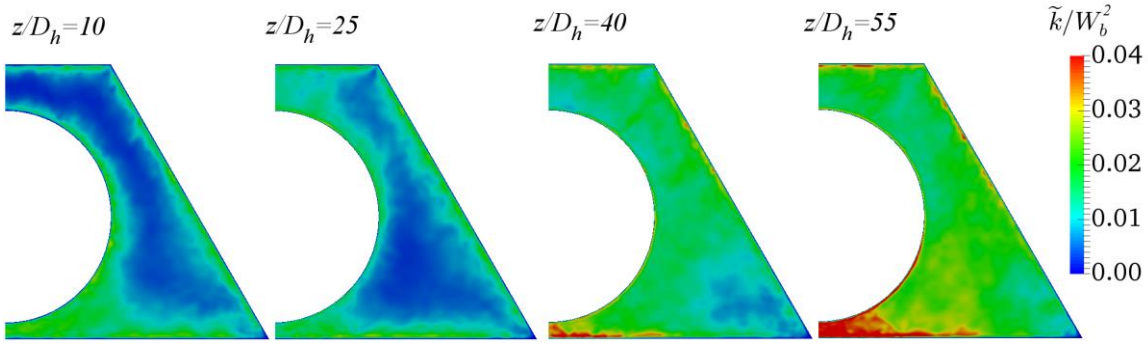

(c)

Figure 5.32: The distributions of the normalized turbulent kinetic energy $\widetilde{k}/W_b^2$. a) MC_L3 b) MC_S2 c)MC_S3

5.2.7.5 The Turbulent Quantities Profiles across the Channel

To investigate the distribution of turbulent quantities across the channel more closely, profiles are plotted at four lines that have been used for the statistics of the mean flow earlier. Figure 5.33 shows the profiles of turbulent quantities along NL in the narrow gap.

Consider the region close to the heated rod wall first. At the start of the heated section (z/D_h=10, 20), the streamwise turbulence (w'') is similar in all cases except in case MC_S2, where w'' is higher than in the other cases. The shape of w'' maintains largely the same and the amplitude increases slowly but steadily in this case (MC_S2). For case MC_L3, w'' is initially lower than in MC_S2, but catches up with it at z/D_h=30, and maintains a similar value as in MC_S2 at later stations. For case MC_S3, again w'' is somewhat slightly lower than in MC_S2 initially, but it increases rapidly and becomes much greater than in any other cases at the end (z/D_h=60). The shape is also different, exhibiting a peak in the wall region.

The streamwise turbulence (w'') in the adiabatic-wall region of the narrow gap is very similar in all the cases initially (z/D_h=10, 20). Downstream, w'' increases steadily and strongly in the two strong buoyancy-influenced cases (MC_L3 & MC_S3). The behaviour of w'' in the narrow gap described above is clearly very complex, and largely influenced by buoyancy. Another important contributor is the redistribution of mass flow to this region as described earlier. The local velocity and *Re* are higher in this region downstream (see Figure 5.29 (a)), which also contribute to increase turbulence there.

The transverse turbulence component (u'') consists of the conventional turbulence and that due to the large flow structures discussed earlier. This turbulence (u'') is similar at the initial station (z/D_h=10) in all mixed convection cases. It reduces significantly at z/D_h=20 and maintains at this level at later stations in the two strong-buoyancy cases (MC_L3 &

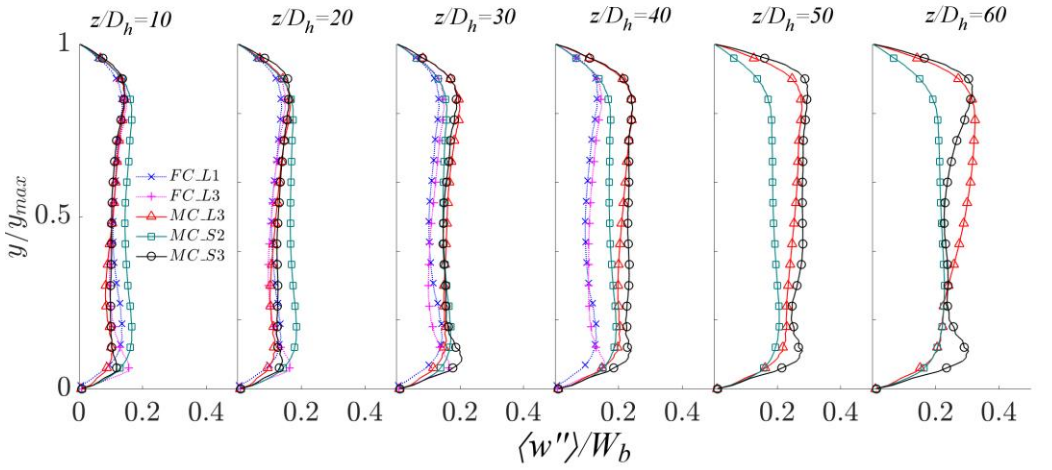

(a)

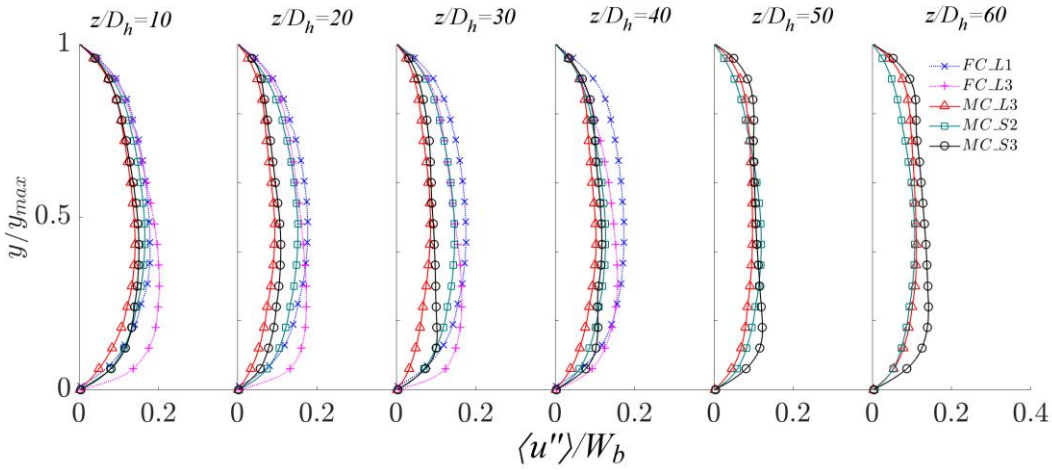

(b)

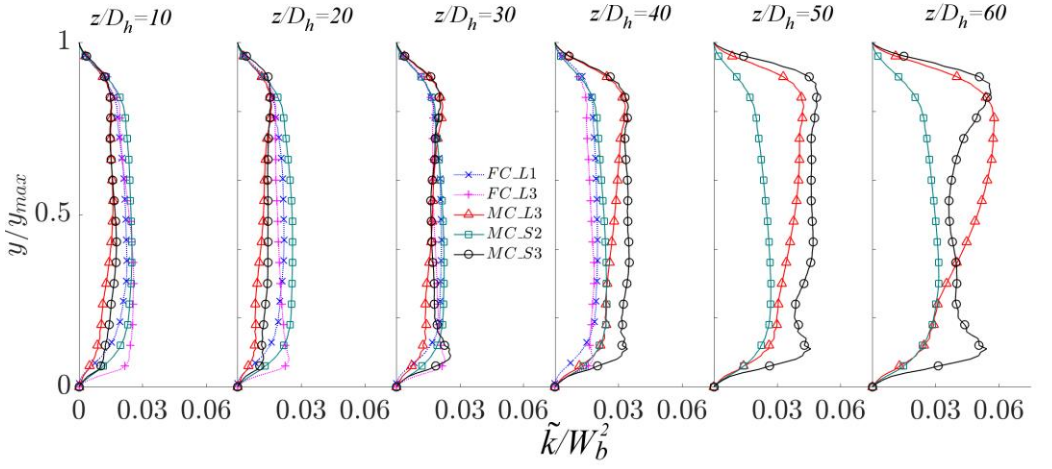

(c)

Figure 5.33: Profiles of turbulent components along NL a) $\langle w'' \rangle / W_b$ b) $\langle u'' \rangle / W_b$ c) $\tilde{k}/W_b^2$.

MC_S3), except that in MC_S3, the u'' tends to be higher close to the heated wall, and it much higher at the last station (z/D_h=60), which may be linked to the high w'' there. The u'' in the weaker buoyancy case MC_S2 also reduces downstream, but a much slower pace, only reaching the same low level at z/D_h=40. The above reduction in u'' is largely related to the reduced large flow structures in the mixed convection cases, even though the "conventional" turbulence case varies, probably in a manner similar to w''.

The distribution of the total turbulent kinetic energy ($\tilde{k}$) is naturally dependant on the sum of its components, reflecting both the conventional turbulence and the large flow structures. The values are particularly different in the different cases towards the downstream stations (z/D_h=50, 60). Near the adiabatic wall, the turbulent ($\tilde{k}$) is much higher in the two high-buoyancy cases (MC_L3 & MC_S3). Close to the heated wall, however, $\tilde{k}$ in MC_L3 is much lower, at a value similar to that in MC_S2. The difference between $\tilde{k}$ in the heated/unheated regions is likely due to the influence of buoyancy and the largest difference occurs in MC_L3. It is likely that MC_S3 experienced a relatively strong recovery as far as buoyancy is concerned.

Figure 5.34 shows profiles of turbulent components along BL in the wide gap at several axial locations for all cases. Typical wall shear flow characteristics can be seen for the streamwise turbulence intensity in all cases. However, the profiles for the spanwise turbulence intensity are quite different. MC_L3 and MC_S2 profiles are rather flat across the gap unlike in forced convection case FC_L3. The presence of subtle peaks, however, can also be seen in MC_S3 suggesting an effect of strong heating causing large variations of properties in the flow (as in FC_L3). For the streamwise turbulence, the peaks for all mixed convection cases differ from each other. A smaller and lower peak can be seen for MC_L3

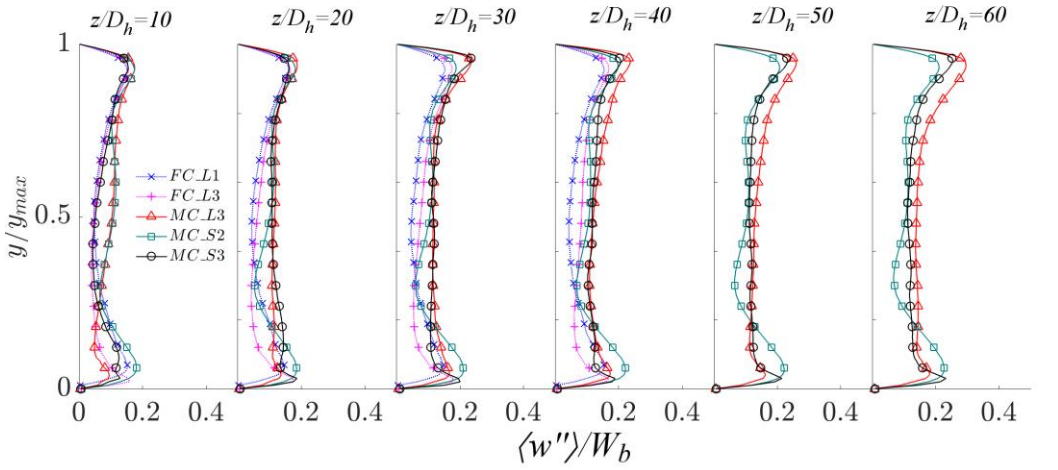

(a)

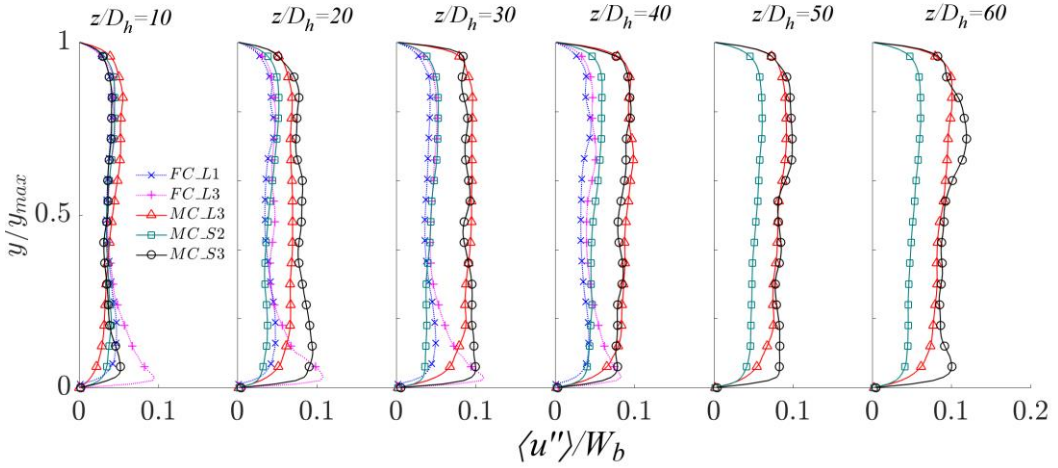

(b)

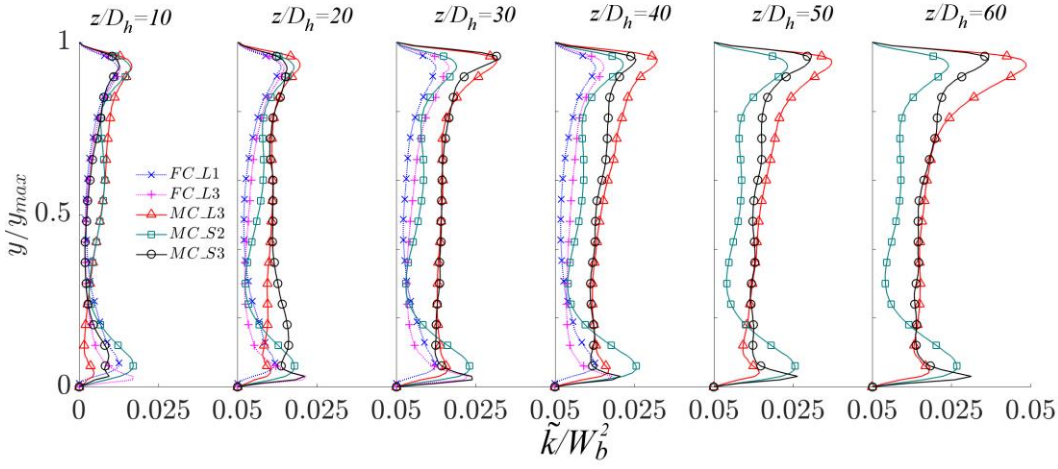

(c)

Figure 5.34: Profiles of turbulent components along BL a) $\langle w'' \rangle / W_b$ b) $\langle u'' \rangle / W_b$ c) $\tilde{k}/W_b^2$.

in the heated wall. Yet it achieves the highest peak near the unheated wall ion this case. The w'' has a sharp peak close to the heated wall in MC_S3, even though the value of the peak is mostly lower than in MC_S2. In all cases, the overall turbulence ($\tilde{k}$) increases significantly in the heated section, both in the heated and unheated wall regions. The increase is, however, stronger in the unheated wall region. In addition, the $\tilde{k}$ in MC_L3 is the highest of all cases near the unheated wall but lowest of all cases near the heated wall. Again, the differences near the two-walls are largely due to buoyancy.

In Figure 5.35, typical wall shear flow characteristics can again be observed for all cases near the wall along ML. A reduction can be seen in the turbulence intensities near the heating inlet along in high-buoyancy cases (as seen in the wide gap). These turbulence intensities then increase downstream. The spanwise turbulence for all cases is flat in the core region with a comparable magnitude between the high-buoyancy cases. The total kinetic energy is dominated by the streamwise turbulence component. MC_L3 has the lowest peak near the wall and MC_S3 has the highest peak, while the peak in MC_S2 is maintained unchanged from the start of heating which is also the case in the streamwise component (w'').

Lastly, the turbulent quantities along MC in the narrow gap are studied. It can be seen that the in high-buoyancy cases, the turbulence intensities are small at the upstream stations ($z/D_h \leq 30$) but increase downstream. MC_S2 shows a higher streamwise turbulence intensity and a lower spanwise turbulence intensity in comparison to the forced convection cases in the narrow gap. This is true and maintained down the heated channel, where the resultant total turbulent kinetic energy of MC_S2 is also lower than those of both of the forced convection cases (FC_L1 and FC_L3) in the narrow gap, while it has a comparable magnitude towards the main channel (i.e., $y/y_{max} \sim 1$). In high-buoyancy cases, the

magnitude of the turbulence intensities is comparable to that in the forced convection cases, initially (z/D_h=10), but increases down the heated channel for the streamwise component and reduced in the spanwise component in the narrow gap (i.e., $y/y_{max} < 0.5$). The streamwise turbulence intensity dominates the turbulent kinetic energy along MC, which also shows a reduction in magnitude near heating inlet before recovering down the heated channel.

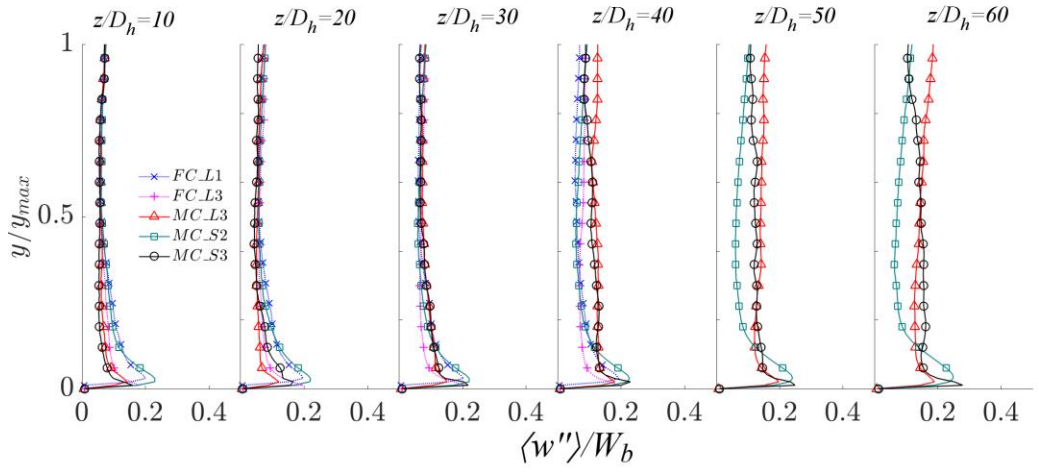

(a)

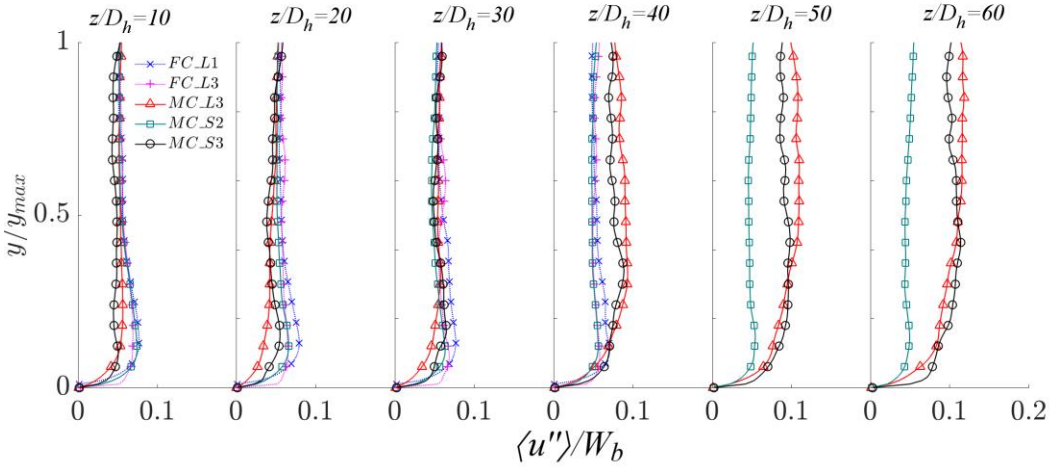

(b)

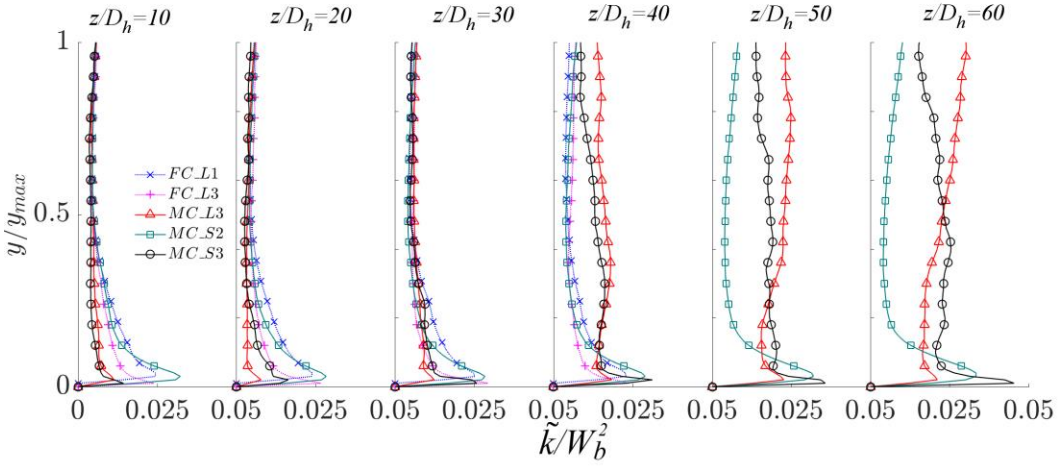

(c)

Figure 5.35: Profiles of turbulent components along ML a) $\langle w'' \rangle / W_b$ b) $\langle u'' \rangle / W_b$ c) $\widetilde{k}/W_b^2$.

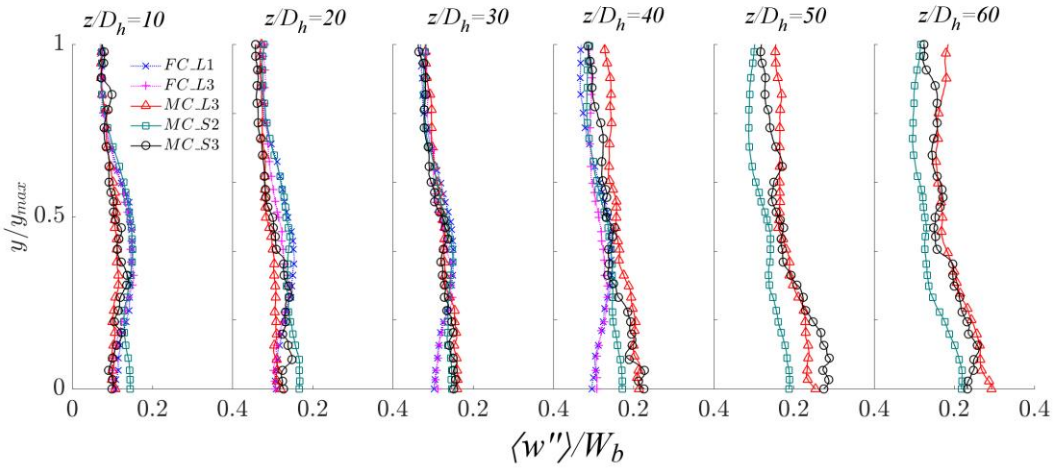

(a)

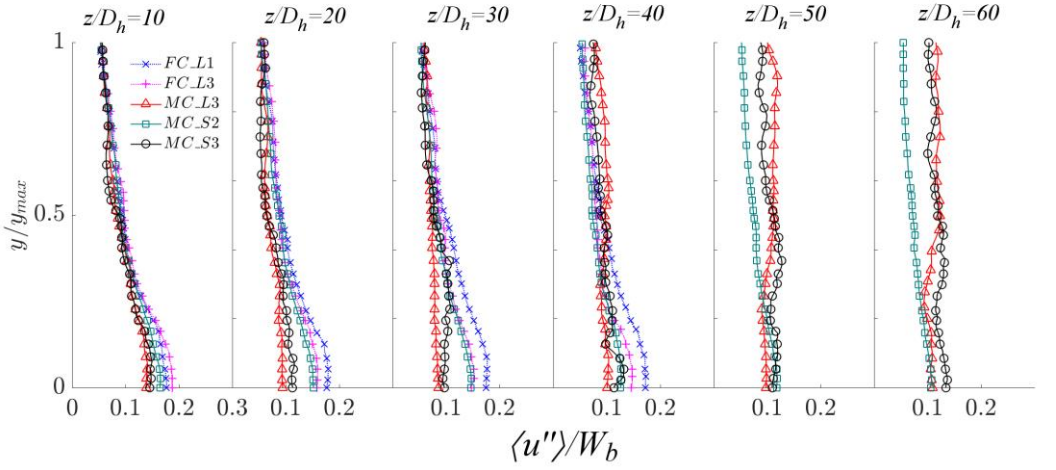

(b)

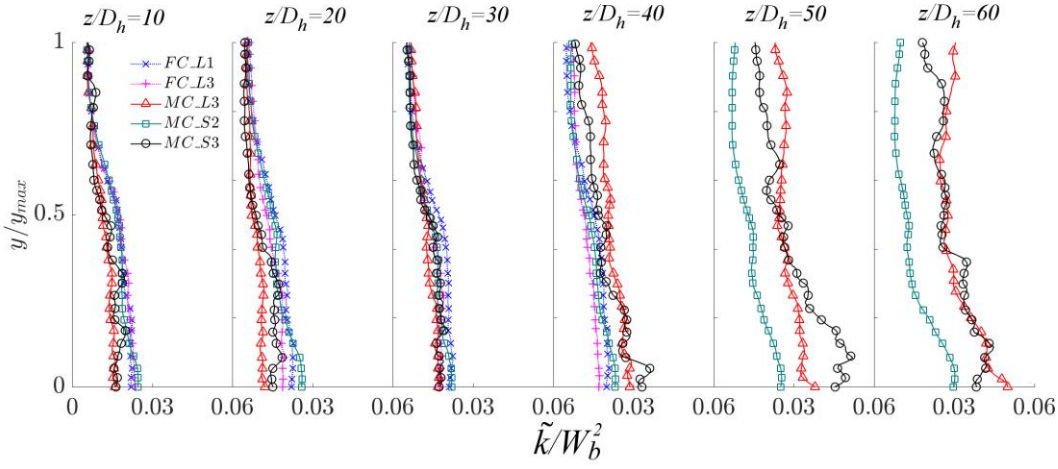

(c)

Figure 5.36: Profiles of turbulent components along MC a) $\langle w'' \rangle / W_b$ b) $\langle u'' \rangle / W_b$ c) $\widetilde{k}/W_b^2$.

5.3 Summary

LES of mixed convection of water at supercritical pressure has been conducted. Three cases were studied: MC_S2 is a weak buoyancy case with $Bo^*=2.5\times10^{-6}$ and MC_L3 and MC_S3 are two strong buoyancy cases with $Bo^*=2\times10^{-5}$ and 1×10^{-5}, respectively. In addition, the hydraulic diameter of MC_L3 is 10 times of that of the other two cases. This means that the heat flux (and temperature change) in MC_L3 is much smaller than that in the other two cases, and the thermal properties variations are very small. Any effect on heat transfer, in this case, is due to buoyancy only, which is not necessarily true in the other two cases.

The results of the mixed convection were compared with two forced convection flows, FC_L1 and FC_L3 with weak and strong heating respectively.

It has been found that the averaged *Nu* on the heated rod surface of the weak buoyancy case (MC_S2) is similar to that of the weak forced convection (FC_L1). (see Figure 5.10). The heat transfer (*Nu*) is more strongly reduced in MC_L3 initial in the upstream section, but it recovers to a level similar to that of MC_S2 later. The *Nu* is very significantly reduced in MC_S3; it is only 1/3 of that in MC_S2 at z/D_h=20. And less than half at z/D_h=60 for example. However, some recovery clearly appears after z/D_h=20 and the *Nu* is slightly higher in this case than in FC_L3.

The reasons causing the heat transfer deterioration (reduced *Nu*) are very complex. Especially, heat transfer effectively varies around the channel sub-regions. A number of observations can be used to illustrate the potential reasons for the changes. Firstly, the streamwise turbulence (w'') close to the heated rod is much smaller in MC_S3 than in MC_S2

at all stations in the heated section, except near the narrow gap (Figure 5.30). The turbulence near the unheated wall is stronger in MC_S3 than in MC_S2, but this does not have any effect on *Nu* on the heated rod.

Secondly, the large swing flow structures near the narrow gap are only weakened downstream in case MC_S2, but it is nearly non-existing in the strong buoyancy case (MC_S3) (Figure 5.12).

Thirdly, the mixing velocity in the narrow gap is much higher in MC_S2 than in MC_S3 (Figure 5.26). Note, however, this parameter is not completely independent to the factor described in point 2.

Lastly, the thermal properties of the fluid are very significantly different in MC_S3 than in MC_S2 (and in MC_L3). This may be a significant contributor to the difference in *Nu* in the various vases. However, this effect is difficult to quantify.

Chapter 6

Conclusion and Future Work

The present PhD study is aimed at developing new knowledge on the flow instability in a flow channel of the non-uniform cross-section with supercritical water. The focus of the study is divided into two parts. The first part is on the effect of flow acceleration due to thermal expansion in the supercritical water and the second part is on the effect of buoyancy in the supercritical water. This chapter concludes the work that has been done.

6.1 The Effect of Flow Acceleration due to Thermal Expansion in Supercritical water

Large eddy simulation has been carried out to study the effect of the flow acceleration due to thermal expansion, where the buoyancy effect is neglected. The pseudocritical temperature plays an important role in the heat transfer under such flow conditions. The effect of flow acceleration due to thermal expansion is strong when T_{pc} is in between the bulk and wall temperature ($T_b < T_{pc} < T_w$), while mild effect of variation of properties is found when

both the wall and the bulk fluid temperatures are below T_{pc} ($T_b < T_w < T_{pc}$). The former condition is characterised as high heating case, while the latter is the low heating case.

The existence of pseudo oscillating large flow structures is demonstrated to occur in the narrow gap. The general structures are similar in all cases although the structures in the high heating conditions have been observed to become weaker. This shows that the effect of thermal expansion is to reduce the fluctuations down the heating channel. In parallel with the reduction in heat transfer, turbulent quantities have also been found to reduce in high heating cases. The dominated unsteady flow modes were studied by the POD analysis. In a low heating case, a pair of symmetric oscillating modes dominates the unsteady flow, defining the nature of the oscillating flow patterns observed in such flows. In the strongest heating case, such symmetrical oscillating mode pair is significantly weakened. In the place of a new non-oscillatory structure, which contributes significantly to the overall structure, it makes the overall flow swinging weaker.

The general trend of the profiles of the turbulent quantities in the present study also shows an agreement with the numerical study of Duan & He [13]. As the heat flux increases, the trend of turbulent quantities of the present study (mainly in the main channel and across the gap) show interesting similarities to those of buoyancy-influenced cases of the Duan & He [13]. This suggests that the effect of thermal expansion and that of the buoyancy effect of constant properties flow (based on Boussinesq approximation) appear to be similar. This conclusion is also similar to the findings of Tanaka *et al.* [31].

6.2 The Effect of Buoyancy in Supercritical Water

The buoyancy influences in the flow of supercritical water in a trapezoid annulus have been studied. The outcome from the study is as follows:

Three cases have been considered in the present study; i.e., a weak buoyancy case of $Bo^* = 2.5\times10^{-6}$ and two-strong buoyancy cases which are $Bo^*=1\times10^{-5}$ & 2×10^{-5}. The dimension of the last Bo^* case is 10 times larger than that of the other two cases. Consequently, the heat flux and the variations of thermal properties are much smaller than those in the other two cases. In fact, the heat transfer in $Bo^*=2\times10^{-5}$ is solely influenced by the buoyancy (i.e., the Boussinesq approximation can be assumed). In the other two buoyancy cases ($Bo^*=2.5\times10^{-6}$ & 1×10^{-5}), both the effects of buoyancy and effect of the variations of thermal properties are strong. These mixed convection cases are compared with forced convection cases of weak and strong heating as discussed earlier.

The results obtained from the averaged *Nu* on the heated rod surface show that in the weak buoyancy case ($Bo^*=2.5\times10^{-6}$), the heat transfer (*Nu*) is similar to that in the weak forced convection case. Meanwhile, in the high-buoyancy cases, the *Nu* is strongly reduced at the beginning of the upstream section, with a larger reduction for the case with a non-negligible effect of the variation of thermal properties (i.e., the case with a smaller dimension) ($Bo^*=1\times10^{-5}$). Both of the high-buoyancy cases show a recovery of heat transfer after some distances (z/D_h>20). The highest buoyancy case (the Boussinesq-approximation-like case) recovers to a level similar to that in the weak buoyancy case. *Nu* in $Bo^*=1\times10^{-5}$, on the other hand, is less than half of the level of the weak buoyancy case at z/D_h=60, which is slightly higher than that in the strong-heating forced convection case.

There are several possible reasons that may cause heat transfer deterioration in flows considered in the present study. Some of the key potential reasons are as follows:

i) Firstly, in a high-buoyancy case with the non-negligible variation of properties, ($Bo^{*}=1\times10^{-5}$), the streamwise turbulence (w'') is very low near the heating wall in every location compared to those in the low-buoyancy case. The streamwise turbulence is higher near the outer wall, but this does not contribute to heat transfer on the heated rod.

ii) Secondly, the swinging large flow structures are almost non-existent in the high-buoyancy case, whilst in the low-buoyancy case, the flow structures are only weakened somewhat.

iii) Thirdly, the mixing velocity in low buoyancy-influence is much higher than that of the high buoyancy-influence case. This is not particularly independent to the point (ii).

iv) Lastly, the variation of the thermal properties is significant in $Bo^{*}=1\times10^{-5}$ but not in the other two mixed convection cases. This is probably the dominant factor to the differences in Nu levels in the various cases, but this effect is difficult to quantify.

6.3 Suggestion for Future Work

Some recommendations for potential future studies in developing further understanding of the flow in heated supercritical water to expand the present study are detailed below.

The present study only considered a trapezoid annulus, as a “model” for the triangular

configuration of a tight rod bundle. A configuration with a closer representation of the real geometry such as the subchannel configuration of the rod bundle or a full rod bundle could further improve the knowledge on the large flow structures in such conditions. For a full rod bundle, the heat transfer may be influenced by a network of flow structures rather than just a single structure in one particular gap.

Another investigation that can be considered is the study of the effect of asymmetric heating on the flow structure in the tight gaps. Non-uniform heating may complicate the behaviour of the instability existing in the tight gaps, but most studies only considered a uniform heating. It will be particularly interesting in a full rod bundle configuration, where a network of flow structures may co-exist and interact with each other.

In the rod bundle, spacers are usually used to maintain the locations of the pins. It has been found from literature that spacers may improve local heat transfer. It would be interesting to investigate the effect of spacers on the large flow structures in the tight gap and consequently its heat transfer.

List of Publications

1. M. M. Amin, Y. Duan, S. He, (2017), Large eddy simulation of forced convection at supercritical pressure in a channel of non-uniform cross-section, 5th Int. Symp. ISSCWR-8, Chengdu, China, March 13-15 2017

2. M. M. Amin, Y. Duan, S. He, Large Eddy Simulation Study on Forced Convection Heat Transfer to Water at Supercritical Pressure in a Trapezoid Annulus. ASME. ASME J of Nuclear Rad Sci. (2017), 4(1), 011007-011007-14. doi:10.1115/1.4038161.

3. M. M. Amin M, Duan Y, He S. Study of the buoyancy influences to the flow and heat transfer in the supercritical water. (in preparation)

4. M. M. Amin, Duan Y, He S. Heat transfer in mixed convection at the tight gaps. (in preparation)

References

[1] J. Buongiorno, P.E. MacDonald, Progress Report for the FY-03 Generation-IV R&D Activities for the Development of the SCWR in the U.S., (2003) 38.

[2] S. Mokry, I. Pioro, P. Kirillov, Y. Gospodinov, Supercritical-water heat transfer in a vertical bare tube, Nucl. Eng. Des. 240 (2010) 568–576. doi:10.1016/j.nucengdes.2009.09.003.

[3] I. Pioro, S. Mokry, Thermophysical Properties at Critical and Supercritical Conditions, Heat Transf. - Theor. Anal. Exp. Investig. Ind. Syst. (2011).

[4] J. Vujić, R.M. Bergmann, R. Škoda, M. Miletić, Small modular reactors: Simpler, safer, cheaper?, Energy. 45 (2012) 288–295. doi:10.1016/j.energy.2012.01.078.

[5] Z. Chen, P. Zhao, G. Zhou, H. Chen, Study of core flow distribution for small modular natural circulation lead or lead-alloy cooled fast reactors, Ann. Nucl. Energy. 72 (2014) 76–83. doi:10.1016/j.anucene.2014.04.032.

[6] Y. Ahn, J.I. Lee, Study of various Brayton cycle designs for small modular sodium-cooled fast reactor, Nucl. Eng. Des. 276 (2014) 128–141. doi:10.1016/j.nucengdes.2014.05.032.

[7] M.K. Rowinski, T.J. White, J. Zhao, Small and Medium sized Reactors (SMR): A review of technology, Renew. Sustain. Energy Rev. 44 (2015) 643–656. doi:10.1016/j.rser.2015.01.006.

[8] J. Lee, J.I. Lee, H.J. Yoon, J.E. Cha, Supercritical Carbon Dioxide turbomachinery design for water-cooled Small Modular Reactor application, Nucl. Eng. Des. 270 (2014) 76–89. doi:10.1016/j.nucengdes.2013.12.039.

[9] Y. Ahn, J. Lee, S.G. Kim, J.I. Lee, J.E. Cha, S.-W. Lee, Design consideration of supercritical CO_2 power cycle integral experiment loop, Energy. (2015). doi:10.1016/j.energy.2015.03.066.

[10] H.J. Yoon, Y. Ahn, J.I. Lee, Y. Addad, Potential advantages of coupling supercritical CO_2 Brayton cycle to water cooled small and medium size reactor, Nucl. Eng. Des. 245 (2012) 223–232. doi:10.1016/j.nucengdes.2012.01.014.

[11] IAEA, Heat Transfer Behaviour and Thermohydraulics Code Testing for Supercritical Water Cooled Reactors (SCWRs), IAEA-TECDOC-1746, Vienna, 2014.

[12] Y. Duan, S. He, Large eddy simulation of a buoyancy-aided flow in a non-uniform channel – Buoyancy effects on large flow structures, Nucl. Eng. Des. 312 (2017) 191–204. doi:10.1016/j.nucengdes.2016.05.007.

[13] Y. Duan, S. He, Heat transfer of a buoyancy-aided turbulent flow in a trapezoidal annulus, Int. J. Heat Mass Transf. 114 (2017) 211–224. doi:10.1016/j.ijheatmasstransfer.2017.06.070.

[14] I.L. IL Pioro, H.F.H. Khartabil, R.B.R. Duffey, Heat transfer to supercritical fluids flowing in channels - Empirical correlations (survey), Nucl. Eng. Des. 230 (2004) 69–91. doi:10.1016/j.nucengdes.2003.10.010.

[15] J. Wang, H. Li, S. Yu, T. Chen, Investigation on the characteristics and mechanisms of unusual heat transfer of supercritical pressure water in vertically-upward tubes, Int. J. Heat Mass Transf. 54 (2011) 1950–1958. doi:10.1016/j.ijheatmasstransfer.2011.01.008.

[16] I.L. Pioro, R.B. Duffey, Experimental heat transfer in supercritical water flowing inside channels (survey), Nucl. Eng. Des. 235 (2005) 2407–2430. doi:10.1016/j.nucengdes.2005.05.034.

[17] V.A. Kurganov, Y.A. Zeigarnik, I. V. Maslakova, Heat transfer and hydraulic resistance of supercritical-pressure coolants. Part I: Specifics of thermophysical properties of supercritical pressure fluids and turbulent heat transfer under heating conditions in round tubes (state of the art), Int. J. Heat Mass Transf. 55 (2012) 3061–3075. doi:10.1016/j.ijheatmasstransfer.2012.01.031.

[18] X. Cheng, T. Schulenberg, Heat Transfer at Supercritical Pressures - Literature Review and Application to an HPLWR, (No. FZKA--6609). Forschungszentrum Karlsruhe GmbH Technik und Umwelt (Germany). Inst. fuer Kern-und Energietechnik., 2001.

[19] V.A. Kurganov, Y.A. Zeigarnik, I. V. Maslakova, Heat transfer and hydraulic resistance of supercritical-pressure coolants. Part II: Experimental data on hydraulic

resistance and averaged turbulent flow structure of supercritical pressure fluids during heating in round tubes under normal and deteriorate, Int. J. Heat Mass Transf. 58 (2013) 152–167. doi:10.1016/j.ijheatmasstransfer.2012.10.072.

[20] J.Y. Yoo, The Turbulent Flows of Supercritical Fluids with Heat Transfer, Annu. Rev. Fluid Mech. 45 (2013) 495–525. doi:10.1146/annurev-fluid-120710-101234.

[21] M.M. Rahman, J. Dongxu, M.S. Beni, H.C. Hei, W. He, J. Zhao, Supercritical water heat transfer for nuclear reactor applications: A review, Ann. Nucl. Energy. 97 (2016) 53–65. doi:10.1016/j.anucene.2016.06.022.

[22] D. Huang, W. Li, A brief review on the buoyancy criteria for supercritical fluids, Appl. Therm. Eng. 131 (2018) 977–987. doi:10.1016/j.applthermaleng.2017.12.042.

[23] A.A. Bishop, R.O. Sandberg, L.S. Tong, Forced Convection Heat Transfer to Water at Near-Critical Temperatures and Supercritical Pressures, in: Chem. Eng. under Extrem. Cond. Proc. A.I. Ch.E.-I. Chem.E, Symp. Ser. No. 2, United States, 1964: pp. 77–85.

[24] N. Zuber, An analysis of thermally induced flow oscillations in the near-critical and super-critical thermodynamic region, NAS 3-11422, Final Report, 1966.

[25] J.W. Ackerman, Pseudoboiling Heat Transfer to Supercritical Pressure Water in Smooth and Ribbed Tubes, J. Heat Transfer. 92 (1970) 490. doi:10.1115/1.3449698.

[26] E. Stewart, P. Stewart, A. Watson, Thermo-Acoustic Convection Oscillations in Forced Heat Transfer To Supercritical Pressure Water, Int. J. Heat Mass Transf. 16 (1973) 257–270.

[27] S. Koshizuka, N. Takano, Y. Oka, N. Engineering, Numerical analysis of deterioration phenomena in heat transfer to supercritical water, Int. J. Heat Mass Transf. 38 (1995) 3077–3084.

[28] H. Li, H. Wang, Y. Luo, H. Gu, X. Shi, T. Chen, E. Laurien, Y. Zhu, Experimental investigation on heat transfer from a heated rod with a helically wrapped wire inside a square vertical channel to water at supercritical pressures, Nucl. Eng. Des. 239 (2009) 2004–2012. doi:10.1016/j.nucengdes.2009.05.011.

[29] W.B. Hall, J.D. Jackson, Laminarization of a turbulent pipe flow by buoyancy forces. ASME paper, no 69-HT-55, 1969.

[30] P.J.P. Bourke, D.J.D. Pulling, L.E. LE Gill, W.H. Denton, Forced convective heat transfer to turbulent CO_2 in the supercritical region, Int. J. Heat Mass Transf. 13 (1970) 1339–1348. doi:10.1016/0017-9310(70)90074-8.

[31] H. Tanaka, A. Tsuge, M. Hirata, N. Nishiwaki, Effects of buoyancy and of acceleration owing to thermal expansion on forced turbulent convection in vertical circular tubes-criteria of the effects, velocity and temperature profiles, and reverse transition from turbulent to laminar flow, Int. J. Heat Mass Transf. 16 (1973) 1267–1288. doi:10.1016/0017-9310(73)90135-X.

[32] K. Yamagata, K. Nishikawa, S. Hasegawa, K. Nishmawa, S. Hasegawa, Forced Convective Heat Transfer to Supercritical Water Flowing in Tubes, Int. J. Heat Mass Transf. 15 (1972) 2575–2593. doi:10.1016/0017-9310(72)90148-2.

[33] J.H. Bae, J.Y. Yoo, H. Choi, Direct numerical simulation of turbulent supercritical flows with heat transfer, Phys. Fluids. 17 (2005) 105104. doi:10.1063/1.2047588.

[34] B. Shiralkar, P. Griffith, The Effect of Swirl, Inlet Conditions, Flow Direction, and Tube Diameter on the Heat Transfer to Fluids at Supercritical Pressure, J. Heat Transfer. 92 (1970) 465–471.

[35] J.D. Jackson, W.B. Hall, Influences of buoyancy on heat transfer to fluids flowing in vertical tubes under turbulent conditions, Turbul. Forced Convect. Channels Bundles. 2 (1979) 613–640.

[36] J.D. Jackson, W.B. Hall, Forced convection heat transfer to fluids at supercritical pressure, Turbul. Forced Convect. Channels Bundles. 2 (1979) 563–611.

[37] J.H. Bae, J.Y. Yoo, D.M. McEligot, Direct numerical simulation of heated CO2 flows at supercritical pressure in a vertical annulus at Re=8900, Phys. Fluids. 20 (2008) 55108. doi:10.1063/1.2927488.

[38] L.F. Glushchenko, S.I. Kalachev, O.F. Gandzyuk, Determining conditions of existence of deteriorated heat-transfer at supercritical pressures of medium, Therm. Eng. 19 (1972) 107–111.

[39] A.P. Ornatskiy, L.F. Glushchenko, O.F. Gandzyuk, An experimental study of heat transfer in externally-heated annuli at supercritical pressures, Heat Transf. Res. 4 (1972) 25.

[40] B.S. Petukhov, An investigation of heat transfer to fluids flowing in pipes under supercritical conditions, in: Int. Dev. Heat Transf. Proc. 1961-62 Heat Transf. Conf. August 28-September 1, 1961, Univ. Color. Boulder, Color. USA, January 8-12, 1962, Contin. Discuss. Cent. Hall Lect. Theatr. Westmins, The American Society of Mechanical Engineers, 1963.

[41] A.A. Bishop, R.O. Sandberg, L.S. Tong, Forced Convection Heat Transfer to Water at Near-Critical Temperatures and Supercritical Pressures, in: Chem. Eng. under Extrem. Cond. Proc. A.I. Ch.E.-I. Chem.E, Symp. Ser. No. 2, London, UK, June 13–17, 1965, 1965: pp. 77–85.

[42] H.S. Swenson, J.R. Carver, C.R. Kakarala, Heat Transfer to Supercritical Water in Smooth-Bore Tubes, J. Heat Transfer. 87 (1965) 477–483. doi:10.1115/1.3689139.

[43] E.A. Krasnoshchekov, V.S. Protopopov, F. Van, I. V Kuraeva, Experimental investigation of heat transfer for carbon dioxide in the supercritical region, in: Proc. 2nd All-Soviet Union Conf. Heat Mass Transf. Minsk. Belarus, 1964: pp. 26–35.

[44] J.D. Jackson, J. Fewster, Forced convection data for supercritical pressure fluids, HTFS 21540. (1975).

[45] J.D. Jackson, Consideration of the heat transfer properties of supercritical pressure water in connection with the cooling of advanced nuclear reactors, in: 13th Pacific Basin Nucl. Conf. Abstr., 2002.

[46] J. Yu, B. Jia, D. Wu, D. Wang, Optimization of heat transfer coefficient correlation at supercritical pressure using genetic algorithms, Heat Mass Transf. 45 (2009) 757–766. doi:10.1007/s00231-008-0475-4.

[47] W. Chen, X. Fang, A new heat transfer correlation for supercritical water flowing in vertical tubes, Int. J. Heat Mass Transf. 78 (2014) 156–160. doi:10.1016/j.ijheatmasstransfer.2014.06.059.

[48] M. Haghshenas Fard, CFD modeling of heat transfer of CO_2 at supercritical pressures

flowing vertically in porous tubes, Int. Commun. Heat Mass Transf. 37 (2010) 98–102. doi:10.1016/j.icheatmasstransfer.2009.08.004.

[49] Y.-X.X. Hua, Y.-Z.Z. Wang, H. Meng, A numerical study of supercritical forced convective heat transfer of n-heptane inside a horizontal miniature tube, J. Supercrit. Fluids. 52 (2010) 36–46. doi:10.1016/j.supflu.2009.12.003.

[50] S.H. Lee, Numerical study of convective heat transfer to supercritical water in rectangular ducts, Int. Commun. Heat Mass Transf. 37 (2010) 1465–1470. doi:10.1016/j.icheatmasstransfer.2010.09.006.

[51] S. He, W.S.S. Kim, P.X.X. Jiang, J.D.D. Jackson, Simulation of mixed convection heat transfer to carbond dioxide at supercritical pressure, Proceeding Int. Mech. Eng. Part C. 218 (2004) 1281–1296. doi:10.1177/095440620421801101.

[52] S. He, W.S. Kim, J.H. Bae, Assessment of performance of turbulence models in predicting supercritical pressure heat transfer in a vertical tube, Int. J. Heat Mass Transf. 51 (2008) 4659–4675. doi:10.1016/j.ijheatmasstransfer.2007.12.028.

[53] S. He, W.S. Kim, J.D. Jackson, A computational study of convective heat transfer to carbon dioxide at a pressure just above the critical value, Appl. Therm. Eng. 28 (2008) 1662–1675. doi:10.1016/j.applthermaleng.2007.11.001.

[54] M. Behnia, S. Parneix, P.A. Durbin, Prediction of heat transfer in an axisymmetric turbulent jet impinging on a flat plate, Int. J. Heat Fluid Flow. 41 (1998) 1845–1855. doi:10.1016/S0017-9310(97)00254-8.

[55] W.S. Kim, S. He, J.D. Jackson, Assessment by comparison with DNS data of turbulence models used in simulations of mixed convection, Int. J. Heat Mass Transf. 51 (2008) 1293–1312. doi:10.1016/j.ijheatmasstransfer.2007.12.002.

[56] Q.L. Wen, H.Y. Gu, Numerical simulation of heat transfer deterioration phenomenon in supercritical water through vertical tube, Ann. Nucl. Energy. 37 (2010) 1272–1280. doi:10.1016/j.anucene.2010.05.022.

[57] Q.L. Wen, H.Y. Gu, Numerical investigation of acceleration effect on heat transfer deterioration phenomenon in supercritical water, Prog. Nucl. Energy. 53 (2011) 480–486. doi:10.1016/j.pnucene.2011.02.012.

[58] M. Jaromin, H. Anglart, A numerical study of heat transfer to supercritical water flowing upward in vertical tubes under normal and deteriorated conditions, Nucl. Eng. Des. 264 (2013) 61–70. doi:10.1016/j.nucengdes.2012.10.028.

[59] L. Liu, Z. Xiao, X. Yan, X. Zeng, Y. Huang, Numerical simulation of heat transfer deterioration phenomenon to supercritical water in annular channel, Ann. Nucl. Energy. 53 (2013) 170–181. doi:10.1016/j.anucene.2012.08.022.

[60] L. Liu, Z. Xiao, X. Yan, X. Zeng, Y. Huang, Heat transfer deterioration to supercritical water in circular tube and annular channel, Nucl. Eng. Des. 255 (2013) 97–104. doi:10.1016/j.nucengdes.2012.09.025.

[61] M.-T. Kao, M. Lee, Y.-M. Ferng, C.-C. Chieng, Heat transfer deterioration in a supercritical water channel, Nucl. Eng. Des. 240 (2010) 3321–3328. doi:10.1016/j.nucengdes.2010.06.028.

[62] C. Kunik, I. Otic, T. Schulenberg, Large Eddy Simulation Turbulent Flows at Supercritical Pressure, in: 14th Int. Top. Meet. Nucl. React. Therm. Hydraul. (NURETH-14), Toronto, Ontario, Canada, Sept. 25–30, 2011.

[63] B. Ničeno, M. Sharabi, Large eddy simulation of turbulent heat transfer at supercritical pressures, Nucl. Eng. Des. 261 (2013) 44–55. doi:10.1016/j.nucengdes.2013.03.042.

[64] L. Cao, Y. Oka, Y. Ishiwatari, Z. Shang, Fuel, Core Design and Subchannel Analysis of a Superfast Reactor, J. Nucl. Sci. Technol. 45 (2008) 138–148. doi:10.1080/18811248.2008.9711423.

[65] D.S. Rowe, B.M. Johnson, J.G. Knudsen, Implications concerning rod bundle crossflow mixing based on measurements of turbulent flow structure, Int. J. Heat Mass Transf. 17 (1974) 407–419. doi:10.1016/0017-9310(74)90012-X.

[66] A.C. Trupp, R.S. Azad, The structure of turbulent flow in triangular array rod bundles, Nucl. Eng. Des. 32 (1975) 47–84. doi:10.1016/0029-5493(75)90090-4.

[67] P. Carajilescov, N.E. Todreas, Experimental and analytical study of axial turbulent flows in an interior sub-channel of a bare rod bundle, J. Heat Transf. 5 (1976) 262–268. doi:10.1115/1.3450529.

[68] K. Rehme, Experimental observations of turbulent flow through subchannels of rod bundles, Exp. Therm. Fluid Sci. 2 (1989) 341–349. doi:10.1016/0894-1777(89)90023-X.

[69] J.D. Hooper, K. Rehme, Large-scale structural effects in developed turbulent flow through closely-spaced rod arrays, J. Fluid Mech. 145 (1984) 305. doi:10.1017/S0022112084002949.

[70] S.C. Yao, L.E. Hochreiter, W.J. Leech, Heat-transfer augmentation in rod bundles near grid spacers, J. Heat Transfer. 104 (1982) 76. doi:10.1115/1.3245071.

[71] S. Yang, M.K. Chung, Spacer grid effects on turbulent flow in rod bundles, J. Korean Nucl. Soc. 28 (1996) 56–71.

[72] D. Caraghiaur, H. Anglart, W. Frid, Experimental investigation of turbulent flow through spacer grids in fuel rod bundles, Nucl. Eng. Des. 239 (2009) 2013–2021. doi:10.1016/j.nucengdes.2009.05.029.

[73] D.J. Miller, F.B. Cheung, S.M. Bajorek, On the development of a grid-enhanced single-phase convective heat transfer correlation, Nucl. Eng. Des. 264 (2013) 56–60. doi:10.1016/j.nucengdes.2012.11.023.

[74] M. V. Holloway, D.E. Beasley, M.E. Conner, Single-phase convective heat transfer in rod bundles, Nucl. Eng. Des. 238 (2008) 848–858. doi:10.1016/j.nucengdes.2007.08.003.

[75] M. V. Holloway, H.L. McClusky, D.E. Beasley, M.E. Conner, The Effect of Support Grid Features on Local, Single-Phase Heat Transfer Measurements in Rod Bundles, J. Heat Transfer. 126 (2004) 43. doi:10.1115/1.1643091.

[76] K. Podila, Y.F. Rao, M. Krause, J. Bailey, A CFD simulation of 5 × 5 rod bundles with split-type spacers, Prog. Nucl. Energy. 70 (2014) 167–175. doi:10.1016/j.pnucene.2013.08.012.

[77] V.Y. Agbodemegbe, X. Cheng, E.H.K. Akaho, F.K.A. Allotey, An investigation of the effect of split-type mixing vane on extent of crossflow between subchannels through the fuel rod gaps, Ann. Nucl. Energy. 88 (2016) 174–185. doi:10.1016/j.anucene.2015.10.036.

[78] D. Chen, Y. Xiao, S. Xie, D. Yuan, X. Lang, Z. Yang, Y. Zhong, Q. Lu, Thermal-hydraulic performance of a 5 × 5 rod bundle with spacer grid in a nuclear reactor, Appl. Therm. Eng. 103 (2016) 1416–1426. doi:10.1016/j.applthermaleng.2016.05.028.

[79] D. Liu, H. Gu, Mixed convection heat transfer in a 5 × 5 rod bundles, Int. J. Heat Mass Transf. 113 (2017) 914–921. doi:10.1016/j.ijheatmasstransfer.2017.05.113.

[80] K.B. Lee, H.C. Jang, A numerical prediction on the turbulent flow in closely spaced bare rod arrays by a nonlinear k−ϵ model, Nucl. Eng. Des. 172 (1997) 351–357. doi:10.1016/S0029-5493(97)00001-0.

[81] J. Xiong, Y. Yu, N. Yu, X. Fu, H. Wang, X. Cheng, Y. Yang, Laser Doppler measurement and CFD validation in 3 × 3 bundle flow, Nucl. Eng. Des. 270 (2014) 396–403. doi:10.1016/j.nucengdes.2014.02.009.

[82] C.W. Rapley, A.D. Gosman, The prediction of fully developed axial turbulent flow in rod bundles, Nucl. Eng. Des. 97 (1986) 313–325. doi:10.1016/0029-5493(86)90167-6.

[83] E. Baglietto, H. Ninokata, A turbulence model study for simulating flow inside tight lattice rod bundles, Nucl. Eng. Des. 235 (2005) 773–784. doi:10.1016/j.nucengdes.2004.10.007.

[84] J. Gou, Z. Shang, Y. Ishiwarari, Y. Oka, M. Yamakawa, S. Ikejiri, CFD analysis of heat transfer in subchannels of a Super Fast Reactor, Nucl. Eng. Des. 240 (2010) 1819–1829. doi:10.1016/j.nucengdes.2010.03.013.

[85] J. Gou, Y. Ishiwarari, Y. Oka, M. Yamakawa, CFD analyses in tight-lattice subchannels and seven-rod bundle geometries of a Super Fast Reactor, Nucl. Eng. Des. 241 (2011) 1656–1666. doi:10.1016/j.nucengdes.2011.02.013.

[86] Z. Shang, S. Lo, Numerical investigation of supercritical water-cooled nuclear reactor in horizontal rod bundles, Nucl. Eng. Des. 240 (2010) 776–782. doi:10.1016/j.nucengdes.2009.10.029.

[87] Z. Shang, S. Lo, CFD in supercritical water-cooled nuclear reactor (SCWR) with horizontal tube bundles, Nucl. Eng. Des. 241 (2011) 4427–4433.

doi:10.1016/j.nucengdes.2010.09.024.

[88] Z. Shang, S. Chen, Numerical investigation of diameter effect on heat transfer of supercritical water flows in horizontal round tubes, Appl. Therm. Eng. 31 (2011) 573–581. doi:10.1016/j.applthermaleng.2010.10.020.

[89] K. Natesan, T. Sundararajan, A. Narasimhan, K. Velusamy, Turbulent flow simulation in a wire-wrap rod bundle of an LMFBR, Nucl. Eng. Des. 240 (2010) 1063–1072. doi:10.1016/j.nucengdes.2009.12.025.

[90] H. Ninokata, E. Merzari, A. Khakim, Analysis of low Reynolds number turbulent flow phenomena in nuclear fuel pin subassemblies of tight lattice configuration, Nucl. Eng. Des. 239 (2009) 855–866. doi:10.1016/j.nucengdes.2008.10.030.

[91] X. Zhang, S.D. Yu, Large eddy simulation of turbulent flow surrounding two simulated CANDU fuel bundles, Nucl. Eng. Des. 241 (2011) 3553–3572. doi:10.1016/j.nucengdes.2011.06.035.

[92] B. V Dyadyakin, A.S. Popov, Heat transfer and thermal resistance of tight seven-rod bundle, cooled with water flow at supercritical pressures, Trans. VTI. 11 (1977) 244–253.

[93] V.A. Silin, V.A. Voznesensky, A.M. Afrov, The light water integral reactor with natural circulation of the coolant at supercritical pressure B-500 SKDI, Nucl. Eng. Des. 144 (1993) 327–336. doi:10.1016/0029-5493(93)90148-3.

[94] I.L. Pioro, H.F. Khartabil, R.B. Duffey, Heat transfer to supercritical fluids flowing in channels - Empirical correlations (survey), Nucl. Eng. Des. 230 (2004) 69–91. doi:10.1016/j.nucengdes.2003.10.010.

[95] I.L. Pioro, R.B. Duffey, T.J. Dumouchel, Hydraulic resistance of fluids flowing in channels at supercritical pressures (survey), Nucl. Eng. Des. 231 (2004) 187–197. doi:10.1016/j.nucengdes.2004.03.001.

[96] J. Xiong, X. Cheng, Y. Yang, Numerical analysis on supercritical water heat transfer in a 2×2 rod bundle, Ann. Nucl. Energy. 80 (2015) 123–134. doi:10.1016/j.anucene.2015.02.005.

[97] G. Richards, G.D. Harvel, I.L. Pioro, A.S. Shelegov, P.L. Kirillov, Heat transfer profiles of a vertical , bare , 7-element bundle cooled with supercritical Freon R-12, Nucl. Eng. Des. 264 (2013) 246–256. doi:10.1016/j.nucengdes.2013.02.019.

[98] H.Y. Gu, Z.X. Hu, D. Liu, Y. Xiao, X. Cheng, Experimental studies on heat transfer to supercritical water in 2×2 rod bundle with two channels, Nucl. Eng. Des. 291 (2015) 212–223. doi:10.1016/j.nucengdes.2015.05.028.

[99] H.Y. Gu, H.B. Li, Z.X. Hu, D. Liu, M. Zhao, Heat transfer to supercritical water in a 2×2 rod bundle, Ann. Nucl. Energy. 83 (2015) 114–124. doi:10.1016/j.anucene.2015.04.020.

[100] H. Gu, Z. Hu, D. Liu, H. Li, M. Zhao, X. Cheng, Experimental study on heat transfer to supercritical water in 2×2 rod bundle with wire wraps, Exp. Therm. Fluid Sci. 70 (2016) 17–28. doi:10.1016/j.expthermflusci.2015.08.015.

[101] X. Cheng, Y.H.H. Yang, S.F.F. Huang, A simplified method for heat transfer prediction of supercritical fluids in circular tubes, Ann. Nucl. Energy. 36 (2009) 1120–1128. doi:10.1016/j.anucene.2009.04.016.

[102] H. Wang, Q. Bi, L. Wang, H. Lv, L.K.H. Leung, Experimental investigation of heat transfer from a 2×2 rod bundle to supercritical pressure water, Nucl. Eng. Des. 275 (2014) 205–218. doi:10.1016/j.nucengdes.2014.04.036.

[103] A. Ornatsky, L. Glushchenko, E. Siomin, S. Kalatchev, The research of temperature conditions of small diameter parallel tubes cooled by water under supercritical pressure, in: 4th Int. Heat Transf. Conf., Begel House Inc, 1970.

[104] H. Wang, W. Wang, Q. Bi, L. Wang, Experimental study of heat transfer and flow resistance of supercritical pressure water in a SCWR sub-channel, J. Supercrit. Fluids. 100 (2015) 15–25. doi:10.1016/j.supflu.2015.02.011.

[105] J. Yang, Y. Oka, Y. Ishiwatari, J. Liu, J. Yoo, Numerical investigation of heat transfer in upward flows of supercritical water in circular tubes and tight fuel rod bundles, Nucl. Eng. Des. 237 (2007) 420–430. doi:10.1016/j.nucengdes.2006.08.003.

[106] X. Cheng, B. Kuang, Y.H. Yang, Numerical analysis of heat transfer in supercritical water cooled flow channels, Nucl. Eng. Des. 237 (2007) 240–252.

doi:10.1016/j.nucengdes.2006.06.011.

[107] H.Y. Gu, X. Cheng, Y.H. Yang, CFD analysis of thermal–hydraulic behavior in SCWR typical flow channels, Nucl. Eng. Des. 238 (2008) 3348–3359. doi:10.1016/j.nucengdes.2008.06.010.

[108] H.Y. Gu, X. Cheng, Y.H. Yang, CFD analysis of thermal–hydraulic behavior of supercritical water in sub-channels, Nucl. Eng. Des. 240 (2010) 364–374. doi:10.1016/j.nucengdes.2008.08.022.

[109] Y. Zhang, C. Zhang, J. Jiang, Numerical simulation of fluid flow and heat transfer of supercritical fluids in fuel bundles, J. Nucl. Sci. Technol. 48 (2011) 929–935. doi:10.1080/18811248.2011.9711779.

[110] Z. Shang, CFD investigation of vertical rod bundles of supercritical water-cooled nuclear reactor, Nucl. Eng. Des. 239 (2009) 2562–2572. doi:10.1016/j.nucengdes.2009.07.021.

[111] K. Podila, Y.F. Rao, Assessment of CFD for the Canadian SCWR bundle with wire wraps, Prog. Nucl. Energy. 77 (2014) 373–380. doi:10.1016/j.pnucene.2014.02.009.

[112] K. Podila, Y.F. Rao, CFD analysis of flow and heat transfer in Canadian supercritical water reactor bundle, Ann. Nucl. Energy. 75 (2015) 1–10. doi:10.1016/j.anucene.2014.07.039.

[113] K. Rehme, The structure of turbulence in rod bundles and the implications on natural mixing between the subchannels, Int. J. Heat Mass Transf. 35 (1992) 567–581. doi:10.1016/0017-9310(92)90291-Y.

[114] T. Krauss, L. Meyer, Experimental investigation of turbulent transport of momentum and energy in a heated rod bundle, Nucl. Eng. Des. 180 (1998) 185–206. doi:10.1016/S0029-5493(98)00158-7.

[115] A.K.M.F. Hussain, Coherent structures—reality and myth, Phys. Fluids. 26 (1983) 2816. doi:10.1063/1.864048.

[116] L. Meyer, From discovery to recognition of periodic large scale vortices in rod bundles as source of natural mixing between subchannels-A review, Nucl. Eng. Des. 240

(2010) 1575–1588. doi:10.1016/j.nucengdes.2010.03.014.

[117] S.V. Möller, On phenomena of turbulent flow through rod bundles, Exp. Therm. Fluid Sci. 4 (1991) 25–35. doi:10.1016/0894-1777(91)90018-M.

[118] S.V. Möller, Single-phase turbulent mixing in rod bundles, Exp. Therm. Fluid Sci. 5 (1992) 26–33. doi:10.1016/0894-1777(92)90053-8.

[119] T. Krauss, L. Meyer, Characteristics of turbulent velocity and temperature in a wall channel of a heated rod bundle, Exp. Therm. Fluid Sci. 12 (1996) 75–86. doi:10.1016/0894-1777(95)00076-3.

[120] X. Wu, A.C. Trupp, Experimental study on the unusual turbulence intensity distributions in rod-to-wall gap regions, Exp. Therm. Fluid Sci. 6 (1993) 360–370. doi:10.1016/0894-1777(93)90014-A.

[121] X. Wu, A.C. Trupp, Spectral measurements and mixing correlation in simulated rod bundle subchannels, Int. J. Heat Mass Transf. 37 (1994) 1277–1281. doi:10.1016/0017-9310(94)90212-7.

[122] L. Meyer, K. Rehme, Large-scale turbulence phenomena in compound rectangular channels, Exp. Therm. Fluid Sci. 8 (1994) 286–304. doi:10.1016/0894-1777(94)90059-0.

[123] L. Meyer, K. Rehme, Periodic Vortices in Flow Through Channels With Longitudinal Slots or Fins, in: Tenth Symp. Turbul. Shear Flows, The Pennsylvania State University. Pennsylvania, USA. August 14-16, 1995, 1995.

[124] M.S. Guellouz, S. Tavoularis, The structure of turbulent flow in a rectangular channel containing a cylindrical rod - Part 1: Reynolds-averaged measurements, Exp. Therm. Fluid Sci. 23 (2000) 59–73. doi:10.1016/S0894-1777(00)00038-8.

[125] M.S. Guellouz, S. Tavoularis, The structure of turbulent flow in a rectangular channel containing a cylindrical rod - Part 2: Phase-averaged measurements, Exp. Therm. Fluid Sci. 23 (2000) 75–91. doi:10.1016/S0894-1777(00)00039-X.

[126] G.H. Choueiri, S. Tavoularis, Experimental investigation of flow development and gap vortex street in an eccentric annular channel. Part 1. Overview of the flow

structure, J. Fluid Mech. 752 (2014) 521–542. doi:10.1017/jfm.2014.343.

[127] G.H. Choueiri, S. Tavoularis, Experimental investigation of flow development and gap vortex street in an eccentric annular channel. Part 2. Effects of inlet conditions, diameter ratio, eccentricity and Reynolds number, J. Fluid Mech. 768 (2015) 294–315. doi:DOI: 10.1017/jfm.2015.90.

[128] D. Chang, S. Tavoularis, Unsteady Numerical Simulations of Turbulence and Coherent Structures in Axial Flow Near a Narrow Gap, J. Fluids Eng. 127 (2005) 458. doi:10.1115/1.1900140.

[129] D. Chang, S. Tavoularis, Convective Heat Transfer in Turbulent Flow Near a Gap, J. Heat Transfer. 128 (2006) 701. doi:10.1115/1.2194039.

[130] C.Y. Lee, C.H. Shin, W.K. In, Effect of gap width on turbulent mixing of parallel flow in a square channel with a cylindrical rod, Exp. Therm. Fluid Sci. 47 (2013) 98–107. doi:10.1016/j.expthermflusci.2013.01.005.

[131] H.Y. Jeong, K.S. Ha, Y.M. Kwon, Y.B. Lee, D. Hahn, A dominant geometrical parameter affecting the turbulent mixing rate in rod bundles, Int. J. Heat Mass Transf. 50 (2007) 908–918. doi:10.1016/j.ijheatmasstransfer.2006.08.023.

[132] E. Merzari, H. Ninokata, Proper orthogonal decomposition of the flow in a tight lattice rod-bundle, Nucl. Eng. Des. 241 (2011) 4621–4632. doi:10.1016/j.nucengdes.2010.12.005.

[133] B.H. Yan, H.Y. Gu, L. Yu, Numerical simulation of large scale vortex structure and flow pulsation in rectangular channels, Prog. Nucl. Energy. 54 (2012) 29–35. doi:10.1016/j.pnucene.2011.09.006.

[134] B.H. Yan, H.Y. Gu, L. Yu, Numerical simulation of the coherent structure and turbulent mixing in tight lattice, Prog. Nucl. Energy. 54 (2012) 81–95. doi:10.1016/j.pnucene.2011.07.008.

[135] B.H. Yan, L. Yu, URANS simulation of the turbulent flow in a tight lattice: Effect of the pitch to diameter ratio, Prog. Nucl. Energy. 53 (2011) 428–437. doi:10.1016/j.pnucene.2011.02.009.

[136] B.H. Yan, Periodic large scale vortex structure in rectangular channels with non-uniform wall roughness, Nucl. Eng. Des. 241 (2011) 2948–2955. doi:10.1016/j.nucengdes.2011.06.027.

[137] G.T. Chapman, M. Tobak, Observations, theoretical ideas and modeling of turbulent flows: Past, present and future, NASA Techical Memo. 86679. (1985).

[138] S.B. Pope, Turbulent Flows, Cambridge University Press, Cambridge, 2000. doi:10.1017/CBO9780511840531.

[139] P.A. Davidson, Turbulence: An Introduction for Scientists and Engineers, OUP Oxford, 2004.

[140] J.H. Ferziger, M. Peric, Computational methods for fluid dynamics, 2002.

[141] S. Robinson, Coherent Motions In The Turbulent Boundary Layer, Annu. Rev. Fluid Mech. 23 (1991) 601–639. doi:10.1146/annurev.fluid.23.1.601.

[142] J. Jeong, F. Hussain, On the identification of a vortex, J. Fluid Mech. 285 (1995) 69–94. doi:10.1017/S0022112095000462.

[143] R. Cucitore, M. Quadrio, A. Baron, On the effectiveness and limitations of local criteria for the identification of a vortex, Eur. J. Mech. B/Fluids. 18 (1999) 261–282. doi:10.1016/S0997-7546(99)80026-0.

[144] J.C.R. Hunt, A.A. Wray, P. Moin, Eddies, streams, and convergence zones in turbulent flows, in: Cent. Turbul. Res. Proc. Summer Progr. 1988, 1988.

[145] G. Berkooz, P. Holmes, J.L. Lumley, The Proper Orthogonal Decomposition in the Analysis of Turbulent Flows, Annu. Rev. Fluid Mech. 25 (1993) 539–575. doi:10.1146/annurev.fl.25.010193.002543.

[146] L. Sirovich, Turbulence and the dynamics of coherent structures. I. Coherent structures, Q. Appl. Math. 45 (1987) 561–571. doi:10.1090/qam/910462.

[147] E. Merzari, H. Ninokata, E. Baglietto, Numerical simulation of flows in tight-lattice fuel bundles, Nucl. Eng. Des. 238 (2008) 1703–1719. doi:10.1016/j.nucengdes.2008.01.001.

[148] P. Sagaut, Large eddy simulations for incompressible flows : an introduction, 2nd ed.,

Springer, Berlin ; London, 1967.

[149] M. Germano, U. Piomelli, P. Moin, W.H. Cabot, A dynamic subgrid-scale eddy viscosity model, Phys. Fluids A Fluid Dyn. 3 (1991) 1760. doi:10.1063/1.857955.

[150] D.K. Lilly, A proposed modification of the Germano subgrid-scale closure method, Phys. Fluids A. 4 (1992) 633–635. doi:10.1063/1.858280.

[151] C. Meneveau, T.S. Lund, W.H. Cabot, A Lagrangian dynamic subgrid-scale model of turbulence, J. Fluid Mech. 319 (1996) 353. doi:10.1017/S0022112096007379.

[152] F. Nicoud, F. Ducros, Subgrid-scale stress modelling based on the square of the velocity gradient tensor, Flow, Turbul. Combust. 62 (1999) 183–200. doi:10.1023/A:1009995426001.

[153] B.J. Geurts, J. Fröhlich, A framework for predicting accuracy limitations in large-eddy simulation, Phys. Fluids. 14 (2002) 41–44. doi:10.1063/1.1480830.

[154] I.B. Celik, Z.N. Cehreli, I. Yavuz, Index of Resolution Quality for Large Eddy Simulations, J. Fluids. 127 (2005) 949–958. doi:10.1115/1.1990201.

[155] I. Celik, M. Klein, J. Janicka, Assessment Measures for Engineering LES Applications, J. Fluids Eng. 131 (2009) 1–10. doi:10.1115/1.3059703.

[156] H.K. Versteeg, W. Malalasekera, An introduction to computational fluid dynamics: the finite volume method., Longman Scientific and Technical, Harlow, 1995.

[157] F. Archambeau, N. Méchitoua, M. Sakiz, Code Saturne: A Finite Volume Code for the Computation of Turbulent Incompressible Flows - Industrial Applications, Int. J. Finite Vol. 1 (2004).

[158] EDF R&D, Code Saturne 4.2.0 Theory Guide, 2015.

[159] S. Benhamadouche, D. Laurence, LES, coarse LES, and transient RANS comparisons on the flow across a tube bundle, Int. J. Heat Fluid Flow. 24 (2003) 470–479. doi:10.1016/S0142-727X(03)00060-2.

[160] J.P. Van Doormaal, G.D. Raithby, Enhancements of the SIMPLE Method for Predicting Incompressible Fluid Flows, Numer. Heat Transf. 7 (1984) 147–163. doi:10.1080/01495728408961817.

[161] C.M. Rhie, W.L. Chow, Numerical study of the turbulent flow past an airfoil with trailing edge separation, AIAA J. 21 (1983) 1525–1532. doi:10.2514/3.8284.

[162] R. Courant, K. Friedrichs, H. Lewy, On the Partial Difference Equations of Mathematical Physics, IBM J. Res. Dev. 11 (1967) 215–234. doi:10.1147/rd.112.0215.

[163] N. Jarrin, S. Benhamadouche, D. Laurence, R. Prosser, A synthetic-eddy-method for generating inflow conditions for large-eddy simulations, Int. J. Heat Fluid Flow. 27 (2006) 585–593. doi:10.1016/j.ijheatfluidflow.2006.02.006.

[164] U. Piomelli, E. Balaras, Wall-Layer Models for Large-Eddy Simulations, Annu. Rev. Fluid Mech. 34 (2002) 349–374. doi:10.1146/annurev.fluid.34.082901.144919.

Appendix A

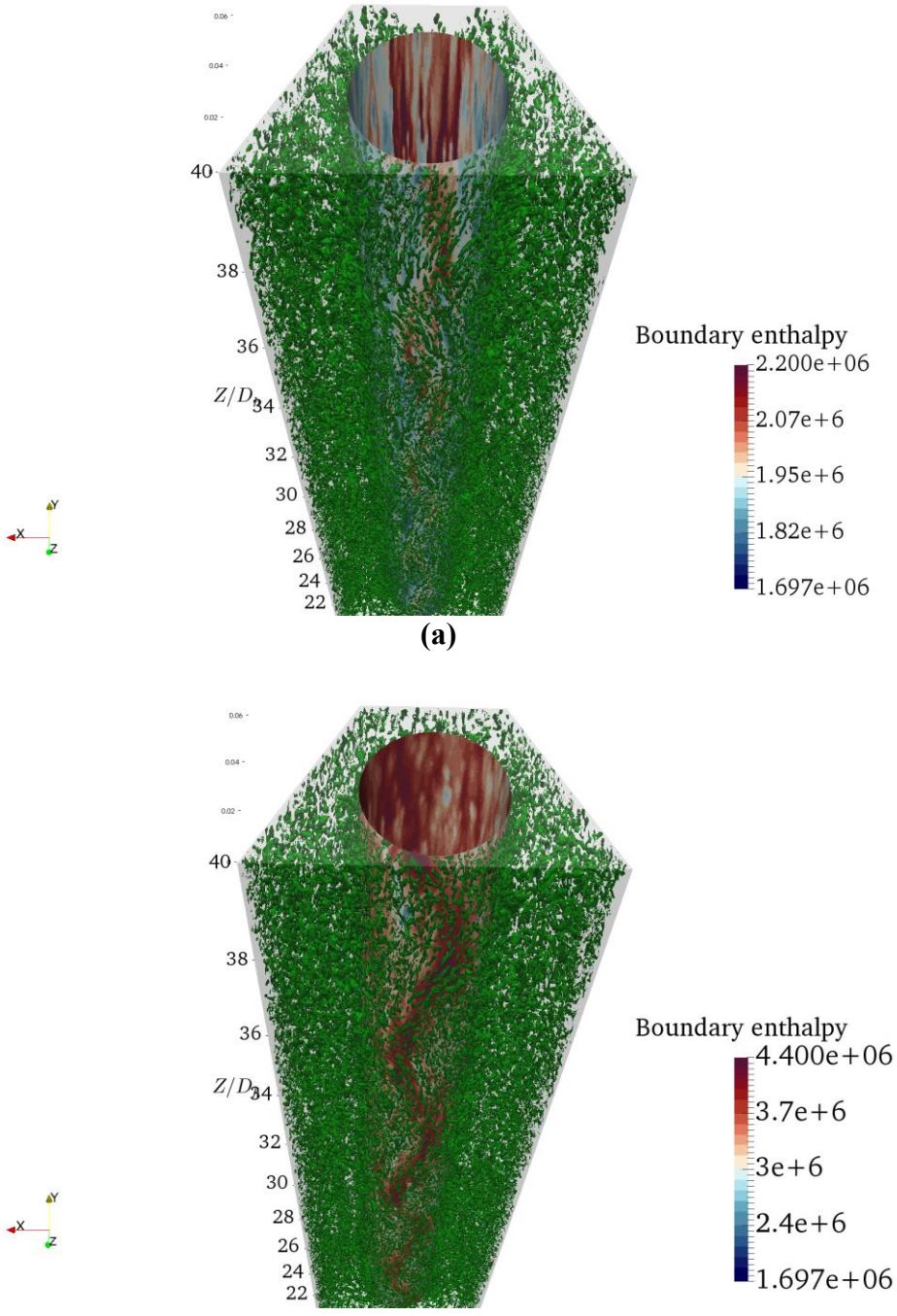

Figure A.1: View of Q-criterion iso-surfaces (Q_{iso}=4) at the bottom of trapezoid annulus at 20D_h towards the outlet (facing the narrow gap). a) q=10kW/m^2 b) q=50kW/m^2 c) q=75kW/m^2

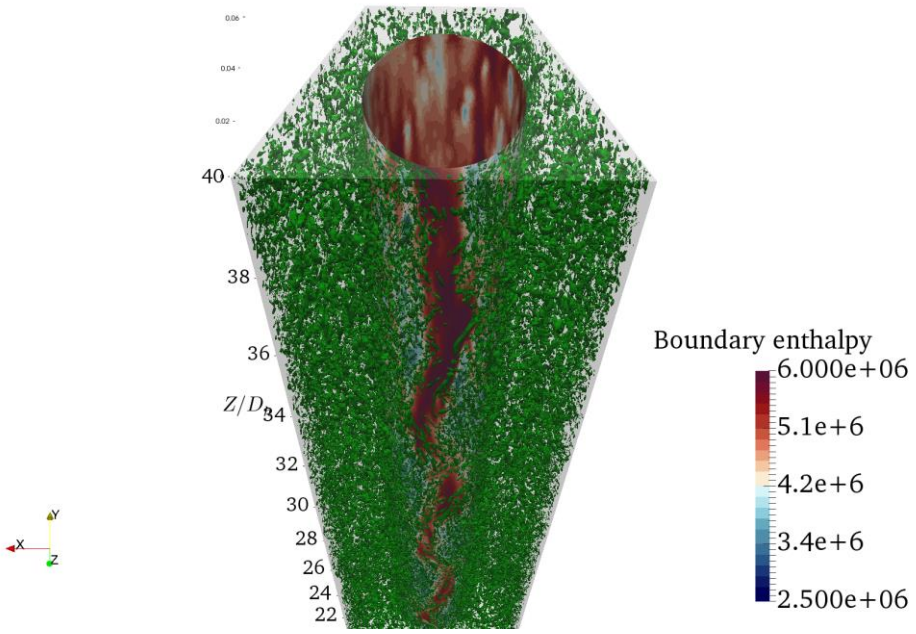
0.06
0.04
0.02
40
38
36
Z/D_{34}
32
30
28
26
24
22
Y
X
Z
Boundary enthalpy
6.000e+06
5.1e+6
4.2e+6
3.4e+6
2.500e+06

(c)

Appendix B

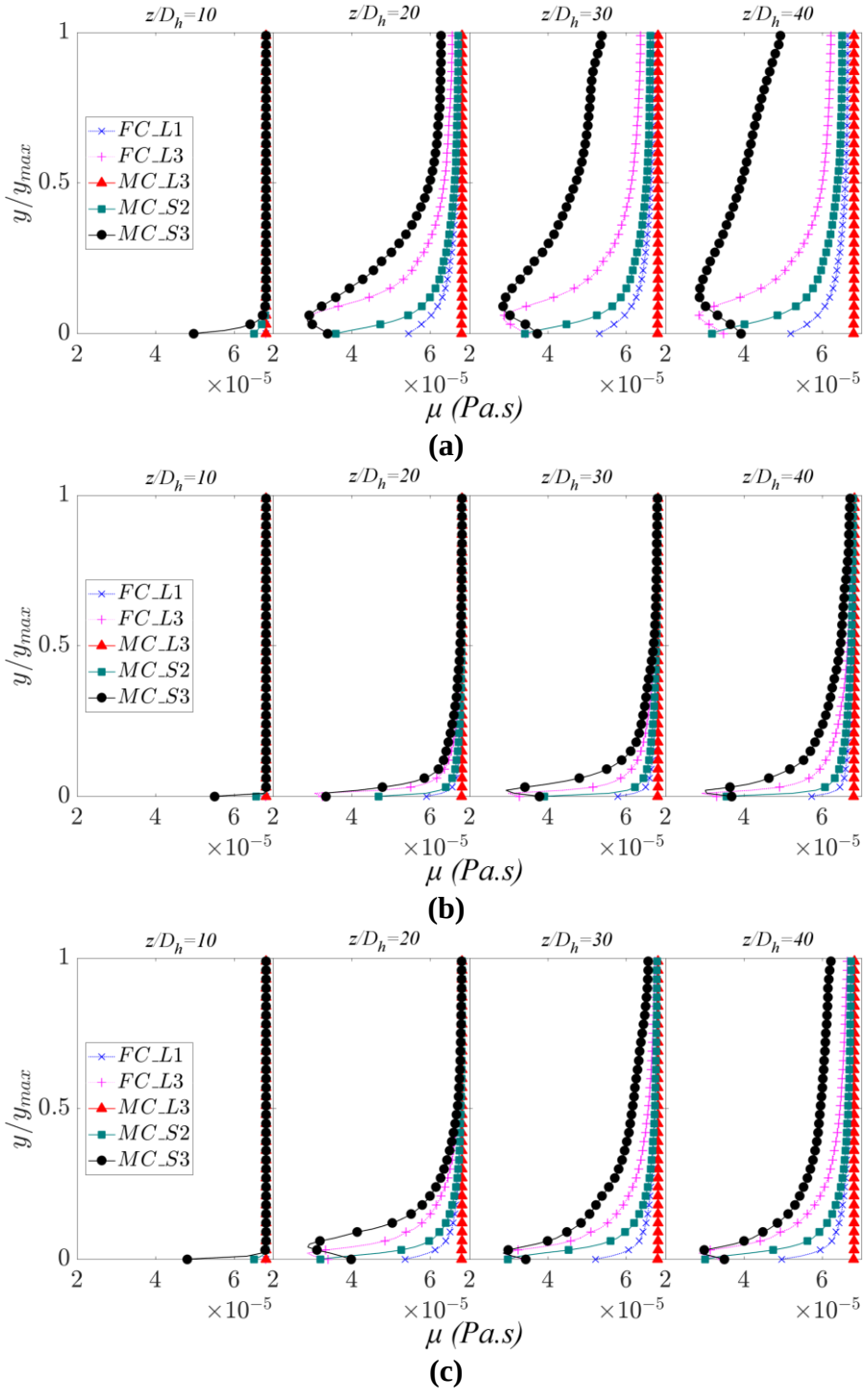

Figure B.1: Dynamic viscosity, μ along a) NL b) ML c) BL

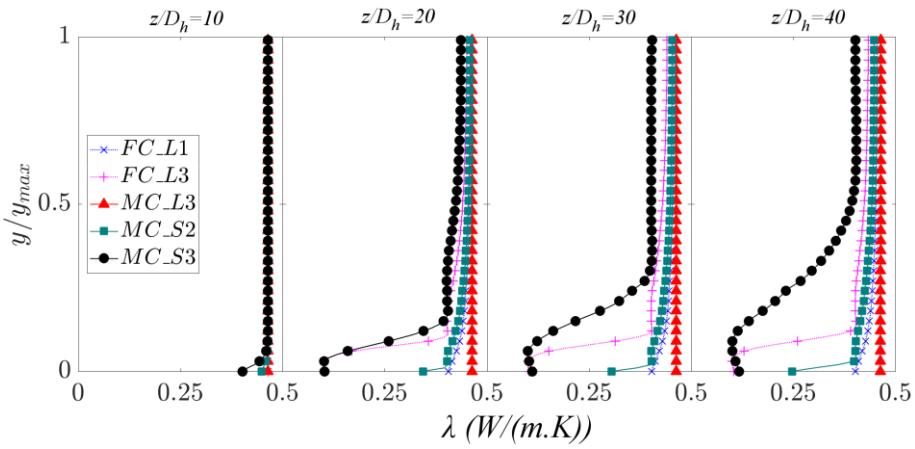

(a)

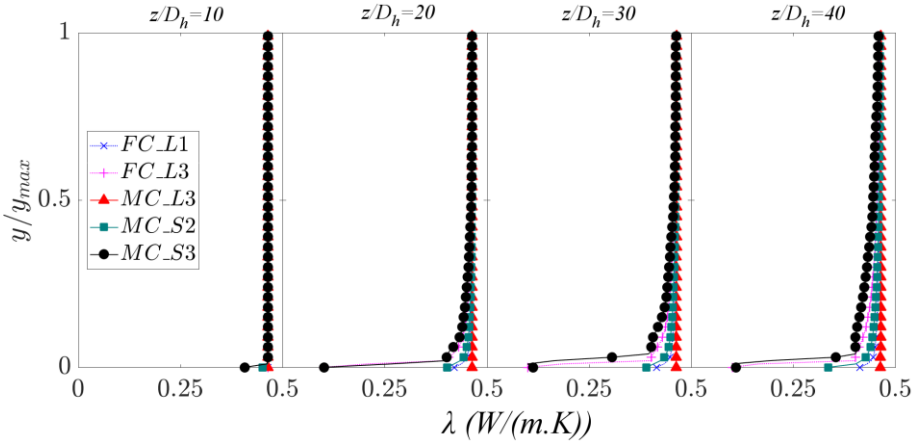

(b)

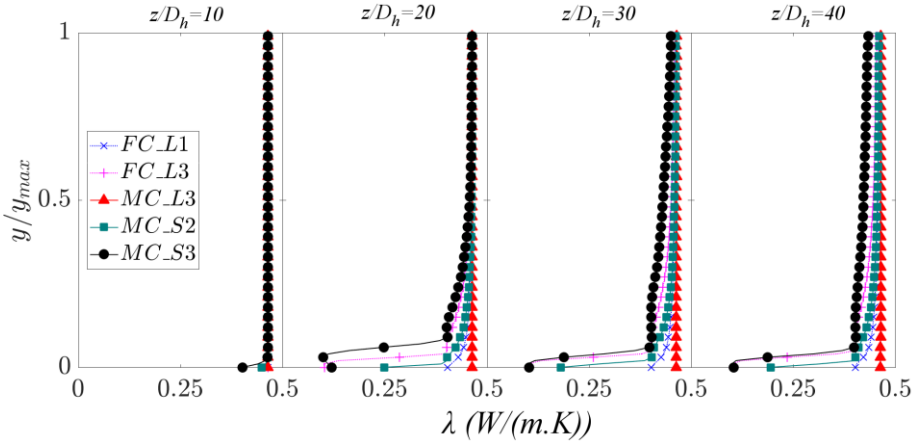

(c)

Figure B.2: Thermal conductivity, λ along a) NL b) ML c) BL

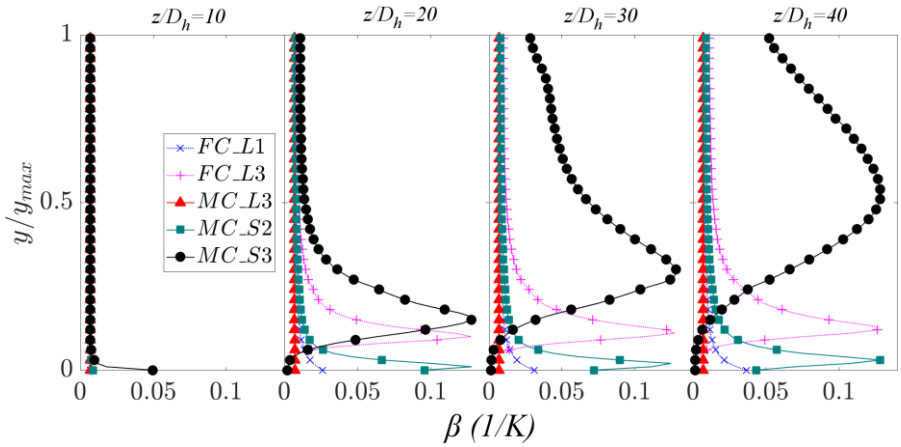

(a)

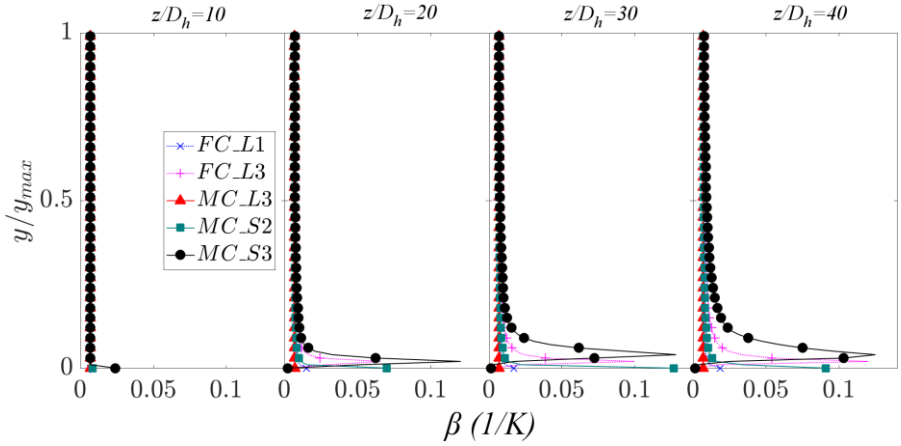

(b)

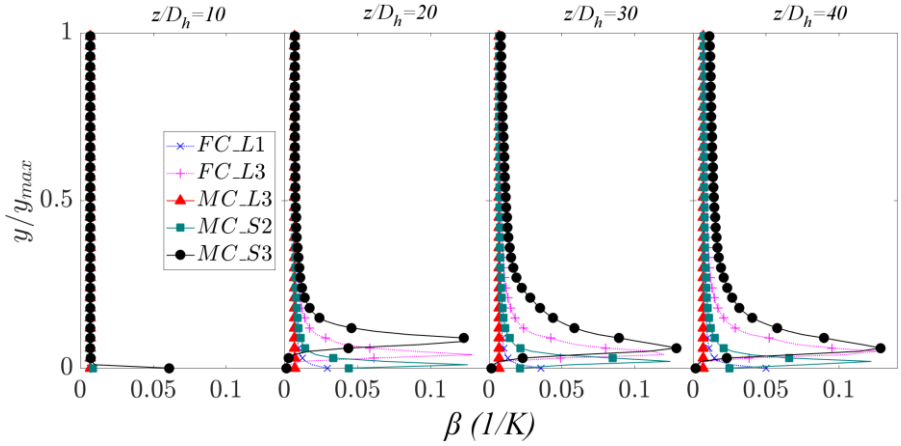

(c)

Figure B.3: Thermal expansion rate, β along a) NL b) ML c) BL